CONSIDERATION OF MICROSTRUCTURAL CHANGES IN THE STUDY OF ADIABATIC SHEAR BANDS

FINAL REPORT

R. C. BATRA

September 1994

U. S. ARMY RESEARCH OFFICE

GRANT NO. DAAL 03-91-G-0084

UNIVERSITY OF MISSOURI - ROLLA
ROLLA, MO 65401

APPROVED FOR PUBLIC RELEASE
DISTRIBUTION UNLIMITED

REPORT DOCUMENTATION PAGE

Form Approved
OMB No. 0704-0188

1. AGENCY USE ONLY (Leave blank)	2. REPORT DATE	3. REPORT TYPE AND DATES COVERED
	September 1994	Final 10 Mar 91 - 9 Sept 94

4. TITLE AND SUBTITLE
Consideration of Microstructural Changes in the Study of Adiabatic Shear Bands

5. FUNDING NUMBERS
DAAL03-91-G-0084

6. AUTHOR(S)
Romesh C. Batra

7. PERFORMING ORGANIZATION NAME(S) AND ADDRESS(ES)
University of Missouri-Rolla
Rolla, MO 65401-0249

8. PERFORMING ORGANIZATION REPORT NUMBER

9. SPONSORING/MONITORING AGENCY NAME(S) AND ADDRESS(ES)
U. S. Army Research Office
P. O. Box 12211
Research Triangle Park, NC 27709-2211

10. SPONSORING/MONITORING AGENCY REPORT NUMBER
ARO 28283.22-EG

11. SUPPLEMENTARY NOTES
The view, opinions and/or findings contained in this report are those of the author(s) and should not be construed as an official Department of the Army position, policy, or decision, unless so designated by other documentation.

12a. DISTRIBUTION/AVAILABILITY STATEMENT
Approved for public release; distribution unlimited.

12b. DISTRIBUTION CODE

13. ABSTRACT *(Maximum 200 words)*
We have analyzed the effect of microstructural changes on the initiation and growth of shear bands. These have been studied by i) developing an adaptive mesh refinement technique to decipher adiabatic shear bands in two-dimensional problems, ii) formulating a three-dimensional finite-deformation theory for dipolar thermoviscoplastic materials and using it to examine the initiation and growth of shear bands in plane strain thermomechanical deformations of dipolar materials, iii) employing an internal variable theory of Brown, Kim and Anand to study the shear band problem, iv) investigating the possibility of phase transformations during the development of adiabatic shear bands in a steel specimen, v) ascertaining the speed of propagation of a shear band in a steel tube, vi) assessing the effect of frictional forces between the loading device and the cylinder ends, and, vii) analyzing the development of a shear band in a FCC single crystal. Principal results obtained during these investigations are summarized in the report.

14. SUBJECT TERMS	15. NUMBER OF PAGES
adiabatic shear bands, microstructural changes, dynamic loading	155
	16. PRICE CODE

17. SECURITY CLASSIFICATION OF REPORT	18. SECURITY CLASSIFICATION OF THIS PAGE	19. SECURITY CLASSIFICATION OF ABSTRACT	20. LIMITATION OF ABSTRACT
UNCLASSIFIED	UNCLASSIFIED	UNCLASSIFIED	UL

TABLE OF CONTENTS

I. STATEMENT OF THE PROBLEM STUDIED

Adiabatic shear bands are narrow regions of intense plastic deformation that form during high strain-rate processes, such as shock loading, ballistic penetration, metal forming, and machining. As these bands generally precede material fracture, a knowledge of factors that inhibit or enhance their growth is essential to the production of durable materials. These bands form in both ferrous and nonferrous alloys.

Johnson[1] has recently pointed out that Tresca[2] in 1878 and Massey[3] in 1921 observed hot lines, now referred to as adiabatic shear bands, during the forging of platinum. Both Tresca and Massey stated that these were the lines of greatest sliding, and also therefore the zones of greatest development of heat. In 1944, Zener and Hollomon[4] observed 32μm wide shear bands during the punching of a hole in a 0.25% C low alloy steel plate and stated that the microstructure of the material within the shear band was martensitic. They added that heating caused by the plastic deformation of the material made it softer and the material became unstable when this thermal softening equalled the combined effects of strain and strain-rate hardening. Further evidence of the change in the microstructure within the shear band to martensite is cited by Rogers [5] in his review article and also by Backman and Finnegan[6]. Stock and Thompson[7], and Bedford, Wingrove, and Thompson[8] have suggested that the material within an adiabatic shear band melts. Even when the material does not melt, the temperatures reached within the band are high enough for phase changes to occur. We note that the peak homologous temperature, i.e., the absolute temperature of a material particle divided by the melting temperature of the material in degrees Kelvin, equal to 0.7 or higher has been estimated from experimental measurements [9,10] and has also been confirmed computationally[11,12]. Different phases of the same material generally have quite different thermophysical properties, and the phase transformations may involve absorption or release of the latent heat, volume change and shearing deformations.

The dynamic torsional experiments of Culver[13] on mild steel, titanium, and 6061-T6 aluminum indicate that the localization began near the peak in the stress-strain curve for each material tested. This observation seems to be borne out by the experimental work of Costin et al.[14] However, recent experimental [9,10] and numerical[11,12] investigations have established that the localization of the deformation initiates in earnest at a value of the average strain much greater than the value at which the shear stress or the effective stress attains its peak value. Experimental findings of Marchand and Duffy[9] on HY-100 steel indicate that the shear strain localization phenomenon consists of three stages. In the first stage, the deformation stays homogeneous. Stage two, stipulated to initiate when the shear stress attains its peak value, involves non-homogeneous deformations of the block. In stage three, the shear stress drops precipitously and the severely deforming region narrows considerably. Thus the stability criterion[15,16] based on the stress attaining a maximum value, will predict the initiation of stage two rather than the beginning of the intense localization of the deformation.

In a departure from the notion of a criterion based on a stress maximum, Clifton[17]

and Bai[18] examined the growth of infinitesimal periodic nonuniformities in an otherwise uniform simple shearing deformation. Burns[19] used a dual asymptotic expansion to include the time dependence of the homogeneous solution in the analysis of the growth of an initially small perturbation. His work suggests that initiation of an unstable shear band, followed by exponential growth, occurs after a critical shear strain corresponding to the peak stress in the homogeneous deformation for the same overall strain rate is reached. On the other hand, Shawki et al.[20], by using both numerical and perturbation techniques, concluded that exponential growth is not a sufficient condition for judging whether or not a shear band forms, as the corresponding homogeneous deformation may also grow extremely rapidly once the peak stress has been reached and growth is not restricted to a narrow band. Anand et al.[21] have generalized Clifton's analysis of small perturbations superimposed upon a uniform simple shearing deformation to 3-dimensional problems.

Both numerical and experimental works indicate that peak strain gradients of 0.2 per μm or higher are reached. A deforming region with such high strain gradients is expected to experience a force which inhibits the growth of inhomogeneities without totally suppressing them. This led Wright and Batra[22] to use a dipolar theory, obtained by modifying the dipolar theory of Green et al. [23] to include strain-rate effects, in the analysis of the shear band problem. Coleman and Hodgdon[24] introduced the mollifying force by adding, to the expression for the stress in the classical flow rule, a term linear in the second spatial gradients of the accumulated strain. Aifantis and his coworkers[25,26] used a different set of reasoning to consider gradients of strain in the theory. Earlier, Dillon and Kratochvil[27] proposed a strain gradient theory of plasticity valid for infinitesimal deformations in which second and third order spatial gradients of the displacement were also taken as independent variables. Their motivations for including higher order gradients were: 1) the basic concept of work hardening due to Seeger[28] in which dislocations interact and therefore the internal forces are not restricted to being of the contact type, and 2) the experimentalist using a better strain gauge observes a change in the non-homogeneous residual deformations in a standard tensile test if he also observes large-scale plastic strains.

In contrast to the consideration of phase transformations and the use of higher order spatial gradients of the displacements, another way to account for structural changes is to use constitutive equations which employ a suitable number of scalar and tensor valued internal variables. Nemat-Nasser[29] has recently reviewed the literature on the use of internal variables in the constitutive theory. Guided by the recent work of Loret[30] and Dafalias[31], Anand[32] has provided a set of constitutive equations appropriate for large deformation elasto-plasticity that include two internal variables: a scalar and a symmetric, traceless second-order tensor as measures which, in an average sense, represent an isotropic and an anisotropic resistance to plastic flow offered by the internal state of the material. The theory allows for a phenomenological modeling of texture development or structural anisotropy.

All of the works on shear banding referred to above have involved analyzing simple shearing deformations of a viscoplastic block containing a material inhomogeneity.

LeMonds and Needleman[33,34], Needleman[35], Anand et al.[36], Zbib and Aifantis[37], Batra and Liu[38,39], Zhu and Batra[40], and Batra and Zhang[41] have studied the phenomenon of shear banding in plane strain deformations of a viscoplastic solid. Whereas Needleman studied a purely mechanical problem, other works have treated a coupled thermomechanical problem. LeMonds and Needleman, and Anand et al. neglected the effect of inertia forces on the ensuing deformations of the body. These investigations have employed different constitutive relations, different techniques to integrate the stiff set of governing partial differential equations and the conventional finite elements. It seems that the use of recently proposed enhanced elements[42-44] designed for the localization problems should enable one to capture the details of the localization problem within reasonable computational resources.

II. BRIEF REVIEW OF COMPLETED WORK

We have analyzed the effect of microstructural changes on the initiation and growth of shear bands. These were studied by i) developing an adaptive mesh refinement technique to decipher adiabatic shear bands in two-dimensional problems, ii) formulating a three-dimensional finite-deformation theory for dipolar thermoviscoplastic materials and using it to examine the initiation and growth of shear bands in plane strain thermomechanical deformations of dipolar materials, iii) employing an internal variable theory of Brown, Kim, and Anand to study the shear band problem, iv) investigating the possibility of phase transformations during the development of adiabatic shear bands in a steel specimen, v) ascertaining the speed of propagation of a shear band in a steel tube, vi) assessing the effect of frictional forces between the loading device and the cylinder ends, vii) analyzing the development of a shear band in a FCC single crystal, and viii) investigating the effect of softening caused by the nucleation and growth of voids. Principal results obtained during these investigations are summarized below.

One way to economize on computational cost, without compromising on accuracy, is to use adaptively refined meshes. For two-dimensional problems, we[45,46] have developed two adaptive mesh refinement techniques that concentrate fine elements within severely deforming regions and coarse elements elsewhere. In one of these techniques, developed for triangular elements, new nodes are added whenever and wherever necessary and thus the element topology changes with every mesh refinement. This is a little hard to implement in existing codes but can delineate shear bands as accurately as desired. The other technique, suitable for quadrilateral elements and easily incorporable in an existing code, keeps the mesh topology fixed but moves nodes around so as to concentrate finer elements in the severely deforming regions and coarser elements elsewhere. Both of these techniques have been successfully used[47,48] to study the localization of deformation into narrow bands originating from an inhomogeneity during high strain-rate plane strain deformations of thermoviscoplastic materials; adaptively refined meshes for a microporous steel block deformed in plane strain tension[48] at a nominal strain-rate of 5000/s are depicted in Fig. 1. The computed results reveal that the use of adaptively refined meshes results in lower errors in the numerical solution as compared to that obtained with a fixed mesh[45,46].

In each case, the computed solution is compared with a higher-order approximate solution. The evolution of the nondimensional temperature at the block centroid with softening first due to temperature rise only and then due to void nucleation and growth only is plotted in Fig. 2. It is apparent that for the material parameters considered herein, the softening caused by void nucleation and growth is significantly more than that caused by the temperature rise.

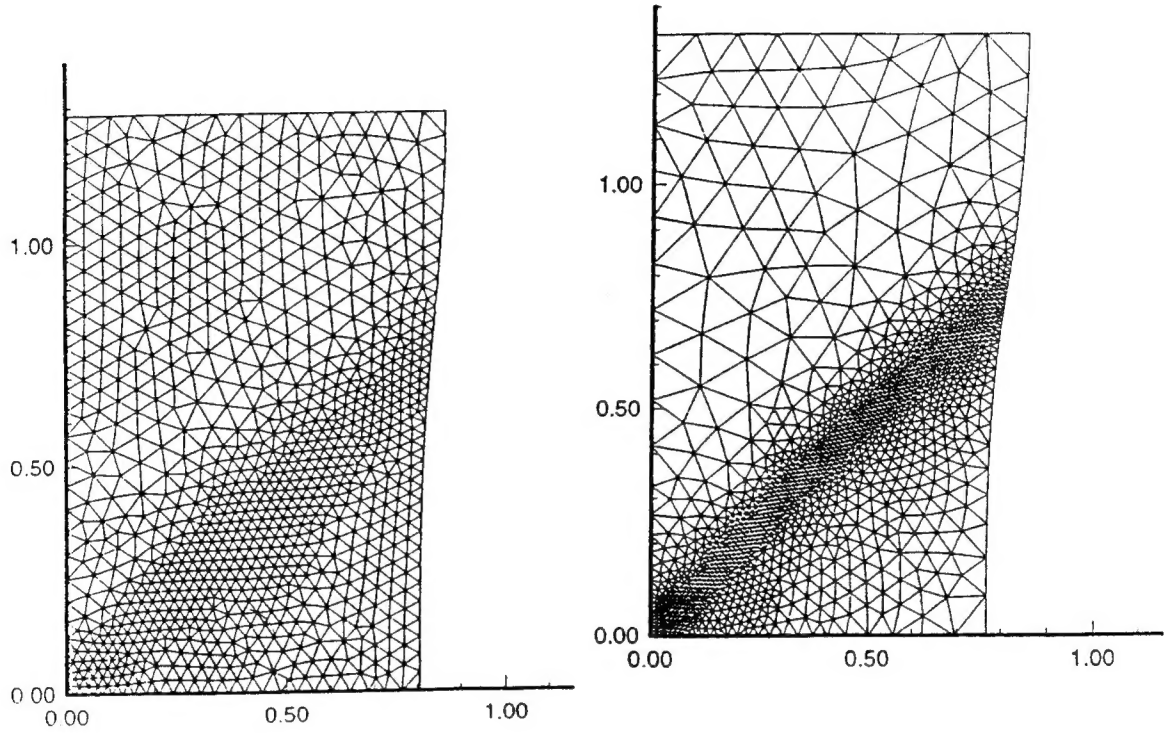

Figure 1. Two adaptively refined meshes during the plane strain tensile deformations of a porous thermoviscoplastic steel block[48].

A comparison[47] of results for an axisymmetric compression problem with those for a plane strain problem reveals that the initiation of shear bands is significantly delayed for the former. When the contact surfaces between the cylinder and the loading device are taken to be rough enough to prevent any sliding between the two, the cylinder deforms into a barrel; however, it deforms into a reversed barrel when the contact surfaces are smooth (*cf.* Fig. 3). These observations are in qualitative agreement with the test findings.

The large plastic deformations of an initially isotropic body change its microstructure and the response of the body to subsequent deformations is anisotropic. One way to account for these microstructural changes is to use an internal variable theory with two

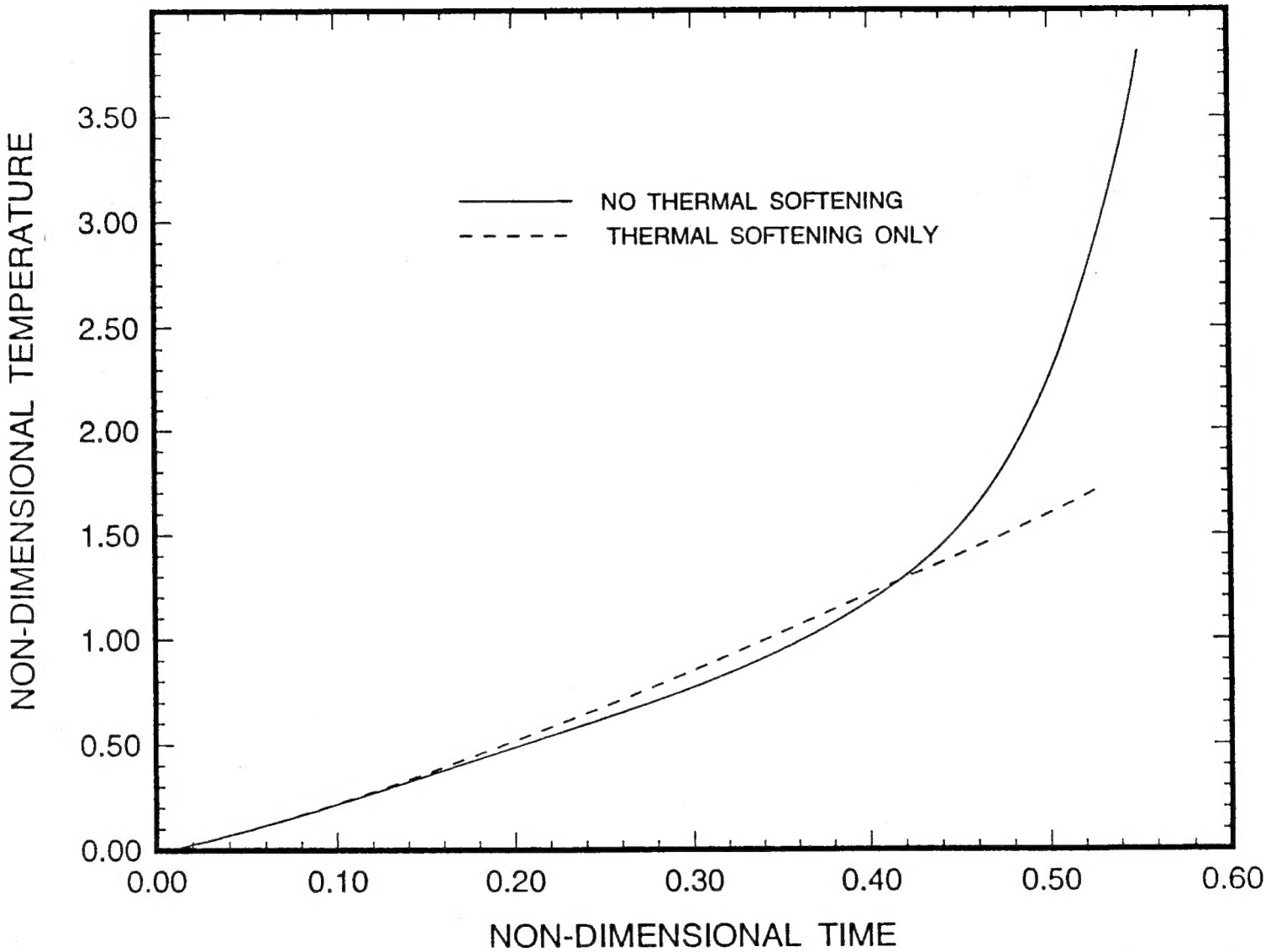

Figure 2. Evolution of the nondimensional temperature at the block centroid with softening due to (a) temperature rise only, and (b) void nucleation and growth only.

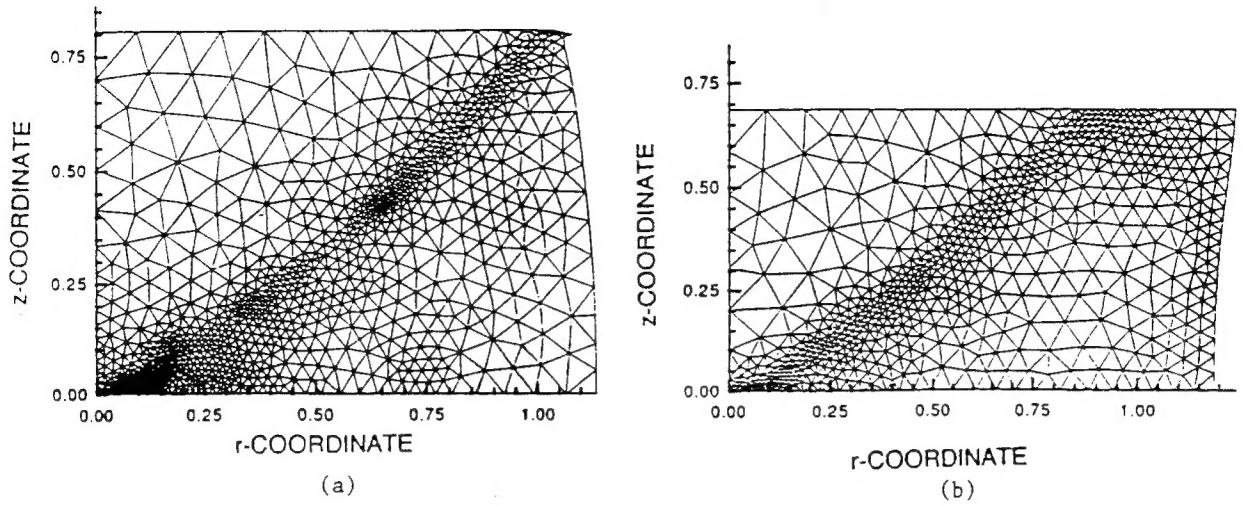

Figure 3. Refined meshes and deformed shapes of cylinders (a) with, and (b) without frictional forces at the contact surfaces[47]. In the undeformed reference configuration, the cylinder height and radius equalled one.

variables: a scalar and a symmetric, traceless second-order tensor which , in an average sense represent an isotropic and anisotropic resistance to plastic flow offered by the internal state of the material. We[49] used such a theory due to Brown, Kim & Anand[50] to assess the effect of anisotropic resistance to plastic flow, also known as kinematic hardening, on the initiation and growth of shear bands in a steel block deformed in plane strain compression at a nominal strain-rate of 5000/s. The qualitative nature of computed results was unaffected by the consideration of kinematic hardening, and was similar to that obtained by using the constitutive relation proposed by Batra[51] and used by Batra & co-workers[45,46,52].

Zener & Hollomon[4], Rogers[5], Wingrove[53] and Kalthoff[54] have pointed out the presence of martensite within a shear band. An explanation given for the occurrence of martensite is that the material within the band is heated to a temperature far above the transformation temperature where ferrite transforms into austenite which is quenched rapidly by the surrounding cooler material and transformed into martensite. By postulating rather simple kinetic equations for the transformation of a mixture of ferrite and cementite into austenite during heating, from austenite to a mixture of austenite and pearlite during cooling and then to martensite or directly from austenite to martensite, accounting for the latent energy required for phase transformations, and volume changes associated with them, and using the rule of mixtures to determine the thermophysical properties of a material point, we[55] have investigated the feasibility of the formation of martensite within a shear band developed in a steel block deformed in plane strain compression. It is evident from the cooling curve for a point within a shear band, shown in Fig. 4, that the austenite is quenched fast enough to be transformed into martensite rather than a mixture of pearlite and austenite.

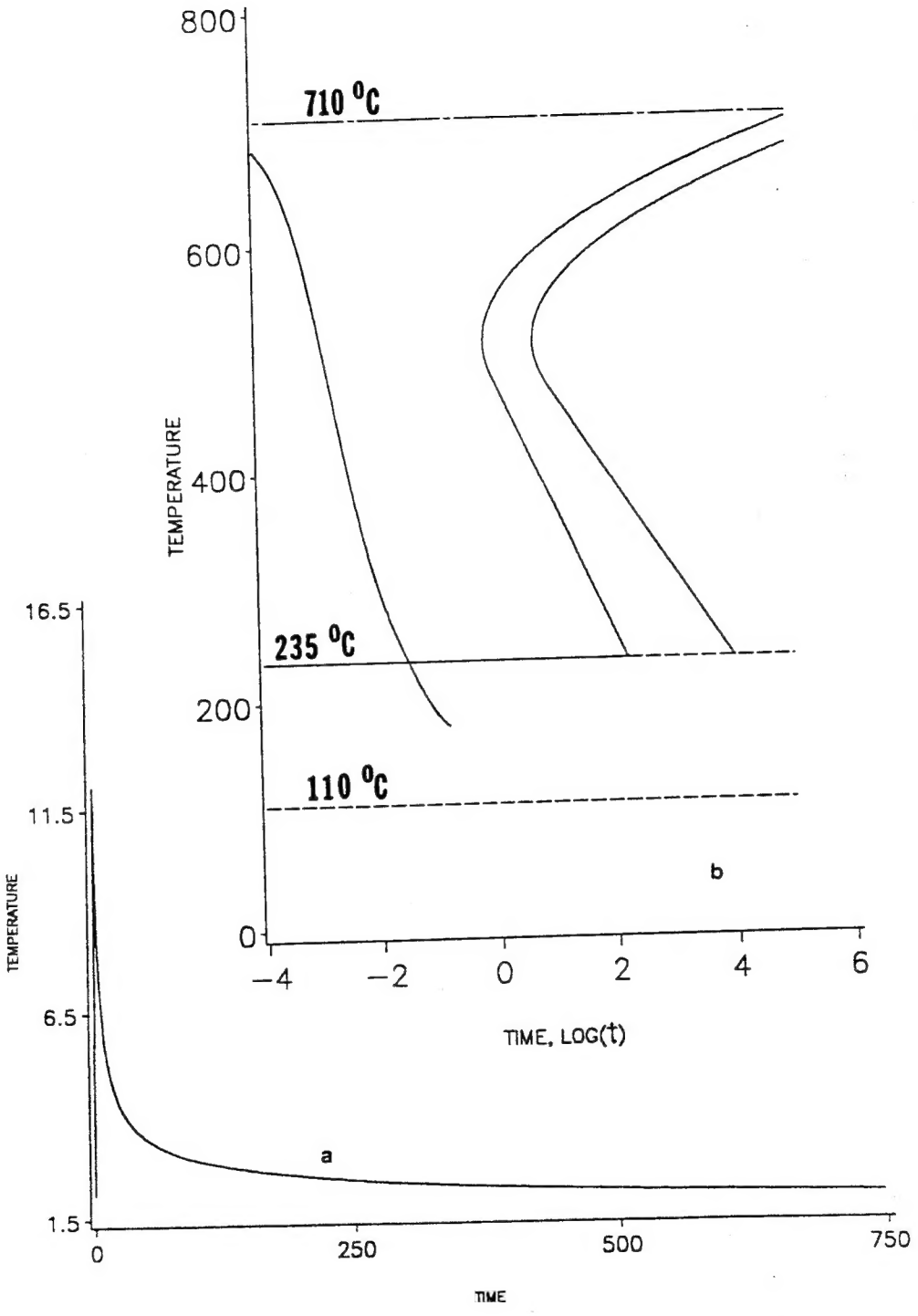

Figure 4. (a) Variation of temperature at a point within the shear band, and (b) cooling curve for the point superimposed on the C-C-T diagram.

Motivated by experimental and numerical observations that the peak strain gradients of the order of 0.2 per μm occur within and in the vicinity of a shear band, Wright & Batra[22] proposed a one-dimensional theory for rate dependent dipolar materials by modifying the dipolar theory of Green *et al.*[23] to include rate effects. We[56] have generalized this theory to study 3-dimensional finite deformations of thermoviscoplastic materials. The theory introduces a material characteristic length in addition to the viscous and thermal lengths. The computed results indicate that the consideration of dipolar effects stiffens the material response in the sense that the rate of growth of the second invariant of the strain-rate tensor and temperature at the point of the initiation of the shear band is lower as compared to that for nonpolar materials. Also, the width of the severely deforming region is more for dipolar materials as compared to that for nonpolar materials. For reasonably fine meshes and suitable values of the material characteristic length, computed results are found to be independent of the finite element mesh.

To understand the micromechanics of shear band formation in polycrystalline materials, we[57] studied the development of shear bands in a FCC single crystal deformed in plane strain compression along the crystallographic direction [010] with the plane of deformation either parallel to the plane (001) or (101) of the single crystal. The material defect is modeled by introducing a temperature perturbation at the centroid of the square block. All twelve slip systems were taken to be potentially active. In the former case, a single shear band making an angle of 45° with the horizontal line ensues from the centroid of the cross-section where the temperature is perturbed. The slip strains on the slip systems (111)[110], (111)[$\bar{1}$10], ($\bar{1}$11)[110], and ($\bar{1}$11)[$\bar{1}$10] are high, and these constitute the primary slip systems. At a nominal strain of 0.108, the maximum angle of rotation of the crystal lattice within the band equals 18.54° counterclockwise. When the plane of deformation is parallel to the plane (101) of the single crystal, the shear band originating from the center of the cross-section makes an angle of 39.5° with the horizontal, and eventually splits into two bands. This is evidenced by the contours of the maximum principal logarithmic strain, plotted in Fig. 5, at four different values of the average strain. Slip systems (111)[$\bar{1}$10] and (111)[011] within the band are found to be more active than other slip systems.

When the FCC single crystal is deformed along the crystallographic direction [380] with the plane of deformation parallel to the plane (001) of the single crystal, it was found that the nonhomogeneity of deformations caused by different amounts of plastic deformation on various slip systems was enough to induce a shear band no matter whether the crystal was compressed or pulled[58]. Each one of the slip systems (111)[$\bar{1}$10], ($\bar{1}$11)[110], ($\bar{1}$11)[$\bar{1}$10], and ($\bar{1}$11)[$\bar{1}$10] contributes essentially equally to the plastic deformation of the crystal and these slip systems become active soon after the load is applied. The same holds for slip systems (111)[011], ($\bar{1}$11)[$\bar{0}$11], ($\bar{1}$11)[101], and (111)[$\bar{1}$01] except that they are active in a region different from that of the previous one. The remaining four slip systems either stay inactive throughout the deformation process, or become active at late stages of the deformation.

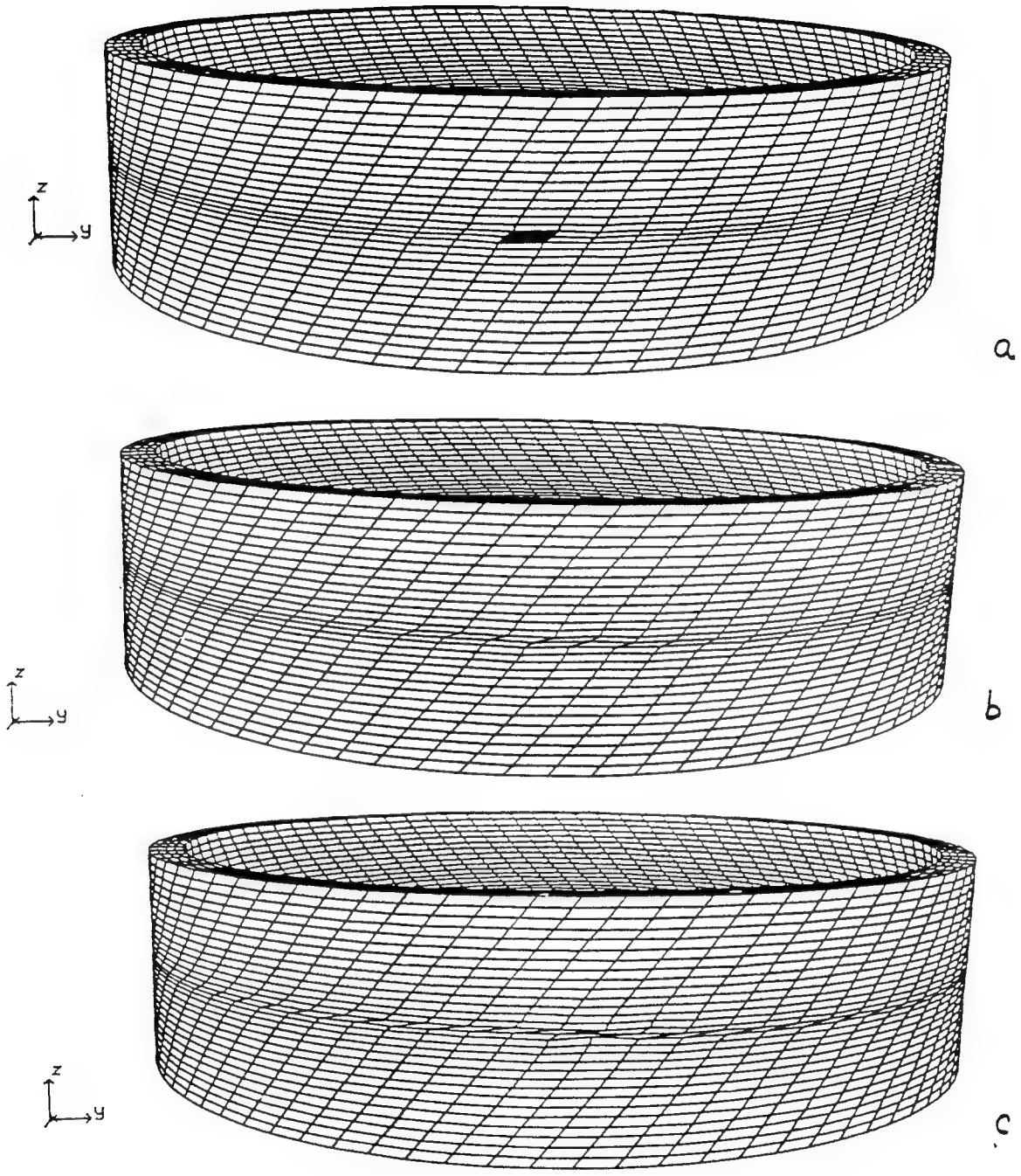

Figure 5. Deformed meshes at (a) t = 140 μs, (b) t = 180 μs, and (c) t = 200 μs for the steel tube twisted at an average strain-rate of 5000/s.

We[59] have simulated numerically Marchand & Duffy's[9] torsion test on a thin-walled steel tube with the objectives of determining whether a shear band initiating from a defect will propagate around the tube simultaneously in both directions or in one direction and ascertaining its speed of propagation. The deformed meshes , at three different times, for the steel tube deformed at a nominal strain-rate of 5000/s are shown in Figs. 5a - 5c. Initially vertical lines are deformed into essentially parallel inclined lines in Fig. 5a indicating that the tube is deformed homogeneously except in a small area adjoining the shaded area. The flow strength of the material in the shaded region is taken to be 10% lower than that of the rest of the material. In Figs. 5b and 5c, a small region near the central section of the tube is deformed severely indicating the localization of the deformation there. The localization region propagates further to the left and right between $t = 180\ \mu s$ and $t = 200\ \mu s$. The band was found to propagate in both directions at the same speed which varied from 180 m/s at the site of the initiation of the band to approximately 1000 m/s at the nearly diametrically opposite point when the tube was twisted at a nominal strain-rate of 5000/s (*cf.* Fig. 6a). Results plotted in Fig. 6b indicate that the band speed increases with an increase in the nominal strain-rate.

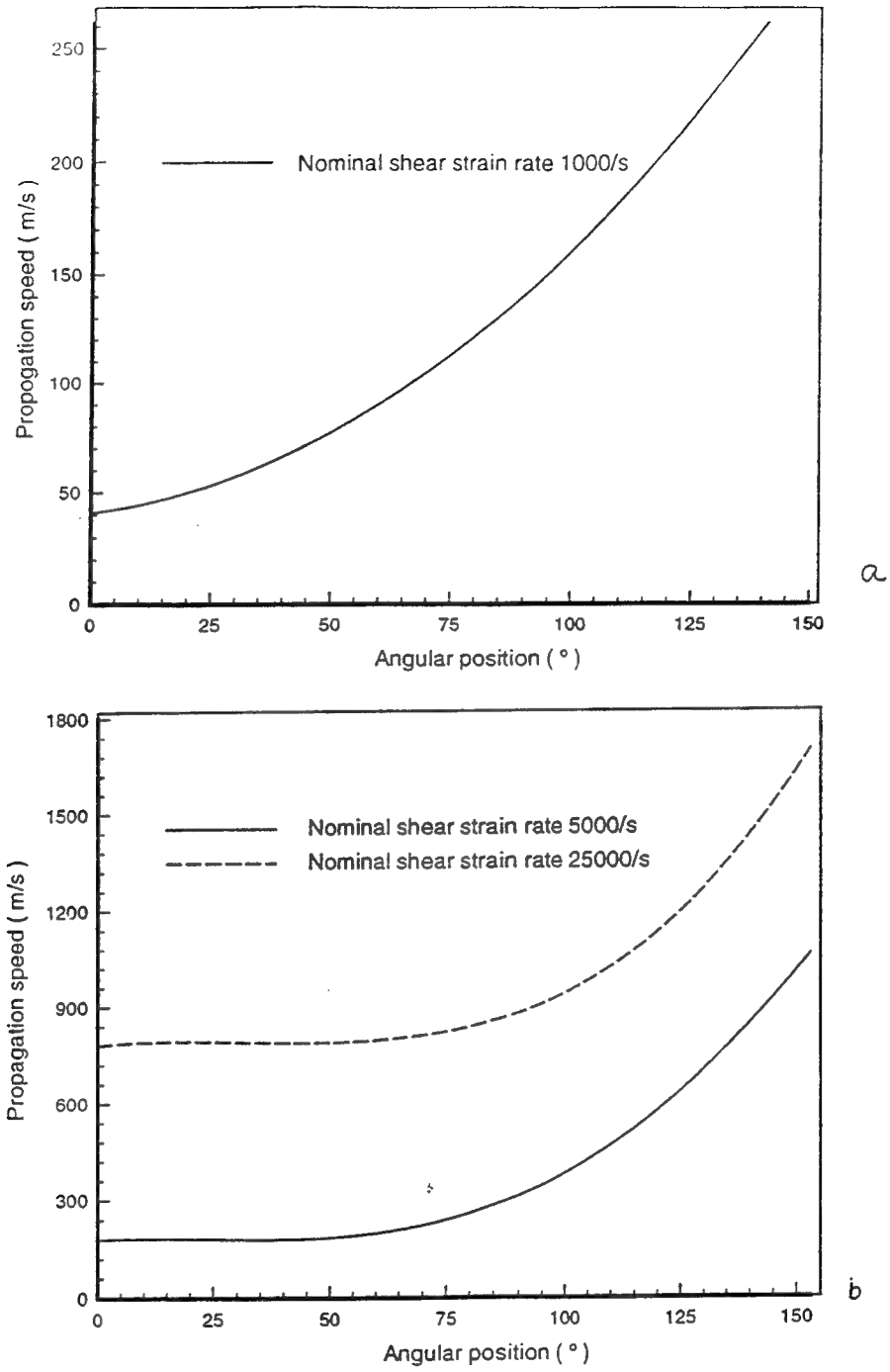

Figure 6. Speed of propagation of the shear band in a steel tube deformed in torsion. The angular position is measured from the center of the weak region.

III. LIST OF PUBLICATIONS

(a) Refereed Journals

1. R. C. Batra and K. I. Ko, An Adaptive Mesh Refinement Technique for the Analysis of Shear Bands in Plane Strain Compression of a Thermoviscoplastic Solid, ***Computational Mechs.***, **10**, 369-379, 1992.

2. R. C. Batra, Analysis of Shear Bands in Simple Shearing Deformations of Nonpolar and Dipolar Viscoplastic Materials, ***Appl. Mechs. Rev.***

3. R. C. Batra and K. I. Ko, Analysis of Shear Bands in Dynamic Axisymmetric Compression of a Thermoviscoplastic Cylinder, ***Int. J. Engng. Sci.***, **31**, 529-547, 1993.

4. R. C. Batra and J. Hwang, An Adaptive Mesh Refinement Technique for Two-Dimensional Shear Band Problems, ***Computational Mechs.***, **12**, 255-268, 1993.

5. Z. G. Zhu and R. C. Batra, Consideration of Phase Transformations in the Study of Shear Bands in a Dynamically Loaded Steel Block, ***J. Eng'g Mat'l Tech.***, **114**, 368-377, 1992.

6. Z. G. Zhu and R. C. Batra, Analysis of Dynamic Shear Bands in an FCC Single Crystal, ***Int. J. Plasticity***, **9**, 653-696, 1993.

7. R. C. Batra and X. T. Zhang, Analysis of Shear Bands in a Dynamically Loaded Viscoplastic Cylinder Containing Two Rigid Inclusions, ***Acta Mechanica***, **100**, 105-114, 1993.

8. Y. Wang and R. C. Batra, Effect of Kinematic Hardening on the Initiation and Growth of Shear Bands in Plane Strain Compression of a Thermoviscoplastic Solid, *Acta Mechanica*, **102**, 217-233, 1994.

9. R. C. Batra and X. Zhang, On the Propagation of a Shear Band in a Steel Tube, *J. Eng'g Materials & Technology*, **116**, 155-161, 1994.

10. R. C. Batra and L. Wang, Analysis of Dynamic Shear Bands Under Combined Loading, *Int. J. Eng'g Analysis & Design*, **1**, 79-90, 1994.

11. R. C. Batra, X. Zhang and T. W. Wright, Critical Strain Ranking of Twelve Materials in Deformations Involving Adiabatic Shear Bands, *J. Appl. Mechs.*, (in press).

12. R. C. Batra and J. Hwang, Dynamic Shear Band Development in Dipolar

Thermoviscoplastic Materials, *Computational Mechs.*, (in press).

13. R. C. Batra and Z. G. Zhu, Effect of Loading Direction and Initial Imperfections on the Development of Dynamic Shear Bands in a FCC Single Crystal, *Acta Mechanica* (in press).

14. R. C. Batra and X. S. Jin, Analysis of Dynamic Shear Bands in Porous Thermally Softening Viscoplastic Materials, *Archives of Mechanics*, (in press).

(b) Conference Proceedings

1. X. T. Zhang and R. C. Batra, Shear Band Development in a Viscoplastic Cylinder, *in Anisotropy and Localization of Plastic Deformation*,(J.-P. Boehler and A. S. Khan, eds.), Elsevier Appl. Sci., pp.103-106, 1991.

2. X. T. Zhang and R. C. Batra, Effect of Different Boundary Conditions on the Development of a Shear Band in a Viscoplastic Cylinder, *in High Temperature Constitutive Modeling: Theory and Application* (A. Freed and K.P. Walker, eds.), AMD Vol. 121, ASME Press, New York, pp. 335-350, 1991.

(c) Doctoral Dissertations

1. K. I. Ko, An Adaptive Mesh Refinement Technique for Two-Dimensional Problems and its Application to the Analysis of Shear Bands, Ph.D. Dissertation, Univ. of Missouri-Rolla, Rolla, February 1992.

2. J. Hwang, Analysis of Dynamic Shear Bands in Plane Strain Compression of Dipolar Thermoviscoplastic Materials by Using an Adaptively Refined Mesh, Ph.D. Dissertation, University of Missouri-Rolla, Rolla, November 1992.

3. X. T. Zhang, Finite Element Analysis of Dynamic Shear Bands in 2-D and 3-D Deformations of Thermoviscoplastic Materials, Doctoral Dissertation, University of Missouri-Rolla, Rolla, October 1993.

(d) Masters' Theses

1. L. Wang, Analysis of Dynamic Shear Bands Under Combined Loading, M.S. Thesis, University of Missouri-Rolla, Rolla, March 1993.

2. C. Adulla, Effect of Prior Quasistatic Loading, Defect Shape, and Defect Size on the Initiation and Growth of Dynamic Adiabatic Shear Bands, University of Missouri-Rolla, Rolla, July 1994.

IV. LIST OF PRESENTATIONS

1. R. C. Batra and C. H. Kim, Analysis of Shear Banding in Twelve Materials, *9th U.S. Army Conf. on Appl. Math. and Computing*, Minneapolis, MN, June 1991.

2. R. C. Batra, K. I. Ko and A. K. Patra, Analysis of Shear Bands in Dynamic Plane Strain Compression of a Viscoplastic Solid, *ASME Appl. Mechs. Conf.*, Columbus, OH, June 1991.

3. Y. H. Cao and R. C. Batra, A Self-Adaptive Finite Difference Scheme for the Analysis of One-Dimensional Shear Banding Problem, *1st U.S. National Cong. on Computational Mechs.*, Chicago, IL, June 1991.

4. X. T. Zhang and R. C. Batra, Shear Band Development in a Viscoplastic Cylinder, *3rd Int. Symp. Plasticity and its Current Appl.*, Grenoble, France, Aug. 1991.

5. R. C. Batra, Analysis of Shear Bands in Plane Strain Deformations, *22nd Midwestern Mechs. Conf.*, Univ. of Missouri, Rolla, MO, Oct. 1991.

6. Z. G. Zhu and R. C. Batra, Effect of Phase Transformations on the Development of Shear Bands in a Steel, *28th Annual Tech. Meeting of the Soc. of Engng Sci.*, Univ. of Florida, Gainesville, Nov. 6 - 8, 1991.

7. X. T. Zhang and R. C. Batra, Effect of Different Temperature Boundary Conditions on the Development of a Shear Band in a Viscoplastic Cylinder, *ASME Winter Annual Meeting*, Atlanta, Dec. 1991.

8. Z. G. Zhu and R. C. Batra, Consideration of Phase Transformations in the Study of Shear Bands in a Dynamically Loaded Steel Block, *ASME Applied Mechanics, Materials and Aerospace Divisions Annual Summer Meeting*, Scottsdale, AZ, April 28 - May 1, 1992.

9. R. C. Batra, Z. G. Zhu and Y. Wang, Consideration of Phase Transformations and Kinematic Hardening in the Study of Shear Bands in a Dynamically Loaded Steel Block, *18th Int. Congress of Theoretical & Appl. Mechs.*, Haifa, Israel, Aug. 22 - 28, 1992.

10. Z. G. Zhu and R. C. Batra, Analysis of Dynamic Shear Bands in a Single Crystal, *29th Annual Tech. Meeting of the Soc. of Engng Sci.*, Univ. of California - San Diego, Sept. 1992.

11. R. C. Batra and J. Hwang, Analysis of Dynamic Shear Bands in Plane Strain Compression of Dipolar Thermoviscoplastic Materials, *Joint SES/ASME/ASCE*

meeting, Univ. of Virginia, Charlottesville, June 6 - 9, 1993.

12. R. C. Batra and Z. G. Zhu, On the Development of Dynamic Shear Bands in a FCC Single Crystal, *Joint SES/ASME/ASCE meeting*, Univ. of Virginia, Charlottesville, 1993.

13. R. C. Batra and X. S. Jin, Analysis of Dynamic Shear Bands in a Porous Thermoviscoplastic Solid, *Fourth Int. Symp. on Plasticity and its Current Applications*, Baltimore, July 19 - 23, 1993. **(invited paper)**.

14. R. C. Batra, Adiabatic Shear Banding in Thermoviscoplastic Materials, *U.S. Naval Academy*, Annapolis, MD, Nov. 19, 1993.

15. R. C. Batra, Analysis of Shear Bands in Thermoviscoplastic Materials, *Northwestern Univ.*, Evanston, Il, Nov. 5, 1993.

16. R. C. Batra, Analysis of Adiabatic Shear Bands in Thermoviscoplastic Materials, *National Taiwan Univ.*, Taipei, Oct. 1993

17. R. C. Batra, Adiabatic Shear Banding in Porous Thermoviscoplastic Materials, *National Chung-Cheng Univ.*, Min-Hsiung, Taiwan, Oct. 1993.

18. R. C. Batra, K. -I. Ko and J. Hwang, Adaptive Mesh Refinement Techniques for Two-Dimensional Localization Problems, *Symp. on Compressive Failure and Localization Phenomena in Fibrous Composites, ASME Winter Annual Meeting*, New Orleans, Nov. 1993.

19. R. C. Batra, Analysis of Shear Bands in Plane Strain Deformations, Seminar, *Rensselaer Polytechnic Institute*, Troy, NY, Jan. 29, 1992.

20. R. C. Batra and C. Adulla, Analysis of Shear Bands in HY100 Steel Under Combined Loading, *12th U.S. National Congress of Applied Mechs.*, Seattle, June, 1994.

21. R. C. Batra, Analysis of Adiabatic Shear Bands in Dynamic Loading of Thermoviscoplastic Materials, *12th U.S. Nat'l Cong. Appl. Mechs.*, Seattle, June, 1994.

V. DEGREES AWARDED

1. K.-I. Ko, Ph.D., 1992.
2. J. Hwang, Ph.D., 1992.
3. X. Zhang, Ph.D., 1993.
4. L. Wang, M.Sc., 1993.
5. C. Adulla, M.Sc., 1994.

VI. PARTICIPATING SCIENTIFIC PERSONNEL

Romesh C. Batra
K. -I. Ko
J. S. Hwang
X. T. Zhang
L. Wang
C. Adulla
Y. H. Cao
Z. G. Zhu
X. S. Jin

VII. TECHNOLOGY TRANSFER

The computer code to analyze the one-dimensional shear banding problem for different materials was sent in September 1992 to Dr. T. Weerasooriya of the U. S. Army Materials Technology Directorate, and in November 1993 to Professors Reza Malek-Madani and S. Garcia of the U.S. Naval Academy. Dr. Weerasooriya has used the code to study the initiation and growth of shear bands in several materials.

The computer code to analyze two-dimensional plane strain shear banding problems was mailed to Dr. T. Weerasooriya in May 1994. The code refines the mesh adaptively.

VIII. BIBLIOGRAPHY

1. W. Johnson, Int. J. Mech. Sci., 29, 301 (1987).

2. H. Tresca, Proc. Inst. Mech. Engr., 30, 301 (1878).

3. H. F. Massey, Proc. Manchester Assoc. Engr., pp. 21-26 (1921).

4. C. Zener and J. H. Hollomon, J. Appl. Phys., 14, 22 (1944).

5. H. C. Rogers, Ann. Rev. Mat. Sci., 9, 283 (1979).

6. M. E. Backman and J. A. Finnegan, in "Metallurgical Effects at High Strain-Rates," R. W. Rhode et al. (eds.), Plenum Press, New York, pp. 531-543 (1973).

7. T. A. C. Stock and K. R. Thompson, Met. Trans., 1, 219 (1970).

8. A. J. Bedford, A. L. Wingrove and K. R. L. Thompson, J. Aust. Inst. Met., 19, 61 (1974).

9. A. Marchand and J. Duffy, J. Mechs. Phys. Solids, 36, 251 (1988).

10. J. H. Giovanola, Mechs. Materials, 7, 59 (1988).

11. T. W. Wright and J. Walter, J. Mech. Phys. Solids, 35, 701 (1987).

12. R. C. Batra and C. H. Kim, J. Mechs. Phys. Solids, 38, 859 (1990).

13. R. S. Culver, "Metallurgical Effects at High Strain-Rates," R. W. Rhode et al. (eds.), p. 519 (1973).

14. L. S. Costin, E. E. Crisman, R. H. Hawley and J. Duffy, Proc. 2nd Oxford Conf. Inst. Phys., London, p. 90 (1980).

15. R. F. Recht, J. Appl. Mech., 31, 189 (1964).

16. M. R. Staker, Acta Met., 29, 263 (1981).

17. R. J. Clifton, "Material Response to Ultra High Loading Rates," NRC National Material Advisory Board (U.S.) Report 356 (1980).

18. Y. L. Bai, "A Criterion for Thermoplastic Shear Instability," in Shock Waves and High Strain Rate Phenomenon in Metals, M. A. Meyers and L. E. Murr (eds.) Plenum Press, p. 227 (1981).

19. T. J. Burns, Sandia National Laboratory Report 83-1907, 1983.

20. T. G. Shawki, R. J. Clifton and G. Majda, ARO Report DAAG 29-81-K-0121/3 (1983).

21. L. Anand, K. H. Kim and T. G. Shawki, J. Mech. Phys. Solids, 35, 381 (1987).

22. T. W. Wright and R. C. Batra, Proc. IUTAM Symp. on Macro-and Micro-Mechanics of High Velocity Deformation and Fracture, K. Kawata and J. Shiori (eds.), Springer-Verlag, pp. 189-201 (1987).

23. A. E. Green, B. C. McInnis and P. M. Naghdi, Int. J. Engr. Sci., 6, 373 (1968).

24. B. D. Coleman and M. L. Hodgdon, Arch. Rat'l. Mech. Anal., 90, 219 (1985).

25. E. C. Aifantis, J. Eng. Mat. Tech., 106, 326 (1984).

26. H. M. Zbib and E. C. Aifantis, Res. Mechanica, 23, 261 (1988).

27. O. W. Dillon and D. Kratochvil, Int. J. Solids Structures, 6, 1513 (1970).

28. A. Seeger, in "Dislocations and Mechanical Properties of Crystals," Wiley (1957).

29. S. Nemat-Nasser, J. Appl. Mech., 50, 1114 (1983).

30. B. Loret, Mech. Mat., 2, 287 (1983).

31. Y. F. Dafalias, J. Appl. Mech., 50, 561 (1983).

32. L. Anand, Int. J. Plasticity, 1, 213 (1985).

33. J. LeMonds and A. Needleman, Mechs. Mat., 5, 339 (1986).

34. J. LeMonds and A. Needleman, Mechs. Mat., 5, 363 (1986).

35. A. Needleman, J. Appl. Mechs., 56, 1 (1989).

36. L. Anand, A. M. Lush and K. H. Kim, in "Thermal Aspects in Manufacturing," M. H. Attia and L. Kops (eds.), ASME-PED-Vol. 30, 89 (1988).

37. H. M. Zbib and E. C. Aifantis, Res. Mechanica, 23, 293 (1988).

38. R. C. Batra and D. S. Liu, J. Appl. Mech., 56, 527 (1989).

39. R. C. Batra and D. S. Liu, Int. J. Plasticity, 6, 227 (1990).

40. Z. G. Zhu and R. C. Batra, Acta Mechanica, 84, 89 (1990).

41. R. C. Batra and X. Zhang, Acta Mechanica, 85, 221 (1990).

42. Y. Leroy, A. Nacar, A. Needleman, and M. Ortiz, in "Advances in Inelastic Analysis," S. Nakazawa, K. William and N. Rebelo (eds.), ASME-AMD Vol. 88, 97 (1987).

43. T. Belytschko, J. Fish and A. Bayliss, Computer Meths. Appl. Mech. Engng., 81, 71 (1990).

44. M. Ortiz, Y. Leroy and A. Needleman, Comp. Meth. Appl. Mech. Engr., 61, 189 (1987).

45. R. C. Batra and K. I. Ko, Computational Mechs.: an Int. J., 10, 369 (1992).

46. R. C. Batra and J. Hwang, Computational Mechs.: an Int. J., 12, 255 (1993).

47. R. C. Batra and K. I. Ko, Int. J. Engng. Sci. 31, 529 (1993).

48. R. C. Batra and X. S. Jin, Analysis of Dynamic Shear Bands in Porous Thermally Softening Viscoplastic Materials, Archives of Mechanics (in press).

49. Y. Wang and R. C. Batra, Acta Mechanica, 102, 217 (1994).

50. S. B. Brown, K. H. Kim and L. Anand, Int. J. Plasticity, 5, 95 (1989).

51. R. C. Batra, Computational Mechs.: an Int. J. 3, 1 (1988).

52. R. C. Batra and De-Shin Liu, J. Appl. Mechs., 56, 527 (1989).

53. A. L. Wingrove, A Note on the Structure of Adiabatic Shear Bands in Steel, Tech. Memo 33, Australian Defence Scientific Service, Defence Standards Lab. Dept. of Supply, Maribyrnong, Victoria (1971).

54. J. F. Kalthoff, Optical Eng'g., 27, 835 (1988).

55. Z. G. Zhu and R. C. Batra, J. Eng'g. Mat'l Tech., 114, 368 (1992).

56. R. C. Batra and J. Hwang, Dynamic Shear Band Development in Dipolar Thermoviscoplastic Materials, Computational Mechanics (in press).

57. G. Z. Zhu and R. C. Batra, Int. J. Plasticity, 9, 653 (1993).

58. R. C. Batra and Z. G. Zhu, Effect of Loading Direction and Initial Imperfections on the Development of Dynamic Shear Bands in a FCC Single Crystal, Acta Mechanica (in press).

59. R. C. Batra and X. Zhang, J. Eng'g. Materials and Technology, 116, 155 (1994).

IX. APPENDIX

A copy of each of the following papers is included in the appendix.

1. Analysis of shear bands in simple shearing deformations of nonpolar and dipolar viscoplastic materials

2. An adaptive mesh refinement technique for the analysis of shear bands in plane strain compression of a thermoviscoplastic solid

3. Consideration of phase transformations in the study of shear bands in a dynamically loaded steel block

4. Effect of kinematic hardening on the initiation and growth of shear bands in plane strain deformations of a thermoviscoplastic solid

5. Analysis of shear bands in dynamic axisymmetric compression of a thermoviscoplastic cylinder

6. Analysis of shear bands in a dynamically loaded viscoplastic cylinder containing two rigid inclusions

7. Analysis of dynamic shear bands in a FCC single crystal

8. An adaptive mesh refinement technique for two-dimensional shear band problems

9. On the propagation of a shear band in a steel tube

Analysis of shear bands in simple shearing deformations of nonpolar and dipolar viscoplastic materials

R C Batra

Department of Mechanical and Aerospace Engineering and Engineering Mechanics, University of Missouri-Rolla, Rolla MO 65401-0249

During the past few years we have studied numerically the initiation and growth of shear bands in nonpolar and dipolar viscoplastic materials being deformed in simple shear, and in nonpolar materials undergoing plane strain deformations. We summarize here our work for the former problem.

1. INTRODUCTION

Narrow regions of intense plastic deformation have been observed during high strain-rate plastic deformation of many metals. These have been called adiabatic shear bands since there is not enough time available for the heat to be conducted away from these regions, and the primary mode of deformation is that of shearing. Tresca (1878) and Massey (1921) observed such bands in the form of a cross during the hot forging of a metal and called them hot lines. The research activity in this field has increased significantly since the time Zener and Hollomon (1944) reported 32 μm wide shear bands during the punching of a hole in a steel plate. Backman and Finnegan (1965) have reported that shear bands initiate at flaws, pits, scratches, and inhomogeneities in the material, and these zones of inhomogeneous deformation propagate from their initiation site like a running crack. The study of shear bands is important because once a shear band initiates, the subsequent deformations of the body are concentrated in this narrow region with the rest of the body undergoing very little, if any, deformations. Also, shear bands usually precede shear fractures. We refer the reader to the papers by Shawki and Clifton (1989) and Batra and Zhu (1991) for additional references.

The foregoing remarks suggest that the modeling of a material inhomogeneity and the material behavior at high temperatures and strain-rates should play significant roles in the study of shear bands. We address these and other issues below.

2. FORMULATION OF THE PROBLEM

In terms of non-dimensional variables, the equations governing the dynamic thermomechanical deformations of a viscoplastic block, shown in Fig 1, and undergoing overall simple shearing deformations, are

$$\alpha w\dot{v} = (ws - l(w\sigma)_{,y})_{,y}, \qquad -1 < y < 1, \tag{1}$$

$$w\dot{\theta} = \beta(w\theta_{,y})_{,y} + w(s\dot{\gamma}_p + l\sigma\dot{d}_p), \qquad -1 < y < 1, \tag{2}$$

$$\dot{s} = \mu(v_{,y} - \dot{\gamma}_p), \tag{3}$$

$$\dot{\sigma} = \mu l(v_{,yy} - \dot{d}_p), \tag{4}$$

$$\dot{\gamma}_p = f(s,\sigma,\psi,\theta,\gamma_p,d_p,l), \tag{5}$$

$$\dot{d}_p = lg(s,\sigma,\psi,\theta,\gamma_p,d_p,l), \tag{6}$$

$$\psi = (s\dot{\gamma}_p + l\sigma\dot{d}_p)/(1 + \psi/\psi_0)^n, \tag{7}$$

where the non-dimensional numbers

$$a = \rho\dot{\gamma}_0^2/s_0H^2 \quad \text{and} \quad \beta = k/\rho c\dot{\gamma}_0H^2 \tag{8}$$

give, respectively, the effect of inertia forces relative to the flow stress of the material and that of heat conduction. Here ρ is the mass density, v the velocity of a material particle in the direction of shearing, w the thickness of the block, s the shearing stress, σ the dipolar shearing stress, l is a material characteristic length, θ the temperature rise, $\dot{\gamma}_0$ the average applied strain rate, $\dot{\gamma}_p$ the plastic strain-rate, $\dot{d}_p$ the dipolar plastic strain-rate, $2H$ the height of the block, c the specific heat, s_0 the yield stress in a quasistatic isothermal simple shearing test conducted at the room temperature, and k the thermal conductivity. The length, time, temperature, and stresses are scaled respectively by H, $\dot{\gamma}_0$, θ_r, and s_0 to obtain their nondimensional counterparts where

$$\theta_r = s_0/\rho c. \tag{9}$$

Throughout this paper, a superimposed dot indicates the material time derivative and a comma followed by y signifies partial differentiation with respect to y. Equations (1) and (2) express, respectively, the balance of linear momentum and the balance of internal energy. Equations (3) through (7) are constitutive assumptions, wherein μ is the shear modulus, ψ is an internal variable used to describe the effect of the history of deformation upon the response of the material, and the functional forms of f and g characterize the material of the body. In Eq (7) ψ_0 and n are material parameters.

For the initial and boundary conditions, we take

$$v(y,0) = 0, \quad s(y,0) = 0, \quad \sigma(y,0) = 0, \quad \theta(y,0) = 0, \tag{10}$$

$$\theta_{,y}(\pm 1,t) = 0, \quad \sigma(\pm 1,t) = 0, \quad v(\pm 1,t) = \begin{cases} \pm t/t_r, & 0 \le t \le t_r, \\ \pm 1, & t \ge t_r. \end{cases} \tag{11}$$

That is, the block is initially at rest, is stress free, and is at a uniform temperature. The lower and upper surfaces of the block are thermally insulated, and equal and opposite shearing speeds are prescribed on them. The boundary conditions for σ are justified since a narrow band forms around $y = 0$ and the velocity gradients are constants near $y = \pm 1$.

Our account of dipolar effects differs from that of Coleman and Hodgdon (1985) and Zbib and Aifantis (1988). Whereas we include dipolar stresses corresponding to second-order gradients of velocity in the balance of linear momentum and the balance of internal energy, the two papers cited above include gradients of strain only in the constitutive function f. Note that our formulation of the problem reduces to that for simple materials by taking $l = 0.0$.

Sometimes we used initial and/or boundary conditions different from those given in (10) and (11), and also modeled a material inhomogeneity by perturbing the temperature field. Such variations to the formulation of the problem are delineated whenever applicable. Also whenever possible we exploited the symmetry or antisymmetry of deformations about $y = 0$ and solved the problem on the domain [0,1].

We note that the coupled partial differential equations (1) through (7) are highly nonlinear. Their approximate solution under the side conditions (10) and (11) has been obtained by the finite element method. This is accomplished by first reducing the governing equations to a set of coupled ordinary differential equations by using the Galerkin approximation, which are then integrated with respect to time t by using the Gear (1971) method included in the subroutine LSODE developed by Hindmarsh (1983). The details of the aforestated solution technique have been given by Batra and Kim (1990a). We note that Batra (1987) integrated the ordinary differential equations by using the Crank-Nicolson method. His results are in qualitative agreement with those obtained subsequently by using the Gear method.

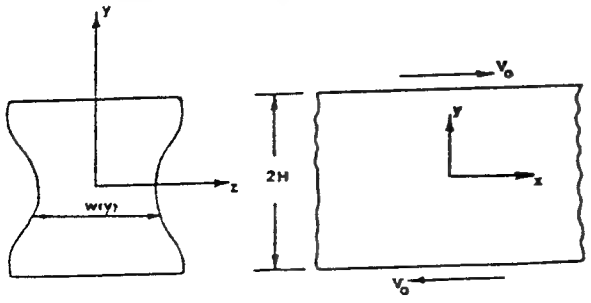

FIG 1. A schematic sketch of the problem studied.

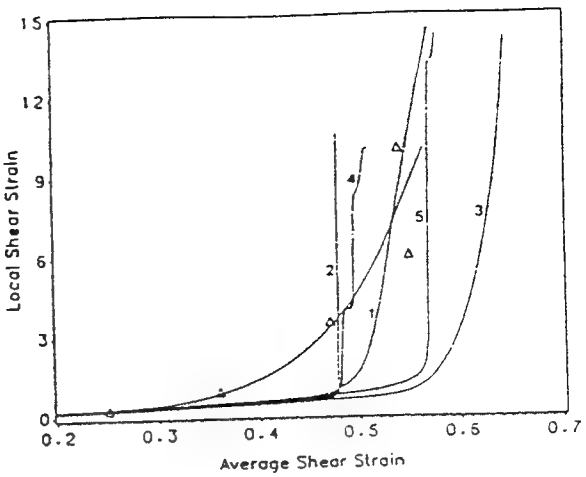

FIG 2. Growth of the local shear strain within the band as the specimen deforms. Curve 1, Bodner-Partom; Curve 2, Litonski (nonpolar); Curve 3, Wright-Batra dipolar; Curve 4, power law; Curve 5, Johnson-Cook; Δ experimental data from Marchand and Duffy's paper.

3. RESULTS

3.1 Effect of constitutive relations

Batra and Kim (1990b) assumed the block to be of uniform thickness and modeled the material inhomogeneity by assuming that the initial temperature of the material near $y = 0$ was slightly higher than that of the rest of the material. They found values of material parameters in the Bodner-Partom (1975) constitutive relation, Litonski law (1977), Johnson-Cook law (1983), Power law (e.g. see Costin et al 1980), and the Wright-Batra (1987) dipolar theory by ensuring that the computed shear stress-shear strain curve for a block without any defect matched well with that reported by Marchand and Duffy (1988) for a HY-100 steel specimen subjected to torsional loading at room temperature and deformed at a nominal strain-rate of 3300 sec^{-1}. The magnitude of the temperature perturbation was determined by numerical experiments so that the sharp drop in stress

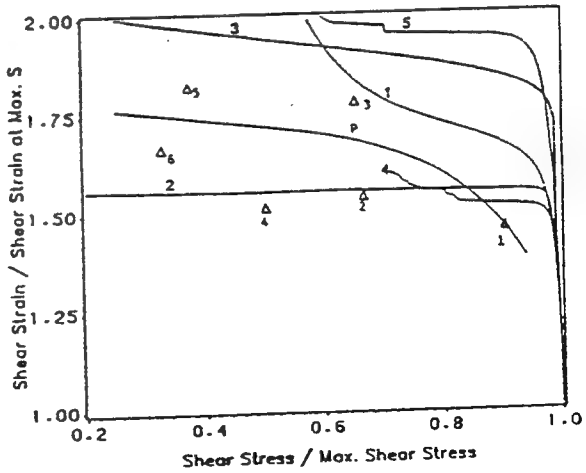

FIG 3. Plot of the normalized shear strain vs the normalized shear stress during the time shear stress is dropping with increasing strain. See FIG 2 for legends of curves.

occurred at about the test value of the nominal strain. Subsequently, various solution variables for tests done at nominal strain rates of 1600 sec^{-1} and 1400 sec^{-1} were compared with the experimental findings.

Figure 2 depicts the growth of the shear strain within the band, taken here to be the strain at $y = 0$, as the specimen deforms. Whereas the Litonski law, the Power law, and the Johnson-Cook law give a rapid increase in the local strain once a shear band initiates, the Bodner-Partom law and the Wright-Batra dipolar theory give general trends in agreement with the experimental data. A similar conclusion can be drawn from the results plotted in Fig 3, which exhibits normalized shear strain versus the normalized shear stress during the time the shear stress is dropping. Note that the abscissa represents a nonuniformly stretched out time scale. The band width, defined as the width of the region over which the plastic shear strain varies by no more than 5% of its value at the center, was found to be 2 μm, 14 μm, 14 μm, 6 μm, and 51 μm, respectively, for the Litonski law, the Power law, the Bodner-Partom law, the Johnson-Cook law, and the Wright-Batra dipolar theory. When the shear stress at the specimen center had dropped to 66% of its maximum value, Marchand and Duffy (1988) found the band width to be between 20 μm and 55 μm depending upon the point of observation around the circumference of the steel tube. Marchand and Duffy defined the band width to be the width of the region, surrounding the band center, over which the plastic strain remains uniform.

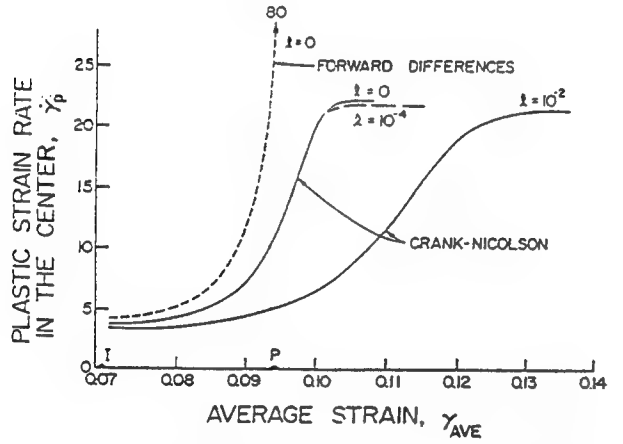

FIG 4. Evolution of the plastic strain-rate at the band center for nonpolar and dipolar materials.

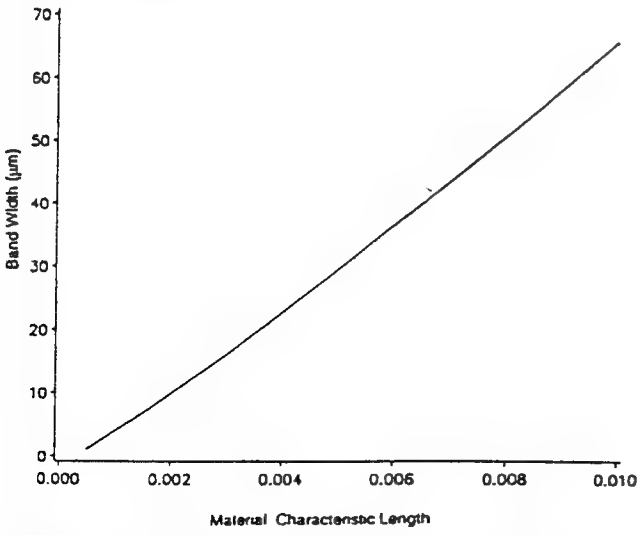

FIG 5. Dependence of the band width upon the material characteristic length l.

3.2 Effect of material characteristic length l.

Wright and Batra (1987) perturbed the homogeneous solution for the simple shearing problem by introducing a temperature perturbation just before the shear stress attained its peak value and assumed simple expressions for the constitutive functions f and g. From the evolution of the plastic strain-rate at the specimen center plotted in Fig 4, it is clear that the consideration of dipolar effects delays the initiation of the shear band. The shear band is assumed to initiate when the plastic strain-rate at the specimen center grows rapidly. Also the strain-rate increases gradually for $l = 10^{-2}$ but quite rapidly for $l = 0.0$. The dependence of the band-width upon l, as computed by Batra and Kim (1988) and depicted in Fig 5, shows that the band-width increases with an increase in the value of l.

Zhang and Batra (1992) analyzed the stability of the homogeneous solution of equations (1) through (7) and assumed that the flux of linear momentum is essentially uniform in the spatial variable and $|s, y| < \Gamma |\theta_y|$, where Γ is defined in terms of the material variables. They showed that an increase in the thermal conductivity and the material characteristic length has a stabilizing effect, and an increase in the block height has a destabilizing effect on small perturbations superimposed on the homogeneous solution. The specific heat did not appear in the stability criterion.

Batra (1987) studied the interaction between two shear bands and found that the bands that would grow independently in simple materials ($l = 0.0$) coalesced in dipolar materials even when the material characteristic length equalled 1/20 of the distance between them at the time of their initiation. Kwon and Batra (1988) introduced multiple defects by perturbing the uniform temperature within the block when the material just starts deforming plastically to that given by a cosine function which assumes relative maximum values at several points in the block. They found that for simple materials, the deformation localized at points where the perturbed temperature had relative minima for $\dot{\gamma}_0 = 500$ sec^{-1} and at the locations of the relative maxima at $\dot{\gamma}_0 \geq 1000$ sec^{-1}. For dipolar materials with $l = 0.01$, the deformation localized near the block boundaries at $\dot{\gamma}_0 = 500$ sec^{-1} and at the locations of the relative maxima when $\dot{\gamma}_0 = 50{,}000$ sec^{-1}. For both simple and dipolar materials the initiation of the localization was considerably delayed as compared to that when the temperature perturbation had only one maxima at the specimen center.

3.3 Unloading wave from the shear band

Wright and Walter (1987) found that for thermally softening and strain-rate hardening materials the shear stress within the

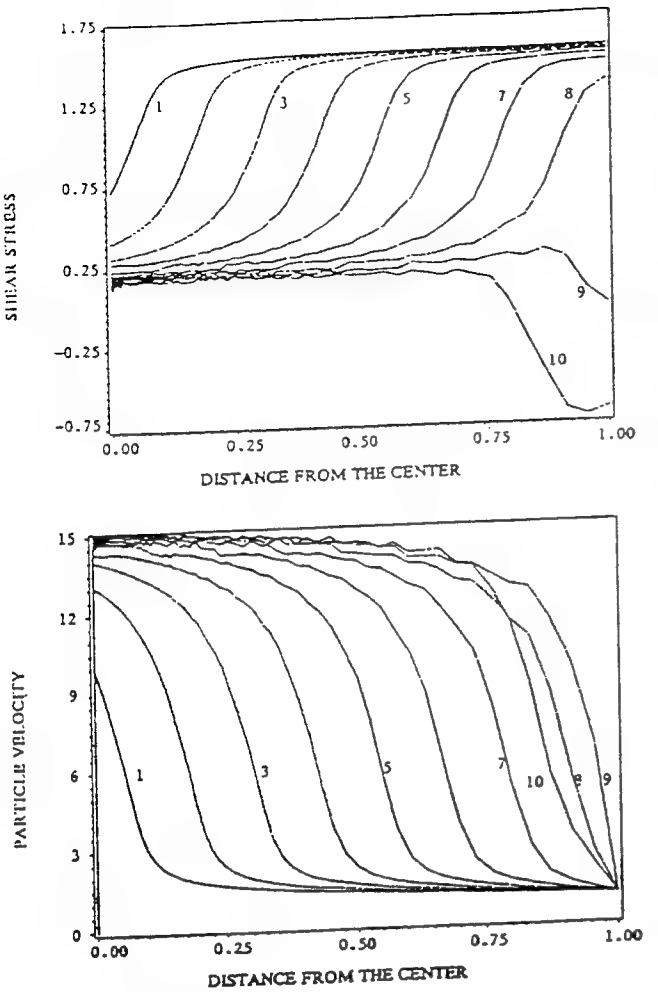

FIG 6. Distribution of the shear stress and the particle velocity within the specimen at different times during the localization of the deformation for nonpolar materials. These curves are plotted at intervals of 0.1 μs with Curve 1 at t = 64.0 μs, Curve 2 at t = 64.1 μs, etc; the time being reckoned from the instant of introducing the perturbation.

band dropped precipitously. Batra and Kim (1990) also considered the effect of material elasticity and work-hardening and modeled the material by the Litonski flow rule. Their computed distribution of the shear stress and the particle velocity within the specimen at intervals of one-tenth of a microsecond starting from the instant when the deformation begins to localize is shown in Fig 6. It is clear that an unloading elastic shear wave emanates outwards from the region of severe deformation. The computed speed, 3,178 m/sec, of this wave essentially equals the analytical value of 3,190 m/sec. It takes 0.807 μs for the shear wave to reach the outer boundary where it is reflected back with a negative value of the shear stress.

Computations for dipolar materials, and for simple materials but using the other four flow rules did not result in the emanation of an unloading elastic wave from the severely deformed region. Of course, no such wave would be found if the inertia forces were neglected.

3.4 Effect of thermal conductivity

Batra and Kim (1991) used the Litonski law, the Bodner-Partom law, and the Johnson-Cook law to model the viscoplastic response of the material and computed results for five different values, namely, 0, 5, 50, 500, and 5000 W/m°C of the thermal conductivity k. The thickness of the block was assumed to vary smoothly, with the thickness at the specimen center being 5% smaller than that at the boundary. For each of these three constitutive relations, the rates of evolution of the temperature and the shear strain at the specimen center were steepest for $k = 0$, and decreased with an increase in the value of k. The computed band-width depends upon how far the localization has progressed, or how much the shear stress at the specimen center has dropped. This is evidenced by the results plotted in Fig 7. For k = 50 and 500 W/m°C the band-width seems to reach a stable value as the shear stress within the band drops. For k = 5,000 W/m°C an interesting situation developed in that the band-width decreased at first with the drop in the shear stress at the specimen center, reached a plateau at $s_a/s_{max} = 0.85$, and then started to increase. Here s_a equals the average shear stress in the block. The rate of change of the band-width with respect to s_a/s_{max} does depend upon the constitutive relation employed. A plausible explanation for this computed decrease and increase of the band-width is that as the shear stress at the specimen center drops and the plastic strain-rate increases sharply, the heat generated due to plastic working raises the temperature there more than at other points in the block. Initially, the rate of heat loss to outer parts of the block is less than the rate of heat generation at the specimen center, and the temperature there rises, making the material there softer and thus easier to deform. As the temperature gradients build up, the rate of heat loss increases, more of the material surrounding the specimen center is heated up enough so as to deform severely and the band-width increases.

The plots of the band-width w computed when s_a/s_{max} equalled 0.95, 0.90, 0.85, 0.80, 0.75, and 0.70 versus $(k)^{1/2}$ revealed that w decreased with a decrease in the value of k, for each of the three constitutive relations used, and that the relationship between w and $(k)^{1/2}$ was not linear as asserted by Dodd and Bai (1985). The Litonski and the Johnson-Cook flow rules gave zero band-width for $k = 0$, but the Bodner-Partom law gave a finite value of the band-width for $k = 0$.

3.5 Effect of initial temperature

Wang et al (1988) tested titanium alloy TB2 (Ti-8Cr-5 Mo-5V-3 Al) specimens in compression at different environmental temperatures and concluded that the susceptibility to adiabatic shearing increased at lower environmental temperatures. In order to assess the effect of the initial specimen temperature on the initiation of shear bands, Kim and Batra (1992) assumed the dependence, shown in Fig 8, of the specific heat, thermal conductivity and the shear modulus of a plain carbon steel upon the temperature. They modeled the viscoplastic response of the material by the Bodner-Partom flow rule and computed results for six different values, namely, θ_0 = 83°K, 200°K, 300°K, 343°K, 407°K, and 423°K

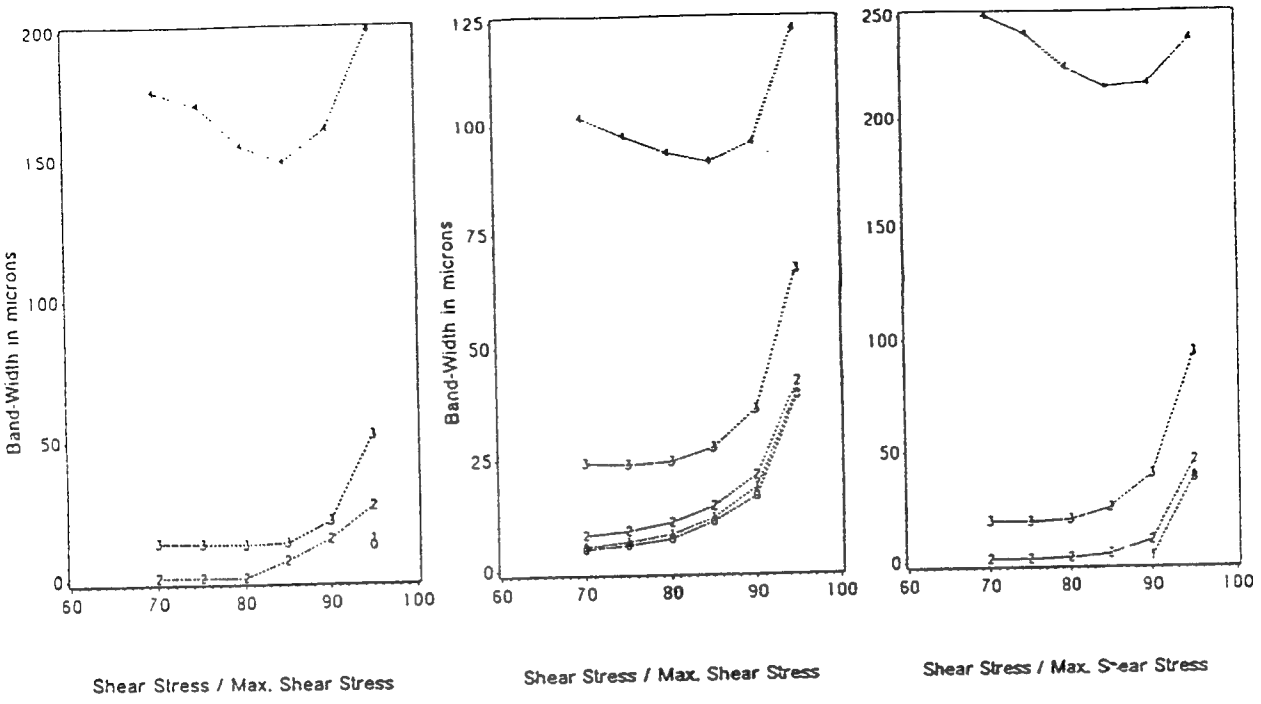

FIG 7. Dependence of band-width upon s_a/s_{max}. Curve 0 for $k = 0$; Curve 1, $k = 5$ W/m°C; Curve 2, $k = 50$ W/m°C; Curve 3, $k = 500$ W/m°C; curve 4, $k = 5{,}000$ W/m°C.

of the initial temperature. The specimen thickness at its center was taken to be 5% smaller than that at its edges. One way to study the localization of the deformation is to observe at different instants the deformed position of an initially straight line. We recall that Marchand and Duffy (1988) used this technique to find the plastic strain at a point. In Fig. 9, we have plotted the deformed positions of an initially straight line at $s_a/s_{max} = 1.0$, 0.95, 0.85, and 0.75. For each value of θ_0 considered, the deformation has become nonhomogeneous by the time the average shear stress s_a attains its peak value s_{max}. As θ_0 increases, the width of the central severely deformed region increases. From the plots given in Fig 10 of the shear strain γ_{loc} at the band center versus the average strain, it is clear that higher initial temperatures of the specimen delay the initiation of the localization of the deformation.

3.6 Effect of defect size

Batra (1987) studied the effect of different temperature perturbations on the initiation and growth of shear bands in a material obeying the Litonski law. He found that a shear band formed sooner with an increase in the height of the temperature perturbation. Larger temperature perturbations caused the shear band to initiate even before the peak in the shear stress-shear strain curve was reached. Also, a wider perturbation resulted in the shear strain localization at a lower rate as compared to the narrow perturbation of the same amplitude.

Batra and Kim (1992) recently studied the effect of the thickness variation on the development of shear bands in twelve different materials. The viscoplastic response of each material was modeled by the Johnson-Cook law. Figure 11 depicts the localization ratio versus logδ when $s_a/s_{max} = 1.0$ and 0.85, where δ is the percentage decrease in the thickness of the specimen at the center relative to that at its edges, and the localization ratio equals the maximum shear strain within the severely deforming region divided by the nominal strain in the specimen. The localization ratio depends strongly upon logδ; larger defects result in more severe localization of the deformation for the same value of s_a/s_{max}. The defect

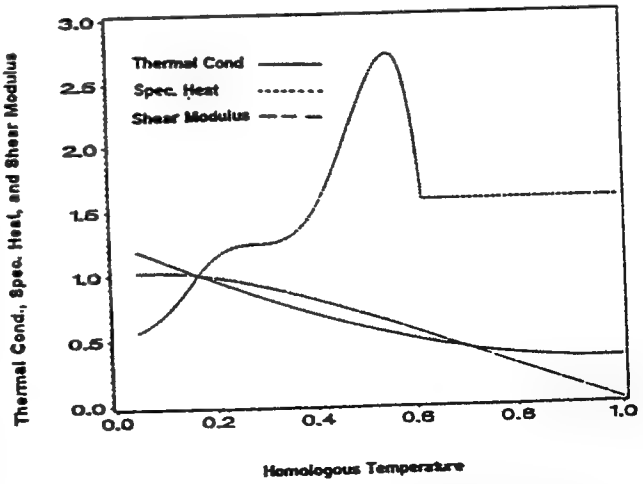

FIG 8. Dependence of the non-dimensional specific heat, thermal conductivity, and shear modulus upon the homologous temperature. The values of material variables are scaled so as to equal 1.0 at the room temperature.

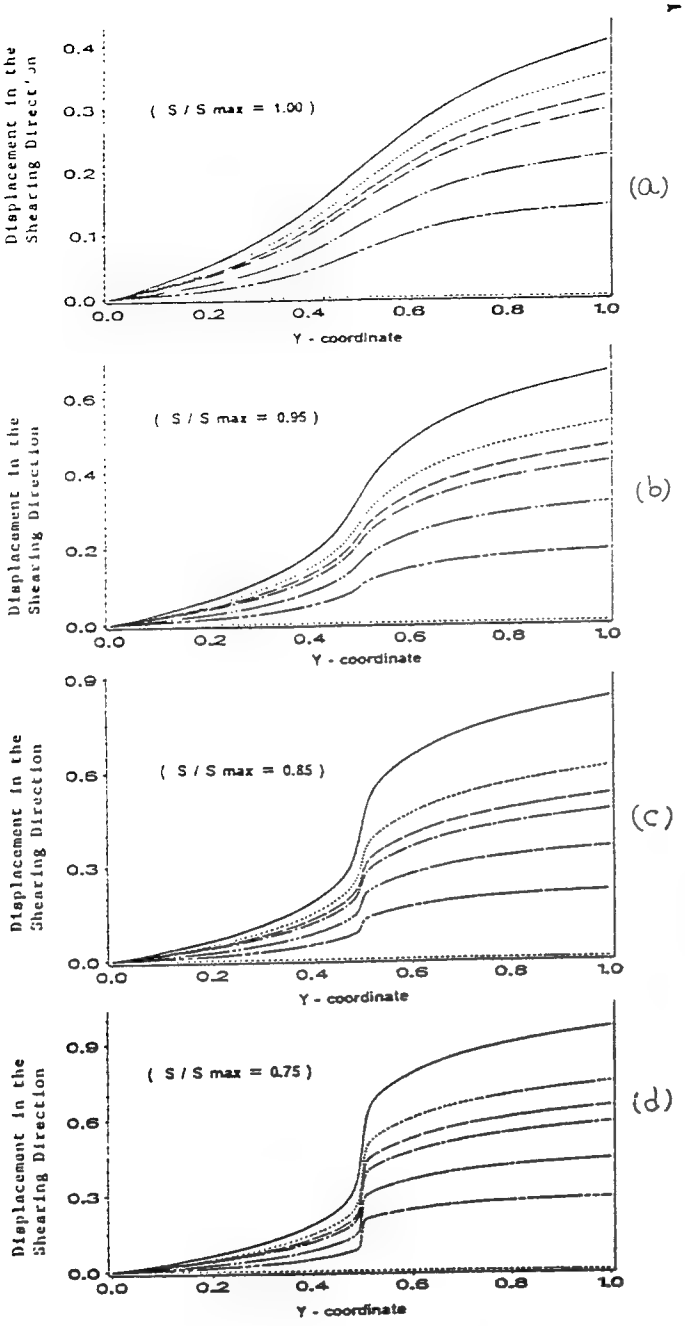

FIG 9. Deformed positions of an initially straight line at s_z/s_{max} = 1.0, 0.95, 0.85, and 0.75. —— θ_0 = 83°K, — θ_0 = 200°K, —— θ_0 = 300°K, ·-·-· θ_0 = 343°K, -·-·- θ_0 = 407°K, and —·—·— θ_0 = 523°K.

size affects not only the nominal strain when a shear band initiates, but also the growth of the shear band. The homologous temperature, defined as the ratio of the absolute temperature of a material point to the melting temperature of the material, versus logδ plots in Figs 12a and 12b reveal that the homologous temperature is essentially independent of the defect size at s_z/s_{max} = 1.0 and 0.85. Note that the vertical scales in these figures are such that small differences in the values of the homologous temperatures are greatly exaggerated.

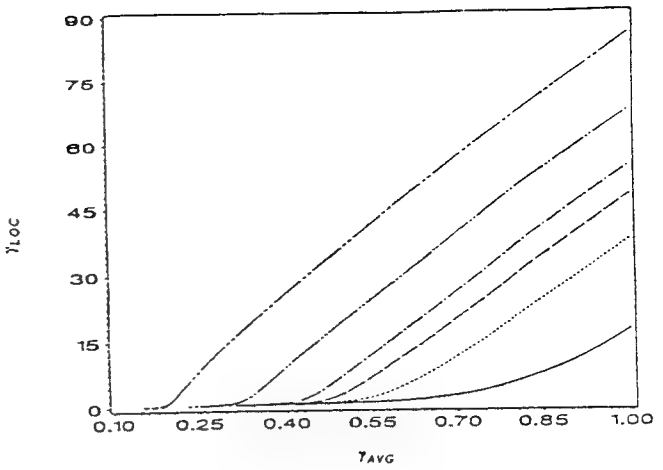

FIG 10. Evolution of plastic strain within the band for different values of the initial temperature. See Fig 9 for legends to curves.

3.7 Effect of inertia forces

Figure 13 exhibits the evolution of the plastic strain-rate at the specimen center with and without the consideration of inertia forces. In order to disregard the effect of inertia forces, the value of α in Eq (1) was reduced by a factor of 10^5. It is clear that the consideration of inertia forces delays the initiation of the shear band when the material is modeled by the Bodner-Partom flow rule. Similar results were obtained for the other four flow rules stated in Sec 3.1. Batra (1988) studied the shear banding problem for $\dot{\gamma}_0 = 50\ s^{-1}$, 500 s^{-1}, 5,000 s^{-1}, and 50,000 s^{-1}, and concluded that inertia forces start playing a significant role at $\dot{\gamma}_0 = 5{,}000\ s^{-1}$. Since only discrete values of $\dot{\gamma}_0$ were considered, this conclusion is tenuous. For a quaststatic problem, no unloading wave will emanate outwards from the severely deformed region.

3.8 Effect of mass matrix

In the aforestated results, we used a consistent mass matrix in the discrete formulation of the problem. Figure 14 shows the effect of different mass matrices on the evolution of the plastic strain-rate at the specimen center. For beam bending problems, the higher-order (average) mass matrix accelerates the rate of convergence of the solution. This can not be verified for the present problem since the analytical solution is not known.

3.9 Shear bands in a bimetallic body

Batra and Kwon (1989) studied the phenomenon of shear banding in a bimetallic body. The domains [-1,0) and (0,1] were assumed to be made of different materials and a temperature perturbation symmetric about $y = 0$ was considered. For a fixed set of material properties, the effect of the applied average strain-rate; and for a given prescribed strain-rate, the effect of varying the shear modulus, thermal conductivity, and the coefficient of thermal softening of one material relative to the other were examined. It was found that a shear band formed in the material that softened more readily.

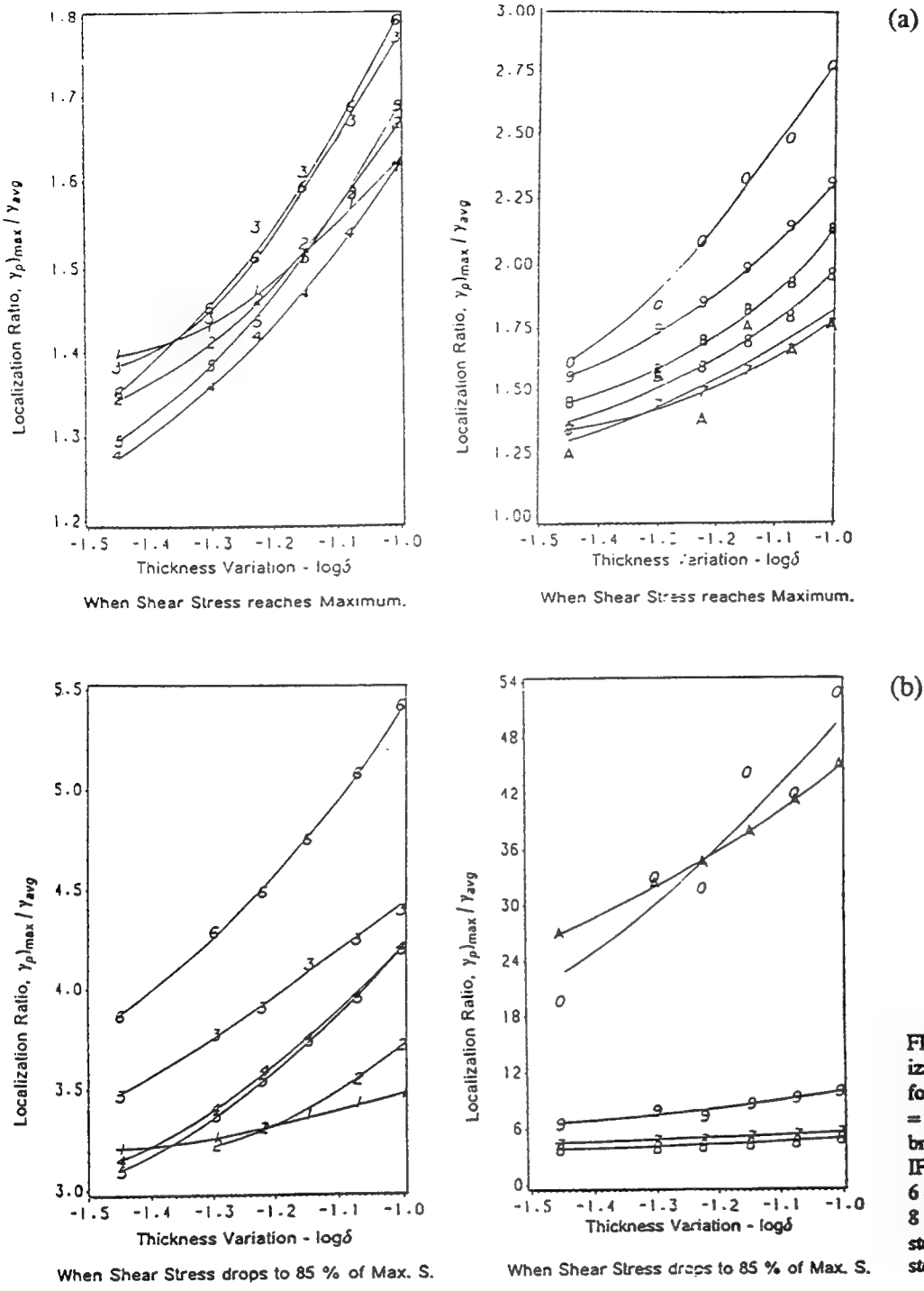

FIG 11. Dependence of the localization ratio upon the defect size for (a) $s_d/s_{max} = 1.0$ and (b) $s_d/s_{max} = 0.85$. (1 - Copper, 2 - Cartridge brass, 3 - Nickel 200, 4 - Armco IF iron, 5 - Carpenter electric iron, 6 - 1006 steel, 7 - 2024 aluminum, 8 - 7039 aluminum, 9 - low alloy steel, 0 - S-7 tool steel, A - Tungsten alloy, B - Depleted Uranium).

4. CONCLUSIONS

We have summarized some of our results on the initiation and growth of shear bands in a thermally softening elastic-viscoplastic body undergoing overall simple shearing deformations. It is unrealistic to expect a good agreement between the computed results and the experimental findings since we have studied a one-dimensional problem and most test configurations require analysis of either two- or three-dimensional problems. One of the unresolved issues is finding a suitable constitutive model valid for high temperatures and strain-rates found in a shear band.

ACKNOWLEDGEMENTS

This work was supported by the U.S. Army Research Office grant DAAL03-91-G-0084 and the NSF grant MSS 9121279 to the University of Missouri-Rolla.

REFERENCES

Backman ME and Finnegan SA, 1973, The propagation of adiabatic shear, in *Metallurgical Effects at High Strain-Rates* (Rohde RW et al, eds), 531-543, Plenum, New York.

Batra RC, 1987, The initiation and growth of, and the interaction among, adiabatic shear bands in simple and dipolar materials, *Int J Plasticity* 3, 75-89.

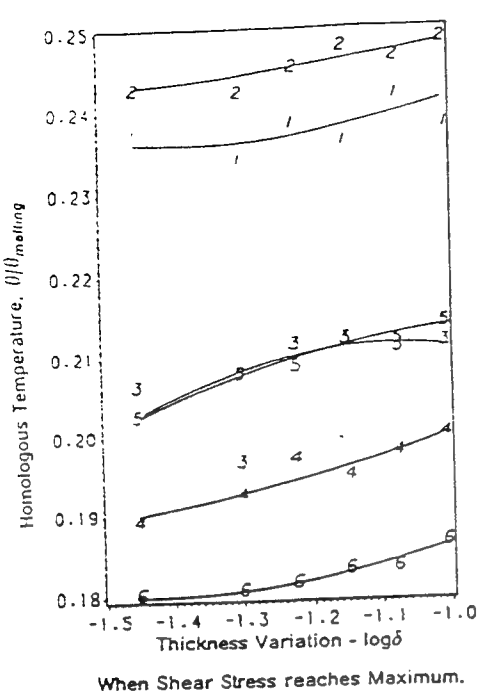

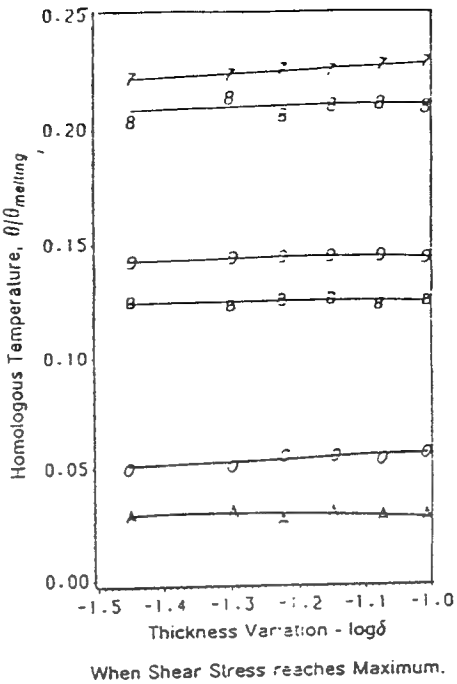

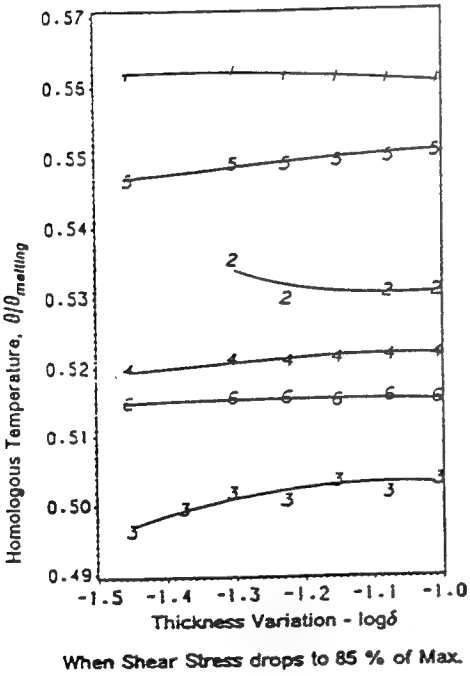

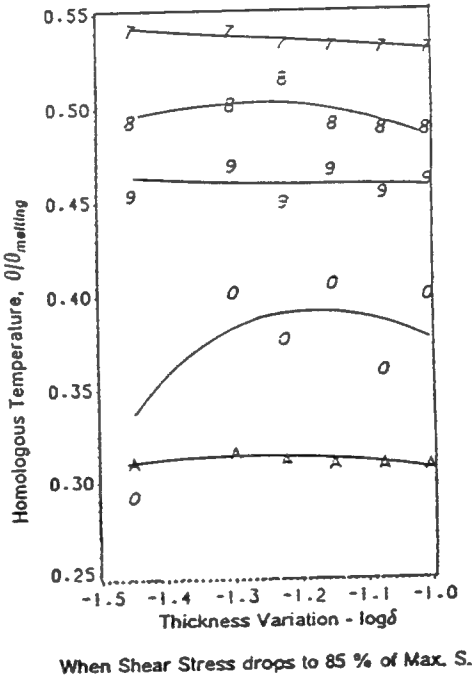

FIG 12. Dependence of the homologous temperature at the band center upon the defect size for (a) $s_g/s_{max} = 1.0$ and (b) $s_g/s_{max} = 0.85$. (See Fig 11 caption for explanations.)

Batra RC, 1988, Effect of nominal strain-rate on the initiation and growth of adiabatic shear bands in steels, *J Appl Mech* 55, 229-230.

Batra RC and Kim CH, 1988, Effect of material characteristic length on the initiation, growth, and band width of adiabatic shear bands in dipolar materials, *J de Physique* 49(C3) 41-46.

Batra RC and Kim CH, 1990a, Adiabatic shear banding in elastic-viscoplastic nonpolar and dipolar materials, *Int J Plasticity* 6, 127-141.

Batra RC and Kim CH, 1990b, Effect of viscoplastic flow rules on the initiation and growth of shear bands at high strain rates, *J Mech Phys Solids* 38, 859-874.

Batra RC and Kim CH, 1991, Effect of thermal conductivity on the initiation, growth, and bandwidth of adiabatic shear bands, *Int J Eng Sci* 29, 949-960.

Batra RC and Kim CH, 1992, Analysis of shear banding in twelve materials, *Int J Plasticity* (to appear).

Batra RC and Kwon YW, 1989, Adiabatic shear banding in a bimetallic body, *Acta Mech* 77, 281-297.

Batra RC and Zhu ZG, 1991, Dynamic shear band development in a thermally softening bimetallic body containing two voids, *Acta Mech* 86, 31-52.

Bodner SR and Partom Y, 1975, Constitutive equations for elastic-viscoplastic strain-hardening materials, *J Appl Mech* 42, 385-389.

Coleman BD and Hodgdon ML, 1985, On shear bands in ductile materials, *Arch Rational Mech Anal* 90, 219-247.

Dodd B and Bai Y, 1985, Width of adiabatic shear bands, *Mat Sci Technol* 1, 38-40.

Gear CW, 1971, *Numerical initial value problems in ordinary differential equations*, Prentice-Hall, Englewood Cliffs NJ.

Hindmarsh AC, 1983, ODEPACK, a systematized collection of ODE solvers, in Stepleman RS et al (eds), *Scientific Computing*, North-Holland, Amsterdam, 55-64.

Johnson GR and Cook WH, 1983, A constitutive model and data for metals subjected to large strains, high strain rates and high temperatures, in *Proc 7th Int Symp Ballistics*, The Hague, The Netherlands, pp. 1-7.

Computational Mechanics (1992) 10, 369–379

Computational Mechanics

An adaptive mesh refinement technique for the analysis of shear bands in plane strain compression of a thermoviscoplastic solid

R. C. Batra and K.-I. Ko

Department of Mechanical and Aerospace Engineering and Engineering Mechanics, University of Missouri—Rolla, Rolla, MO 65401-0249, USA

Abstract. We have developed an adaptive mesh refinement technique that generates elements such that the integral of the second invariant of the deviatoric strain-rate tensor over an element is nearly the same for all elements in the mesh. It is shown that the finite element meshes so generated are effective in resolving shear bands, which are narrow regions of intense plastic deformation that form in high strain-rate deformation of thermally softening viscoplastic materials. Here we assume that the body is deformed in plane strain compression at a nominal strain-rate of 5000 sec^{-1}, and model a material defect by introducing a temperature perturbation at the center of the block.

1 Introduction

In nearly all of the previous numerical studies of shear bands in two-dimensional problems involving a viscoplastic material (e.g., see Needleman 1989; Batra and Liu 1989; Batra and Zhu 1991), a fixed finite element mesh has been used. Since shear bands are narrow regions of intense plastic deformation, their satisfactory resolution requires either a very fine mesh throughout the computational domain, in which case the solution in most of the domain outside the shear band is overcomputed, or an adaptively refined mesh that concentrates more elements in the severely deforming region and fewer elements outside of it. Batra and Kim (1990) developed an adaptive mesh refinement technique for the analysis of one-dimensional shear banding problems by ensuring that the scaled residuals of the equations expressing the balance of linear momentum and the balance of internal energy were uniformly distributed. They subdivided elements having large scaled residuals and observed that high values of the scaled residuals occurred, in general, in non-overlapping regions. Their technique did not combine elements with low values of the scaled residuals, and for this reason did not result in an optimum mesh. We make no attempt to review all of the literature on adaptive mesh refinement and two-dimensional adiabatic shear banding problems. For the former, we refer the reader to Safjan et al. (1991) and Zienkiewicz and Zhu (1991), and for the latter to Batra and Zhu (1991).

2 Formulation of the problem

We use a fixed set of rectangular Cartesian coordinates with origin at the centroid of a square block (cf. Fig. 1) to analyze its plane strain thermomechanical deformations. We assume that the block is made of a thermally softening viscoplastic material. In terms of the referential description, governing equations are:

$$(\rho J)^{\cdot} = 0, \quad \rho_0 \dot{v}_i = T_{i\alpha,\alpha}, \quad \rho_0 \dot{e} = -Q_{\alpha,\alpha} + T_{i\alpha} v_{i,\alpha}, \tag{1–3}$$

where

$$J = \det F_{i\alpha}, \quad F_{i\alpha} = x_{i,\alpha}, \quad x_{i,\alpha} = \partial x_i / \partial X_\alpha, \tag{4}$$

x_i is the present location of a material particle that occupied place X_α in the reference configuration,

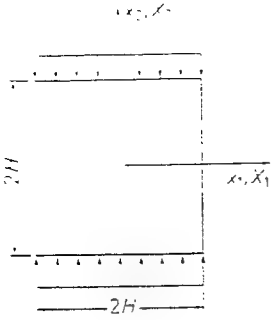

Fig. 1. A schematic sketch of the problem studied

ρ its present mass density, ρ_0 its mass density in the reference configuration, v_i its present velocity, T_{iz} the first Piola–Kirchoff stress tensor, Q_z the heat flux per unit reference area, e the specific energy, a superimposed dot indicates the material time derivative, and a repeated index implies summation over the range of the index. For the constitutive relations we take

$$\sigma_{ij} = -B\left(\frac{\rho}{\rho_0} - 1\right)\delta_{ij} + 2\mu D_{ij}, \qquad T_{iz} = \frac{\rho_0}{\rho} X_{z,j}\sigma_{ij} \tag{5.1, 5.2}$$

$$2\mu = \frac{\sigma_0}{\sqrt{3}I}(1 + bI)^m(1 - v\theta) \tag{6}$$

$$2D_{ij} = v_{i,j} + v_{j,i}, \qquad 2I^2 = \bar{D}_{ij}\bar{D}_{ij}, \qquad \bar{D}_{ij} = D_{ij} - \tfrac{1}{3}D_{kk}\delta_{ij} \tag{7.1–7.3}$$

$$Q_z = \frac{\rho_0}{\rho} X_{z,j} q_j, \qquad q_i = -k\theta_{,i} \tag{8.1, 8.2}$$

$$\dot{e} = c\dot{\theta} + B\left(\frac{\rho}{\rho_0} - 1\right)\frac{\dot{\rho}}{(\rho_0\rho)}. \tag{9}$$

Here σ_{ij} is the Cauchy stress tensor, B may be thought of as the bulk modulus for the material of the block, $\mathbf{D}$ is the strain-rate tensor, σ_0 the yield stress of the material in a quasistatic simple tension or compression test, parameters b and m characterize the strain-rate sensitivity of the material, I is the second invariant of the deviatoric strain-rate tensor $\bar{\mathbf{D}}$, v is the coefficient of thermal softening, k equals the thermal conductivity of the material, c the specific heat, and θ the temperature rise of a material particle.

We introduce non-dimensional variables, indicated below by a superimposed bar, as follows.

$$\bar{t} = t\dot{\gamma}_0, \quad \bar{I} = I/\dot{\gamma}_0, \quad \bar{b} = b\dot{\gamma}_0, \quad \bar{\rho} = \rho/\rho_0, \quad \bar{\boldsymbol{\sigma}} = \boldsymbol{\sigma}/\sigma_0, \quad \bar{\mathbf{T}} = \mathbf{T}/\sigma_0,$$
$$\bar{B} = B/\sigma_0, \quad \bar{v} = v\theta_r, \quad \bar{\theta} = \theta/\theta_r, \quad \bar{\boldsymbol{v}} = \boldsymbol{v}/v_0, \quad \bar{\boldsymbol{x}} = \boldsymbol{x}/H, \quad \bar{\boldsymbol{X}} = \boldsymbol{X}/H, \tag{10a}$$
$$\delta = \rho_0 v_0^2/\sigma_0, \quad \beta = k/(\rho_0 c v_0 H),$$

where

$$\theta_r \equiv \sigma_0/(\rho_0 c), \quad \dot{\gamma}_0 \equiv v_0/H. \tag{10b}$$

In Eq. (10) $2H$ is the height of the square block, θ_r the reference temperature, v_0 is the steady value of the velocity applied to the top and bottom surfaces in the x_2-direction, and $\dot{\gamma}_0$ equals the average applied strain-rate. Henceforth we use non-dimensional variables and drop the superimposed bars. We presume that the deformations of the block are symmetrical about the horizontal and vertical centroidal axes, and study the deformations of the material in the first quadrant.

For the boundary conditions we take

$$v_2 = 0, \quad T_{12} = 0, \quad Q_2 = 0 \quad \text{on} \quad x_2 = X_2 = 0, \tag{11.1}$$
$$v_1 = 0, \quad T_{21} = 0, \quad Q_1 = 0 \quad \text{on} \quad x_1 = X_1 = 0, \tag{11.2}$$

$$T_{11} = 0, \quad T_{21} = 0, \quad Q_1 = 0 \quad \text{on} \quad X_1 = H, \tag{11.3}$$

$$v_2 = -h(t), \quad T_{12} = 0, \quad Q_2 = 0 \quad \text{on} \quad X_2 = H. \tag{11.4}$$

The boundary conditions (11) signify that the boundaries of the block are insulated, the right surface is traction free, there is no tangential traction acting on the top surface, and the top surface moves downward at a prescribed speed $h(t)$. The boundary conditions (11.1) and (11.2) follow from the assumed symmetry of deformations about the X_1 and X_2 axes.

For the initial conditions we take

$$\rho(x,0) = 1, \quad v_1(x,0) = 0.37x_1, \quad v_2(x,0) = -x_2, \tag{12.1–12.3}$$

$$\theta(x,0) = 0.2(1-r^2)^9 e^{-5r^2}, \quad r^2 = X_1^2 + X_2^2. \tag{12.4, 12.5}$$

The initial conditions on the velocity field represent the situation when the transients have died out. Batra and Liu (1989) found this velocity field by taking

$$h(t) = t/0.005, \quad 0 \leqq t \leqq 0.005,$$
$$= 1, \qquad t \geqq 0.005,$$

assuming that the initial temperature distribution is uniform, and computing the solution till the steady state had been reached. The changes in the mass density and the computed temperature rise were found to be insignificant to justify assuming that the initial mass density is uniform. The assumptions (12.2) and (12.3) result in a smaller value of the CPU time needed to analyze the problem and do not affect the qualitative nature of the results. The initial temperature distribution given by (12.4) models a material inhomogeneity; the amplitude of the perturbation can be thought of as representing the strength of the singularity.

Equations obtained by combining (1) through (9) are to be solved under the side conditions (11) and (12). Since these coupled equations are highly nonlinear, it is not clear whether or not they have a unique solution. Here we find their approximate solution by first reducing the partial differential equations to a set of coupled, nonlinear, and ordinary stiff differential equations by using the Galerkin approximation. The number of these equations equals four times the number of nodes in the finite element discretization of the domain. We use three-noded isoparametric triangular elements and the lumped mass matrix obtained by the row-sum technique. These stiff ordinary differential equations are integrated with respect to time by using the backward difference Adam's method included in the subroutine LSODE (e.g., see Hindmarsh 1971). We could not use the Gear method because of the limited core storage available to us. The computer code developed by Batra and Liu (1989) was suitably modified to solve the present problem.

3 Adaptive mesh refinement technique

We first select a coarse mesh and find a solution of the aforestated problem. This mesh is refined so that

$$a_e = \int_{\Omega_e} I \, d\Omega, \quad e = 1, 2, \ldots, n_{el}, \tag{13}$$

is nearly the same for each element Ω_e. In (13), n_{el} equals the number of elements in the coarse mesh and Ω_e is one of the elements. Since one may not have an idea where the solution will exhibit sharp gradients, we choose the coarse mesh to be uniform. The motivation behind making a_e the same over each element Ω_e is that within the region of localization of the deformation values of I are very high as compared to those in the remaining region. Other variables such as the temperature rise, the maximum principal strain, and the equivalent strain which are also quite large within the band will be suitable replacements for I in Eq. (13). The refined mesh will depend upon the variable used in Eq. (13). In order to refine the mesh, we find

$$\bar{a} = \frac{1}{n_{el}} \sum_{e=1}^{n_{el}} a_e, \quad \xi_e = \frac{a_e}{\bar{a}}, \quad h_e = \frac{\bar{h}_e}{\xi_e}, \quad \text{and} \quad H_n = \frac{1}{N_e} \sum_{e=1}^{N_e} h_e, \quad n = 1, 2, \ldots, n_{od}. \tag{14–17}$$

Here, $\bar{h}_e$ is the size of the element Ω_e in the coarse mesh, N_e equals the number of elements meeting at node n, and n_{od} equals the number of nodes in the coarse mesh. We refer to H_n as the nodal element size at node n.

In order to generate the new mesh, we first discretize the boundary by following the procedure given by Cescotto and Zhou (1989). Let AB be a segment of the contour to be discretized, s the arc length measured from point A, and H_A and H_B be nodal element sizes for nodes located at points A and B, respectively. From a knowledge of the values of H at discrete points, corresponding to the nodes in the coarse mesh, on AB we define a piecewise linear continuous function $H(s)$ that takes the previously computed values at the node points. In order to discretize AB for the new mesh, we start from point A if $H_A < H_B$; otherwise we start from B. For the sake of discussion, let us assume that A is the starting point. We first find temporary positions of nodes on the segment AB by using the following recursive procedure. Assume that points $1, 2, \ldots, k$ have been found. Then the temporary location of point $(k+1)$ is given by

$$s_{k+1} = s_k + \tfrac{1}{2}[H(s_k) + H(s^*_{k+1})], \tag{18}$$

where

$$s^*_{k+1} = s_k + H(s_k). \tag{19}$$

Referring to Fig. 2, the above procedure will give rise to the following four alternatives: $a = b = 0$, $a < b$, $a > b$, $a = b \neq 0$. If $a = b = 0$, then the temporary locations of node points are their final positions. Depending upon whether $a < b$ or $b \leqq a$, the node points 2 to p or 2 to $p+1$ are moved, the displacement of a node being proportional to the value of H there, so that either node p or node $(p+1)$ coincides with B. This determines the final positions of nodes on the segment AB.

Having discretized the boundary, we use the concept of advancing front (e.g., see Lo 1985; Peraire et al. 1987, 1988; Habraken and Cescotto 1990) to generate the elements. An advancing front consists of straight line segments which are available to form a side of an element. Thus, to start with, it consists of the discretized boundary. We choose the smallest line segment (say side AB) connecting the two adjoining nodes, and determine the nodal element size $H_M \equiv H(s_M) = (H_A + H_B)/2$ at the midpoint M of AB. We set

$$\delta = \begin{cases} 0.8\,\overline{AB} & \text{if} \quad H_M < 0.8\,\overline{AB}, \\ H_M & \text{if} \quad 0.8\,\overline{AB} \leqq H_M \leqq 1.4\,\overline{AB}, \\ 1.4\,\overline{AB} & \text{if} \quad 1.4\,\overline{AB} < H_M, \end{cases} \tag{20}$$

and find point C_1 at a distance δ from A and B (cf. Fig. 3). Here $\overline{AB}$ equals the length of segment AB. We search for all nodes on the active front that lie inside the circle with center at C_1 and

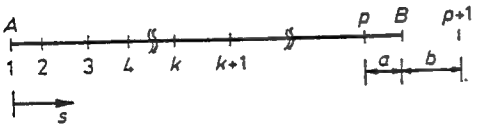

Fig. 2. Discretization of a boundary segment for mesh refinement

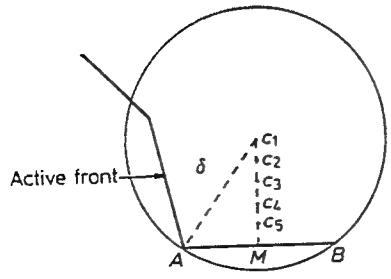

Fig. 3. Advancing front and new element generation

radius δ, and order them according to their distance from C_1 with the first node in the list being closest to C_1. At the end of this list are added points C_1, C_2, C_3, C_4, and C_5, which lie on C_1M and divide it into five equal parts. We next determine the first point C in the list that satisfies the following three conditions.

(i) Area of triangle ABC > 0.

(ii) Sides AC and BC do not cut any of the existing sides in the front.

(iii) If any of the points $C_1, C_2, \ldots, C_5$ is chosen, that point is not too close to the front.

The triangle ABC is an element in the new mesh. If C is one of the points $C_1, C_2, \ldots, C_5$, then a new node is also created. The advancing front is updated by removing the line segment AB from it, and adding line segments AC and CB to it. The element generation process ceases when there is no side left in the active front.

We determine the values of solution variables at a newly created node by first finding out to which element in the coarse mesh this node belongs, and then finding values of solution variables at this node by interpolation. This process and that of searching for line segments and points in the aforestated element generation technique consume a considerable amount of CPU time. These operations are optimized to some extent by using the heap list algorithm (e.g., see Löhner, 1988) for deleting and inserting new line segments, and quadtree structures and linked lists for searching line segments and points and also for the interpolation of solution variables at the newly created nodes.

4 Results and discussion

We assume that the block is made of a typical steel and assign the following values, also used by Batra and Liu (1989), to various parameters.

$$b = 10{,}000\,\text{sec}, \quad \sigma_0 = 333\,\text{MPa}, \quad k = 49.2\,\text{W m}^{-1}\,^{\circ}\text{C}^{-1}, \quad m = 0.025, \quad c = 473\,\text{Jkg}^{-1}\,^{\circ}\text{C}^{-1},$$
$$\rho_0 = 7{,}800\,\text{kg/m}^3, \quad \text{B} = 128\,\text{GPa}, \tag{21}$$
$$\nu = 0.0222\,^{\circ}\text{C}^{-1}, \quad v_0 = 25\,\text{m sec}^{-1}, \quad H = 5\,\text{mm}, \quad h(t) = 1.0.$$

Here we have made an exception to our notation and indicated dimensional quantities to clarify the units used. As stated earlier, the transients are assumed to have died out, the top surface moves downward with the prescribed speed v_0, and the average strain-rate at which the block is being deformed equals $5000\,\text{sec}^{-1}$. For values given in (21), $\theta_r = 89.6\,^{\circ}\text{C}$, and the non-dimensional melting temperature equals 0.5027. We note that the value of the thermal softening coefficient ν has been purposely taken to be high so as to reduce the computational time. It should not affect the qualitative nature of the results reported herein. The test data to find values of material parameters at strain-rates, strains, and temperatures likely to occur in a shear band is not available.

Figure 4 depicts the initial coarse mesh at time $t = 0$, and the generated refined meshes at non-dimensional time $t = 0.025$, 0.040, and 0.047. We note that the non-dimensional time also equals the average strain. In the solution of the problem, the mesh was also adaptively refined at $t = 0.015$, 0.030, and 0.035; however, these are not shown here for the sake of brevity. The times at which the mesh is refined were selected manually, and are to some degree arbitrary. A possible criterion could be to refine the mesh when the second invariant of the strain-rate tensor or the temperature at the center has risen by a certain amount. The meshes shown in Fig. 4 vividly reveal that the refinement technique outlined in Sect. 3 gives rise to nonuniform meshes with finer mesh in the severely deforming region and coarse mesh elsewhere. We did not impose any restriction on the number of new nodes that can be introduced when the mesh is refined. Practical considerations such as the core storage available may require this kind of restriction.

In Fig. 5 we have plotted the contours of the second invariant I of the deviatoric strain-rate tensor at $t = 0.019$, 0.032, 0.042, and 0.047 in the deformed configuration. These plots suggest that as the block continues to be deformed, the deformation localizes into a band whose width keeps on decreasing. Contours of successively increasing values of I originate from the center of the block and propagate outward. The contours of the temperature rise at $t = 0.019$, 0.032, 0.042, and 0.047

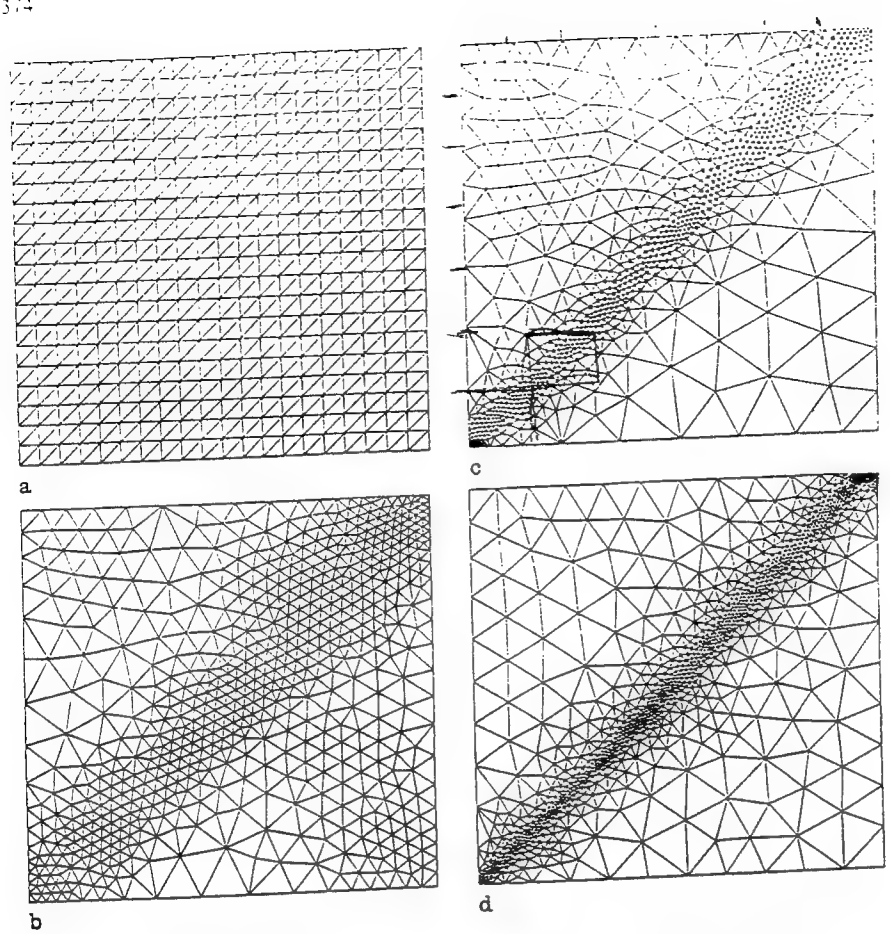

Fig. 4 a–d. Finite element meshes at **a** $t = 0.0$, **b** $t = 0.025$, **c** $t = 0.040$, and **d** $t = 0.047$

are exhibited in Fig. 6. The distribution of the velocity field in the deforming region at $t = 0.047$ is shown in Fig. 7. These plots support Tresca's (1878) and Massey's (1921) assertions that the tangential velocity is discontinuous across a shear band. In our work the velocity field is forced to be continuous throughout the domain. The sharp jumps in v_1 and v_2 across the shear band lend credence to the discontinuity of the tangential velocity across the shear band. The plot of the effective stress s_e, defined as

$$s_e = \sqrt{\tfrac{2}{3}}(1 - v\theta)(1 + bI)^m,$$

in Fig. 8 reveals that s_e drops considerably within the shear band. All of the aforestated observations are in qualitative agreement with Batra and Liu's (1989) results, except that the results reported herein are sharper in the sense that the region of localized deformation is considerably narrower and the computed values of I_{max} for the same value of θ_{max} are higher. Here I_{max} and θ_{max} denote, respectively, the peak values of the second invariant of the deviatoric strain-rate tensor and the temperature rise. For example, at $\theta_{max} = 0.45$, Batra and Liu (1989) found $I_{max} = 21$. Here, we get $I_{max} = 91$ for the same value of θ_{max}. We note that Batra and Liu (1989) used 9-noded quadrilateral elements and employed a fixed 16×16 mesh.

In an attempt to elucidate the improvement, if any, in the computed results obtained by using adaptively refined meshes, we have plotted in Fig. 9 the evolution, at the block center, of the second invariant I of the deviatoric strain-rate tensor, the temperature rise, and the effective stress for three different meshes. Two of these meshes with 441 and 841 nodes, and consisting of uniform linear triangular elements are fixed, while the third one was adaptively refined at times $t = 0.015$, 0.025, 0.030, 0.035, 0.040, and 0.047 with uniform linear triangular elements and 441 nodes at $t = 0$

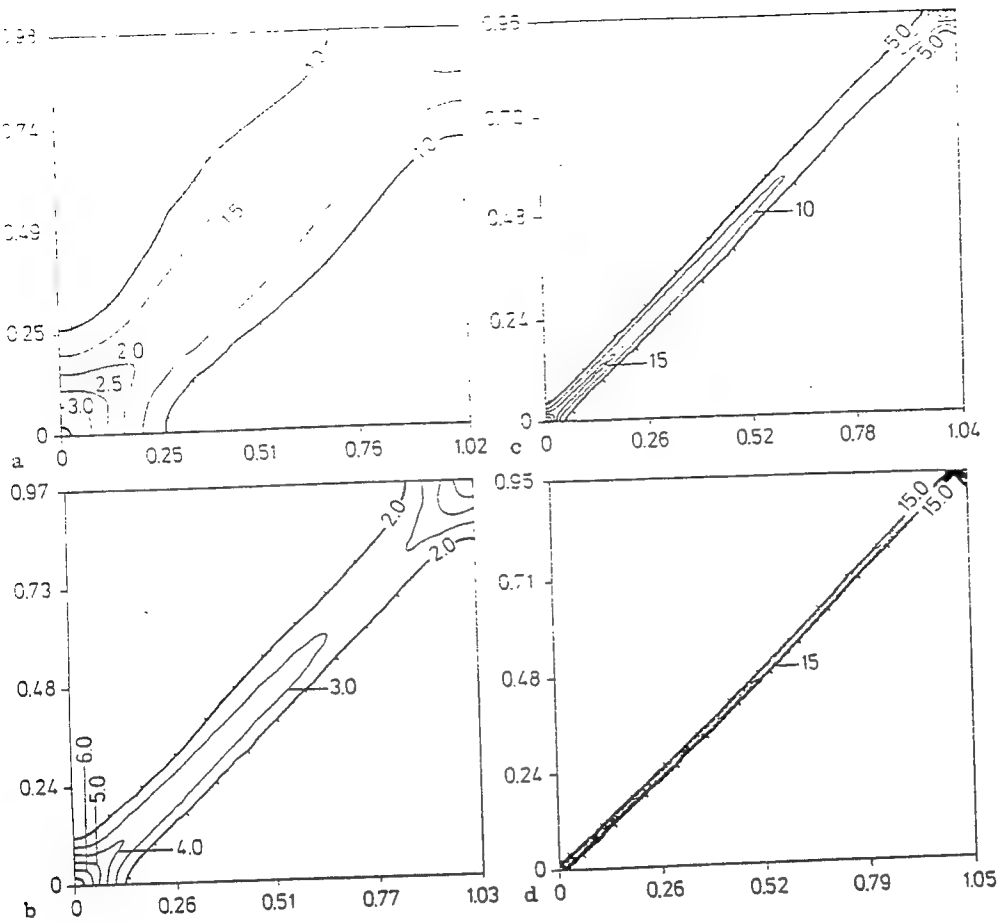

Fig. 5 a–d. Contours of the second invariant of the deviatoric strain-rate tensor at **a** $t = 0.019$, **b** $t = 0.032$, **c** $t = 0.042$, and **d** $t = 0.047$

and nonuniform linear triangular elements with 1200 nodes at $t = 0.047$. Out of the three variables s_e, I, and θ, the evolution of I is affected most by the successive refinements of the mesh. For the two fixed meshes with 441 and 841 nodes, I at the specimen center seems to reach a plateau, which is misleading. Also after the deformation has started to localize, the temperature rise and its rate of increase are higher for the adaptively refined mesh than those for either of the other two fixed meshes. For the solution with the adaptively refined mesh, I at the block center increases from 10 at $\gamma_{avg} = 0.035$ to nearly 52 at $\gamma_{avg} = 0.045$, giving a rate of increase of strain-rate of $10^{11}\ \text{sec}^{-2}$. If one assumes that the deformation begins to localize earnestly at $\gamma_{avg} = 0.035$, then the generalized strain, defined as $\int I\,dt$, at the block center increases by 0.3 in two microseconds. The larger drop in s_e in spite of the sharp increase in the value of I indicates that thermal softening dominates over the strain-rate hardening effects. It is due to the rather high value of the thermal softening coefficient ν used here. Note that increasing the value of nondimensional I from 10 to 100 changes the value of $(1 + bI)^m$ from 1.65 to 1.75.

We now investigate the change, if any, in the approximate solution caused by refining the mesh. This task would be easy if the analytical solution of the problem were known. Since such is not the case and there is little hope of finding an analytical solution of the problem in the near future, we compare our approximate solution with a higher-order approximate solution (Hinton and Campbell, 1974) obtained by smoothening out the computed solution. Let g be one of the solution variables to be smoothened. For the three-noded triangular element, we write

$$g(\xi, \eta) = a\xi + b\eta + c, \tag{23}$$

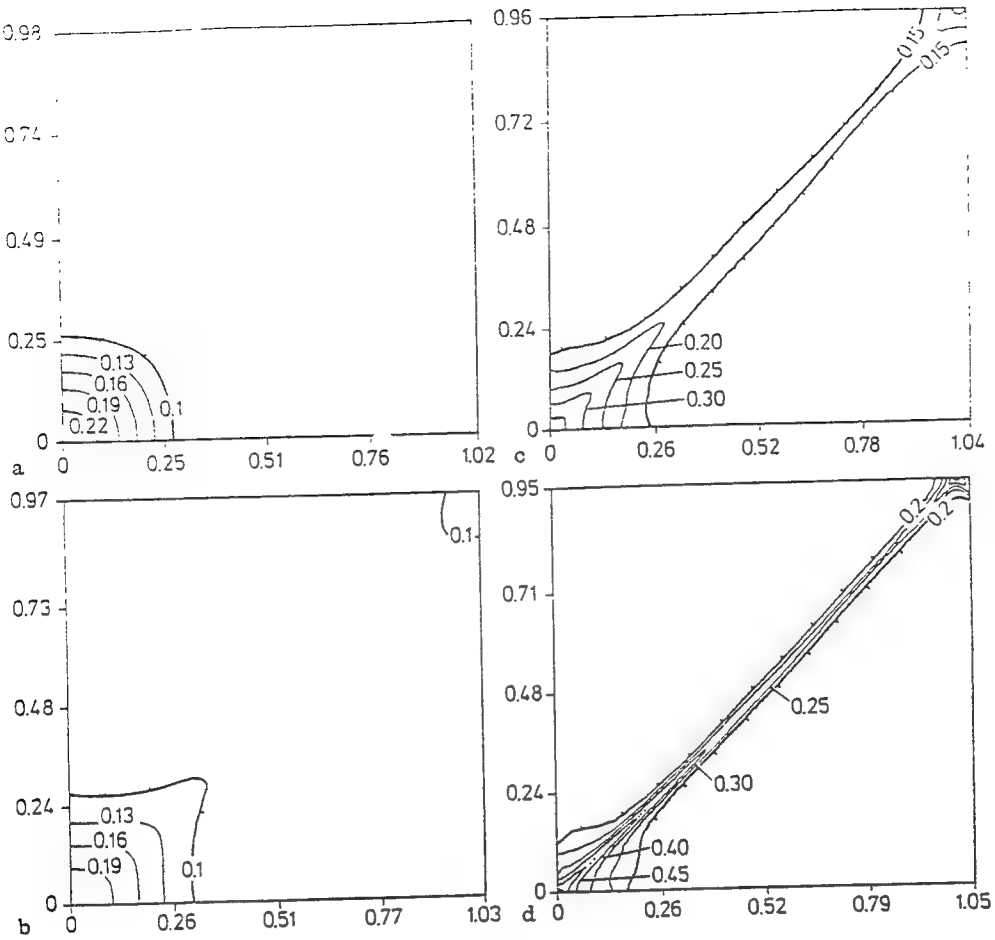

Fig. 6 a–d. Contours of the temperature rise at **a** $t = 0.019$, **b** $t = 0.032$, **c** $t = 0.042$, and **d** $t = 0.047$

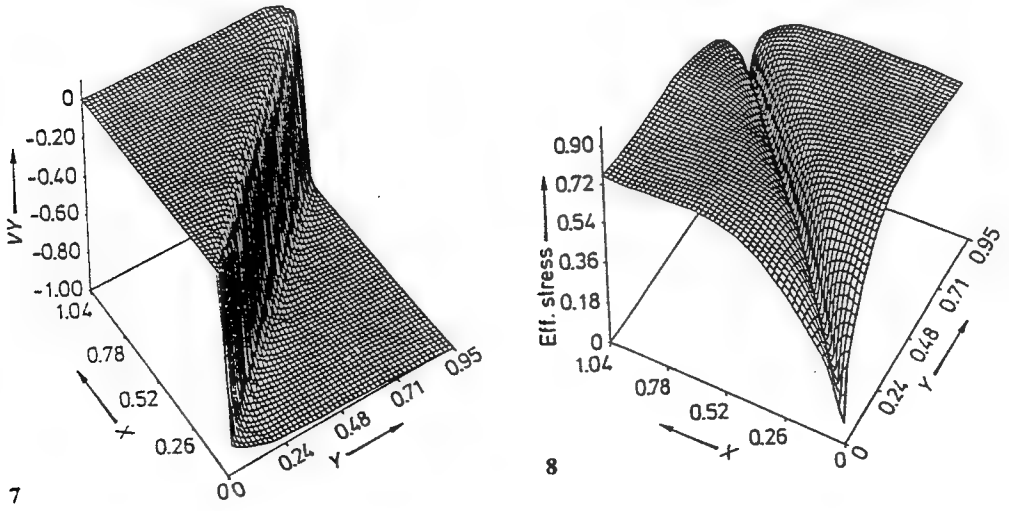

Figs. 7 and 8. Distribution 7 of the velocity field at $t = 0.047$, and 8 of the effective stress at $t = 0.047$

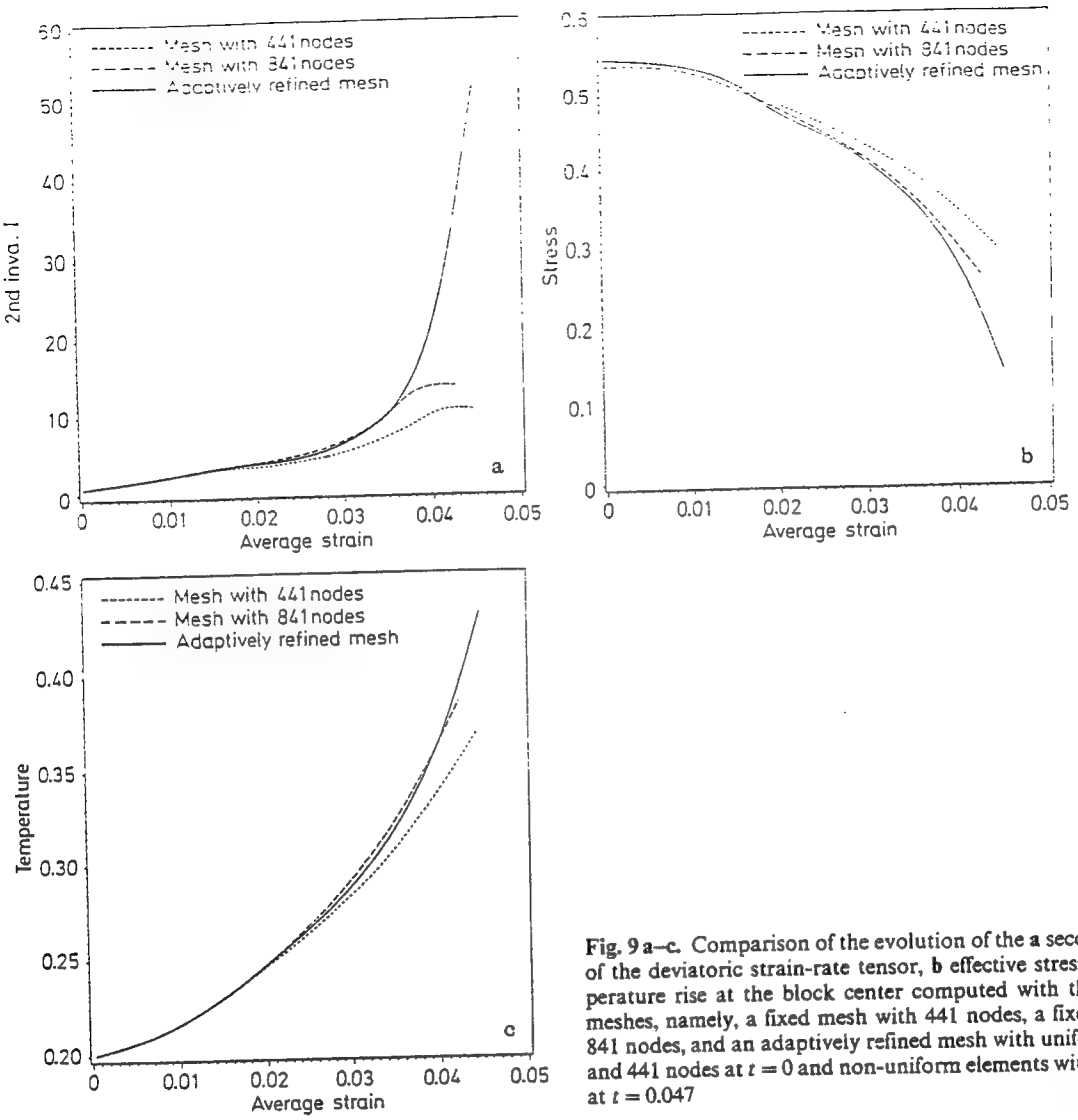

Fig. 9 a–c. Comparison of the evolution of the **a** second invariant of the deviatoric strain-rate tensor, **b** effective stress, and **c** temperature rise at the block center computed with three different meshes, namely, a fixed mesh with 441 nodes, a fixed mesh with 841 nodes, and an adaptively refined mesh with uniform elements and 441 nodes at $t = 0$ and non-uniform elements with 1200 nodes at $t = 0.047$

where ξ and η are area coordinates of a point, and constants a, b, and c are determined from the values of g at three quadrature points located within the triangular element. From (23) we can evaluate g at the vertices of the triangle. Then the value g_n^* of the smoothened solution at a node n is given by

$$g_n^* = \frac{1}{N_e} \sum_{n=1}^{N_e} g_n, \tag{24}$$

where N_e equals the number of elements sharing the node n, and the summation sign on the right-hand side implies the sum of the values of g at node n evaluated for each element meeting at that node. Knowing g^* at each node, we can interpolate its value at any other point by using the finite element basis functions. We define the percentage error η in the deviatoric strain-rate tensor $\bar{\mathbf{D}}$ by the relation

$$\eta = \left(\frac{\|\mathbf{e}\|_0^2}{\|\mathbf{e}\|_0^2 + \|\bar{\mathbf{D}}\|_0^2} \right)^{1/2} \times 100, \tag{25}$$

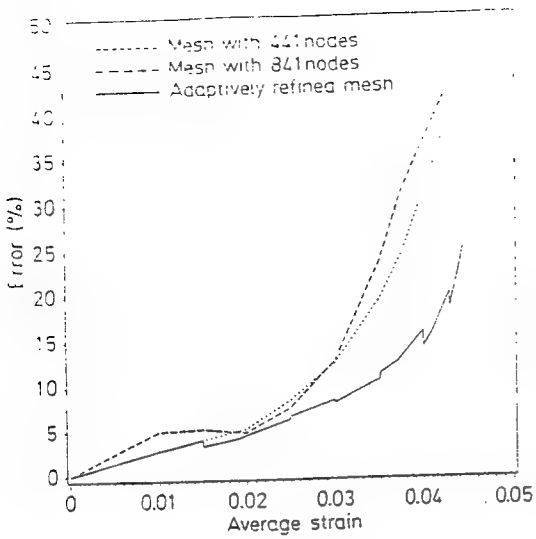

Fig. 10. Comparison of the error in the computed approximate solution and the higher-order approximate solution for three different meshes: fixed mesh with 441 nodes, fixed mesh with 841 nodes, and an adaptively refined mesh

where

$$\mathbf{e} = \bar{\mathbf{D}} - \bar{\mathbf{D}}^*, \qquad \|\mathbf{e}\|_0^2 = \sum_{e=1}^{N_{el}} \int_{\Omega_e} \mathbf{e}^T \mathbf{e} \, d\Omega, \tag{26.1, 26.2}$$

and N_{el} equals the number of elements in the mesh. The plot of the percentage error η in Fig. 10 for the three meshes shows that the error is lower for the approximate solution obtained by using the adaptively refined mesh as compared to the other two meshes. That the error measure is rather crude is indicated by the slightly larger errors obtained with a fixed mesh of 841 nodes as compared to that with 441 nodes. It could be due to the larger errors caused by smoothening out of the approximate solution with 841 nodes since the band in this case is more intense than that for the mesh with 441 nodes.

5 Conclusions

We have used adaptively refined meshes to study the initiation and growth of shear bands in a square block made of a viscoplastic material. The mesh is refined at various times to ensure that the integral of the second invariant of the deviatoric strain-rate tensor over each element is nearly the same for all elements in the mesh. It generates a non-uniform mesh with small elements in regions where the strain-rate is high and large elements elsewhere. It is shown that such meshes are quite effective in analyzing problems in which the deformation localizes into narrow bands of intense plastic deformation. A comparison of the computed solution with a higher-order approximate solution reveals that the use of the adaptively refined meshes leads to lower error in the approximate solution as compared to that obtained with a fixed mesh. For the problem studied herein, the band forms in about two microseconds, and at a homologous temperature of 0.99 at the specimen center, the maximum strain-rate there equals $4.65 \times 10^5 \, \text{sec}^{-1}$.

Acknowledgements

This work was supported by the U.S. Army Research Office Grant DAAL03-91-G-0084 and the U.S. NSF grant M SS-9121279 to the University of Missouri–Rolla. Some of the computations were performed on the NSF sponsored supercomputer center in Ithaca, NY.

References

Batra, R. C.; Liu, D.-S. (1989): Adiabatic shear banding in plane strain problems. J. Appl. Mech. 56, 527–534
Batra, R. C.; Zhu, Z. G. (1991): Dynamic shear band development in a bimetallic body containing a void. Int. J. Sol. Struct. 27, 1829–1854
Cescotto, S.; Zhou, D. W. (1989): A variable density mesh generation for planar domains. Comm. Appl. Num. Meth. 5, 473–481
Habraken, A. M.; Cescotto, S. (1990): An automatic remeshing technique for finite element simulation of forming processes. Int. J. Num. Meth. Eng. 30, 1503–1525
Hindmarsh, A. C. (1983): ODEPACK, A systematized collection of ODE solvers. In: Stepleman, R. S. et al. (eds): Scientific computing, pp 55–64. Amsterdam, North-Holland
Hinton, E.; Campbell, J. S. (1974): Local and global smoothing of discontinuous finite element functions using a least squares method. Int. J. Num. Meth. Eng. 8, 461–480
Lo, S. H. (1985): A new mesh generation scheme for arbitrary planar domains. Int. J. Num. Meth. Eng. 21, 1403–1426
Löhmer, R. (1988): Some useful data structures for the generation of unstructured grids. Comm. Appl. Num. Meth. 4, 123–135
Massey, H. F. (1921): The flow of metal during forging. Proc. Manchester Assoc. Engrs. 21–26
Needleman, A. (1989): Dynamic shear band development in plane strain. J. Appl. Mech. 56, 1–9
Peraire, J.; Vahdati, M.; Morgan, K.; Zienkiewicz, O. C. (1987): Adaptive remeshing for compressible flow computations J. Comp. Phys. 72, 449–466
Peraire, J.; Peiro, J.; Formaggia, L.; Horgan, K.; Zienkiewicz, O. C. (1988): Finite element Euler computations in three dimensions. Int. J. Num. Meth. Eng. 26, 2135–2159
Safjan, A.; Demkowicz, L.; Oden, J. T. (1991): Adaptive finite element methods for hyperbolic systems with application to transient acoustics. Int. J. Num. Meth. Eng. 32, 677–707
Tresca, H. (1878): On further application of the flow of solids. Proc. Inst. Mech. Eng. 30, 301–345
Zienkiewicz, O. C.; Zhu, J. Z. (1991): Adaptivity and mesh generation. Int. J. Num. Meth. Eng. 32 783–810

Communicated by S. N. Atluri, February 11, 1992

Consideration of Phase Transformations in the Study of Shear Bands in a Dynamically Loaded Steel Block

Z. G. Zhu

R. C. Batra
Fellow ASME

Department of Mechanical and Aerospace Engineering and Engineering Mechanics, University of Missouri-Rolla, Rolla, MO 65401-0249

We study plane strain thermomechanical deformations of a square block made of steel, and model a material defect in it by a rigid non-heat-conducting ellipsoidal inclusion located at the center of the block. The boundaries of the block are presumed to be thermally insulated, and its top and bottom surfaces compressed vertically at a prescribed rate. The loading pulse is assumed to be made up of three parts; an initial segment in which the speed increases from zero to the steady value, the steady part, and the third part in which the speed decreases gradually to zero and is maintained at zero subsequently. In the undeformed state, the specimen is assumed to be fully annealed, isotropic, and its microstructure to be a mixture of coarse ferrite and cementite. A material point is presumed to start transforming into austenite once its temperature exceeds the transformation temperature; the rate of transformation is controlled by a simple kinetic equation. Proper account is taken of the latent heat required for the transformation, the associated volume change, and the variation in the thermophysical properties. The complete thermomechanical problem is analyzed during the loading and unloading phase till all of the body points have essentially come to rest, and the energy equation is solved subsequently. It is found that the austenite is quenched rapidly enough by the surrounding material for it to be converted into martensite rather than pearlite or a mixture of pearlite and martensite.

Introduction

Shear bands in a dynamically loaded metal block often occur when softening caused by the heating of the material exceeds the combined effects of strain and strain-rate hardening, and generally precede shear fractures. These bands have been observed by Tresca (1878) and Massey (1921), who called them hot lines. Zener and Hollomon (1944) measured 32 μm wide shear bands during the punching of a hole in a steel plate, and stated that some of the region within the band etched white, thereby suggesting the presence of martensite within the band. Roger (1979), in his review article, has alluded to similar observations and hypothesized that hot material within the band is quenched fast enough by the surrounding colder material that austenite within the band is transformed into martensite. Lindholm and Johnson (1983) have reported on the presence of martensite within a shear band formed in AMS6418 steel. Giovanola (1988) has measured temperatures close to 1100°C in shear bands formed in 4340 VAR (vacuum arc remelted) steel, which is well above the transformation temperature of ferrite and cementite into austenite. Wingrove (1971), based on electron microscopic observations, concluded that, indeed, transformation into martensite occurred within the band.

We note that previous analytical and numerical works (e.g., see Zhu and Batra (1990) for a list of references) on the analysis of shear bands in a dynamically loaded steel block did not consider the possibility of phase transformations. Here we postulate rather simple kinetic equations for the transformation of the mixture of ferrite and cementite into austenite during heating, and from austenite to martensite or pearlite during cooling. It is shown that the material within the band is indeed cooled fast enough by the surrounding material that the austenite is transformed into martensite, and the total time taken from the beginning of the loading phase to the cooling of the body to a nearly uniform temperature equals 150 milliseconds.

Formulation of the Problem

We use a fixed set of rectangular Cartesian coordinates with origin at the centroid of the square block (cf. Fig. 1) to analyze its plane strain thermomechanical deformations. We assume that the block is made of steel, and in the stress-free reference configuration the material is fully annealed, isotropic, and its microstructure is a mixture of coarse ferrite and cementite. Furthermore, there is a non-heat-conducting rigid ellipsoidal inclusion with its major and minor axes coinciding with the centroidal axes of the cross-section. In terms of the referential description, governing equations are:

Contributed by the Materials Division for publication in the JOURNAL OF ENGINEERING MATERIALS AND TECHNOLOGY. Manuscript received by the Materials Division February 24, 1992; revised manuscript received March 22, 1992. Associate Technical Editor: D. Hui.

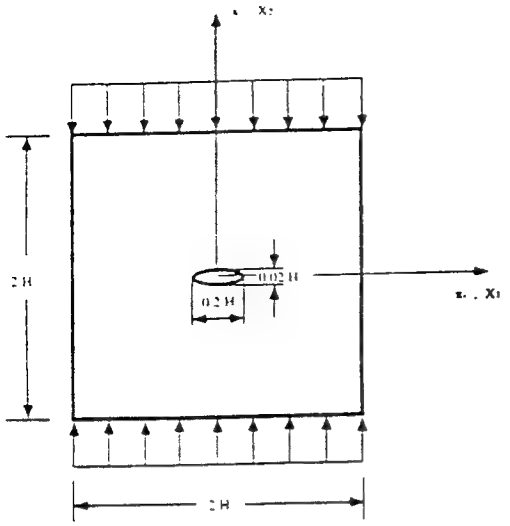

Fig. 1 A schematic sketch of the problem studied

$$(\rho J)^{\cdot} = 0, \tag{1}$$

$$\rho_0 \dot{v}_i = T_{i\alpha,\alpha}, \tag{2}$$

$$\rho_0 \dot{e} = -Q_{\alpha,\alpha} + T_{i\alpha} v_{i,\alpha} + \dot{Q}_L, \tag{3}$$

where

$$J = \det F_{i\alpha}, \quad F_{i\alpha} = x_{i,\alpha}, \quad x_{i,\alpha} = \partial x_i / \partial X_\alpha, \tag{4}$$

x_i is the present location of a material particle that occupied place X_α in the reference configuration, ρ its present mass density, ρ_0 its mass density in the reference configuration, v_i its present velocity, $T_{i\alpha}$ the first Piola-Kirchoff stress tensor, Q_α the heat flux per unit reference area, e the specific energy, a superimposed dot indicates the material time derivative, and a repeated index implies summation over the range of the index. Equations (1), (2), and (3) express, respectively, the balance of mass, balance of linear momentum, and the balance of internal energy. For the constitutive relations we take

$$\sigma_{ij} = -B\left(\frac{\rho}{\rho_0} - 1\right)\delta_{ij} + 2\mu D_{ij} - 3K(e_{th} + e_{ph})\delta_{ij}, \tag{5.1}$$

$$T_{i\alpha} = \frac{\rho_0}{\rho} X_{\alpha,j}\sigma_{ij}, \quad 2\mu = \frac{\sigma_0}{\sqrt{3I}}(1 + bI)^m(1 - \nu(\theta - \theta_0)), \tag{5.2,3}$$

$$2D_{ij} = v_{i,j} + v_{j,i}, \quad 2I^2 = \hat{D}_{ij}\hat{D}_{ij}, \quad \hat{D}_{ij} = D_{ij} - \frac{1}{3} D_{kk}\delta_{ij}, \tag{5.4,5,6}$$

$$Q_\alpha = \frac{\rho_0}{\rho} X_{\alpha,j} q_j, \quad q_i = -k\theta_{,i}, \tag{5.7,8}$$

$$\rho_0 \dot{e} = \rho_0 c\dot{\theta} + \frac{\rho_0 \dot{\rho}}{\rho^2}\left[B\left(\frac{\rho}{\rho_0} - 1\right) + 3K(e_{th} + e_{ph})\right], \tag{5.9}$$

$$e_{th} = 3\int_{\theta_0}^{\theta} \hat{\alpha}(\theta)d\theta, \quad e_{ph} = \frac{\Delta v_{ph}}{v}, \tag{5.10,11}$$

$$\frac{\Delta v_{ph}}{v} = -(f_\gamma + f_m)\xi_1 + f_m\xi_2,$$

$$\dot{Q}_L = \dot{Q}_{1L} + \dot{Q}_{2L} + \dot{Q}_{3L}. \tag{5.12,13}$$

Here σ_{ij} is the Cauchy stress tensor, B may be thought of as the bulk modulus for the material of the block, K equals the bulk modulus, $\mathbf{D}$ is the strain-rate tensor, σ_0 the yield stress of the material in a quasistatic simple tension or compression test, parameters b and m characterize the strain-rate sensitivity of the material, I is the second invariant of the deviatoric strain-rate tensor $\hat{\mathbf{D}}$, ν is the coefficient of thermal softening, k equals the thermal conductivity, c the specific heat, θ the temperature rise of a material particle, $\hat{\alpha}$ the coefficient of thermal expansion, ξ_1 the dilatational strain for complete transformation of austenite (γ-phase) to pearlite or the strain of volume shrinkage for complete transformation of ferrite and cementite to austenite, ξ_2 the dilatational strain for complete transformation of austenite to martensite, $\dot{Q}_{1L}$ the rate of latent heat for the transformation from the mixture of ferrite and cementite to γ-phase, $\dot{Q}_{2L}$ the rate of latent heat for the transformation from γ-phase to pearlite, $\dot{Q}_{3L}$ is the rate of latent heat for the transformation of γ-phase to martensite, f_γ is the volume fraction of the γ-phase, and f_m the volume fraction of the martensite phase present at a spatial location. Batra (1988) and Batra and Liu (1989) have used Eq. (5.1) with μ given by (5.3) to study the steady-state penetration problem and the initiation and growth of shear bands in a viscoplastic material. Batra and Jayachandran (1992) have shown that for the penetration problem, it and the constitutive relations proposed by Bodner-Partom (1975) and Brown et al. (1989) give essentially identical results. The last term on the right-hand side of Eq. (5.1) accounts for the pressure induced by dilatation associated with the phase changes, and should not affect plastic deformations of the body.

The thermophysical properties of a material point are determined from their values for different phases, the volume fractions of these phases making up that material particle, and the rule of mixtures. That is

$$\eta = f_\alpha\eta_\alpha + f_\gamma\eta_\gamma + f_m\eta_m \tag{6}$$

where η_α, η_γ, and η_m are the values of η for the α-phase, γ-phase, and martensite, respectively. Strictly speaking, the α-phase is ferrite. For simplicity, we take the material properties of the mixture of ferrite and cementite to be the same as that of pearlite, also referred to as the α-phase. We note that the three phases need not be present simultaneously at a point. Budiansky (1970) has derived expressions for thermophysical parameters for an isotropic composite in terms of volume fractions and thermophysical constants of the constituents. Inoue (1989) has obtained expressions for Young's modulus, Poisson's ratio, the coefficient of thermal expansion, and the volumetric dilatation due to phase changes for the mixture in terms of the values of these parameters for the constituents and their volume fractions. Of these, the global values of the coefficient of thermal expansion and the volumetric dilatation obey Eq. (6). Inoue (1989) has assumed an expression like Eq. (6) for the potential (or yield) function for a mixture. Here, for simplicity, we use Eq. (6) to evaluate all of the material parameters needed in this study.

The kinetic equation for the phase transformation from the α-phase to the γ-phase is taken to be

$$\dot{f}_\gamma = \begin{cases} \dfrac{\dot{\theta}}{25}, & \text{for } \dot{\theta} > 0,\ 725^\circ\text{C} \le \theta \le 750^\circ\text{C}, \\ 0, & \text{otherwise.} \end{cases} \tag{7.1}$$

Thus

$$f_\gamma = (\theta - 725)/25, \quad \text{for } \dot{\theta} > 0,\ 725^\circ\text{C} \le \theta \le 750^\circ\text{C}. \tag{7.2}$$

Similarly, the latent heat release rate for the transformation from α-phase to γ-phase is assumed to have the form

$$\dot{Q}_{1L} = \begin{cases} -\dfrac{\dot{\theta}}{25} Q_1, & 725^\circ\text{C} \le \theta \le 750^\circ\text{C},\ \dot{\theta} > 0, \\ 0, & \text{otherwise.} \end{cases} \tag{8}$$

Whether or not γ-phase changes back to α-phase depends upon the cooling rate at a point. Referring to Fig. 2, the transformation from γ-phase to pearlite is assumed to begin as soon as the cooling curve for a point intersects parabola A, and is presumed to have completed by the time the cooling

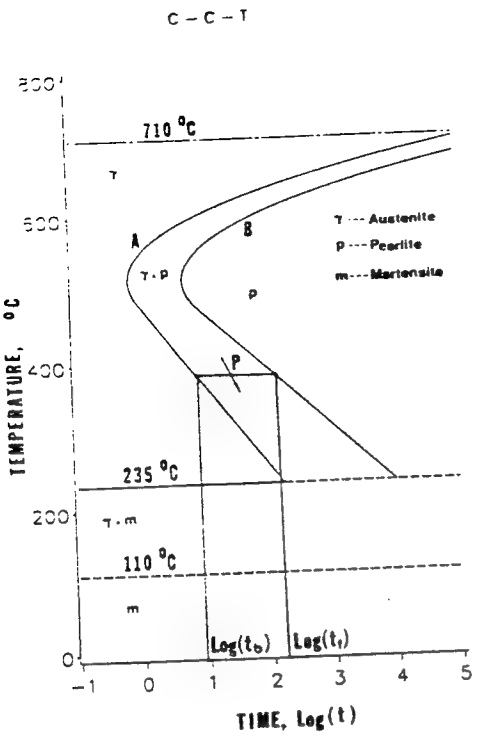

Fig. 2 Phase diagram during continuous cooling for a typical steel

curve intersects parabola B. At any intermediate point P, we assume that the rate of conversion from γ-phase to pearlite and the corresponding rate of release of the latent heat are given by

$$\dot{f}_\alpha = \frac{k}{\ln 10} \max\left(\frac{1}{\log t'}, \frac{1}{t_{\text{eff}}}\right), \quad t' = t - t^* > t_b, \tag{9}$$

$$\dot{Q}_{3L} = Q_{3L}\dot{f}_\alpha, \tag{10}$$

where

$$k = \frac{1}{t_f - t_b}, \tag{11.1}$$

$$t_{\text{eff}} = t_b^{1-f_\alpha} t_f^{f_\alpha}, \tag{11.2}$$

t_b and t_f are defined in Fig. 2, and t^* equals the time when the temperature reaches 710°C during the cooling process. Thus, we assume that f_α increases linearly from 0 to 1 between times $\log t_b$ and $\log t_f$. Note that the abscissa in Fig. 2 equals the logarithm of time.

If the temperature of a material point where γ-phase is present reaches 235°C during the cooling process, we assume that the γ-phase starts transforming into martensite, the rate of transformation and the rate of latent heat release being given by

$$\dot{f}_m = \begin{cases} -\frac{1}{125} f_\gamma^* \dot{\theta}, & \dot{\theta} < 0, \quad 110°\text{C} \le \theta \le 235°\text{C}, \\ 0, & \text{otherwise}, \end{cases} \tag{12}$$

$$\dot{Q}_{3L} = Q_{3L}\dot{f}_m. \tag{13}$$

Here f_γ^* equals the volume fraction of the γ-phase present at the material particle when its temperature cools down to 235°C.

Inoue (1989), in his review article, has summarized a theory of elastoviscoplasticity that incorporates the effect of phase transformations, and has also listed kinetic equations for phase transformations used by different investigators. These kinetic equations are considerably more involved than Eqs. (7.1), (9), and (12), and require a knowledge of material parameters not available in any handbook. The constitutive relations (7.1), (9), and (12) are based on the observations from the phase diagram, which indicate that ferrite transforms into austenite at about 725°C, and that above this temperature, and depending upon the carbon content, different volume fractions of these phases may be in equilibrium. Thus, one will need to know the initial carbon content and also study the diffusion of carbon. Such details are warranted in the analysis of the mechanics of phase transformations; however, we omit these herein. Realizing that the phase diagram refers to the equilibrium situation and the transformation from one phase to another does not occur instantaneously, we have taken (7.1), (9), and (12) as the constitutive relations for f_γ and f_α.

We introduce non-dimensional variables, indicated below by a superimposed bar, as follows.

$$\bar{\sigma} = \sigma/\sigma_r, \quad \bar{s} = s/\sigma_r, \quad \bar{T} = T/\sigma_r, \quad \bar{B} = B/\sigma_r, \quad \bar{K} = K/\sigma_r,$$
$$\bar{Q}_L = Q_L/\sigma_r, \quad \bar{x} = x/H, \quad \bar{X} = X/H, \quad \dot{\gamma}_0 \equiv v_0/H, \quad \bar{v} = v/v_0,$$
$$\bar{I} = I/\dot{\gamma}_0, \quad \bar{D} = D/\dot{\gamma}_0, \quad \bar{t} = t\dot{\gamma}_0, \quad \bar{b} = b\dot{\gamma}_0, \quad \bar{\nu} = \nu\theta_r, \quad \theta_r \equiv \frac{\sigma_r}{\rho_r c_r},$$
$$\bar{\alpha} = \alpha\theta_r, \quad \bar{\rho} = \rho/\rho_r, \quad \bar{\rho} = \rho_0/\rho_r, \quad \bar{c} = c/c_r, \quad \delta \equiv \rho_r v_0^2/\sigma_r,$$
$$\beta = \frac{k_r}{\rho_r c_r v_0 H}, \quad \bar{k} = k/k_r. \tag{14}$$

The subscript r on a quantity indicates its reference value, usually that for the initial ferrite and cementite phases, 2H equals the length of a side of the square cross-section, v_0 is the value of the steady velocity applied on the top and bottom surfaces, and $\dot{\gamma}_0$ equals the average applied strain rate. Henceforth, we work in terms of nondimensional variables and drop the superimposed bar. We note that the nondimensional number δ indicates the importance of inertia forces relative to the yield stress of the material, and β equals the thermal length.

We assume that all four sides of the square cross-section are thermally insulated, the two vertical sides are traction free, there is no tangential traction on the top and bottom edges, and a preassigned vertical velocity is prescribed on these edges. Thus, it is reasonable to assume that the deformations of the block are symmetrical about the horizontal and vertical centroidal axes. We study deformations of the material lying in the first quadrant and impose on it the following boundary conditions.

$$v_1 = 0, \quad T_{12} = 0, \quad Q_1 = 0 \quad \text{at} \quad x_1 = X_1 = 0, \tag{15.1}$$

$$v_2 = 0, \quad T_{21} = 0, \quad Q_2 = 0 \quad \text{at} \quad x_2 = X_2 = 0, \tag{15.2}$$

$$T_{11} = 0, \quad T_{12} = 0, \quad Q_1 = 0 \quad \text{on} \quad X_1 = H, \tag{15.3}$$

$$T_{12} = 0, \quad v_2 = -h(t), \quad Q_2 = 0 \quad \text{on} \quad X_2 = H, \tag{15.4}$$

$$v_1 = 0, \quad v_2 = 0, \quad Q_\alpha N_\alpha = 0$$

on the surface of the rigid inclusion. (15.5)

The boundary conditions on the edges $X_1 = 0$ and $X_2 = 0$ follow from the presumed symmetry of deformations, and those on the inclusion surface are implied by the assumptions that the inclusion is rigid and non-heat-conducting. The function $h(t)$ is given by

$$h(t) = t/0.005, \qquad 0 \le t \le 0.005, \tag{16.1}$$

$$= 1, \qquad 0.005 \le t \le 0.5055, \tag{16.2}$$

$$= 1 - \frac{t - 0.5055}{0.005}, \qquad 0.5055 \le t \le 0.5105, \tag{16.3}$$

$$= 0, \qquad t \ge 0.5105. \tag{16.4}$$

The duration of the loading pulse is believed to be large enough to cause the phase transformation from α-phase to γ-phase to occur. It will be interesting to see if the cooling of austenite due to the heat loss from the material within the band to the

surrounding material is rapid enough to facilitate its transformation into martensite or not.

For the initial conditions, we take

$$\rho(\mathbf{x},0)=1, \quad \mathbf{v}(\mathbf{x},0)=0, \quad \theta(\mathbf{x},0)=\theta_0, \quad f_\alpha(\mathbf{x},0)=1.0,$$
$$f_\gamma(\mathbf{x},0)=0, \quad f_m(\mathbf{x},0)=0. \quad (17)$$

That is, the body is initially at rest, has a uniform mass density and temperature, and all of the material is a mixture of ferrite and cementite.

Computational Considerations

The problem formulated above is highly nonlinear. It is almost impossible to prove the existence and uniqueness of its solution. Here we find an approximate solution of the problem by first reducing the coupled nonlinear partial differential equations governing the thermomechanical deformations of the block to a set of coupled, nonlinear, and ordinary stiff differential equations by using the Galerkin approximation. At each node point in the mesh, two components of the velocity, the temperature and the mass density are taken as unknowns. A finite element mesh consisting of 4-noded quadrilateral elements with 2 × 2 Gauss quadrature rule and lumped mass matrix is employed. The stiff ordinary differential equations are integrated with respect to time by using the backward difference Adam's method included in the subroutine LSODE (e.g., see Hindmarsh, 1971). The Gear method, also included in LSODE, could not be used because of the limited core storage available. The computer code developed by Batra and Liu (1989) was suitably modified to solve the present problem.

The temperature at a quadrature (Gauss) point within an element is computed from a knowledge of its values at the node points. The temperature and its rate of change at a quadrature point determine, according to Eqs. (7.1), (9), and (12), the phase transformation at that point. The value of a thermophysical property at a quadrature point is determined by using Eq. (6).

Results and Discussion

We assume that in the unstressed reference configuration the microstructure is a mixture of coarse ferrite and cementite, and assign the following values to various parameters. Parameters that are taken to have the same value for all three phases are indicated without any subscripts.

$$b=10{,}000\ \text{s}, \quad \rho_r=7860\ \text{kg m}^{-3}, \quad B=128\ \text{GPa},$$
$$c=473\ \text{J kg}^{-1}\ ^\circ\text{C}^{-1}, \quad v_0=25\ \text{m/s}, \quad H=5\ \text{mm},$$
$$\theta_0=25^\circ\text{C}, \quad K=159(1-1.47\times10^{-4}\,\theta)\text{GPa},$$
$$-Q_{1L}=Q_{2L}=0.628\times10^9\ \text{Jm}^{-3}, \quad Q_{3L}=0.542\times10^9\ \text{Jm}^{-3},$$
$$e_{ph}^{\gamma\alpha}=-e_{ph}^{\alpha\gamma}=0.007, \quad e_{ph}^{\gamma m}=0.044, \quad \xi_1=0.007, \quad \xi_2=0.044,$$
$$\alpha_\alpha=14\times10^{-6}\ ^\circ\text{C}^{-1}, \quad \alpha_\gamma=21\times10^{-6}\ ^\circ\text{C}^{-1},$$
$$\alpha_m=13\times10^{-6}\ ^\circ\text{C}^{-1},$$
$$k_\alpha=49.216(1-5.05\times10^{-4}\,\theta)\text{Wm}^{-1}\ ^\circ\text{C}^{-1},$$
$$k_\gamma=15(1+7.48\times10^{-4}\,\theta)\text{Wm}^{-1}\ ^\circ\text{C}^{-1},$$
$$k_m=43.1(1-5.03\times10^{-4}\,\theta)\text{Wm}^{-1}\ ^\circ\text{C}^{-1},$$
$$\sigma_r=\sigma_{0\alpha}=333\ \text{MPa}, \quad \sigma_{0\gamma}=190\ \text{MPa}, \quad \sigma_{0m}=1600\ \text{MPa},$$
$$\nu_m=2.5\times10^{-4}\ ^\circ\text{C}^{-1},$$
$$\text{for } 0\le\theta\le600^\circ\text{C}, \quad \nu_\alpha=1.51\times10^{-3}\ ^\circ\text{C}^{-1},$$
$$\nu_\gamma=1.392\times10^{-3}\ ^\circ\text{C}^{-1},$$
$$\text{for } \theta>600^\circ\text{C}, \quad \nu_\alpha=1.11\times10^{-4}\ ^\circ\text{C}^{-1},$$
$$\nu_\gamma=1.83\times10^{-4}\ ^\circ\text{C}^{-1}. \quad (18)$$

Here we have made an exception to our notation and indicated dimensional quantities to clarify units used. The value of the temperature θ in expressions for several variables is measured in °C. For assigned values of v_0 and H, the average applied strain-rate equals 5000 sec^{-1}. The superscripts $\gamma\alpha$ and γm on e_{ph} indicate that the volumetric strain for complete transformation from γ-phase to pearlite and from γ-phase to martensite equal 0.007 and 0.044, respectively. Values of material parameters associated with different phases are taken from Reed-Hill (1973) and Yu et al. (1979).

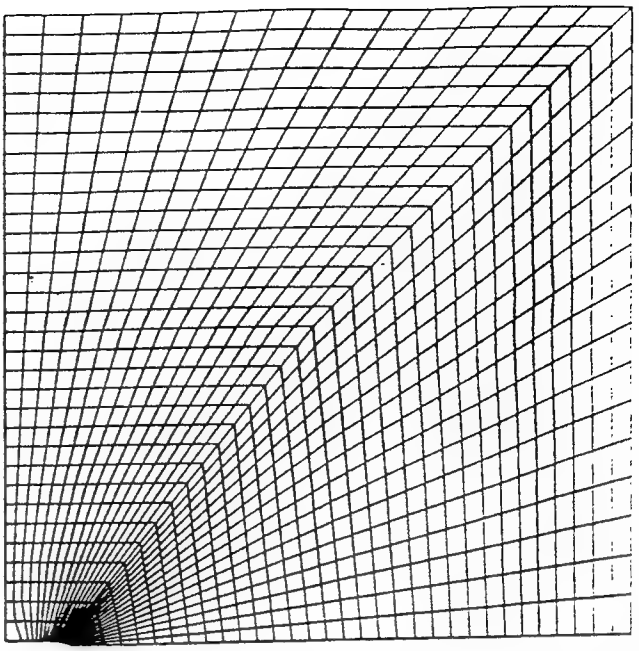

Fig. 3 Discretization of the domain into the finite element mesh used to analyze the problem

Figure 3 depicts the discretization of the domain into the finite element mesh used to analyze the problem. The mesh is fine in regions adjoining the tip of the ellipsoidal inclusion where severe deformations are expected to occur. Since we use an updated Lagrangian description of motion, the spatial coordinates of nodes are updated after every time increment. The size of the time increment is selected adaptively by the subroutine LSODE in order to solve the given problem within the prescribed accuracy during each time increment. Herein the values of the absolute and relative tolerances required by LSODE were each set equal to 10^{-2}. Since the analytical solution of the problem is unknown, it is impossible to estimate the total error in the solution at any instant. During the course of the solution of the problem the deformed region had to be remeshed twice; this was indicated by the negative value of the Jacobian at a Gauss point. The values of the solution variables at nodes in the new mesh were obtained first by finding to which elements in the previous mesh these nodes belonged, and then using an interpolation technique.

Figure 4 depicts contours of the maximum principal logarithmic strain ϵ, defined as,

$$\epsilon=\ln\lambda_1$$

where λ_1^2 is the largest eigenvalue of the left or right Cauchy-Green tensor, at four different values of the nondimensional time t. These contours are plotted in the referential description and suggest that the material around the tip of the ellipsoidal inclusion deforms severely, and these intense deformations propagate along directions making an angle of nearly ±45 deg with the horizontal. In order to decipher clearly the magnitude of deformations in different regions, we have plotted in Fig. 5 the evolution of the maximum principal logarithmic strain

at several points; the approximate locations of these points are given in Fig. 5(*a*). Point 1 adjoins the inclusion tip, points 36, 2, 38, and 3 are on the horizontal line through point 1 and situated in that order from point 1; points 31, 37, and 32 are vertically above points 36, 2, and 38, respectively. Since the ordinate is $\ln \lambda_1$, the maximum stretch at point 2 exceeds 12. The deformations at points 2, 31, and 37 eventually become larger than those at points 1 and 36, implying thereby that the severest deformations occur at points a little bit away from the inclusion tip. Intense deformations of the region surrounding point 17 seem to propagate vertically more than along the line passing through points 17 and 21. For comparison purposes we have also plotted the evolution of ϵ at point 35, which is far removed from the inclusion tip. The value of the maximum principal logarithmic strain at point 35 evolves slowly in the beginning, and its rate of growth picks up at an average strain of 0.375. However, its overall deformations remain minuscule as compared to the deformations of the material surrounding point 2.

The evolution of the nondimensional temperature and the effective deviatoric stress s_e at several points is shown in Figs. 6 and 7, respectively. The effective stress s_e is given by

$$s_e = \left(\frac{1}{2} tr(\mathbf{s}\mathbf{s}^T)\right)^{1/2} = \frac{\sigma_0}{\sqrt{3}} (1+bI)^m (1-\nu(\theta-\theta_0)), \quad (19a)$$

where

$$\mathbf{s} = \boldsymbol{\sigma} - \frac{1}{3}\sigma_{kk}\mathbf{1}. \quad (19b)$$

The sharp drop in the value of the effective stress at points 1, 2, 5, and 36 signifies the phase transformation from α-phase to γ-phase there, since σ_0 for the γ-phase is considerably lower than that for the mixture of ferrite and cementite. Thus, the material at point 36 is transformed into austenite first, followed by that at points 1, 2, and 5. Once the speed of material particles on the top surface has been reduced to zero, the average strain remains constant subsequently. However, the effective stress at these points does change, and will increase substantially once the phase transformation from austenite to martensite takes place. However, these changes are not shown in Fig. 7.

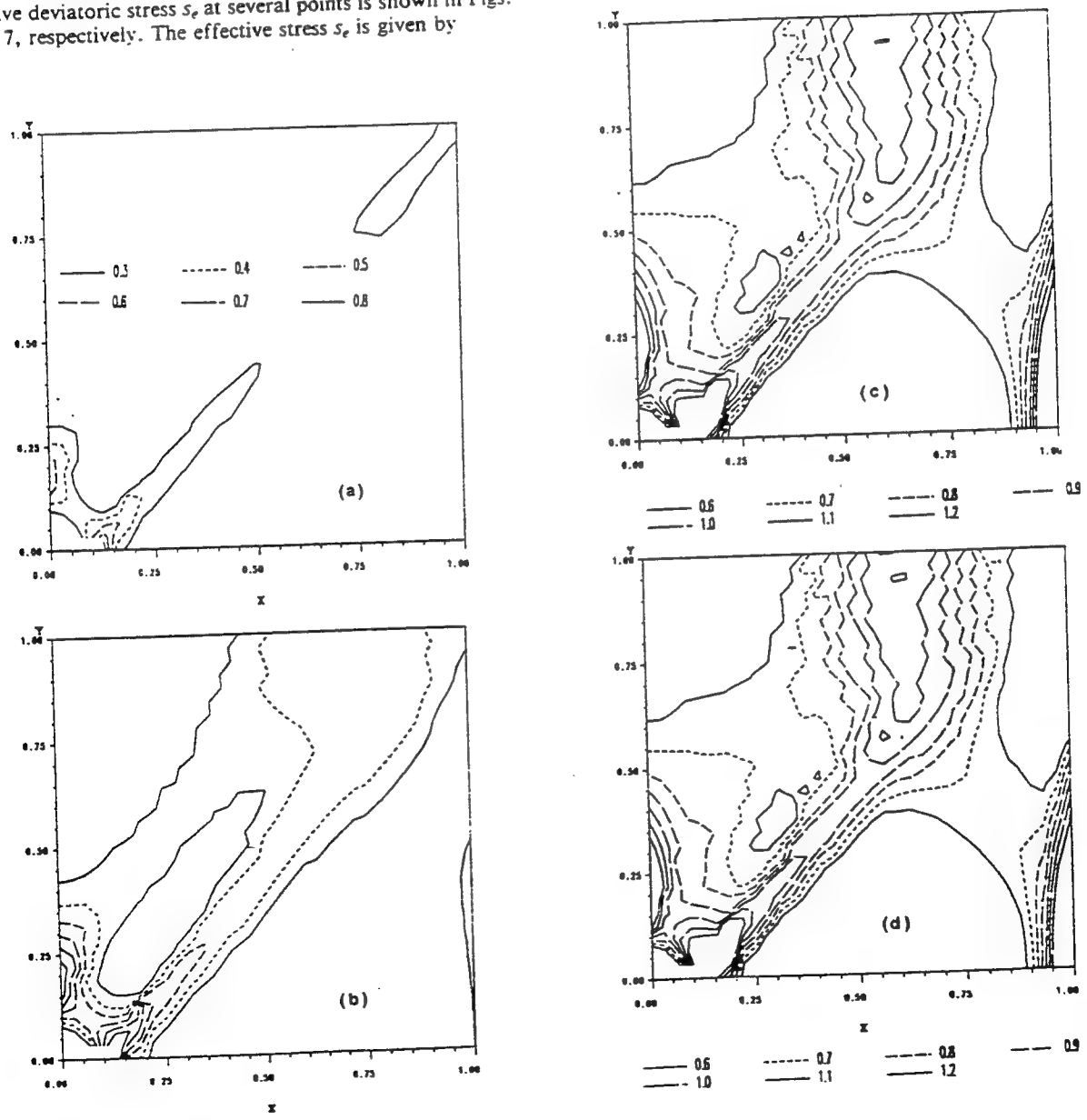

Fig. 4 Contours of the maximum principal logarithmic strain at four different values of the nondimensional time t. (*a*) t = 0.1687, (*b*) t = 0.2523, (*c*) t = 0.5105, and (*d*) t = 0.6710.

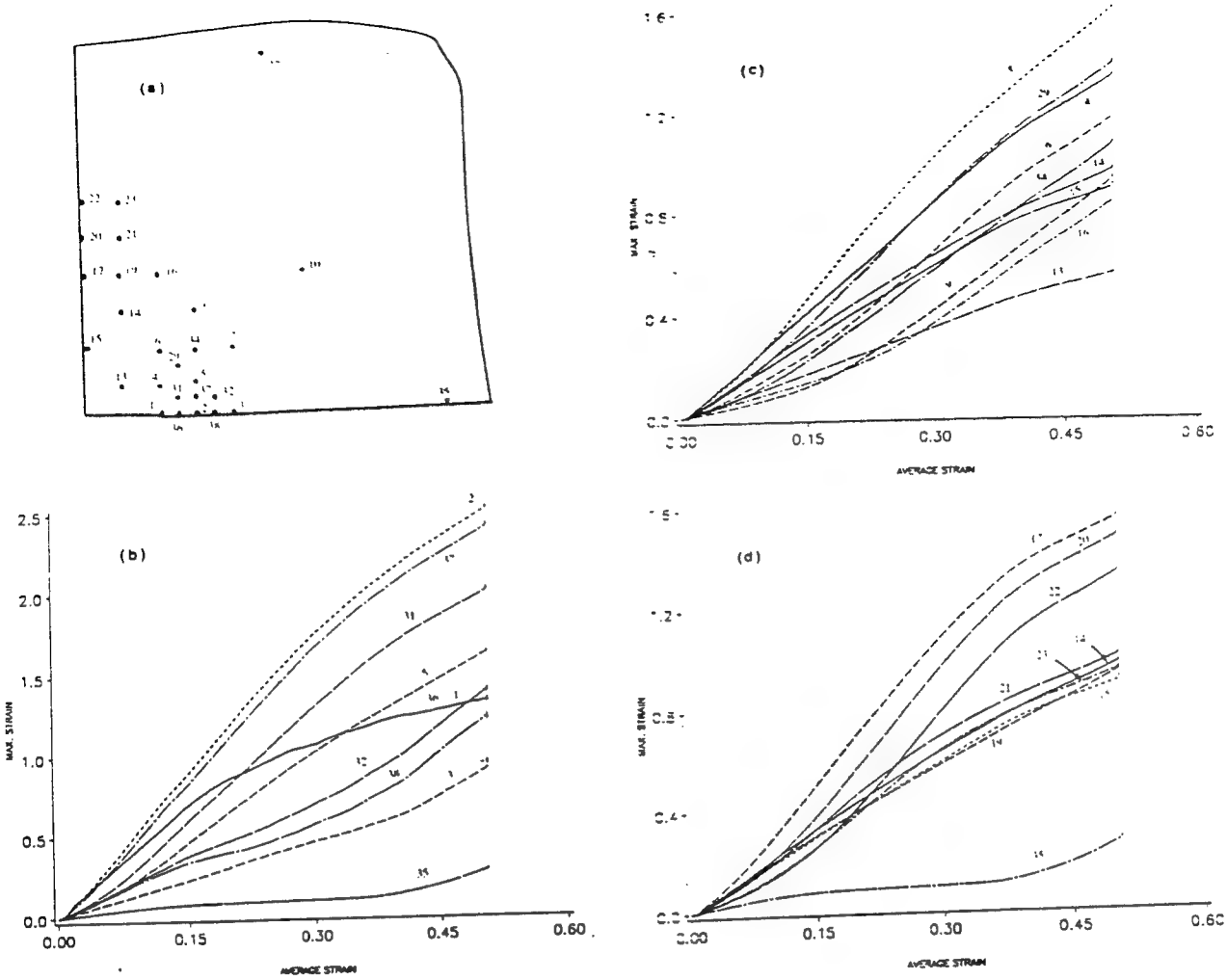

Fig. 5 Evolution of the maximum principal logarithmic strain at several points; the approximate location of these points is also shown

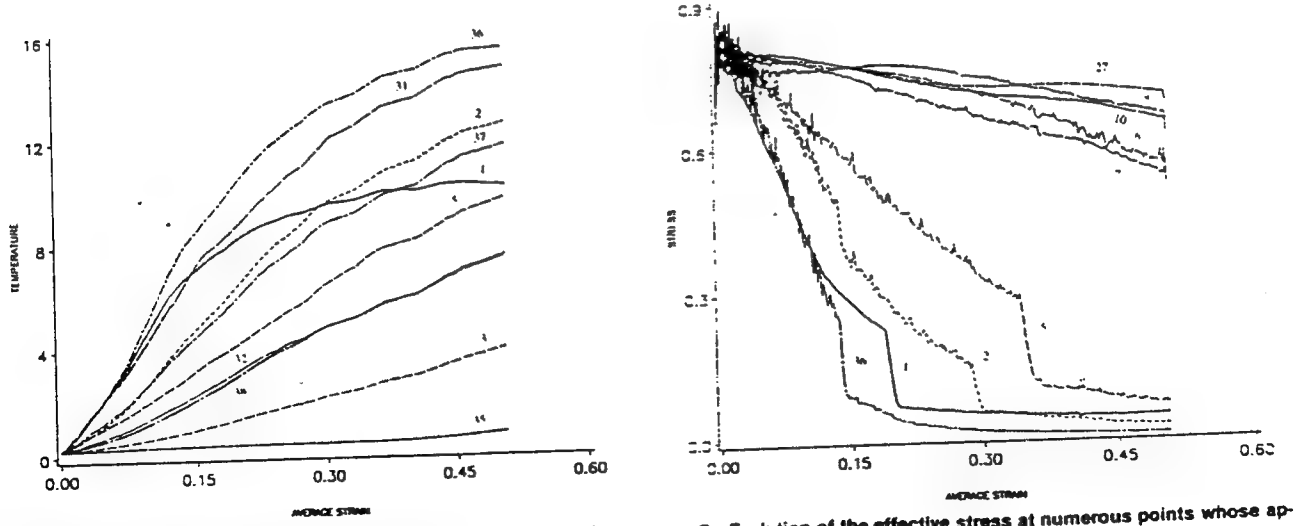

Fig. 6 Evolution of the nondimensional temperature at several points; the approximate location of these points is shown in Fig. 5

Fig. 7 Evolution of the effective stress at numerous points whose approximate locations are shown in Fig. 5

The values of the nondimensional temperature need to be multiplied by 89.6°C to obtain their corresponding values in °C. Whereas the temperature at point 1 seems to level off, that at other points continues to increase. Zhu and Batra (1990) studied a similar problem earlier in which no account was taken of the phase transformations, all of the material parameters were assumed not to depend upon temperature and the softening of the material due to its being heated up was modeled

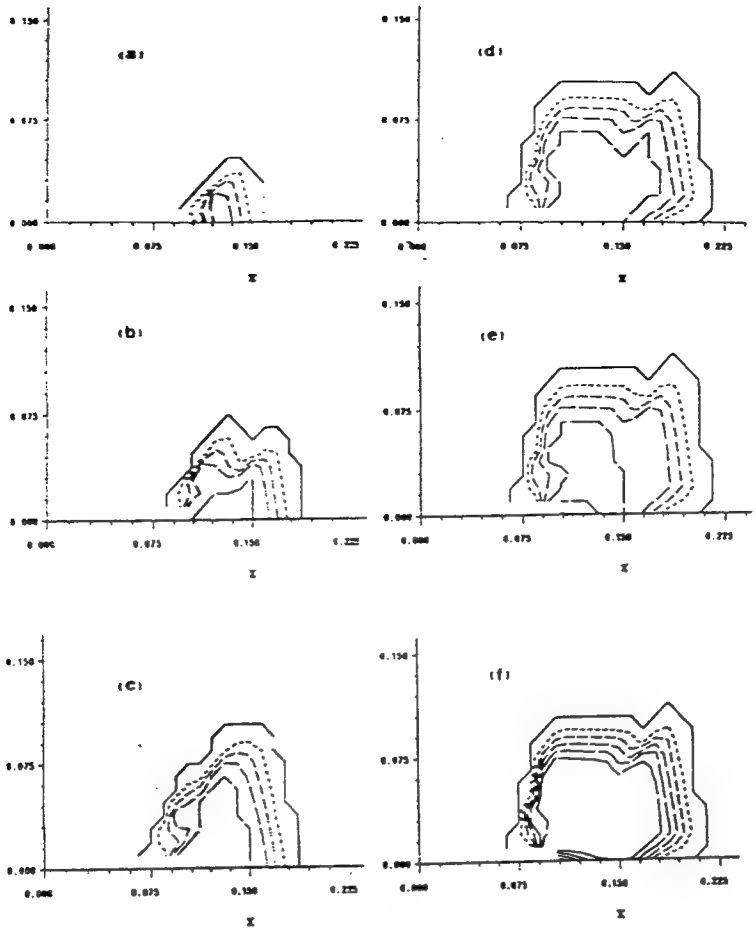

Fig. 8 Contours of the volume fraction of austenite at different values of time t. (a) t = 33.7 μs, (b) t = 67.5 μs, (c) t = 102 μs, (d) t = 134 μs, (e) t = 29.8 milliseconds (ms), and (f) t = 99.9 ms. ——— f_γ = 0.0, ····· f_γ = 0.25, - - - f_γ = 0.5, — — — f_γ = 0.75, ——— f_γ = 1.0.

by an exponential rather than a linear function. In that case (cf. Fig. 9(*a*) of Zhu and Batra, 1990), the temperature at point 1 was always higher than that at other points surrounding it, and the maximum principal logarithmic strain ϵ at point 1 increased sharply once a shear band initiated. A glance at Fig. 5 shows that ϵ at point 1 levels off, and there is no transition in the rate of growth of ϵ. In the present problem it is hard to decipher when a shear band initiated.

In Fig. 8 we have plotted, in the reference configuration, contours of the volume fraction of austenite at time t equal to 33.7 μs, 67.5 μs, 102 μs, 134 μs, 29.8 millisec (ms), and 99.5 ms. The horizontal and vertical scales have been enlarged to clarify the contours. We recall that the vertical velocity on the top surface is reduced to zero at t = 102 μs, and is kept at zero subsequently. Thus, no external work is done on the system for $t \geq 102$ μs, and the heat conduction from the hotter to the colder regions tends to equilibrate the temperature everywhere. All material particles had essentially come to rest at t = 134 μs, and only the heat equation was solved for $t \geq 134$ μs. Since we have assumed a simple kinetic equation for the phase transformation from α to γ phase, some of the material is converted into austenite even after the top surface is brought to and maintained at rest. A comparison of the contours of the volume fraction of austenite with those of the maximum principal logarithmic strain reveals that some of the material outside of the shear band has also transformed into austenite. We do not get a very sharp and narrow band, primarily because the finite element mesh used is not very fine. The available computational resources limited the size of the problem, and hence the mesh that could be used to analyze it.

Whether or not austenite is transformed into pearlite or into martensite depends upon how fast heat can be conducted out of the hotter regions by the surrounding colder material. Figure 9 depicts the variation of the temperature at point P with coordinates (0.1, 0.0368) in the reference configuration. The cooling curve for this point is also plotted on the C-C-T (continuous-cooling-transformation) diagram. The peak temperature at point P reached almost 1075°C, which is well above 750°, the temperature at which the transformation is assumed to have completed. Since the cooling curve for P does not intersect parabola A on the C-C-T diagram, the austenite present at point P is transformed directly into martensite. Similar reasoning applied at several points indicated that quenching of the hotter material caused by the surrounding colder material was strong enough to cause austenite to be transformed directly into martensite. The contours, in the reference configuration, of the volume fraction of martensite at four different values of time are exhibited in Fig. 10. The horizontal and vertical scales have been expanded to distinguish among the different contours. These plots evidence that a significant portion of austenite has been transformed into martensite. Because of the thermally insulated boundaries, the block cools down to a uniform temperature which is above 110°C. Therefore, all of the austenite cannot be transformed into martensite. However, if the block boundaries were able to exchange heat with the surroundings, then the material will cool down to the

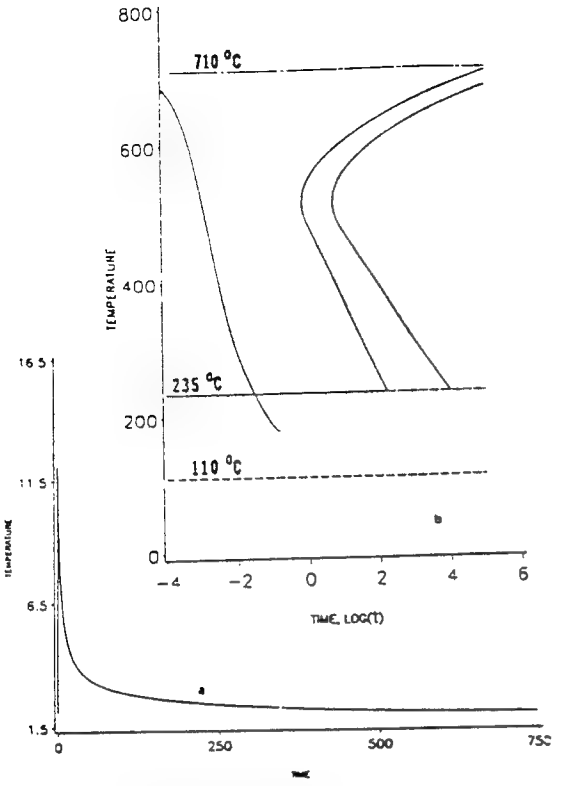

Fig. 9 (*a*) Variation of temperature with time at point P (0.1, 0.0368), (*b*) Cooling curve for point P superimposed on the C-C-T diagram.

room temperature eventually. The cooling curve for a typical point, shown in Fig. 9, indicates that it will not intersect either one of the two parabolas; the same was found to be the case for other points considered. Therefore, all of the austenite at a point will be transformed into martensite. Figure 10(*e*) shows contours of martensite for this case. The temperature contours at four different times, depicted in Fig. 11, reveal that only a small region near the inclusion tip is heated up significantly, and that the temperature distribution within the block becomes essentially uniform at time $t = 99.9$ ms.

A similar study conducted at an average strain-rate of 1000 s^{-1} gave results qualitatively similar to the ones reported herein. The main reason for our not getting narrow shear bands is that the finite element mesh used is not fine enough. As stated earlier, a fine mesh could not be used because of the limited computing resources available. A fine mesh should result in sharper gradients of temperature across the shear band, and possibly higher values of temperature within it, thus facilitating the transformation from α-phase to γ-phase. Here we have not accounted for the effect of the stress and/or strain on the phase transformations; Inoue (1989) has given kinetic equations for such phase transformations.

Conclusions

We have analyzed plane strain thermomechanical deformations of a steel block of square cross-section and loaded in compression at an average strain-rate of 5000 s^{-1}. Hardening of the material due to strain-rate effects and its softening caused by its being heated up are accounted for. We have also considered the possible transformation of the material from the mixture of ferrite and cementite to γ-phase and back into

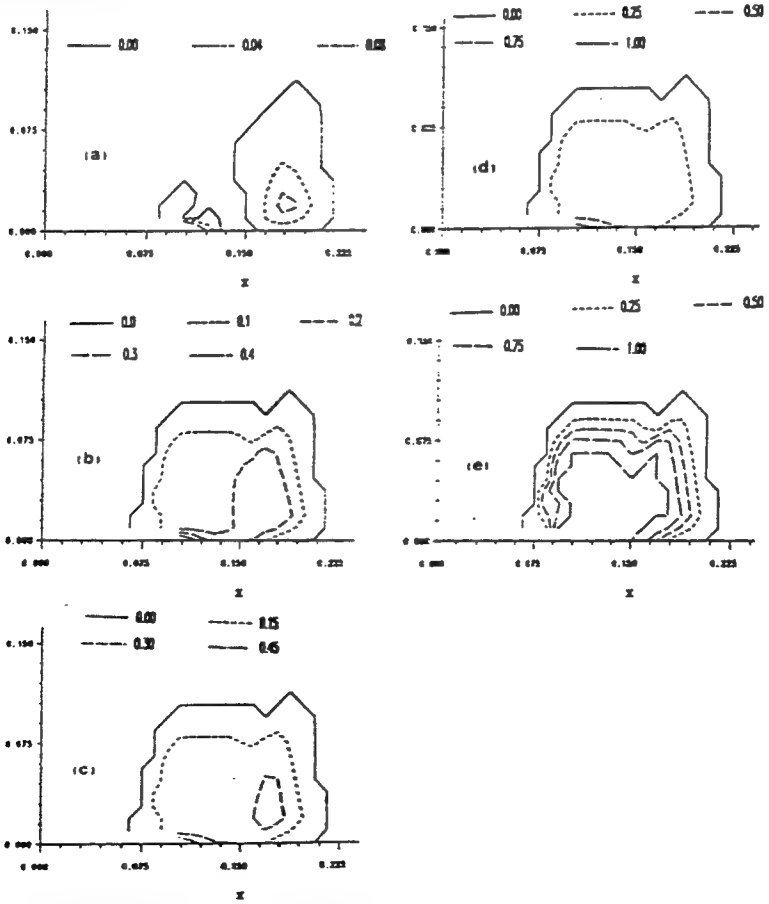

Fig. 10 Contours of the volume fraction of martensite at four different values of time *t*. (*a*) $t = 29.8$ ms, (*b*) $t = 49.8$ ms, (*c*) $t = 59.8$ ms, (*d*) $t = 99.9$ ms. (*e*) Contours of the volume fraction of martensite if all of the block had cooled down to the room temperature of 25°C.

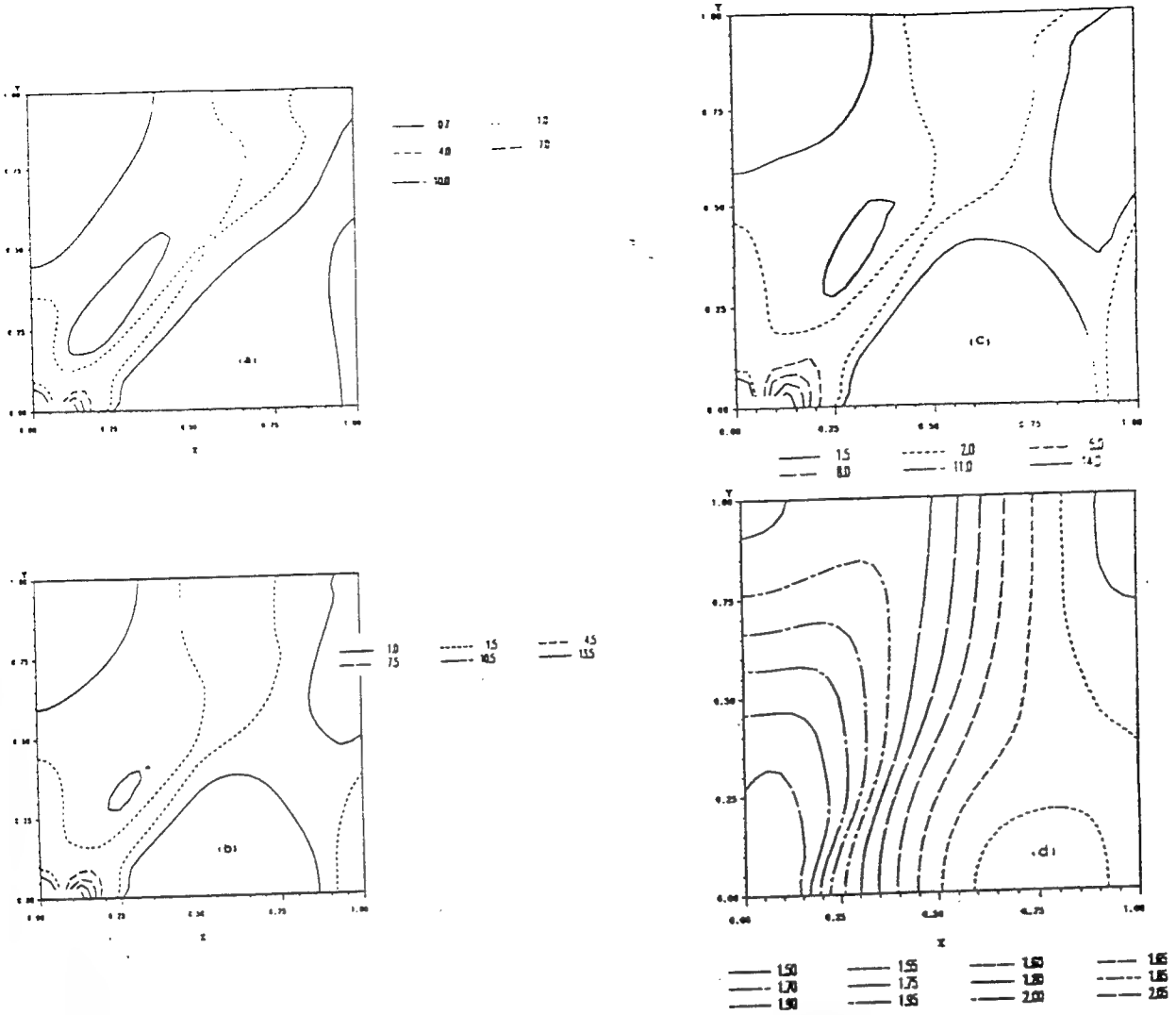

Fig. 11 Contours of temperature at four different values of time t. (*a*) t = 50.5 μs, (*b*) t = 84.5 μs, (*c*) t = 134 μs, and (*d*) t = 99.9 ms.

either pearlite or martensite. The thermophysical properties of a material point consisting of more than one phase are determined by the rule of mixtures. The loading pulse is made up of an initial transient loading part of 1 μs duration, a steady part of 100 μs, and the unloading part of 1 μs; subsequently, the bottom and top surfaces are held fixed. A material defect is modeled by a rigid non-heat-conducting ellipsoidal inclusion located at the block center. The deformations are presumed to be symmetrical about the centroidal axes parallel to the bounding faces, and thus deformations of the material in the first quadrant are studied.

It is found that a narrow band of intense plastic deformation initiates at the inclusion tip and propagates along directions making an angle of approximately ± 45 deg with the horizontal. Much of the material within and adjoining the band is heated up to a temperature above 725°C, where the transformation from the mixture of ferrite and cementite to the γ-phase is presumed to begin. This hotter material is quenched by the cold material surrounding it at a rapid enough rate that the γ-phase is transformed directly into martensite.

Acknowledgments

This work was supported by the U.S. Army Research Office grant DAAL03-91-G-0084 and the U.S. NSF grant MSS9121279 to the University of Missouri-Rolla. Some of the computations were performed on the NSF sponsored supercomputer center in Ithaca, NY.

References

Batra, R. C., and Jayachandran, R., 1992, "Effect of Constitutive Models on Steady State Axisymmetric Deformations of Thermoelastic-Viscoplastic Targets," *Int. J. Impact Engr.*, Vol. 12, pp. 209–226.

Batra, R. C., and Liu, D. S., 1989, "Adiabatic Shear Banding in Plane Strain Problems," ASME *Journal of Applied Mechanics*, Vol. 56, pp. 527–534.

Bodner, S. R., and Partom, Y., 1975, "Constitutive Equations for Elastic-Viscoplastic Strain-Hardening Materials," ASME *Journal of Applied Mechanics*, Vol. 42, pp. 385–389.

Brown, S. B., Kim, K. H., and Anand, L., 1989, "An Internal Variable Constitutive Model for Hot Working of Metals," *Int. J. Plasticity*, Vol. 5, pp. 95–130.

Budiansky, B., 1970, "Thermal and Thermoelastic Properties of Isotropic Composites," *J. Comp. Mat.*, Vol. 4, pp. 286–295.

Gear, C. W., 1971, *Numerical Initial Value Problems in Ordinary Differential Equations*, Prentice-Hall, Englewood Cliffs, NJ.

Giovanola, J. H., 1988, "Adiabatic Shear Banding Under Pure Shear Loading," *Mechs. Materials*, Vol. 7, pp. 59–87.

Hindmarsh, A. C., 1983, "ODEPACK, A Systematized Collection of ODE Solvers," *Scientific Computing*, R. S. Stepleman et al., eds., North-Holland, Amsterdam, pp. 55–64.

Inoue, T., 1989, "Inelastic Constitutive Relationships and Applications to Some Thermomechanical Processes Involving Phase Transformations," *Thermal Stresses III*, R. B. Hetnarski, ed., North-Holland, Amsterdam, pp. 192–278.

Lindholm, U. S., and Johnson, G. R., 1983, "Strain-Rate Effects in Metals at Large Strain Rates," *Material Behavior Under High Stresses and Ultrahigh Loading Rates*, J. Mescall and V. Weiss, eds., Plenum Press, NY, pp. 61–79.

Massey, H. F., 1921, "The Flow of Metal During Forging," *Proc. Manchester Assoc. Engineers*, pp. 21–26.

Reed-Hill, R. E., 1973, *Physical Metallurgy Principles*, Van Nostrand Co., New York.

Roger, H. C., 1979, "Adiabatic Plastic Deformation," *Ann. Rev. Mat. Sci.*, Vol. 9, pp. 283–319.

Tresca, H., 1878, "On Further Application of the Flow of Solids," *Proc. Inst. Mech. Engr.*, Vol. 30, pp. 301–345.

Wingrove, A. L., 1971, "A Note on the Structure of Adiabatic Shear Bands in Steel," Tech. Memo 33, Australian Defence Scientific Service, Defence Standards Lab., Department of Supply, Maribyrnong, Victoria.

Yu, H. J., Wolfstieg, U., and Macherauch, E., 1979, "Berechnung der Abschreckeigenspannungen in Stahlzylindern unter Berücksichtigung der Umwandlungsvorgänge," *Arch. Eisenhuttenwes*, Vol. 50, pp. 81–84.

Zener, C., and Hollomon, J. H., 1944, "Effect of Strain Rate Upon Plastic Flow of Steel," *J. Appl. Phys.*, Vol. 15, pp. 22–32.

Zhu, Z. G., and Batra, R. C., 1990, "Dynamic Shear Band Development in Plane Strain Compression of a Viscoplastic Body Containing a Rigid Inclusion," *Acta Mechanica*, Vol. 84, pp. 89–107.

Acta Mechanica 102, 217–233 (1994)

ACTA MECHANICA

Effect of kinematic hardening on the initiation and growth of shear bands in plane strain deformations of a thermoviscoplastic solid

Y. M. Wang and **R. C. Batra**, Rolla, Missouri

(Received March 5, 1992; revised June 24, 1992)

Summary. We study dynamic thermomechanical deformations of an elasto-viscoplastic body deformed in plane strain compression at a nominal strain-rate of 5000 sec^{-1}. The boundaries of the block are assumed to be perfectly insulated. We model the thermoviscoplastic response of the material by the Brown–Kim–Anand constitutive relation in which the evolution of the microstructural changes is accounted for by two internal variables, viz. a scalar and a traceless symmetric second order tensor. The former accounts for the isotropic hardening of the material, and the latter for the kinematic hardening. We model a material defect by introducing a temperature perturbation in the stress-free reference configuration. It is found that the consideration of kinematic hardening does not change the qualitative nature of results.

1 Introduction

Adiabatic shear bands are narrow regions of intense plastic deformation that form during high strain-rate processes, such as shock loading, ballistic penetration, metal forming, and machining. They are called adiabatic since the bands, once they initiate, are fully developed in a few microseconds, and there is not enough time for the heat to be conducted away from the severely deforming region. The primary mode of deformation within the band is that of shearing. Previous numerical [1], [2] and analytical [3] studies have shown that the thermal conductivity affects significantly the band-width. Because of the intense deformations of the material within and surrounding the shear band, the structure of the material changes during the development of the band. One way to account for these structural changes is to use constitutive equations which employ a suitable number of scalar and tensor valued internal variables. Anand [4] has given a set of constitutive equations appropriate for large deformation elasto-viscoplasticity that include two internal variables: a scalar and a symmetric, traceless second-order tensor which, in an average sense, represent an isotropic and an anisotropic resistance to plastic flow offered by the internal state of the material. Brown, Kim, and Anand [5] tested in compression an iron-2% silicon alloy and an 1100-type aluminum alloy at high temperatures and determined the specific forms of the constitutive functionals and the values of material parameters for these alloys. Here we use such a constitutive relation to assess the effect of anisotropic resistance to plastic flow, also known as kinematic hardening, on the initiation and growth of shear bands.

Even though Tresca [6] and Massey [7] observed hot lines, now called shear bands, during the forging of a hot metal in 1878 and 1921, respectively, the research activity in this field picked up since 1944 when Zener and Hollomon [8] observed 32 μm wide shear bands during the punching of a hole in a low carbon steel plate. Zener and Hollomon postulated that the heat produced due

where

$$U(t) = \begin{cases} v_0 t / t_r, & 0 \leqq t \leqq t_r, \\ v_0, & t \geqq t_r. \end{cases} \tag{2.20}$$

That is, all bounding surfaces are thermally insulated, the right surface is traction free, conditions due to the assumed symmetry of deformations apply on the left and bottom surfaces, and on the top surface zero tangential tractions, and a time dependent vertical component of velocity is prescribed. Thus, the contact between the loading device and the upper surface of the body is assumed to be smooth. The assigned vertical velocity on the top surface increases from zero to the steady value v_0 in time t_r.

For the initial conditions we take

$$\varrho(\boldsymbol{X}, 0) = \varrho_0, \quad \boldsymbol{v}(\boldsymbol{X}, 0) = \boldsymbol{0}, \quad \boldsymbol{\sigma}(\boldsymbol{X}, 0) = \boldsymbol{0}, \quad \boldsymbol{B}(\boldsymbol{X}, 0) = \boldsymbol{0}, \quad s(\boldsymbol{X}, 0) = s_0,$$
$$\theta(\boldsymbol{X}, 0) = \theta_0 + \delta \left(1 - \frac{r^2}{2}\right)^{18} \exp\ (-5r^2), \quad r^2 = X_1^2 + X_2^2. \tag{2.21}$$

These imply that the body is initially at rest, is stress free, has a uniform mass density, and a nonuniform temperature distribution. The initial temperature is higher in a small region around the origin; the magnitude δ of the perturbation signifies, in some sense, the strength of the material defect.

We note that there is no yield or loading surface assumed in our work, and the constitutive relations employed fall in the category of "unified theories of viscoplasticity". A material point is presumed to undergo elastic deformations at all times. The constraint $\operatorname{tr} \boldsymbol{B} = 0$ does not require any special consideration since it is satisfied at time $t = 0$ because of the initial conditions, and Eqs. (2.6) and (2.8) give $\operatorname{tr} \mathring{\boldsymbol{B}}(\cdot, 0) = 0$. Thus, $\operatorname{tr} \boldsymbol{B}(\cdot, t) = 0$ for every t.

3 Computational considerations

The stiff coupled nonlinear equations (2.1)–(2.3), (2.5), (2.8), and (2.9) are to be solved for ϱ, $\boldsymbol{v}$, θ, $\boldsymbol{\sigma}$, $\boldsymbol{B}$, and s. Since $\varepsilon_m{}^p$ appears only as $\dot{\varepsilon}_m{}^p$ in Eqs. (2.6), (2.9), and (2.10), we substituted for it from Eq. (2.7), and thus did not take it as one of the variables to be solved for. It is extremely difficult, if not impossible, to prove the existence and/or uniqueness of their solution under the prescribed initial and boundary conditions. Here we seek their approximate solution by the finite element method. A set of nonlinear coupled stiff ordinary differential equations is derived from (2.1)–(2.3), (2.5), (2.8), and (2.9) by using the Galerkin method, and are then integrated with respect to time by using the backward difference Adam's method included in the subroutine LSODE developed by Hindmarsh [13]. The subroutine adjusts the time step size adaptively to compute a solution of the ordinary differential equations within the prescribed tolerance. The parameters RTOL and ATOL which control the relative and absolute tolerance in the solution variables were each set equal to 10^{-7}. The coordinates of nodes in the finite element mesh were updated after each time step.

4 Computation and discussion of results

In order to compute numerical results, we assigned the following values to various geometric and material parameters:

$$\varrho_0 = 7860\ \text{kg m}^{-3}, \quad E = 168\ \text{GPa}, \quad \nu = 0.3, \quad \mu = 64.6\ \text{GPa},$$
$$A = 6.346 \times 10^{15}\ \text{sec}^{-1}, \quad Q = 100\ \text{KJ mole}^{-1}, \quad R = 8.3145\ \text{J mole}^{-1}\,^{\circ}\text{K}^{-1},$$
$$c = 473\ \text{J kg}^{-1}\,^{\circ}\text{C}^{-1}, \quad k = 49.22\ \text{W m}^{-1}\,^{\circ}\text{C}^{-1}, \quad \bar{s} = 405\ \text{MPa}, \tag{4.1}$$
$$\theta_0 = 25\,^{\circ}\text{C}, \quad \delta = 25\,^{\circ}\text{C}, \quad m = 1.0, \quad a = 1.5,$$
$$\xi = 3.25, \quad h_0 = 5000\ \text{MPa}, \quad H = 5\ \text{mm},$$
$$v_0 = 25\ \text{m sec}^{-1}, \quad t_r = 10^{-6}\ \text{sec}.$$

Thus, the nominal strain-rate equals $5000\ \text{sec}^{-1}$ and the prescribed speed on the top surface increases from zero to the steady value of $25\ \text{m sec}^{-1}$ in one microsecond. In order to study the effect of isotropic and kinematic hardening on the development of the shear band, we studied the following seven different cases.

Case 1: $c_1 = c_2 = 0, \quad n = 0.002.$

Case 2: $c_1 = c_2 = 0, \quad n = 0.05.$

Case 3: $c_1 = 2(10^{-2})\,\mu, \quad c_2 = 0, \quad n = 0.002.$

Case 4: $c_1 = 10^{-2}\,\mu, \quad c_2 = 0, \quad n = 0.002.$

Case 5: $c_1 = 2(10^{-2})\,\mu, \quad c_2 = 5(10^5)\ \text{sec}^{-1}, \quad n = 0.002.$

Case 6: $c_1 = 10^{-2}\,\mu, \quad c_2 = 10^5\ \text{sec}^{-1}, \quad n = 0.002.$

Case 7: $c_1 = 10^{-2}\,\mu, \quad c_2 = 2(10^5)\ \text{sec}^{-1}, \quad n = 0.002.$

There is no kinematic hardening for the first two cases, and a comparison of results for them should delineate the effect of the saturation value s^* of s. Results for the other five problems should help illustrate the relative significance of the two terms on the right-hand side of Eq. (2.8.1), giving the evolution of $\boldsymbol{B}$, on the development of the shear band. Jayachandran and Batra [14] studied the effect of various parameters in the constitutive relations on the response of the defect free body deformed in plane strain compression and found that an increase in the value of $h_0, n, m, \bar{s}$, and Q enhances the hardening of the material, and an increase in the value of ξ, a, and A furthers the softening of the material. However, they neither considered kinematic hardening nor studied the nucleation and growth of a shear band.

In the results presented below, a fixed mesh consisting of 32×32 four-noded quadrilateral elements was used, and all integrals defined on an element were evaluated by using the 2×2 quadrature rule. The elements are squares in the initial stress-free configuration, but are quadrilateral for subsequent times because of their unequal deformations in the horizontal and vertical directions. Results computed with a 64×64 mesh of four-noded quadrilateral elements agreed qualitatively with those obtained with the 32×32 mesh, the quantitative difference between the values of temperature at the origin was less than 5% during the entire process of the development of the band. This was not viewed as critical, and because of the considerable savings

in the CPU time resulting from the use of the 32 × 32 mesh, it was employed for all of the seven cases.

Below we present and discuss results in terms of the following nondimensional variables indicated by a superimposed bar

$$\bar{x} = x/H, \quad \bar{X} = X/H, \quad \bar{v} = v/v_0, \quad \bar{\sigma} = \sigma/\tilde{s}, \quad \bar{\boldsymbol{B}} = \boldsymbol{B}/\tilde{s}, \quad \bar{\theta} = \frac{\theta}{\theta_0}, \quad \bar{t} = tv_0/H. \tag{4.2}$$

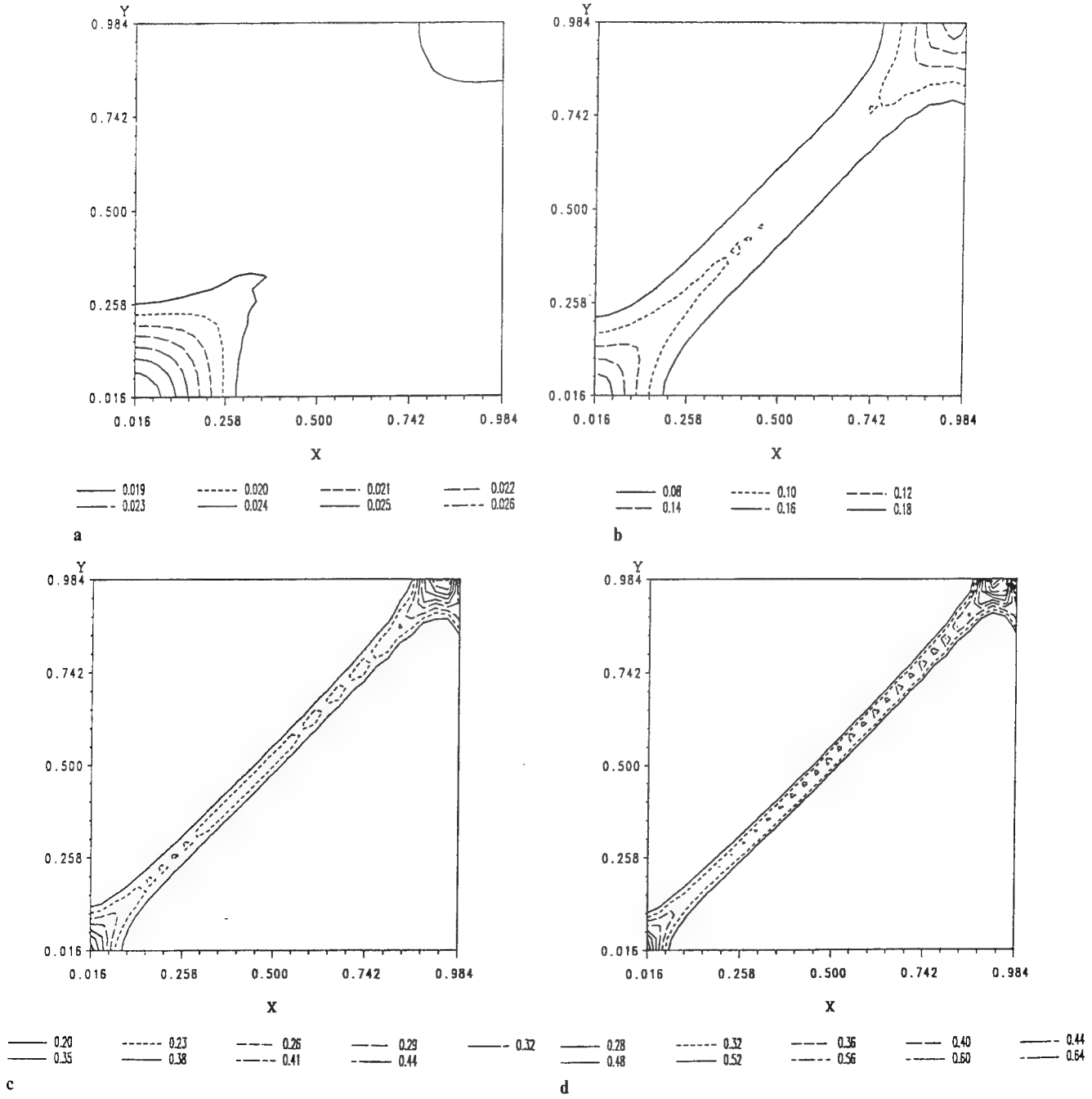

Fig. 2. Contours of the maximum principal logarithmic strain at four different values of the average strain. **a** $\gamma_{avg} = 0.0175$, **b** $\gamma_{avg} = 0.0576$, **c** $\gamma_{avg} = 0.0776$, **d** $\gamma_{avg} = 0.0889$

Here $2H$ equals the height of the block. Henceforth, we use only nondimensional variables and drop the superimposed bar. Because the prescribed downward speed on the top surface increases from zero to one in time t_r, the average strain is slightly less than the nondimensional time.

Figure 2 depicts, in the reference configuration, the contours of the maximum principal logarithmic strain ε, defined as

$$\varepsilon = \ln \lambda, \tag{4.3}$$

where λ^2 equals the maximum eigenvalue of the right ($\boldsymbol{F}^T\boldsymbol{F}$) or the left ($\boldsymbol{F}\boldsymbol{F}^T$) Cauchy-Green tensor, at four different values of the average strain (γ_{avg}) for case 6. Unless otherwise noted, the results presented below are for case 6; the results for other cases are qualitatively similar to those presented herein. The contours of the maximum principal logarithmic strain suggest that a small region surrounding the center of the cross-section undergoes severe deformations, and these intense deformations propagate along the main diagonal. The severely deforming region progressively narrows down. The reason the domain extends from 0.016 to 0.984 and not from 0.0 to 1.0 in the horizontal and vertical directions is that the X_1- or X_2-coordinate of the quadrature point nearest to the left or right and bottom or top surfaces is 0.016 and 0.984. The software used to plot the contours interpolates the data at numerous points from that provided at the quadrature points. We note that the results reported herein are qualitatively similar to those obtained by Zhu and Batra [14] who used a different constitutive relation and did not consider kinematic hardening. By finding the distance through which the contour of $\varepsilon = 0.35$ had travelled from $t = 0.08$ to 0.091 25, its average speed of propagation was found to be 208 m/sec. This speed depends upon the state of deformation of the material within the band and also upon the constitutive relation employed. The contours of temperature resemble those of the maximum principal logarithmic strain and are not shown here.

We have plotted in Fig. 3 the variation of the velocity in the x_1- and x_2-directions at $\gamma_{avg} = 0.0889$. It is clear that the body is divided into two deforming triangular regions, one adjoining the top surface that is moving downward at the prescribed speed, and the other abutting the horizontal centroidal plane. Theses two domains are connected by a narrow transitional region in which the speed in the vertical direction increases sharply from essentially zero to nearly 1.0. The thickness of this transitional layer, which is related to the band-width, equals two elements for the mesh used herein. A finer mesh will probably result in even shaper gradients of the speed within this transition zone. This significant change of speed across the thin transitional layer supports the assertions of Tresca [6] and Massey [7] that the tangential velocity is discontinuous across the shear band. In our work, the velocity field is forced to be continuous within an element and across interelement boundaries. Therefore, jumps in the tangential velocity across a shear band cannot be delineated.

The distribution at $\gamma_{avg} = 0.0889$ of the effective stress σ_e, defined as

$$\sigma_e^2 = \frac{3}{2}\,\mathrm{tr}\,(\boldsymbol{\sigma}' - \boldsymbol{B})^2, \tag{4.4}$$

and the effective back-stress B_e given by

$$B_e^2 = \frac{3}{2}\,\mathrm{tr}\,(\boldsymbol{B}^2) \tag{4.5}$$

within the block is exhibited in Fig. 4. As expected, the effective stress within the shear band drops. However, the drop is not as precipitous as that found by Batra and Liu [15] who modeled

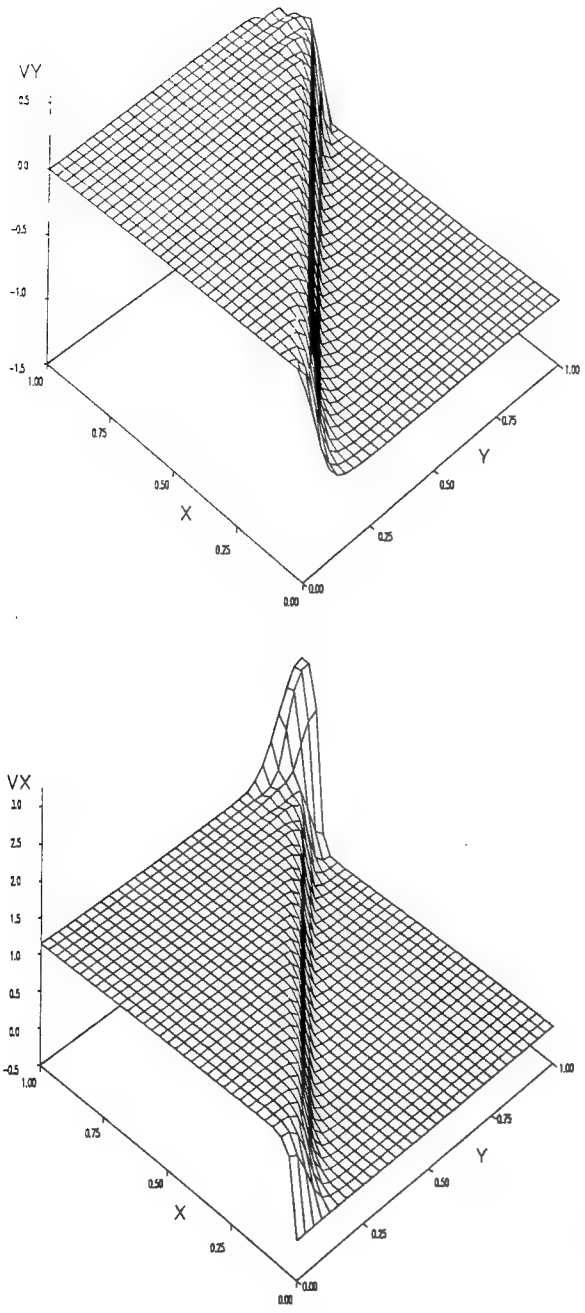

Fig. 3. Distribution of the x_1- and x_2-components of the velocity within the deforming region at $\gamma_{avg} = 0.0889$

thermal softening by an affine function of temperature and assumed a rather large value of the thermal softening coefficient. Zhu and Batra [14] assumed an exponentially decaying softening function and obtained results somewhat similar to that shown here. The effective back-stress B_e within the band is more than that elsewhere in the body, which is consistent with the assumption that the rate of evolution of the back-stress is proportional to the plastic strain-rate. The plastic strain-rate is high at points within the band, and is negligible elsewhere.

The deformed mesh at $\gamma_{avg} = 0.0889$ plotted in Fig. 5 vividly illustrates that the two elements within the band are significantly deformed and the rest of the body has undergone very little distortion. From results presented thus far, we estimate that at time $t = 0.09$ a large segment of

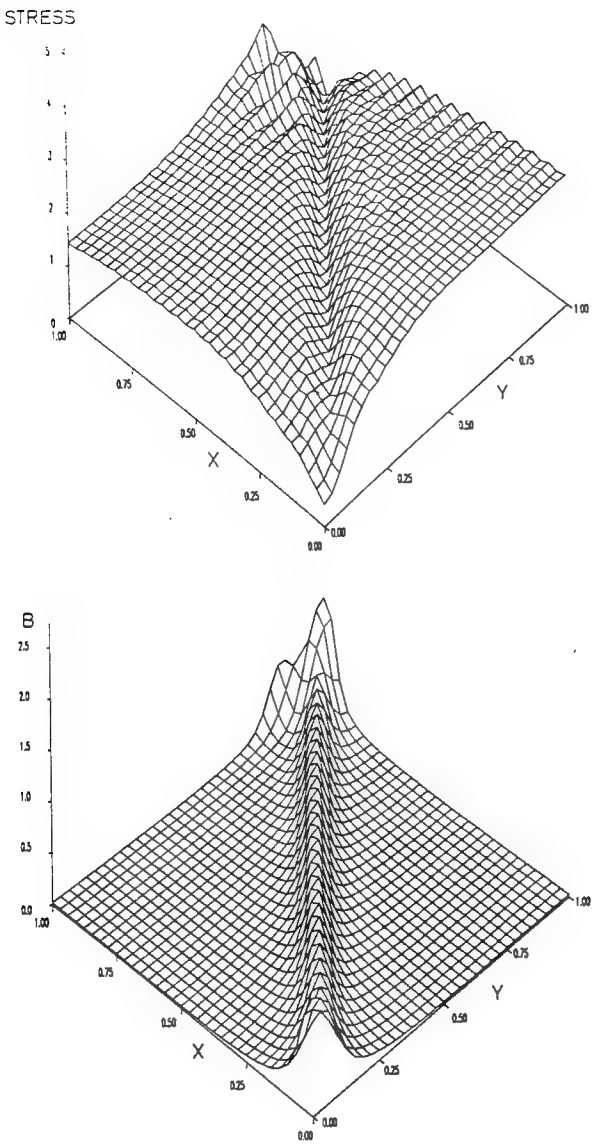

Fig. 4. Distribution of the effective stress and the effective back-stress within the deforming region at $\gamma_{avg} = 0.0889$

the band in the deformed configuration is directed along the line EF that makes an angle of 43° with the horizontal. The orientation of the band changes a little with time. The distribution of the maximum principal logarithmic strain and temperature within the band at different times is exhibited in Fig. 6. These curves reveal that the strain and temperature distributions within the band are nonuniform; the strain and the temperature assume their highest values near the origin and fall off rather rapidly with the distance from O along OEF. In order to decipher the variation of the strain, temperature, effective back-stress, and the rate of dissipation of the energy density defined as tr $(\boldsymbol{\sigma}\, \boldsymbol{D}^p)$ across the band, we have plotted, in Figs. 7 and 8, the distribution of these on lines PQ and RS perpendicular to the estimated centerline of the band; these lines are shown in Fig. 7. The abscissa equals the distance from the band centerline of a point along line PQ or RS, and is assigned negative values for points lying above OEF. These plots provide evidence that a narrow band forms around OEF. A finer mesh would probably have resulted in a smoother variation of the strain along PQ and RS, and also in a narrower band. Because of the rather small

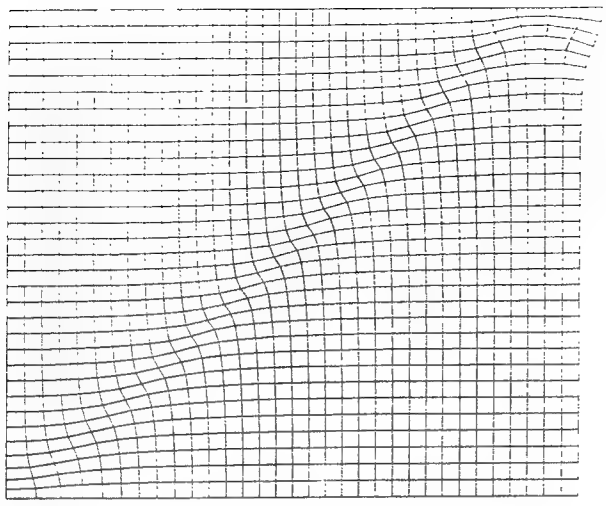

Fig. 5. Deformed mesh at $\gamma_{avg} = 0.0889$

value of the thermal conductivity, the energy dissipation rate can be regarded as being proportional to the rate of change of temperature. Thus, the temperature changes rapidly at points within the band and slowly at material points outside of it. The energy dissipation rate is a little lower at $t = 0.09$ than that at $t = 0.08$ because of the drop in the value of σ caused by increased thermal softening of the material.

Figure 9 shows the evolution of the maximum principal logarithmic strain, the temperature, the effective back-stress, and the rate of dissipation of the energy density at or near the centroid of the cross-section for four different cases, viz. cases 1, 4, 6, and 7. We note that for case 1 the back-stress always stays at zero. For case 4 the evolution of the back-stress $\boldsymbol{B}$ is proportional to $\boldsymbol{D}^p$, and for cases 5 through 7, the present value of the back-stress retards the evolution of $\boldsymbol{B}$. The value of c_2 multiplying $\boldsymbol{B}$ in its evolution equation in case 7 is twice that for case 6. If the rapid increase of the maximum principal logarithmic strain at $X_1 = X_2 = 0.0066$ is taken as the criterion to decide when a shear band initiates, then the shear band is delayed by the consideration of the back-stress. An increase in the value of c_2 results in the band forming a little sooner. For the average strain-rate of 5000 $\sec^{-1}$ considered herein, the nondimensional time of 0.10 equals 20 microseconds. The evolution of the temperature at the origin is affected less by the consideration of the back-stress and the values assigned to c_1 and c_2 in the evolution equation for $\boldsymbol{B}$. Whereas the temperature vs. average strain curves are concave upward for the problems studied herein, those obtained by Zhu and Batra [14] were concave downward. In both cases, the values of the thermal conductivity and the specific heat were the same. It seems that the curvature of the temperature vs. average strain curve depends upon the way a material defect is modeled. Zhu and Batra [14] considered a rigid non-heat-conducting thin ellipsoidal inclusion, which resulted in a severe stress concentration near the inclusion tips, and the temperature there increased sharply in the beginning and slowly afterward. As expected, the back-stress is highest for case 4 and least for case 1 at any instant of time. For each of the four cases for which results are plotted in Fig. 9, the energy dissipation rate attains a peak value at time $t \cong 0.075$, the rate for the no back-stress case being always higher than that for the other three cases. Thus, the rate of increase of temperature at the origin will decrease for $t \geqq 0.075$. This is not transparent from the plots of the evolution of the temperature, mainly because of the scale used.

We have plotted in Fig. 10 the load displacement curves for cases 1, 4, 6 and 7, both with and without the initial temperature perturbation. Since the nondimensional height of half of the

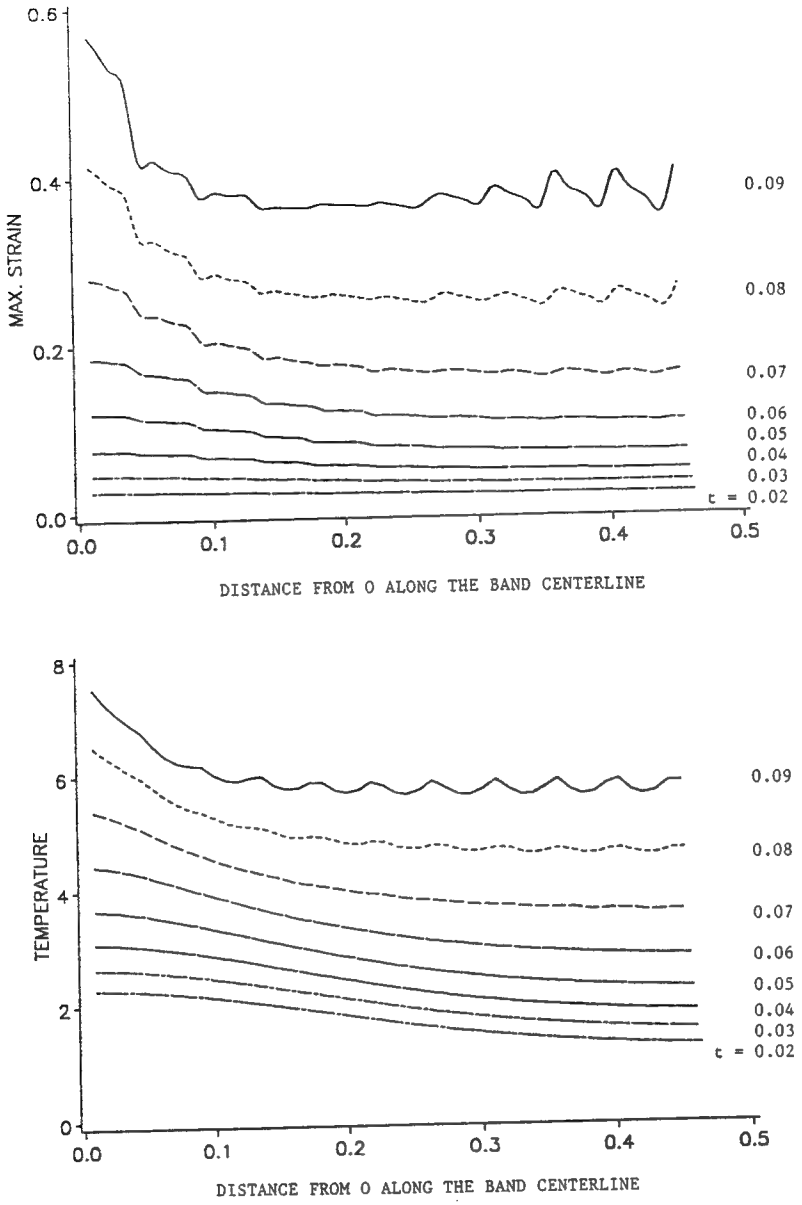

Fig. 6. Variation of the maximum principal logarithmic strain and the temperature along the estimated centerline OEF of the band at different times

block equals one and the block is being compressed at a nondimensional average strain-rate of one after the initial rise to the steady value, the nondimensional vertical displacement of a point on the top surface is slightly less than the nondimensional time. The applied load P is computed by using the relation

$$P = -\int \sigma_{22}(x_1, \bar{x}_2)\, dx_1,$$

where $\bar{x}_2$ is the current x_2-coordinate of a point on the top surface and the limits of integration extend from $x_1 = 0$ to the value of x_1 for points on the right edge. The values of P are significantly

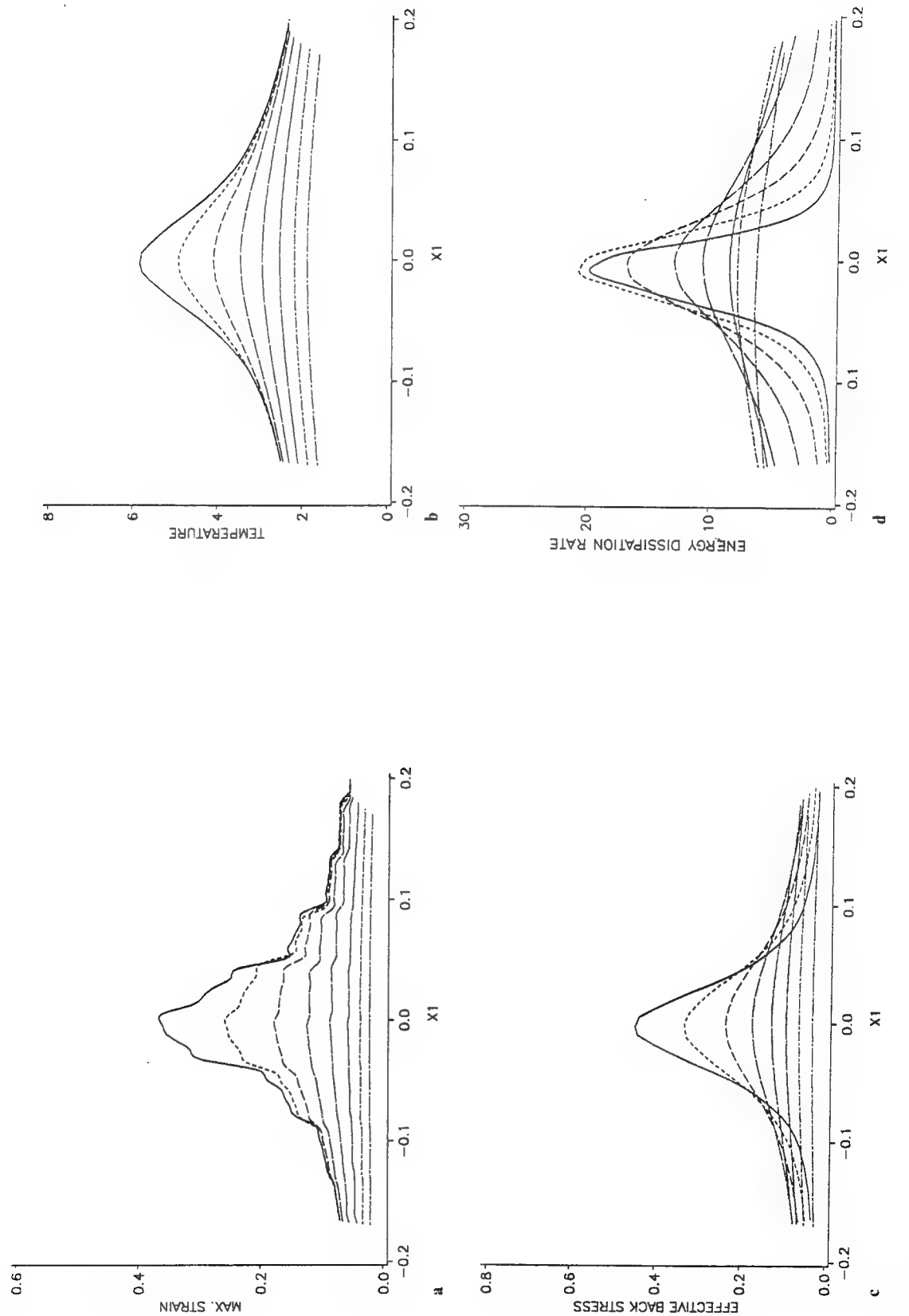
MAX. STRAIN
X1
a
TEMPERATURE
X1
b
EFFECTIVE BACK STRESS
X1
c
ENERGY DISSIPATION RATE
X1
d

Fig. 7. a–d

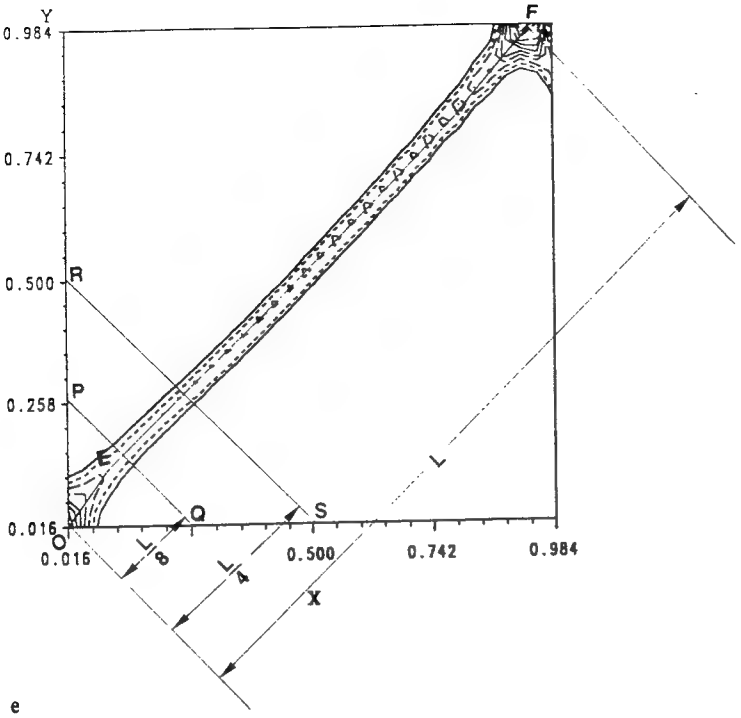

Fig. 7. Distribution at different times, starting with $t = 0.02$, of **a** the maximum principal logarithmic strain, **b** the temperature, **c** the effective back-stress, and **d** the rate of dissipation of the energy density on line PQ. **e** Estimated centerline OEF of the band, and locations of two transverse lines PQ and RS perpendicular to OEF. The curves are for $t = 0.02$, 0.03, 0.04, 0.05, 0.06, 0.07, 0.08, and 0.09

higher than those of the effective stress since the hydrostatic component of the stress tensor and the back-stress make noticeable contributions to the load. The upper set of curves is obtained by assuming that the initial temperature is uniform. Initially, the applied load increases almost linearly in each case due to the linear increase of the applied speed. The heating of the block, because of its plastic deformations, softens it and the load required to deform it decreases. This decrease in the load with increasing compression of the block is more once a shear band has initiated than when there is no band formed. Thus, the development of a shear band results in a decrease in the load carrying capacity of the body. The oscillations in the load displacement curves are probably due to the inertia forces, and can be attributed, at least partially, to the fact that the deformation of the top row of elements is not homogeneous and the computation of tractions at boundary points is less accurate as compared to the solution within the block. It is very likely that the use of a finer mesh would decrease the oscillations in P, but this could not be verified because of the limited computational resources available to us. Also, a finer mesh would improve the resolution of the deformation within the band.

5 Conclusions

We have studied the initiation and growth of a shear band in an elastoviscoplastic body being deformed in plane strain compression at a nominal strain-rate of $5000\,\text{sec}^{-1}$. The effect of inertia forces and the coupling between the thermal and mechanical aspects of the

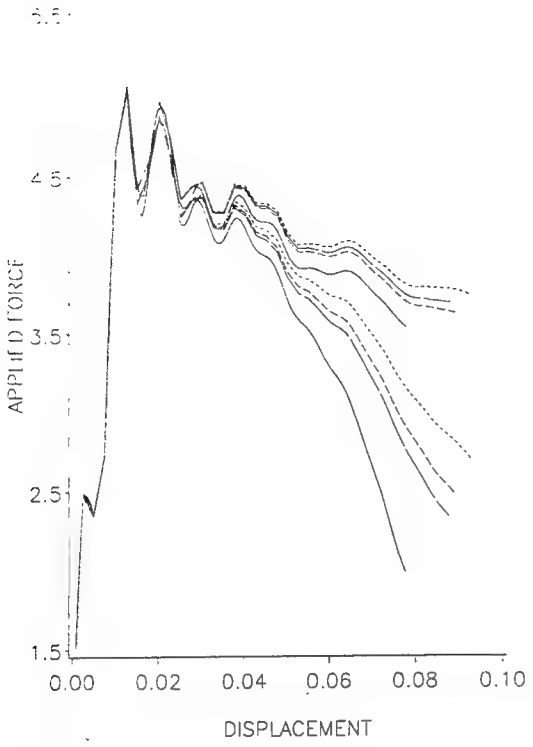

Fig. 10. The load displacement curves for cases 1, 4, 6, and 7. The upper set of curves corresponds to no temperature perturbation. —— Case 1, ····· case 4, ------- case 6, — — — — case 7

deformation is included in the problem formulation and its solution. The effect of texture development on the ensuing deformations is considered by including in the theory two internal variables, a scalar to account for the isotropic hardening of the material and a symmetric traceless second-order tensor to account for the kinematic hardening. The constitutive theory used is due to Anand and his co-workers [4], [5]. The computed results show that the consideration of kinematic hardening does not alter the qualitative nature of results. Also, the results agree qualitatively with those obtained earlier by Batra and co-workers [11], [14], [15], who used a different constitutive relation that does not require the integration with respect to time of the Cauchy stresses, and hence requires fewer computational resources. Because of a lack of test results detailing the evolution of the microstructure within the band in plane strain compression problems, it is not clear which constitutive theory should be used. Also, the determination of the values of material parameters in either theory for high strain-rates and elevated temperatures found within a shear band is still an open problem.

Acknowledgements

This work was supported by the U.S. Army Research Office grant DAAL03-91-G-0084 and the National Science Foundation grant MSS9 121 279 to the University of Missouri-Rolla. Some of the computations were performed on the NSF sponsored supercomputer center at the Cornell University, Ithaca, NY.

References

[1] Batra, R. C., Kim, C. H.: Effect of thermal conductivity on the initiation, growth, and band width of adiabatic shear bands. Int. J. Eng. Sci. **29**, 949–960 (1991).
[2] Merzer, A. M.: Modeling of adiabatic shear band development from small imperfection. J. Mech. Phys. Solids **30**, 323–338 (1982).
[3] Dodd, B., Bai, Y.: Width of adiabatic shear bands. Mat. Sci. Tech. **1**, 38–40 (1985).
[4] Anand, L.: Constitutive equations for hot working of metals. Int J. Plasticity **1**, 213–231 (1985).
[5] Brown, S. B., Kim, K. H., Anand, L.: An internal variable constitutive model for hot working of metals. Int. J. Plasticity **5**, 95–130 (1989).
[6] Tresca, H.: On further application of the flow of solids. Proc. Inst. Mech. Engrs. **30**, 301–345 (1878).
[7] Massey, H. F.: The flow of material during forging. Proc. Manchester Assoc. Eng. 21–26 (1921).
[8] Zener, C., Hollomon, J. H.: Effect of strain-rate on plastic flow of steel. J. Appl. Phys. **15**, 22–32 (1944).
[9] Rogers, H. C.: Adiabatic plastic deformation. Ann. Rev. Mat. Sci. **9**, 283–311 (1979).
[10] Shawki, T., Clifton, R. J.: Shear band formation in thermal viscoplatic materials. Mech. Mat. **8**, 13–43 (1989).
[11] Batra, R. C., Zhu, Z. G.: Dynamic shear band development in a bimetallic body containing a void. Int. J. Solids Struct. **27**, 1829–1854 (1991).
[12] Zbib, H. M., Shawki, T. G., Batra, R. C. (eds.): Material instabilities. Appl. Mech. Rev. **45**, 3(2) (1992).
[13] Hindmarsh, A. C.: ODEPACK – A systematized collection of ODE solvers. In: Scientific computing (Stepleman, R. S., et al., eds.). Amsterdam: North-Holland 1983.
[14] Zhu, Z. G., Batra, R. C.: Dynamic shear band development in plane strain compression of a viscoplastic body containing a rigid inclusion. Acta Mech. **84**, 89–107 (1990).
[15] Batra, R. C., Liu, D. S.: Adiabatic shear banding in plane strain problems. J. Appl. Mech. **56**, 527–543 (1989).

Authors' address: Y. M. Wang and R. C. Batra, Department of Mechanical and Aerospace Engineering and Engineering Mechanics, University of Missouri-Rolla, Rolla, MO 65401-0249, U.S.A.

Acta Mechanica 100, 105—114 (1993)

ACTA MECHANICA

Analysis of shear bands in a dynamically loaded viscoplastic cylinder containing two rigid inclusions

R. C. Batra and **X.-T. Zhang**, Rolla, Missouri

(Received April 14, 1992)

Summary. We study plane strain thermomechanical deformations of a hollow circular cylinder containing two rigid non-heat-conducting ellipsoidal inclusions placed on a radial line symmetrically with respect to the center. These inclusions can be viewed as precipitates or second phase particles in an alloy. The material of the cylinder is presumed to exhibit thermal softening, but strain and strain-rate hardening. The impact load applied on the inner surface of the cylinder is modeled by prescribing a radial velocity and zero tangential tractions at material particles situated on the inner surface. Rigid body motion of the inclusion is considered and no slip condition between the inclusion and the cylinder material is imposed.

It is found that shear bands initiate from points adjacent to inclusion tips near the inner surface of the cylinder and propagate toward this surface. At inclusion tips near the outer surface of the cylinder, the maximum principal logarithmic strain and the temperature are high and the effective stress is low, but severe deformations there do not propagate outward.

1 Introduction and problem formulation

In a previous paper [1] we studied the problem of the initiation and growth of shear bands in a dynamically loaded and thermally softening viscoplastic cylinder undergoing plane strain deformations. Two ellipsoidal voids placed on a radial line symmetrically with respect to the center were taken to be nucleation sites for the bands. Here we study the same problem, except that the voids are replaced by rigid inclusions. Zhu and Batra [2] have investigated the initiation of shear bands from inclusion tips embedded at the centroid of a square cross-section. However, the inclusion was stationary because of the symmetry of the deformations. Here each inclusion can move in the radial direction; we account for its inertia, and compare computed results with those obtained when the inclusions are replaced by voids. This comparison should reveal which one of the two is a stronger defect in the sense that it causes the shear band to initiate sooner.

We note that much of the literature on shear bands is given in the two papers [1], [2] cited above, and refer the reader to these papers for references related to this work. The study of shear bands is important, since they act as precursors to shear fractures, and once a shear band has formed subsequent deformations of the body occur within this narrow region with the rest of the body undergoing very little deformations.

The geometric configuration for the problem studied and the finite element mesh used to analyze it are shown in [1, Figs. 1 and 2]. Here the void of [1] is replaced by an identical non-heat-conducting rigid inclusion. We refer the reader to [1] for the governing equations, boundary conditions, constitutive relations, and a brief description of the method used to solve the problem. Whereas the void surface in [1] was taken to be thermally insulated and traction free, here we require that displacements and surface tractions are continuous across the

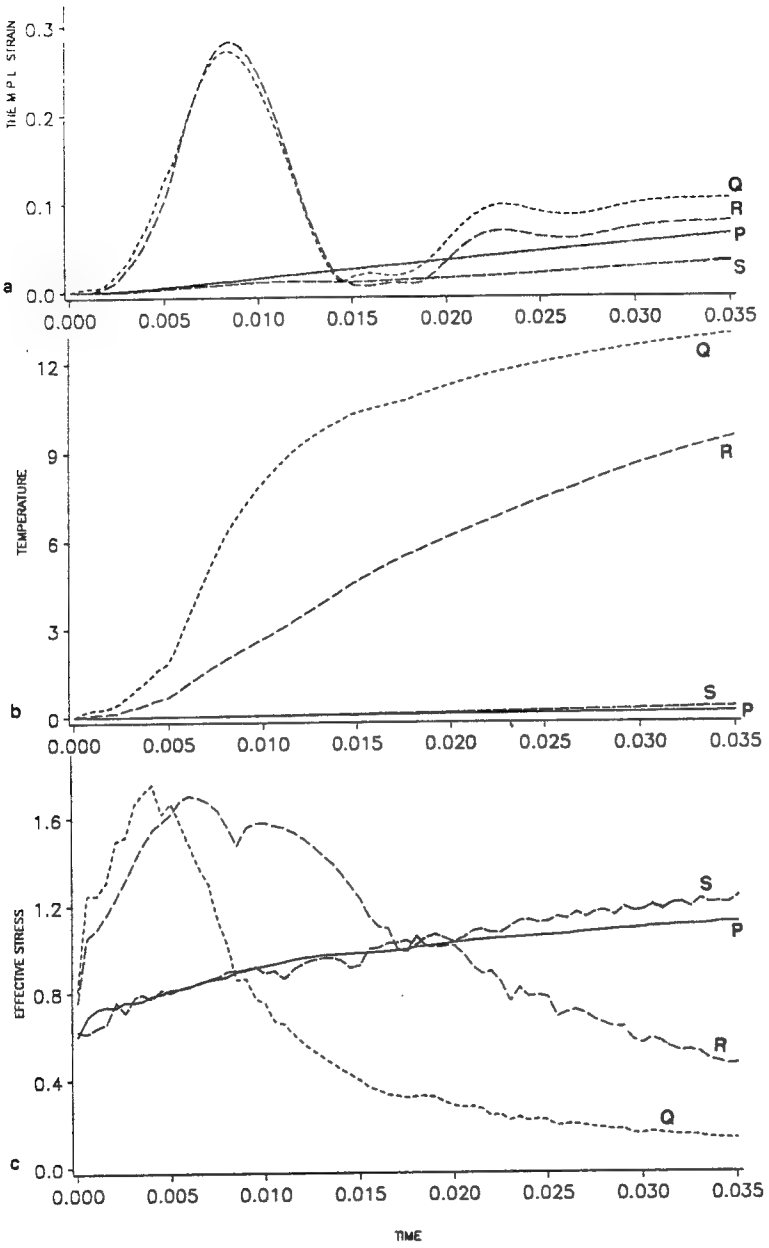

Fig. 2. Evolution of the maximum principal logarithmic strain, temperature, and the effective stress at points *P*, *Q*, *R*, and *S*. Coordinates of these points in the stress-free reference configuration are *P* (0.501 6, 0.001 8), *Q* (0.719 3, 0.003 3), *R* (0.776 4, 0.003 5), and *S* (0.998 4, 0.002 7).

principal logarithmic strain indicate that initially severe deformations occur at points near both inclusion tips, but those at points near the right inclusion tip subside and those at points adjacent to the left inclusion tip become more intense and propagate toward the inner surface. This is confirmed by a plot, given in Fig. 4, of the deformed mesh embedded in a small region surrounding the inclusion. We note that this mesh was not used to solve the problem. Coordinates of node points for this mesh in reference and present configurations were obtained from the coordinates of node points in the mesh in the unstressed reference configuration and the

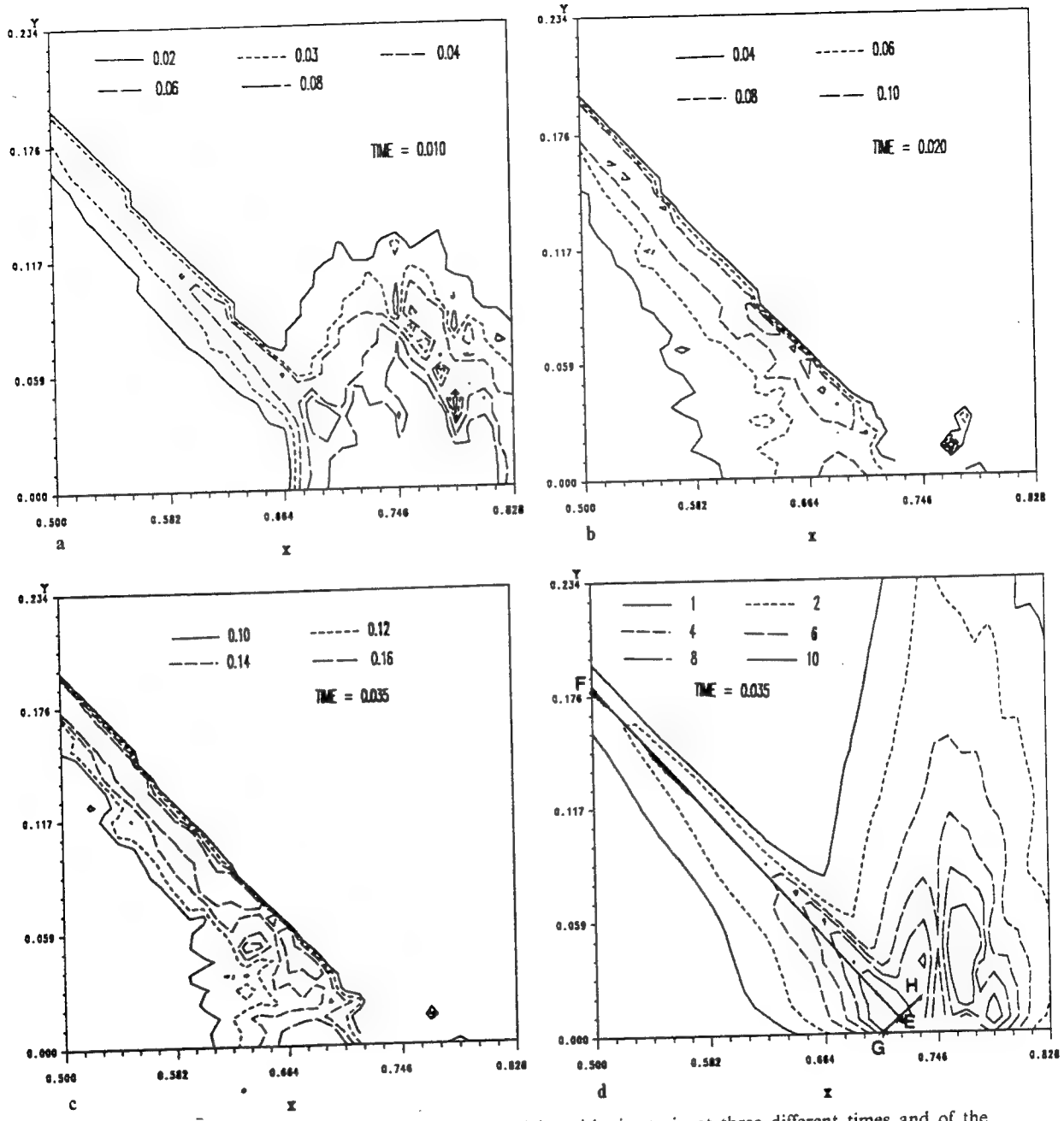

Fig. 3a–d. Contours of the maximum principal logarithmic strain at three different times and of the temperature at $t = 0.035$

solution of the problem. In our earlier investigation [1] involving a void where we have inclusion now, we found that a small region near the right void tip also deformed severely, but these intense deformations did not propagate to distant points. The presently computed results suggest that the temperature rise and stress drop at a point in a two-dimensional problem may make the material there unstable, but this instability need not propagate outward from that point. Perhaps factors such as the rates of temperature rise and of stress drop, and the state of deformation of the material surrounding the point where the stress drop occurs are equally important, too.

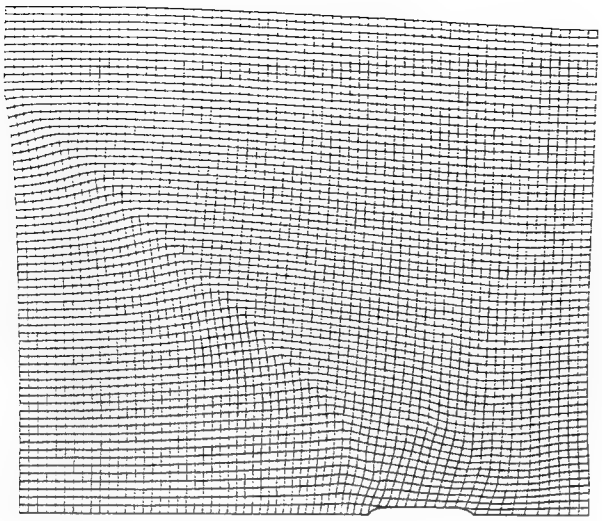

Fig. 4. Deformed mesh embedded in a small region surrounding the rigid inclusion

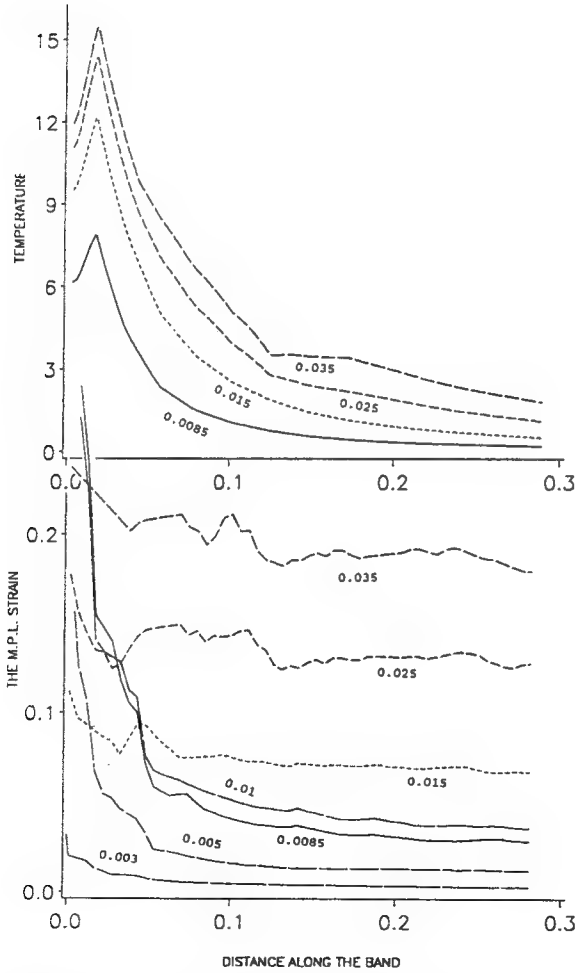

Fig. 5. Variation, at different times, of the maximum principal logarithmic strain within the band, and of the temperature at points on the estimated centerline EF of a shear band

From the contours of ε and the deformed mesh, we estimate the centerline of the shear band to be the line EF shown in Fig. 3d. The variation of the temperature at points on EF and of the maximum principal logarithmic strain within the band for different values of time is shown in Fig. 5. The values of the maximum principal logarithmic strain were obtained by computing its values at several points on a line perpendicular to EF, finding the largest of these values, and assigning that value to the point of intersection of the transverse line with EF. We note that ε varies noticeably at points on the transverse line as depicted below in Fig. 6. As oscillations of the rigid inclusion diminish, the strain within the band tends to become uniform. Whereas the maximum strain occurs at a point close to E, the peak temperature occurs at a point on line EF that is slightly away from E. The distribution, at different times, of the temperature and the maximum principal logarithmic strain at points on line GH (cf. Fig. 3d for the location of line GH) perpendicular to EF is shown in Fig. 6. The abscissa is the distance of a point from G along the line GH. Whereas the temperature at material points on line GH changes gradually as one

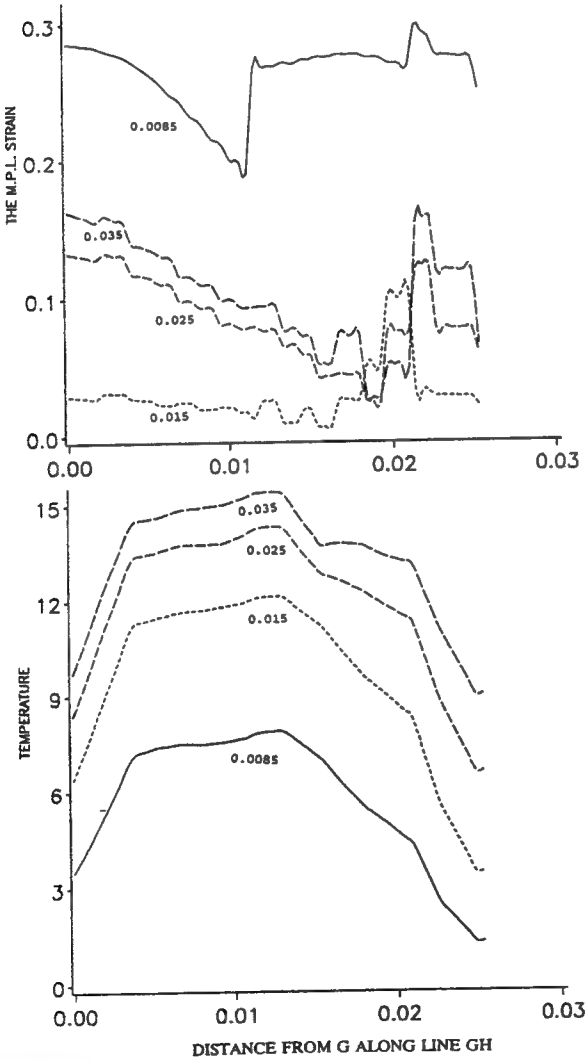

Fig. 6. Variation, at different times, of the maximum principal logarithmic strain and the temperature across the shear band

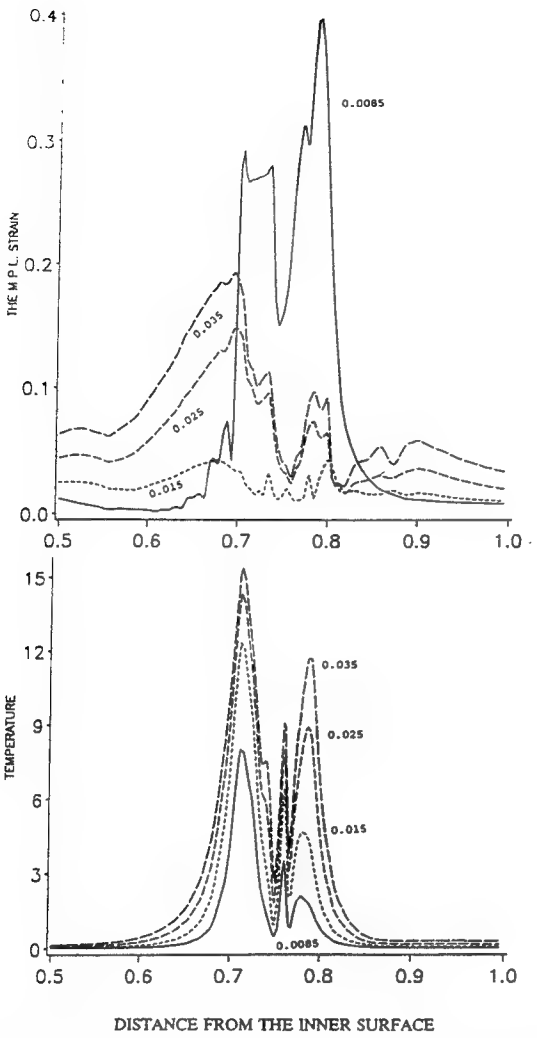

Fig. 7. Variation, at different times, of the maximum principal logarithmic strain and the temperature on a horizontal line tangent to the inclusion tip

moves along the line GH, the strain does not. The computations were stopped when a material point had melted. The melting of one material point does not imply the failure of the body since the neighboring material holds it together. It seems that the use of an adaptively refined mesh would probably result in sharper gradients of temperature and strain along line GH.

The distribution of the maximum principal logarithmic strain and temperature at points on a horizontal line VW tangent to the inclusion is exhibited in Fig. 7. The abscissa in the figure equals the distance from the inner surface of the cylinder (i.e., point V) of a point on line VW. Oscillations of the rigid inclusion affect noticeably the location of the point where peak values of ε occur. The strain and temperature at points near the left inclusion tip are higher than those at points near the right inclusion tip.

Figure 8 depicts how the average pressure

$$p = -\frac{2}{\pi} \int_0^{\pi/2} \sigma_{rr}(r_i, \theta)\, d\theta \tag{5}$$

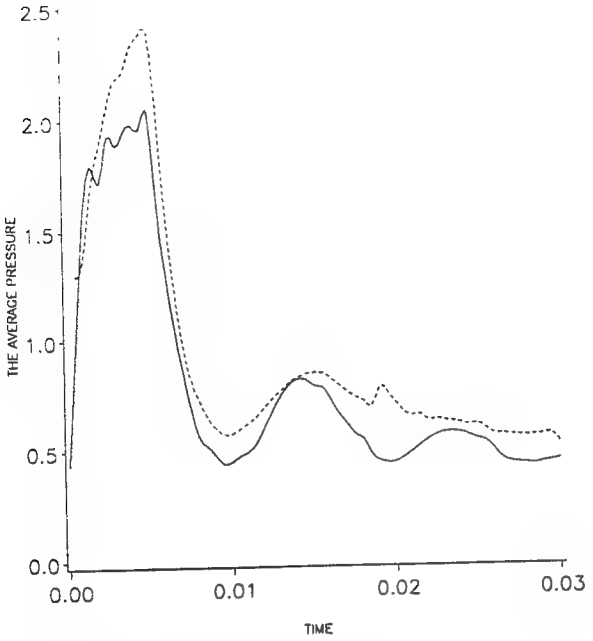

Fig. 8. Variation with time of the average pressure acting on the inner surface of the cylinder. —— inclusion ------ void

on the inner surface of the cylinder varies with time. In Eq. (5), r_i equals the inner radius of the deformed cylinder. The solid curve corresponds to the case of the rigid inclusion and the broken one to that of an identical void. Note that essential boundary conditions are prescribed on the inner surface, and the outer surface is traction free. If the shear band is assumed to initiate when the pressure on the inner surface drops precipitously, then the rigid inclusion causes the shear band to initiate sooner than the void does. Also, the average pressure in the cylinder containing the inclusions stays lower than that in the cylinder having similarly situated voids suggesting that the overall stiffness of the cylinder has been reduced more for the rigid inclusion case.

3 Conclusions

We have studied the problem of the initiation and growth of shear bands in a thermally softening viscoplastic cylinder undergoing plane strain deformations. The cylinder has two non-heat-conducting rigid ellipsoidal inclusions, placed on a radial line symmetrically about the center. The complete dynamic thermomechanical problem, including the inertia of the rigid inclusion, has been analyzed. It is found that because of the oscillations of the rigid inclusion, the point where peak values of the maximum principal logarithmic strain occur keeps on changing with time. A shear band initiates from a point close to the left void tip and propagates toward the inner surface. Even though the maximum principal logarithmic strain at a point near the right inclusion tip also increases, these severe deformations stay confined to a very narrow region surrounding the right inclusion tip. Thus, a material point may become unstable in the sense that the effective stress there decreases with increasing strain, but this instability may not propagate farther because either the state of deformation of the material surrounding the inclusion tip is not conducive to that, or the instability is not severe enough.

Acknowledgements

This work was supported by the U.S. Army Research Office grant DAAL 03-91-G-0084 and the U.S. NSF grant MSS 9121279 to the University of Missouri-Rolla. Some of the computations were performed on the NSF sponsored supercomputer center in Ithaca, NY.

References

[1] Batra, R. C., Zhang, X.-T.: Shear band development in dynamic loading of a viscoplastic cylinder containing two voids. Acta Mech. **85,** 221–234 (1990).
[2] Zhu, Z. G., Batra, R. C.: Dynamic shear band development in plane strain compression of a viscoplastic body containing a rigid inclusion. Acta Mech. **84,** 89–107 (1990).
[3] Batra, R. C., Kim, C. H.: Effect of viscoplastic flow rules on the initiation and growth of shear bands at high strain rates. J. Mech. Phys. Solids **38,** 859–874 (1990).

Authors' address: R. C. Batra and X.-T. Zhang, Department of Mechanical and Aerospace Engineering and Engineering Mechanics, University of Missouri-Rolla, Rolla, MO 65401-0249, U.S.A.

Int. J. Engng Sci. Vol. 31, No. 4, pp. 529–547, 1993
Printed in Great Britain.

0020-7225/93 $6.00 + 0.00

ANALYSIS OF SHEAR BANDS IN DYNAMIC AXISYMMETRIC COMPRESSION OF A THERMOVISCOPLASTIC CYLINDER

R. C. BATRA and K. I. KO

Department of Mechanical and Aerospace Engineering and Engineering Mechanics, University of Missouri-Rolla, Rolla, MO 65401-0249, U.S.A.

Abstract—We study dynamic axisymmetric thermomechanical deformations of a viscoplastic cylinder with its boundaries assumed to be thermally insulated, its mantle traction free, and its top and bottom surfaces compressed at a prescribed rate. We consider two limiting cases of the frictional force between the loading device and the cylinder, i.e. either there is no sliding between the two surfaces, or there is smooth contact. It is found that the shear bands initiate much later when frictional force is neglected than when it is considered. A comparison of the presently computed results with those for the case when the body is assumed to be deformed in plane strain compression reveals that the initiation of shear bands is delayed significantly for the axisymmetric problem.

1. INTRODUCTION

Zener and Hollomon [1] observed 32 μm wide shear bands during the punching of a hole in a low carbon steel plate, and postulated that heating caused by the plastic deformation of the material made it softer and the material became unstable when this thermal softening equalled the combined effects of strain and strain-rate hardening. Subsequent experimental [2, 3] and numerical [4–6] studies have revealed that shear bands generally form at an average strain much more than the one when the shear stress or the effective stress attains its peak value. Backman and Finnegan [7] have pointed out that shear bands initiate from flaws, second phase particles, or other material defects present in the body and propagate like a crack. The analytical and numerical studies have modeled a material defect by introducing (i) a perturbation in temperature or strain-rate, (ii) a geometric imperfection such as a notch or a smooth variation in the thickness of the specimen, (iii) a weak material at the site of the defect, (iv) a void, or (v) a rigid inclusion. Batra [6] studied simple shearing deformations of a viscoplastic body and found that large temperature perturbations caused the shear bands to initiate at an average strain less than the one when the shear stress attained its peak value in a defect-free body.

Wulf [8] tested 7039 aluminum cylinders in compression at average strain-rates of 2000–25,000 s^{-1} and observed that circular cross-sections were deformed into elliptical ones, and shear bands formed in specimens which subsequently failed by crack propagation along the dominant band. Here we study the dynamic thermomechanical deformations of an isotropic circular steel cylinder deformed in compression at a nominal strain-rate of 5000 s^{-1}, and model a material defect by introducing a temperature perturbation at the center of the cylinder. We assume that the deformations of the cylinder are axisymmetric even after a shear band has formed. There is no fracture or failure criterion included in our work; thus, the cylinder can undergo unlimited deformations. The computed results show that shear bands form much later when the contact surfaces between the loading device and the ends of the cylinder are modeled as smooth than when they are taken to be sticking with each other. A comparison of the present results with those when the body is assumed to deform in plane strain compression reveals that the initiation of shear bands is delayed considerably in a body undergoing axisymmetric deformations.

2. FORMULATION OF THE PROBLEM

A schematic sketch of the problem studied is shown in Fig. 1. We use cylindrical coordinates with origin at the center of the cylinder to analyze its axisymmetric deformations, presume that

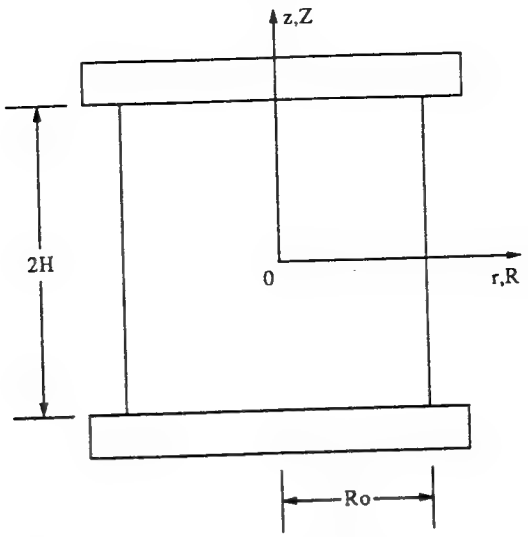

Fig. 1. A schematic sketch of the problem studied.

it is made of a thermally softening viscoplastic material, and is loaded at its ends by an impulsive load. Because of the symmetry of deformations about the horizontal centroidal plane, we analyze deformations of the upper half of the cylinder. In terms of the Lagrangian description of motion, equations governing the thermomechanical deformations of the body are

$$(\rho J)^{\cdot} = 0, \tag{1}$$

$$\rho_0 \dot{\mathbf{v}} = \mathrm{Div}\,\mathbf{T}, \tag{2}$$

$$\rho_0 \dot{e} = -\mathrm{Div}\,\mathbf{Q} + \mathbf{T}\colon \mathrm{Grad}\,\mathbf{v}, \tag{3}$$

$$\mathbf{T} = \frac{\rho_0}{\rho}\boldsymbol{\sigma}\mathbf{F}^{-T}, \qquad \boldsymbol{\sigma} = -B\left(\frac{\rho}{\rho_0} - 1\right)\mathbf{1} + 2\mu\mathbf{D}, \tag{4}$$

$$2\mu = \frac{\sigma_0}{\sqrt{3}\,I}(1 + bI)^m(1 - \nu\theta), \tag{5}$$

$$\mathbf{Q} = \frac{\rho_0}{\rho}\mathbf{F}^{-1}\mathbf{q}, \qquad \mathbf{q} = -k\,\mathrm{grad}\,\theta, \tag{6}$$

$$2\mathbf{D} = \mathrm{grad}\,\mathbf{v} + (\mathrm{grad}\,\mathbf{v})^T, \qquad 2I^2 = \hat{\mathbf{D}}\colon\hat{\mathbf{D}}, \qquad \hat{\mathbf{D}} = \mathbf{D} - \frac{1}{3}(\mathrm{tr}\,\mathbf{D})\mathbf{1}, \tag{7}$$

$$\dot{e} = c\dot{\theta} + \dot{\rho}B\left(\frac{\rho}{\rho_0} - 1\right)\Big/(\rho\rho_0), \qquad J = \det\mathbf{F}, \qquad \mathbf{F} = \mathrm{Grad}\,\mathbf{x}. \tag{8}$$

Equations (1), (2), and (3) express, respectively, the balance of mass, balance of linear momentum, and the balance of internal energy; equations $(4)_2$, $(6)_2$, and $(8)_1$ are, respectively, the presumed constitutive relations for the Cauchy stress $\boldsymbol{\sigma}$, heat flux $\mathbf{q}$ measured per unit area in the present or deformed configuration, and the rate of change of the specific internal energy e. In equations (1)–(8), ρ is the present mass density, ρ_0 the mass density in the reference configuration, $\mathbf{v}$ the velocity of a material particle, the operators Div and Grad signify the divergence and the gradient operations in the reference configuration, the operator grad is the gradient of a quantity in the present configuration, $\mathbf{A}\colon\mathbf{B}$ equals $\mathrm{tr}(\mathbf{A}\mathbf{B}^T)$ for second order tensors $\mathbf{A}$ and $\mathbf{B}$, and a superimposed dot indicates the material time derivative. Furthermore, $\mathbf{F}$ is the deformation gradient, $\mathbf{D}$ the strain-rate tensor, $\hat{\mathbf{D}}$ the deviatoric strain-rate tensor, $\mathbf{x}$ gives the present location of a material particle that occupied place $\mathbf{X}$ in the reference

configuration, $\mathbf{T}$ the first Piola–Kirchhoff stress tensor, $\mathbf{Q}$ the heat flux measured per unit area in the reference configuration, θ the temperature rise, σ_0 is the yield stress in a quasistatic simple compression test, B is the bulk modulus, parameters b and m describe the strain-rate hardening of the material, ν characterizes its thermal softening, k its thermal conductivity, and c the specific heat. Defining the deviatoric stress tensor $\mathbf{s}$ by

$$\mathbf{s} = \boldsymbol{\sigma} + B\left(\frac{\rho}{\rho_0} - 1\right)\mathbf{1} - \frac{2\mu}{3}(\operatorname{tr}\mathbf{D})\mathbf{1} = 2\mu\hat{\mathbf{D}}, \tag{9}$$

we get

$$\left(\frac{1}{2}\operatorname{tr}(\mathbf{s}\mathbf{s}^T)\right)^{1/2} = \frac{\sigma_0}{\sqrt{3}}(1 - \nu\theta)(1 + bI)^m. \tag{10}$$

The constitutive relation $(4)_2$ with μ given by (5) generalizes the one proposed by Litonski [9] for simple shearing deformations of the material. Batra [10] proposed and used equation $(4)_2$ to study the steady-state axisymmetric deformations of a thermoviscoplastic target being penetrated by a fast moving rigid cylindrical rod, and it has been referred to as the Litonski–Batra flow rule. Batra and Jayachandran [11] have shown that the Litonski–Batra flow rule and those proposed by Bodner and Partom [12] and Brown *et al.* [13], when calibrated against a hypothetical compression test and subsequently used to study the axisymmetric steady-state penetration problem, predict essentially identical patterns of target deformations. We note that Bell [14], Lin and Wagoner [15], and Lindholm and Johnson [16] concluded from their test results that the flow stress decreases linearly with the temperature rise for the materials they tested.

We introduce nondimensional variables, indicated below by a superimposed bar, as follows:

$$\bar{\boldsymbol{\sigma}} = \boldsymbol{\sigma}/\sigma_0, \quad \bar{\mathbf{s}} = \mathbf{s}/\sigma_0, \quad \bar{B} = B/\sigma_0, \quad \bar{\mathbf{T}} = \mathbf{T}/\sigma_0, \quad \bar{\mathbf{v}} = \mathbf{v}/v_0, \quad \bar{t} = tv_0/H,$$
$$\bar{\mathbf{x}} = \mathbf{x}/R_0, \quad \bar{\theta} = \theta/\theta_0, \quad \bar{b} = b(v_0/H), \quad \bar{\nu} = \nu\theta_0, \quad \bar{\rho} = \rho/\rho_0,$$
$$\theta_0 \equiv \sigma_0/(\rho_0 c), \quad \bar{\mathbf{D}} = \mathbf{D}H/v_0, \quad \bar{I} = IH/v_0. \tag{11}$$

Here $2H$ is the height of the cylinder, R_0 its radius, and v_0 the imposed speed on the top and bottom surfaces. Henceforth we use nondimensional variables and drop the superimposed bars.

We study only axisymmetric deformations of the viscoplastic cylinder, and presume that they are symmetric about the horizontal centroidal plane. Pertinent boundary conditions for the material in the first quadrant of the R–Z plane are:

$$v_r = 0, \quad T_{zR} = 0, \quad Q_R = 0 \quad \text{on the axis of symmetry} \quad r = R = 0,$$
$$v_z = 0, \quad T_{rZ} = 0, \quad Q_Z = 0 \quad \text{on} \quad z = Z = 0,$$
$$T_{rR} = 0, \quad T_{zR} = 0, \quad Q_R = 0 \quad \text{on the mantle of the cylinder } r = R_0,$$
$$v_z = -U(t), \quad Q_Z = 0 \quad \text{and either } T_{rZ} = 0 \text{ or } v_r = 0, \text{ on the top surface} \quad Z = H. \tag{12}$$

That is, boundary conditions resulting from the presumed symmetry of deformations are applied on the left and bottom faces, the mantle of the cylinder is taken to be traction free, normal velocity is prescribed on the top surface, and either zero radial velocity or zero tangential traction is applied on the top surface, which simulates the condition of no sliding or no frictional force acting between the loading device and the cylinder surface. All bounding surfaces of the cylinder are presumed to be thermally insulated from the surroundings. We take the function $U(t)$ as

$$U(t) = t/0.005, \quad 0 \le t \le 0.005,$$
$$= 1, \quad t \ge 0.005, \tag{13}$$

and the initial conditions as

$$\rho(R, Z, 0) = 1.0, \qquad \mathbf{v}(R, Z, 0) = \mathbf{0},$$
$$\theta(R, Z, 0) = \epsilon(1 - \delta^2)^9 \exp(-5\delta^2), \qquad \delta^2 = R^2 + Z^2. \tag{14}$$

Thus the block is initially at rest, has a uniform mass density, but nonuniform temperature which is high at the origin and rapidly falls off to zero as we move away from it. The initial temperature $(14)_3$ models a material defect and its magnitude ϵ at the origin represents in some sense the strength of the defect.

3. BRIEF DESCRIPTION OF THE SOLUTION TECHNIQUE

The problem formulated above is highly nonlinear and too complicated to solve analytically. It is difficult, if not impossible, to prove an existence and/or a uniqueness theorem for it. Here we seek an approximate solution of the problem numerically by the finite element method, and use an updated Lagrangian description of motion. That is, to find the deformed configuration of the body at time $(t + \Delta t)$ we take its configuration at time t as the reference configuration. However, the deformations during this time interval Δt may be finite. We first reduce the coupled nonlinear partial differential equations governing the thermomechanical deformations of the body to a set of coupled, nonlinear, and ordinary stiff differential equations by using the Galerkin approximation. A finite element mesh consisting of 3-noded triangular elements with 3-point quadrature rule and lumped mass matrix, obtained by the row-sum technique, is used. At each node point of the finite element mesh, two components of the velocity, the temperature and the mass density, are taken as unknowns. The stiff ordinary differential equations are integrated with respect to time by using the backward difference Adam's method included in the subroutine LSODE developed by Hindmarsh [17]. The Gear method, also included in LSODE, could not be used because of the limited core storage available.

We delineate narrow regions of intense plastic deformation by using an adaptive mesh refinement technique developed by Batra and Ko [18] and described in the Appendix. After having obtained solution for a few time steps with a coarse mesh, the mesh is refined so that the integral of the second invariant of the strain-rate tensor over each element is essentially the same. Thus, smaller elements are generated in regions where the material is deforming severely, and coarser elements elsewhere.

4. COMPUTATION AND DISCUSSION OF RESULTS

Assuming that the cylinder is made of a typical steel, we assigned the following values to various material and geometric parameters.

$$b = 10{,}000\,\text{s}, \quad \sigma_0 = 333\,\text{MPa}, \quad k = 49.2\,\text{Wm}^{-1}{}^{\circ}\text{C}^{-1}, \quad m = 0.025,$$
$$c = 473\,\text{Jkg}^{-1}{}^{\circ}\text{C}^{-1}, \quad \rho_0 = 7800\,\text{kg m}^{-3}, \quad B = 128\,\text{GPa},$$
$$\nu = 0.0222^{\circ}\text{C}^{-1}, \quad v_0 = 25\,\text{m s}^{-1}, \quad H = R_0 = 5.0\,\text{mm}, \quad \epsilon = 0.2. \tag{15}$$

We have stated dimensional quantities to clarify the units used. Thus, the cylinder is compressed at an average strain-rate of $5000\,\text{s}^{-1}$. For values given in (15), $\theta_0 = 89.6^{\circ}\text{C}$, and the nondimensional melting temperature θ_m defined as $1/\nu$ equals 0.5027. We have taken a rather large value of the thermal softening coefficient ν so as to reduce the computational time. It should not affect the qualitative nature of results. In view of the lack of test data in a shear band, and the unavailability of detailed information about the evolution of a shear band in a compression problem, one can only see whether or not computed results predict well qualitatively various aspects of the shear band formation.

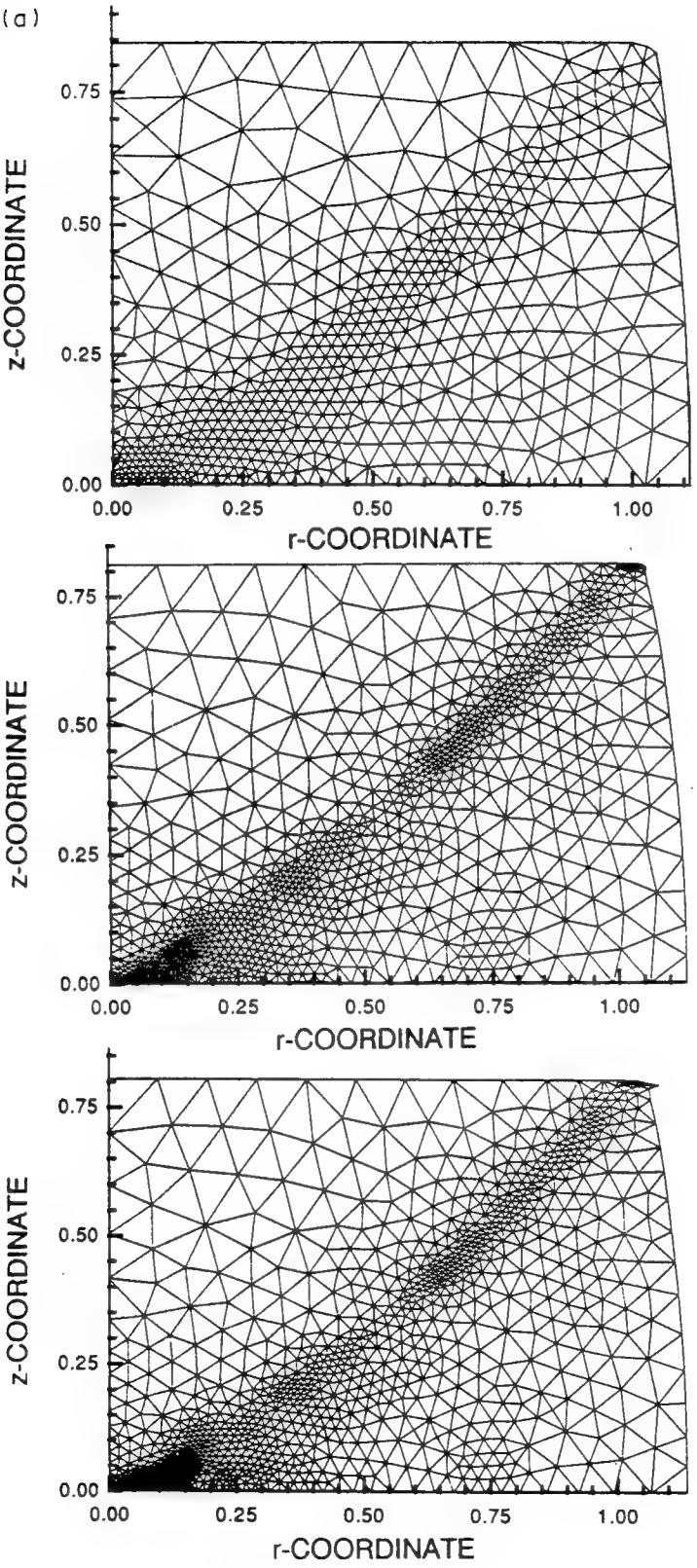

Fig. 2.—(*Caption overleaf*).

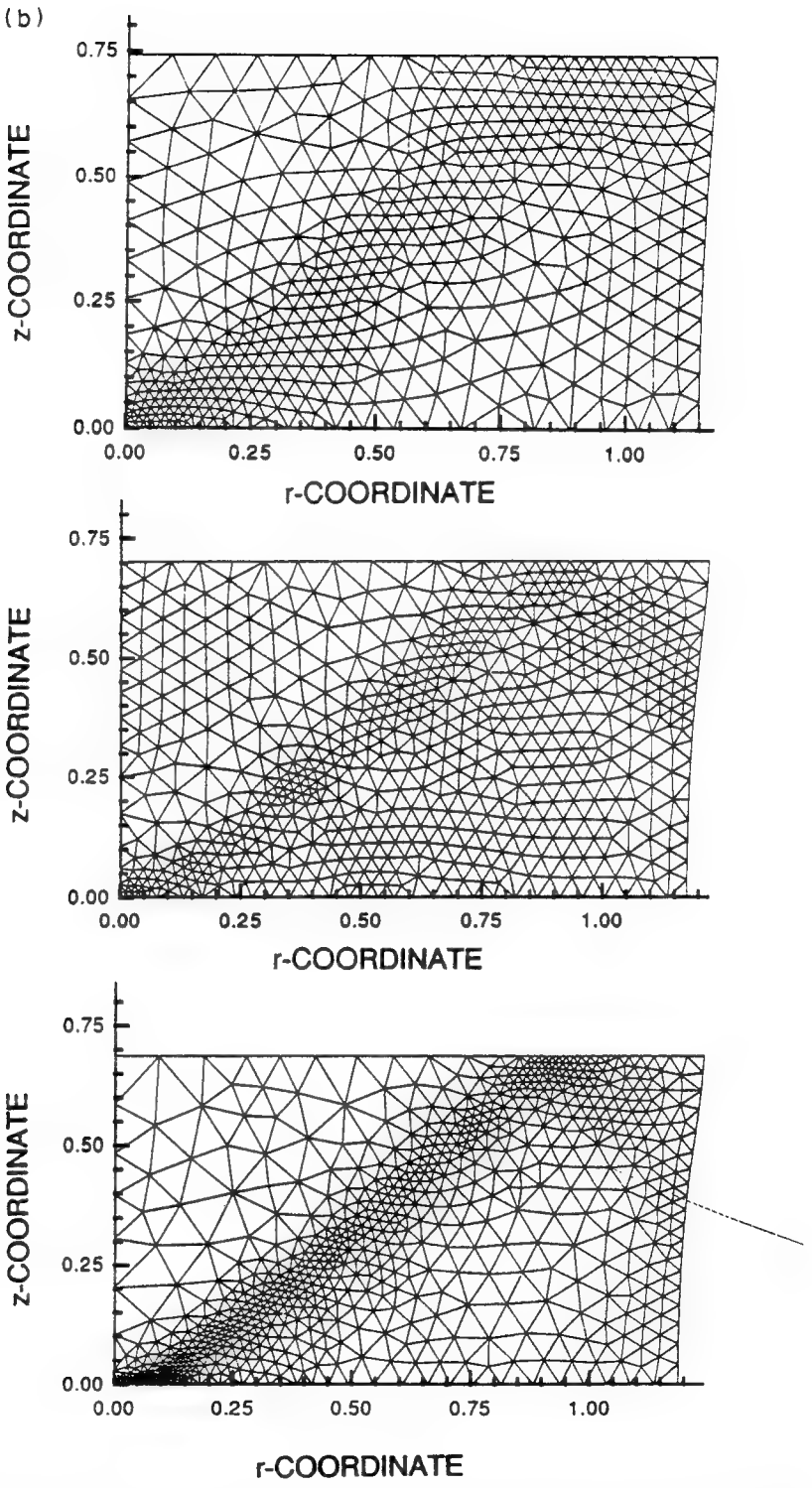

Fig. 2. (a) Refined finite element meshes at nondimensional times $t = 0.160$, 0.190, and 0.197 for the no slipping case; (b) $t = 0.26$, 0.30, and 0.315 for the case of the smooth contact.

The finite element mesh at time $t = 0$ had 400 uniform triangular elements with 441 nodes. The mesh was refined when the second invariant I of the deviatoric strain-rate tensor at the origin equalled 5, and subsequently for every increment of 0.01 in the nondimensional temperature θ at the specimen center. The finite element meshes so generated in the configurations at time $t = 0.160$, 0.190, and 0.197 when there is no slipping allowed at the contact surface between the loading device and the cylinder ends are depicted in Fig. 2(a). These plots discern the barrelling effect observed in compression tests, and also the severely deforming narrow region. The strain-rate near the top right corner is very high, too, and the elements there are deformed significantly. However, such is not the case when the contact surfaces between the loading device and cylinder ends are taken to be smooth. This is clear from the plots of the finite element meshes generated at time $t = 0.26$, 0.30, and 0.315 given in Fig. 2(b). In this case, the lateral displacement of material particles on the end faces is more than that of the similarly situated particles on the centroidal horizontal plane, and there is the reversed barrelling effect. This reversed barrelling was observed by Wulf [19] in high strain-rate compression of titanium and some titanium alloys, who used graphite grease to hold the specimens and also as a lubricant. Even though the average strain in the cylinder is more than that with the no slipping case, the deformations appear to be less intense within the band. This is mainly due to the differences in the deformations of the region near the top right corner for the two cases. To elucidate this, we have plotted in Fig. 3 the evolution of the second invariant I of the deviatoric strain-rate tensor at the top right corner. These plots indicate that the region near the top right corner deforms severely when the loading device is assumed to be glued to the cylinder ends. Computations with no temperature perturbation introduced at the center showed that a shear band initiated from the top right corner and propagated inward when sticking friction was considered, but no such localization effects were observed when the contact surfaces were taken to be smooth.

That the localization of deformation is significantly delayed for the axisymmetric problem with no friction is evidenced by the plot in Fig. 4(a) of the evolution of the second invariant I of

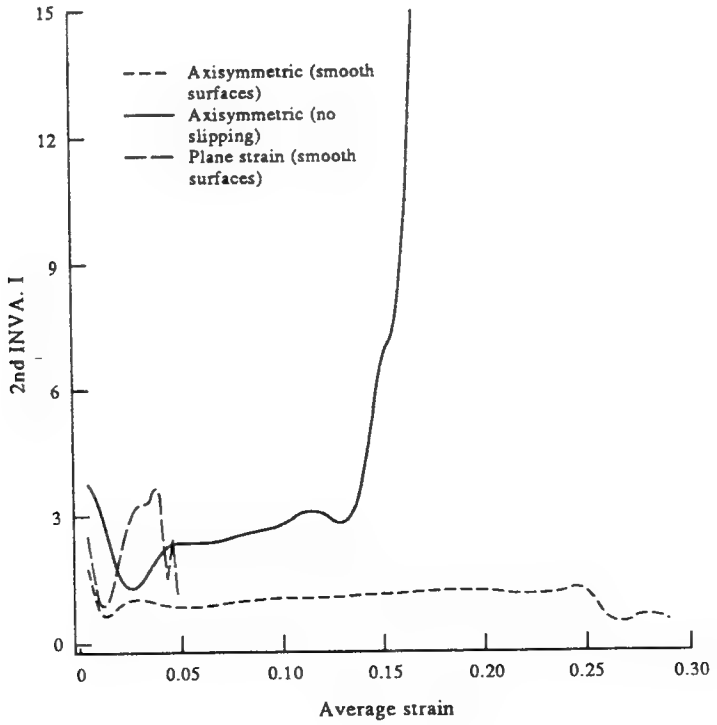

Fig. 3. Evolution of the second invariant of the deviatoric strain-rate tensor at the top right corner.

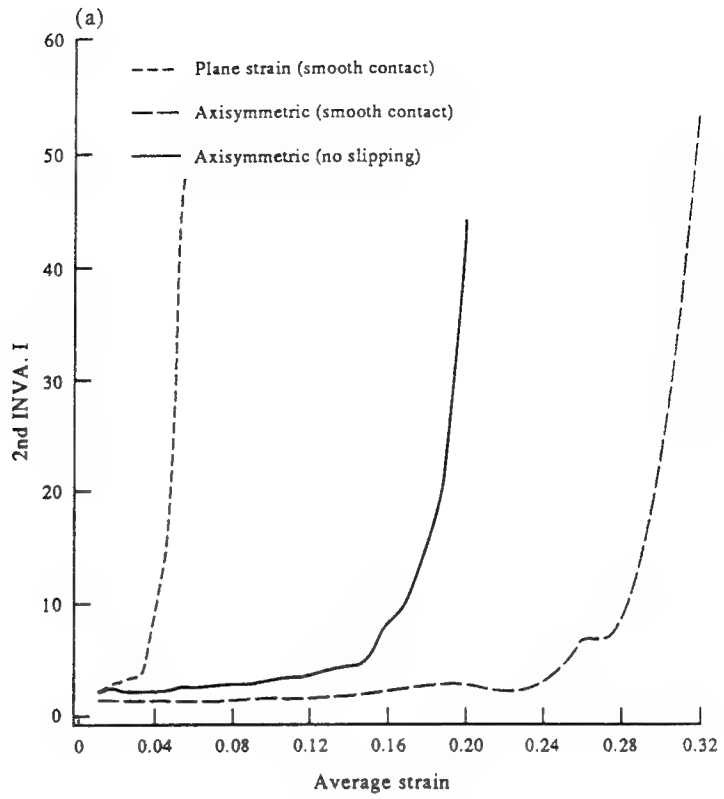

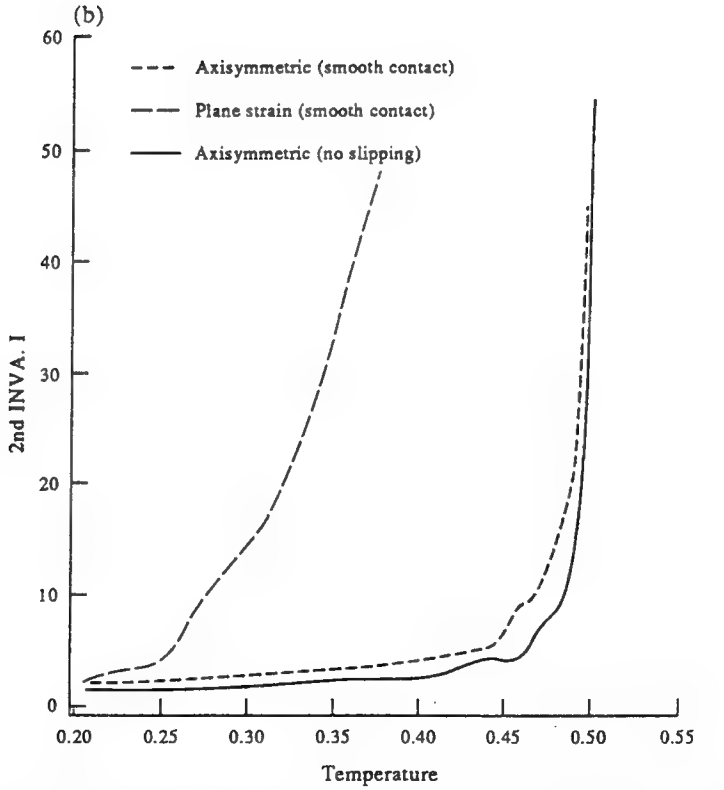

Fig. 4. (a) Evolution of the second invariant of the deviatoric strain-rate tensor at the centroid of the cylinder; (b) variation of the second invariant of the deviatoric strain-rate tensor at the cylinder center with the temperature there.

the deviatoric strain-rate tensor at the centroid of the cylinder. We have also included the corresponding result for the case when a cylindrical body of square cross-section (10×10 mm) and made of the material of the circular cylinder studied herein is deformed in plane strain compression at an average strain-rate of $5000\,s^{-1}$. It is transparent from these plots that the rapid increase in the values of I occurs at the lowest value of the average strain when the body is deformed in plane strain compression and at the highest value of the average strain when the deformations are axisymmetric and the contact surfaces are smooth. Also, during the time I increases rapidly, its rate of increase seems to be the least for axisymmetric deformations with smooth surfaces. However, when I at the cylinder center is plotted against the temperature there [cf. Fig. 4(b)] the effect of boundary conditions at the end faces is minimal. Since the temperature at the cylinder center increases monotonically until the material there melts, the abscissa represents a distorted time scale.

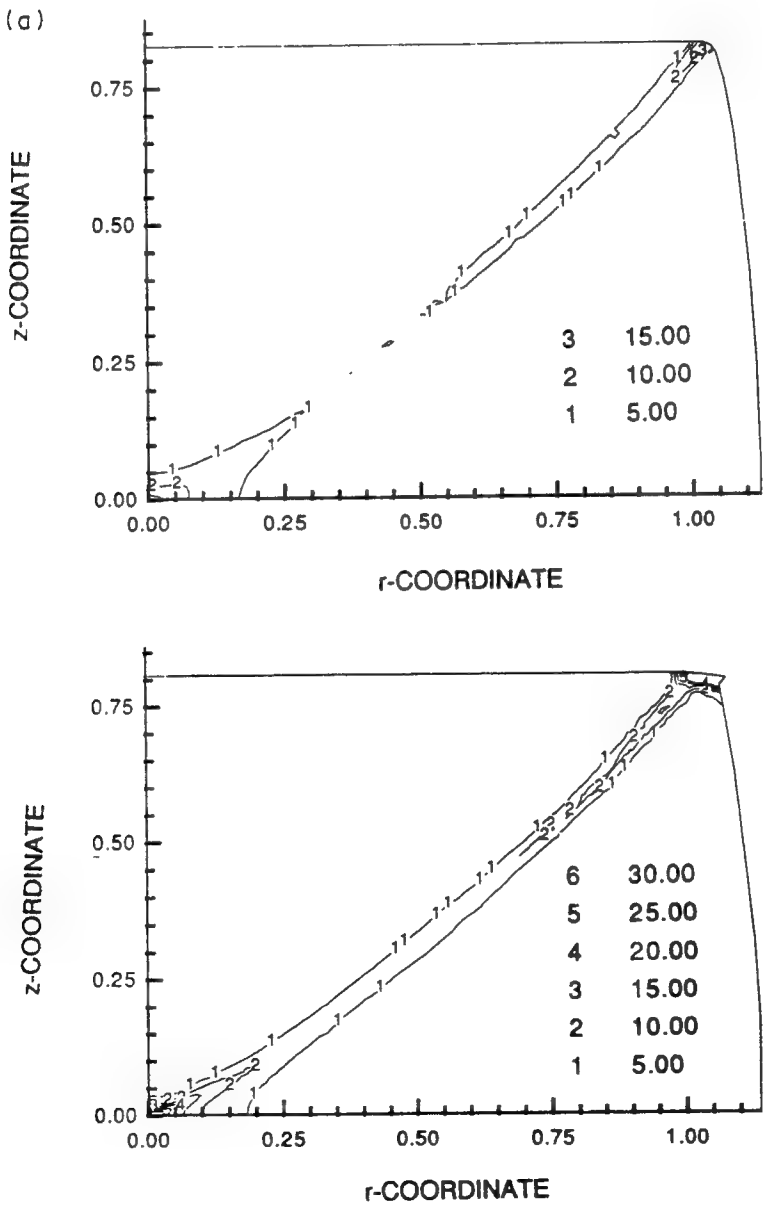

Fig. 5.—(*Caption overleaf*).

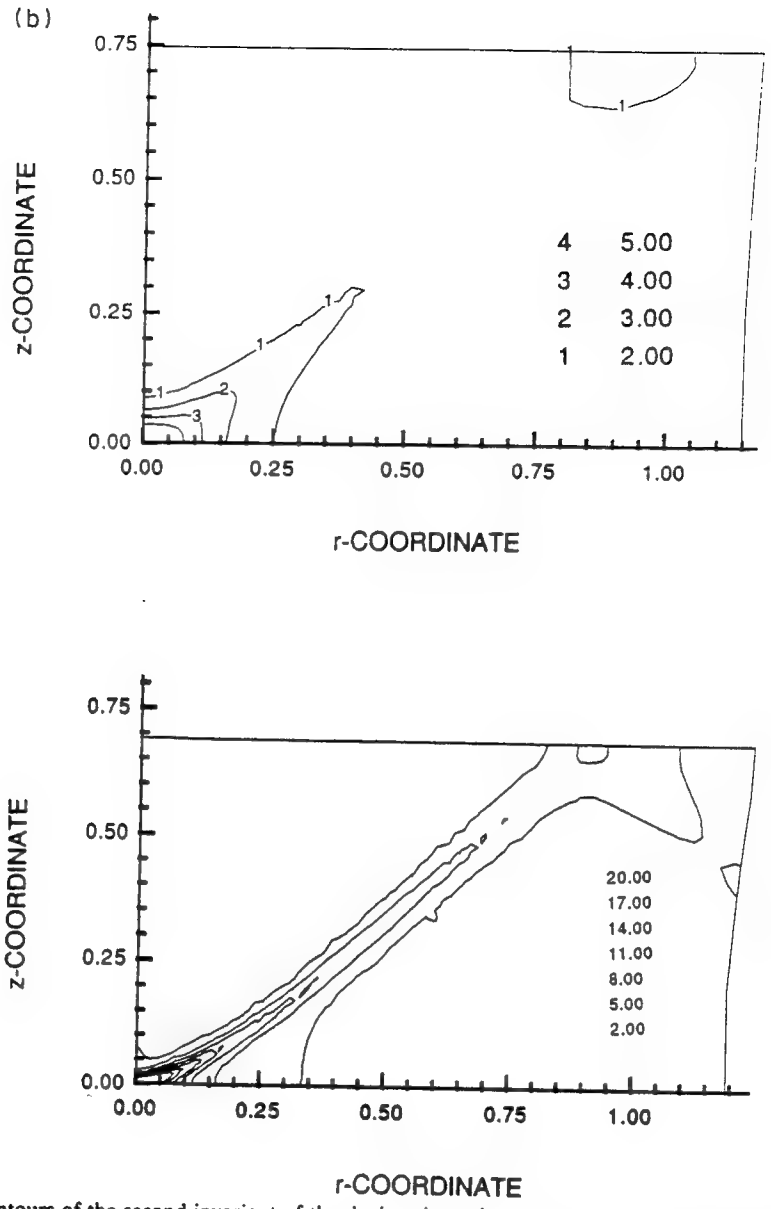

Fig. 5. Contours of the second invariant of the deviatoric strain-rate tensor at two different times: (a) no slipping—$t = 0.180$, 0.197; (b) smooth contact—$t = 0.260$, 0.315.

The contours of the second invariant I of the deviatoric strain-rate tensor at two different times are plotted in Fig. 5(a) for the case of no sliding between the cylinder ends and the loading device, and in Fig. 5(b) for the case of smooth contact. In each case the contours of increasingly higher values of I originate at points where the deformation localizes first and propagate outward. By estimating the distance through which the ends of the contour have diffused out and the time taken to do so, we determine the speed of propagation of the contour of $I = 10$ to be 216 m/s for the one originating at the center and 389 m/s for that initiating at the top right corner. However, when the cylinder ends are taken to be smooth, the contour of $I = 10$ propagates at 313 m/s. We note that Marchand and Duffy [2] estimated the tentative speed of a shear band to be either 255 or 510 m/s depending upon whether or not it propagated in both directions around the specimen circumference. The rather good match between the computed speeds and those given by Marchand and Duffy, while gratifying, is really illusive since the speed of propagation of the shear band depends upon the state of deformation within and around it. We have not established any such correlation between the

computed deformation field and that observed experimentally. We should study a 3-dimensional problem in order to accomplish this.

Figure 6 exhibits contours of temperature at two different times for the two cases studied herein. For the case of sticking surfaces, the temperature at the top right corner is comparable to that at the cylinder center, even though the initial temperature at the center is considerably higher that that at the top right corner. It suggests that the deformations of the region near the top right corner are more intense than those of the material near the center of the cylinder.

The distribution at different times of the second invariant I of the deviatoric strain-rate tensor at points on the horizontal centroidal axis is depicted in Fig. 7. It is clear that the severely deforming region adjoining the centroid of the cylinder becomes narrower as the cylinder continues to be compressed. That the intense deformations are confined to a somewhat narrow band is evidenced by the plots, given in Fig. 8, of the normalized effective stress, temperature, and the second invariant I of the deviatoric strain-rate tensor, at the final time considered, on lines AB and CD perpendicular to the estimated centerline of the shear

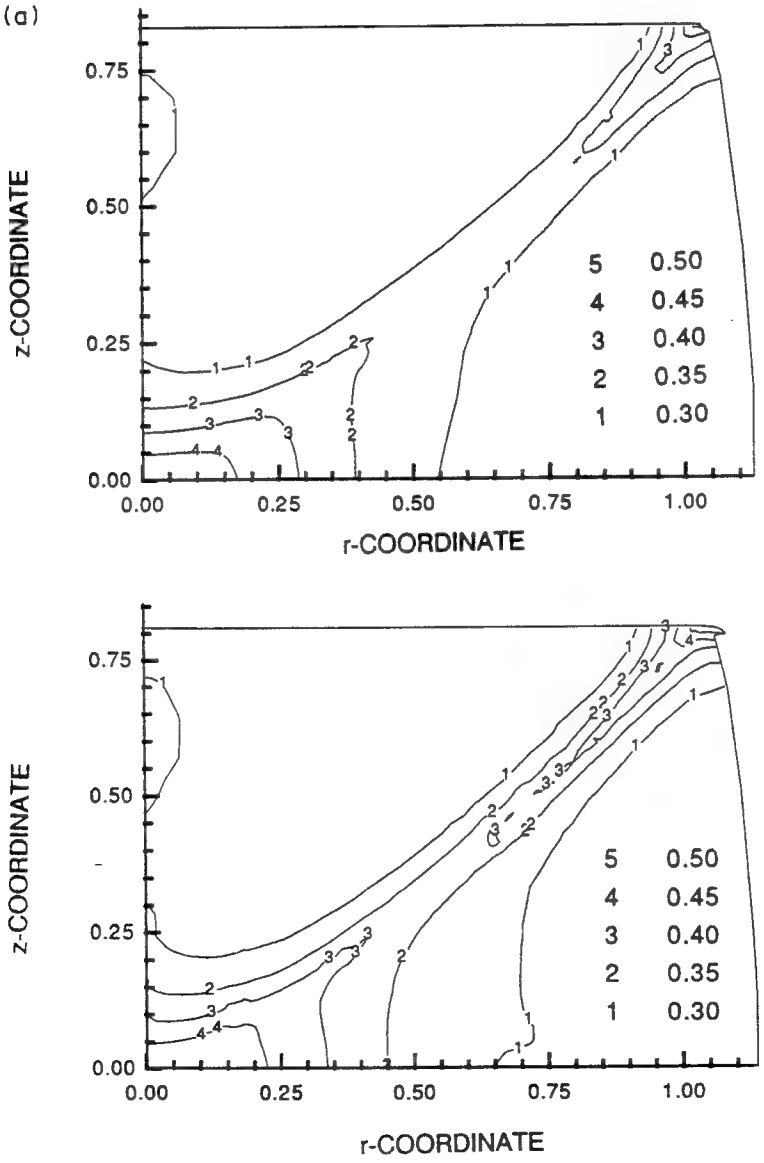

Fig. 6.—(*Caption overleaf*).

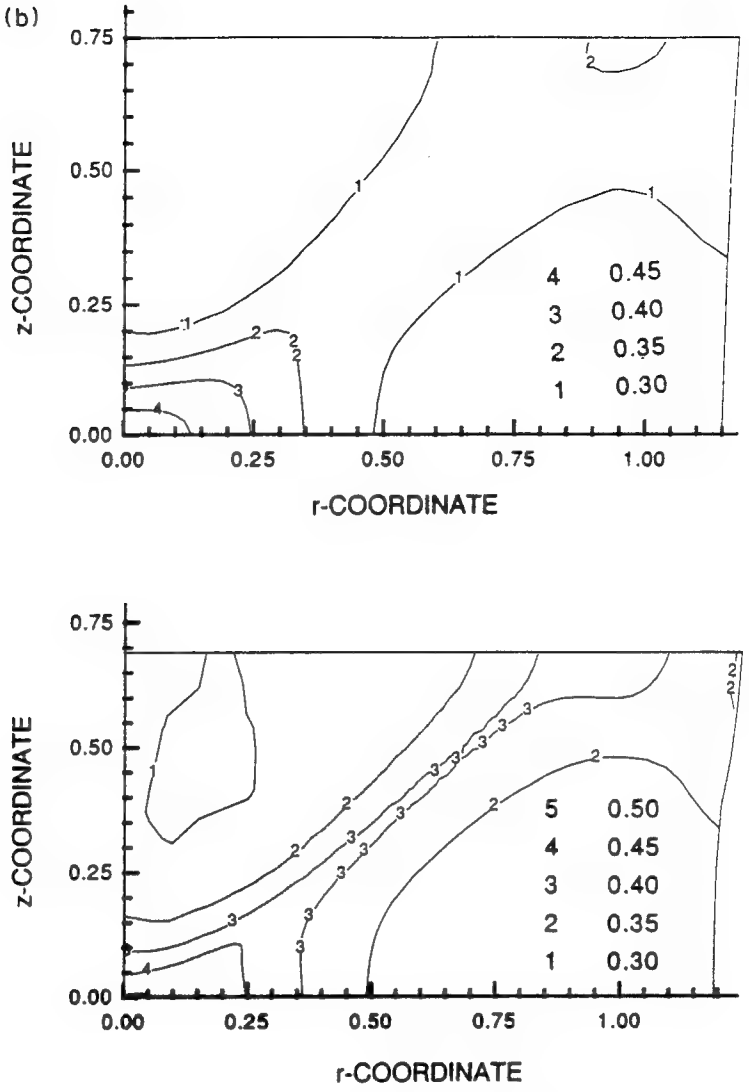

Fig. 6. Contours of the temperature at two different times: (a) no slipping—$t = 0.180$, 0.197; (b) smooth contact—$t = 0.260$, 0.315.

band. A quantity is normalized with respect to its peak value at points on AB or CD, and the abscissa equals the distance of a point from A or C. The centerline of the shear band was determined from the contours of the second invariant I of the deviatoric strain-rate tensor, and was assumed to be made up of two line segments for the case of smooth contacting surfaces, and three line segments when the contact surfaces are rough. These lines are shown in the insert in Fig. 8. Note that the centerline of the band changes with time, which inhibits depicting results using 3-dimensional graphics. The plots in Fig. 8 suggest that a narrow region around the points of intersection of lines AB and CD with the centerline of the band, undergoes intense deformations. The nondimensional effective stress, s_e, is defined as

$$s_e = \left(\frac{1}{2}\mathrm{tr}(\mathbf{ss}^T)\right)^{1/2} = \frac{1}{\sqrt{3}}(1 + bI)^m(1 - \nu\theta). \tag{16}$$

Its lower values at points close to the centerline of the band indicate that thermal softening there exceeds the strain-rate hardening.

The variation of the normalized values of the second invariant of the deviatoric strain-rate tensor, effective stress, and the temperature along the estimated centerline of the band, shown in Fig. 9, indicates that only a narrow region near the center of the cylinder is undergoing

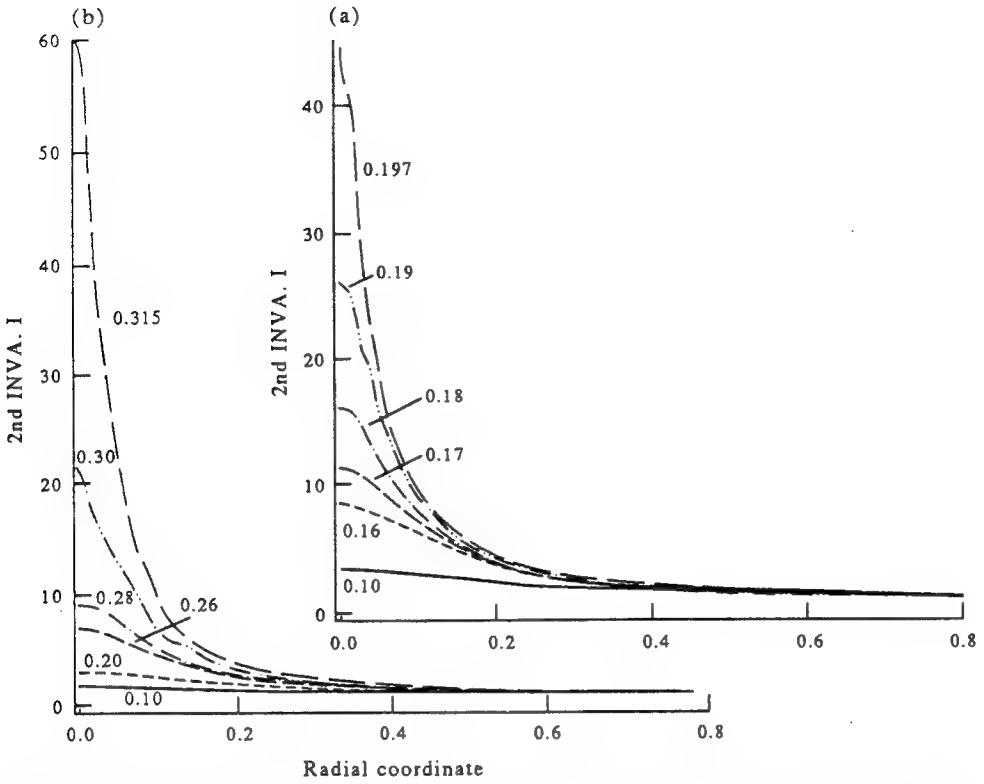

Fig. 7. Variation of the second invariant of the deviatoric strain-rate tensor on the centroidal axis at different times; the time is indicated on the curves: (a) no slipping; (b) smooth contact.

intense deformations. When frictional forces are accounted for, the material near the top right corner is also deforming severely. In this case, the second invariant of the deviatoric strain-rate tensor is higher near the top right corner than that at the cylinder centroid. We note that as the cylinder is compressed different material particles on the mantle of the cylinder contact the loading surface; thus, a new material particle is situated at the top right corner as time varies. Since the temperature rise at a point is a measure of the total energy dissipated there, less energy has been dissipated at points on the centerline of the band that are away from the corners. We stopped the computations as soon as a material point melted. Even though the material there failed, the surrounding material provides strength to the structure and the cylinder can still be compressed further. However, in view of the limited computational resources available to us, this was not attempted.

Figure 10 exhibits the variation with average strain of the average normal traction f_n and the average tangential traction f_t acting on the top surface. These are defined as

$$f_n = -\frac{1}{r_0^2}\int_0^{r_0} \sigma_{zz}(r, \bar{z})r\,dr, \qquad f_t = \frac{1}{r_0^2}\int_0^{r_0} \sigma_{rz}(r, \bar{z})r\,dr, \tag{17}$$

where r_0 is the radius of the cylinder in the deformed configuration. For the case of smooth surfaces f_n decreases gradually, but for the frictional case the transients seem to persist during the entire duration of the simulation. We note that the integrands in equation (17) are evaluated at points on the top surface for which $z = \bar{z}$, and the abscissa in Fig. 10 is proportional to the vertical displacement of the top surface. For the case of rough surfaces, the temperature of material particles adjoining the top surface rises noticeably soon after the load is applied, thus making the material there softer and easier to deform. This accounts for the sharp decrease in the average normal traction required to compress the cylinder at the prescribed rate. Because of the increase in the value of r_0 with time, the variation of the

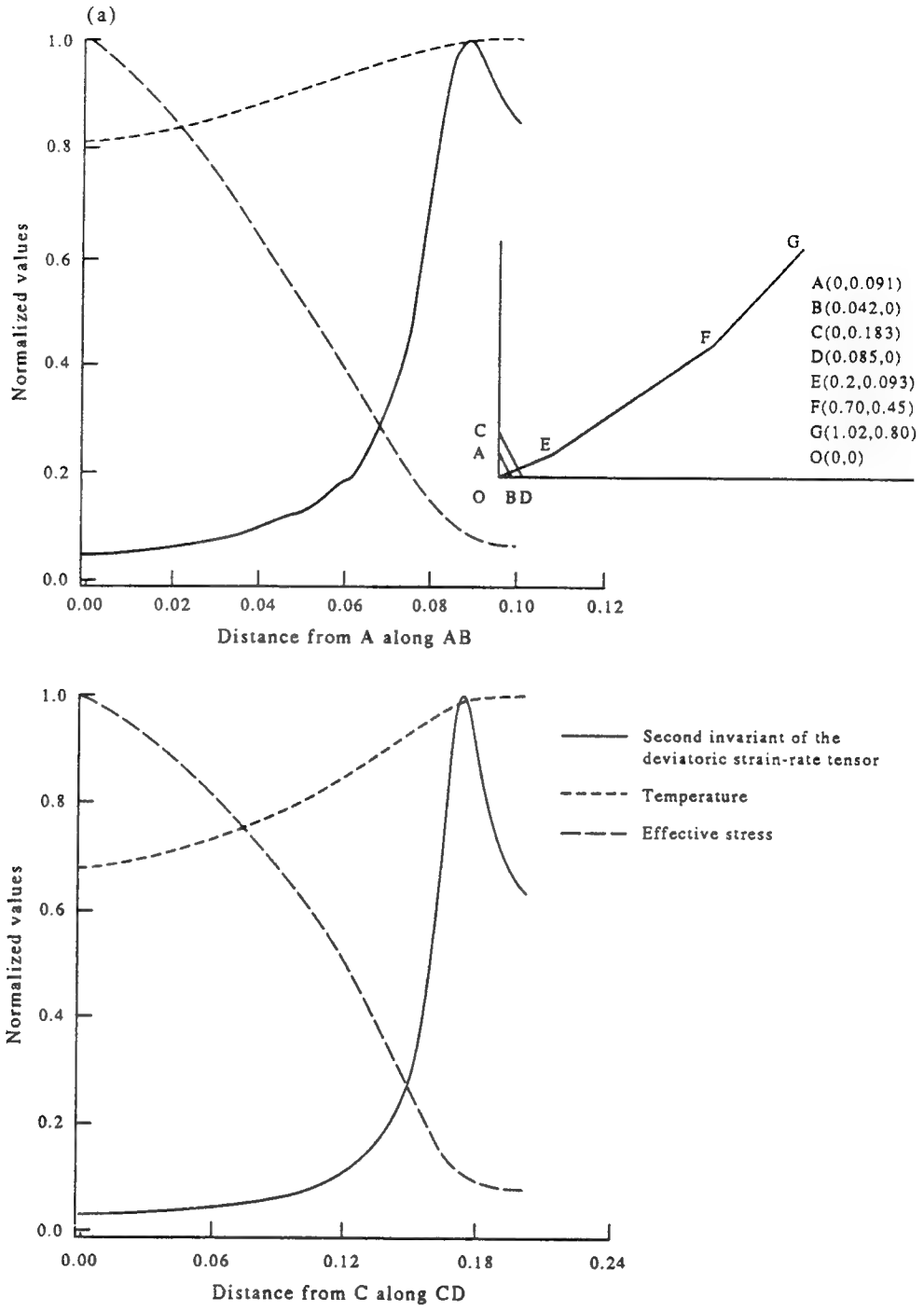

Fig. 8.—(*Caption overleaf*).

total load acting on the top surface with time will be different from that of f_n. It is interesting to see that the average tangential traction on the top cylinder end exceeds the average normal traction there and the two are out of phase with each other, implying thereby that f_t is not proportional to f_n. For the body deformed in plane strain compression, the average normal traction on the top surface is a little less than that for the same body undergoing axisymmetric deformations.

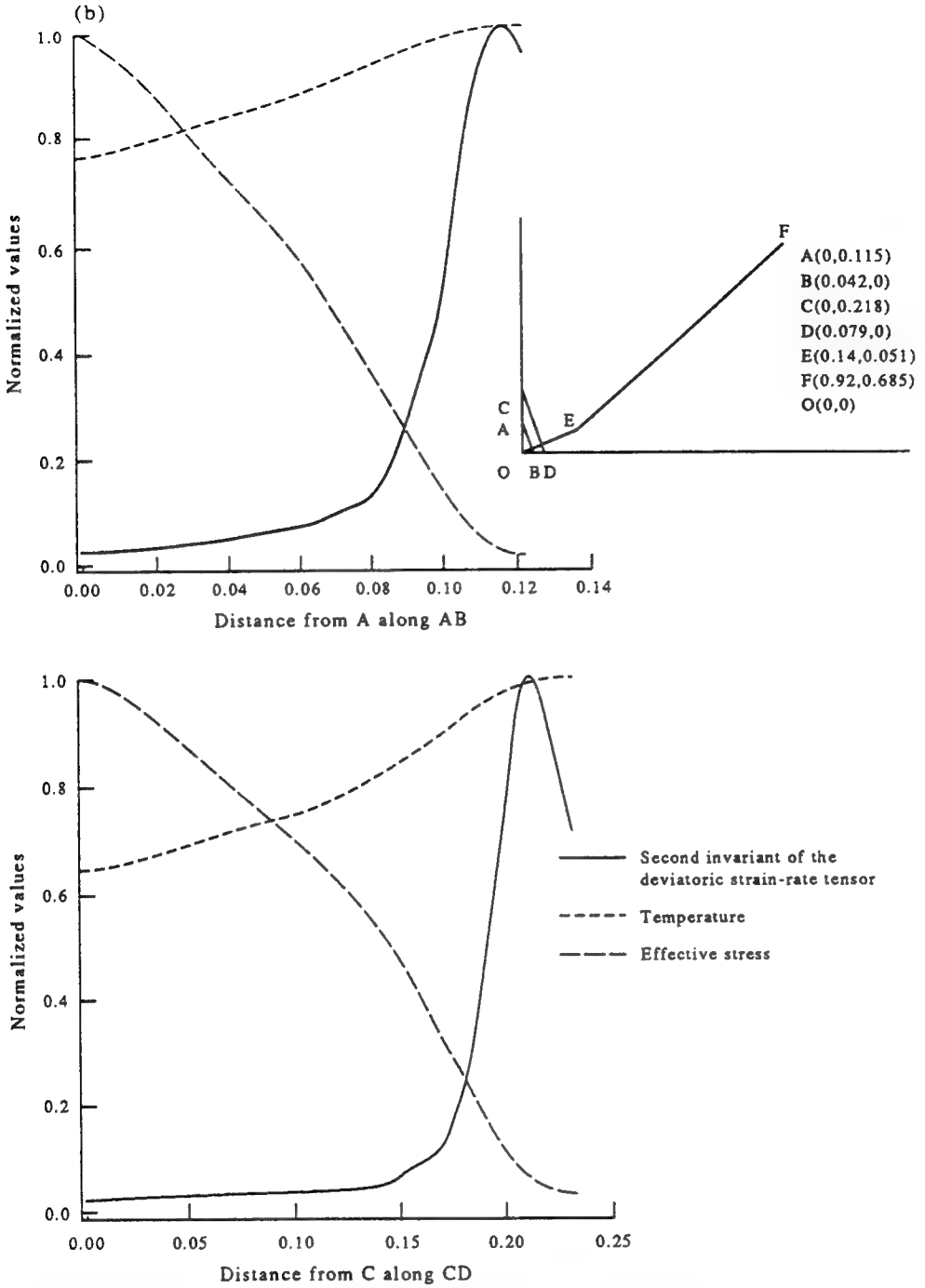

Fig. 8. Variations, at the final time considered, of the normalized effective stress, temperature, and the deviatoric strain-rate tensor on two lines perpendicular to the estimated centerline of the shear band: (a) no slipping; (b) smooth contact.

5. CONCLUSIONS

We have studied the initiation and growth of shear bands in a thermally softening viscoplastic cylindrical body compressed at a nominal strain-rate of $5000\,s^{-1}$. It is presumed that its deformations stay axisymmetric even after a shear band has formed. The loading device can either slide freely on the cylinder end, or does not slide at all. A shear band forms sooner when frictional effects are considered than when they are not. Also, a comparison of the presently computed results with those for the same body deformed in plane strain compression reveals

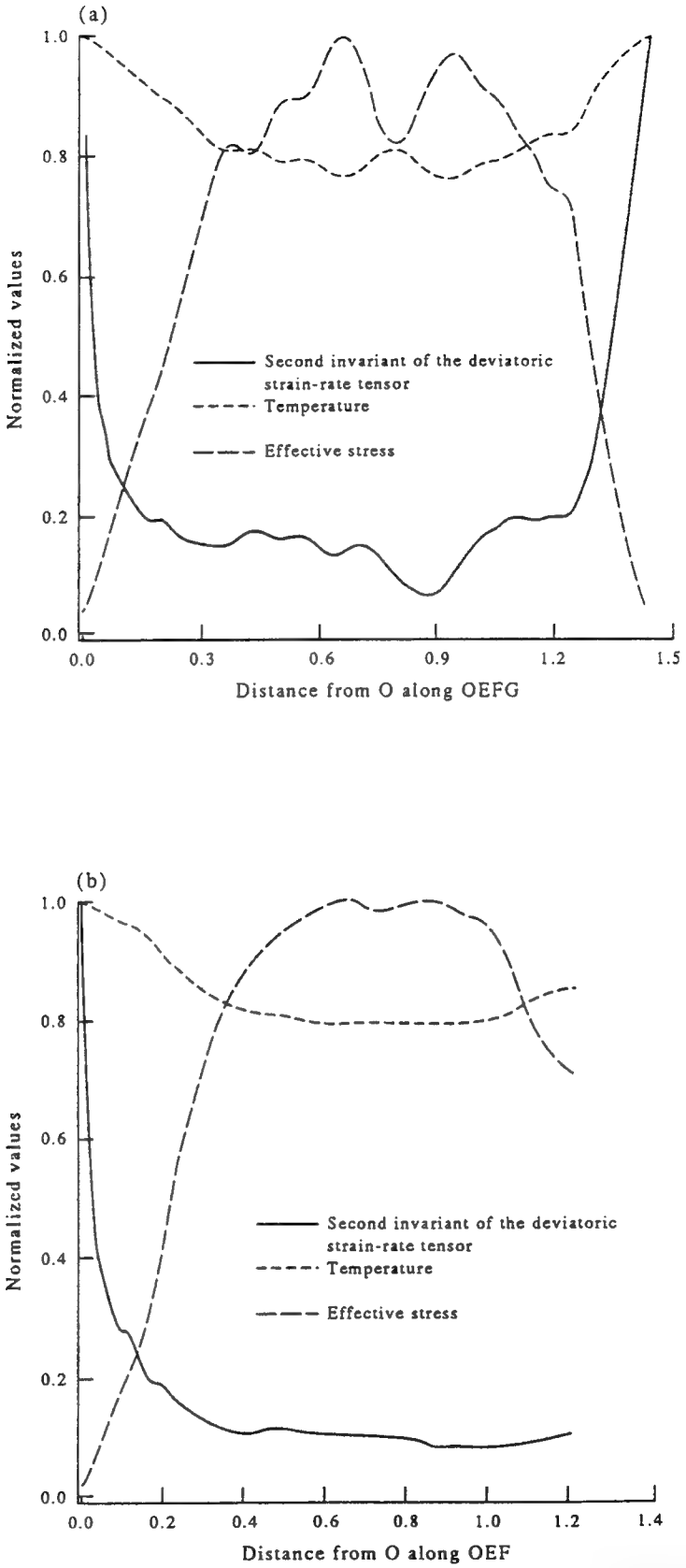

Fig. 9. Variation, at the final time considered, of the normalized effective stress, temperature, and the deviatoric strain-rate tensor on the estimated centerline of the shear band: (a) no slipping; (b) smooth contact.

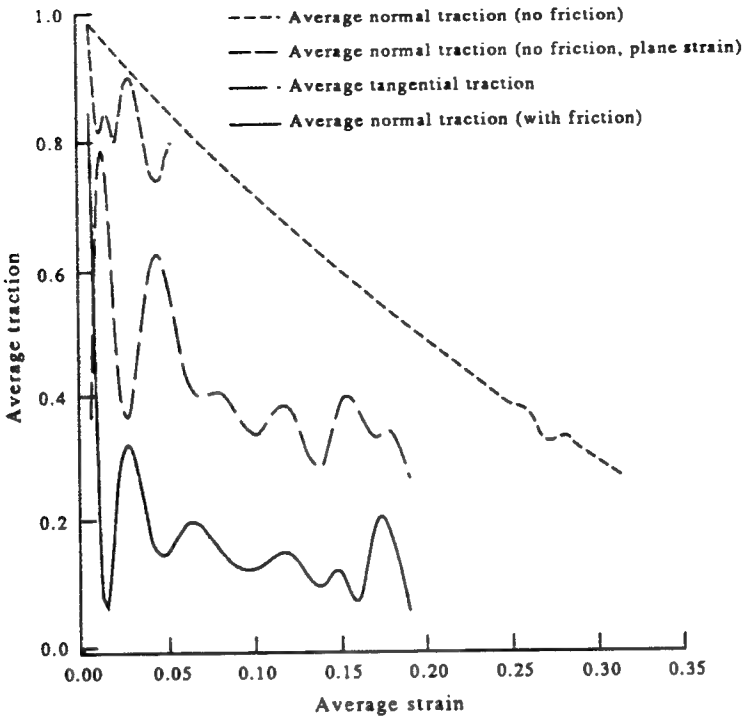

Fig. 10. Variation with time of the average normal and tangential tractions acting on the cylinder ends.

that the initiation of a shear band is significantly delayed in the body undergoing axisymmetric deformations. For the case of no slipping, the strain-rate at the top right corner also increases significantly, and it equals or exceeds that at the center of the cylinder. The deformed shape of the cylinder looks like a barrel when the loading surface is assumed to be glued to the cylinder end, and like a reversed barrel when the surfaces can slide freely over each other. This agrees qualitatively with the experimental findings. The average tangential traction required to prevent sliding of the loading surface over the cylinder end exceeds the average normal traction there, and the two are out of phase with each other.

Acknowledgements—This work was supported by the U.S. Army Research Office grant DAAL03-91-G-0084 and the U.S. NSF grant MSS9121279 to the University of Missouri-Rolla. Some of the computations were performed on the NSF sponsored supercomputer center in Ithaca, New York.

REFERENCES

[1] C. ZENER and J. H. HOLLOMON, *J. Appl. Phys.* **14,** 22 (1944).
[2] A. MARCHAND and J. DUFFY, *J. Mech. Phys. Solids* **36,** 251 (1988).
[3] J. H. GIOVANOLA, *Mech. Mater.* **7,** 73 (1988).
[4] T. W. WRIGHT and J. W. WALTER, *J. Mech. Phys. Solids* **35,** 701 (1987).
[5] R. C. BATRA and C. H. KIM, *J. Mech. Phys. Solids* **38,** 859 (1990).
[6] R. C. BATRA, *Int. J. Plasticity* **3,** 75 (1987).
[7] M. E. BACKMAN and S. A. FINNEGAN, The propagation of adiabatic shear. In *Metallurgical Effects at High Strain-Rates* (Edited by R. W. RHODE *et al.*), pp. 531–543. Plenum Press, New York (1973).
[8] G. L. WULF, *Int. J. Mech. Sci.* **20,** 609 (1978).
[9] J. LITONSKI, *Bull. Acad. Poloinaise Sci.* **25,** 7 (1977).
[10] R. C. BATRA, *Comput. Mech.* **3,** 1 (1988).
[11] R. C. BATRA and R. JAYACHANDRAN, *Int. J. Impact Engng.* **12,** 209 (1992).
[12] S. R. BODNER and Y. PARTOM, *J. Appl. Mech.* **42,** 385 (1975).
[13] S. B. BROWN, K. H. KIM and L. ANAND, *Int. J. Plasticity* **5,** 95 (1989).
[14] J. F. BELL, *Physics of Large Deformation of Crystalline Solids*. Springer, New York (1968).
[15] M. R. LIN and R. H. WAGONER, *Scripta Metall.* **20,** 143 (1986).

[16] U. S. LINDHOLM and G. R. JOHNSON, Strain-rate effects in metals at large strain rates. In *Material Behaviour Under High Stresses and Ultrahigh Loading Rates* (Edited by J. MESCAL and V. WEISS), pp. 61–79. Plenum Press, New York (1983).
[17] A. C. HINDMARSH, ODEPACK, a systematized collection of ODE solvers. In *Scientific Computing* (Edited by R. S. STEPLEMAN *et al.*), pp. 55–64. North–Holland, Amsterdam (1983).
[18] R. C. BATRA and K. I. KO, *Comput. Mech.* In press (1993).
[19] G. L. WULF, *Int. J. Mech. Sci.* **21,** 713 (1979).
[20] S. CESCOTTO and D. W. ZHOU, *Commun. Appl. Numer Meth.* **5,** 473 (1989).
[21] S. H. LO, *Int. J. Numer. Meth. Engng* **21,** 1403 (1985).
[22] J. PERAIRE, M. VAHDATI, K. MORGAN and O. C. ZIENKIEWICZ, *J. Comp. Phys.* **72,** 449 (1987).
[23] J. PERAIRE, J. PEIRO, L. FORMAGGIA, K. HORGAN and O. C. ZIENKIEWICZ, *Int. J. Numer. Meth. Engng* **26,** 2135 (1988).
[24] A. M. HABRAKEN and S. CESCOTTO, *Int. J. Numer. Meth. Engng* **30,** 1503 (1990).
[25] R. LÖHMER, *Commun. Appl. Meth.* **4,** 123 (1988).

APPENDIX

At the referee's suggestion, we describe below the adaptive mesh refinement technique; the material is taken from Ref. [18], wherein results, including error norms, for adaptively refined meshes for a plane strain problem are compared with those obtained with a fixed mesh.

We first select a coarse mesh and find a solution of the problem formulated in Section 2. This mesh is refined so that

$$a_e = \int_{\Omega_e} I \, d\Omega, \qquad e = 1, 2, \ldots, n_{e1}, \tag{A1}$$

is nearly the same for each element Ω_e. In (A1), n_{e1} equals the number of elements in the coarse mesh and Ω_e is one of the elements. Since one may not have an idea where the solution will exhibit sharp gradients, we choose the coarse mesh to be uniform. The motivation behind making a_e the same over each element Ω_e is that within the region of localization of the deformation values of I are very high as compared to those in the remaining region. Other variables such as the temperature rise, the maximum principal strain, and the equivalent strain which are also quite large within the band will be suitable replacements for I in equation (A1). The refined mesh will depend upon the variable used in equation (A1). In order to refine the mesh, we find

$$\bar{a} = \frac{1}{n_{e1}} \sum_{e=1}^{n_{e1}} a_e, \tag{A2}$$

$$\xi_e = \frac{a_e}{\bar{a}}, \tag{A3}$$

$$h_e = \frac{\bar{h}_e}{\xi_e}, \tag{A4}$$

and

$$H_n = \frac{1}{N_e} \sum_{e=1}^{N_e} h_e, \qquad n = 1, 2, \ldots, n_{od}. \tag{A5}$$

Here, $\bar{h}_e$ is the size of the element Ω_e in the coarse mesh, N_e equals the number of elements meeting at node n, and n_{od} equals the number of nodes in the coarse mesh. We refer to H_n as the nodal element size at node n.

In order to generate the new mesh, we first discretize the boundary by following the procedure given by Cescotto and Zhou [20]. Let AB be a segment of the contour to be discretized, s the arc length measured from point A, and H_A and H_B be nodal element sizes for nodes located at points A and B, respectively. From a knowledge of the values of H at discrete points, corresponding to the nodes in the coarse mesh, on AB we define a piecewise linear continuous function $H(s)$ that takes the previously computed values at the node points. In order to discretize AB for the new mesh, we start from point A, if $H_A < H_B$; otherwise we start from B. For the sake of discussion, let us assume that A is the starting point. We first find temporary positions of nodes on the segment AB by using the following recursive procedure. Assume that points $1, 2, \ldots, k$ have been found. Then the temporary location of point $(k+1)$ is given by

$$s_{k+1} = s_k + \frac{1}{2}[H(s_k) + H(s^*_{k+1})], \tag{A6}$$

where

$$s^*_{k+1} = s_k + H(s_k). \tag{A7}$$

Referring to Fig. A1, the above procedure will give rise to the following four alternatives: $a = b = 0$, $a < b$, $a > b$, $a = b \neq 0$. If $a = b = 0$, then the temporary locations of node points are their final positions. Depending upon whether

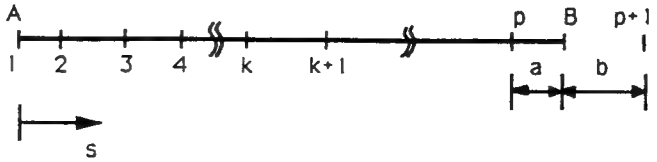

Fig. A1. Discretization of a boundary segment for mesh refinement.

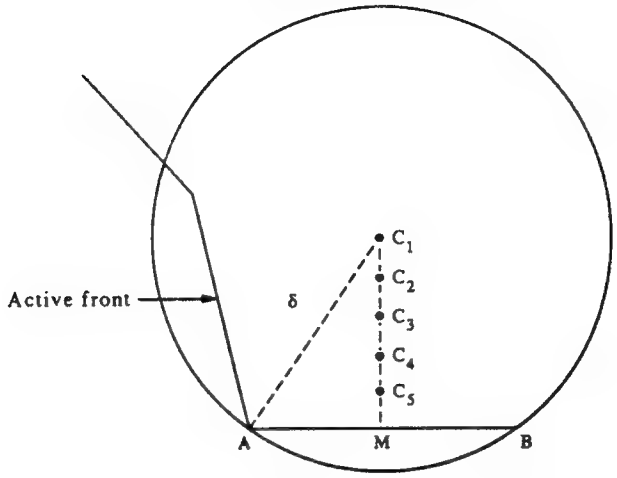

Fig. A2. Advancing front and new element generation.

$a < b$ or $b \le a$, the node points 2 to p or 2 to $p+1$ are moved, the displacement of a node being proportional to the value of H there, so that either node p or node $(p+1)$ coincides with B. This determines the final positions of nodes on the segment AB.

Having discretized the boundary, we use the concept of advancing front (e.g. see Lo [21], Peraire *et al.* [22, 23], and Habraken and Cescotto [24]) to generate the elements. An advancing front consists of straight line segments which are available to form a side of an element. Thus, to start with, it consists of the discretized boundary. We choose the smallest line segment (say side AB) connecting the two adjoining nodes, and determine the nodal element size $H_M \equiv H(s_M) = (H_A + B_B)/2$ at the midpoint M of AB. We set

$$\delta = \begin{cases} 0.8\overline{AB} & \text{if } H_M < 0.8\overline{AB}, \\ H_M & \text{if } 0.8\overline{AB} \le H_M \le 1.4\overline{AB}, \\ 1.4\overline{AB} & \text{if } 1.4\overline{AB} < H_M, \end{cases} \tag{A8}$$

and find point C_1 at a distince δ from A and B (cf. Fig. A2). Here $\overline{AB}$ equals the length of segment AB. We search for all nodes on the active front that lie inside the circle with center at C_1 and radius δ, and order them according to their distance from C_1 with the first node in the list being closest to C_1. At the end of this list are added points C_1, C_2, C_3, C_4, and C_5, which lie on C_1M and divide it into five equal parts. We next determine the first point C in the list that satisfies the following three conditions.

(i) Area of triangle $ABC > 0$.

(ii) Sides AC and BC do not cut any of the existing sides in the front.

(iii) If any of the points $C_1, C_2, \ldots, C_5$ is chosen, that point is not too close to the front. The triangle ABC is an element in the new mesh. If C is one of the points $C_1, C_2, \ldots, C_5$, then a new node is also created. The advancing front is updated by removing the line segment AB from it, and adding line segments AC and CB to it. The element generation process ceases when there is no side left in the active front.

We determine the values of solution variables at a newly created node by first finding out to which element in the coarse mesh this node belongs, and then finding values of solution variables at this node by interpolation. This process and that of searching for line segments and points in the aforestated element generation technique consume a considerable amount of CPU time. These operations are optimized to some extent by using the heap list algorithm (e.g. see Löhmer [25]) for deleting and inserting new line segments, and quadtree structures and linked lists for searching line segments and points and also for the interpolation of solution variables at the newly created nodes.

(Revision received 3 May 1992; accepted 7 July 1992)

International Journal of Plasticity, Vol. 9, pp. 653–696, 1993
Printed in the USA

0749-6419/93 $6.00 + .00

ANALYSIS OF DYNAMIC SHEAR BANDS IN AN FCC SINGLE CRYSTAL

Z.G. ZHU and R.C. BATRA

University of Missouri–Rolla

Abstract—We study plane strain dynamic thermomechanical deformations of an fcc single crystal compressed along the crystallographic direction [010] at an average strain rate of 1000 sec^{-1}. Two cases are studied; one in which the plane of deformation is parallel to the plane (001) of the single crystal, and another one with deformation occurring in the plane $(10\bar{1})$ of the single crystal. In each case, the 12 slip systems are aligned symmetrically about the two centroidal axes. We assume that the elastic and plastic deformations of the crystal are symmetrical about these two axes. The crystal material is presumed to exhibit strain hardening, strain-rate hardening, and thermal softening. A simple combined isotropic–kinematic hardening expression for the critical resolved shear stress, proposed by Weng, is modified to account for the affine thermal softening of the material. When the deformation is in the plane (001) of the single crystal, four slip systems $(111)[1\bar{1}0]$, $(11\bar{1})[1\bar{1}0]$, $(1\bar{1}\bar{1})[110]$, and $(1\bar{1}1)[110]$ are active in the sense that significant plastic deformations occur along these slip systems. However, when the plane of deformation is parallel to the plane $(10\bar{1})$ of the single crystal, slip systems $(1\bar{1}1)[110]$, $(1\bar{1}1)[011]$, $(111)[1\bar{1}0]$, and $(111)[0\bar{1}1]$ are more active than the other eight slip systems. At an average strain of 0.108, the maximum angle of rotation of a slip system within a shear band, about an axis perpendicular to the plane of deformation, is found to be 20.3° in the former case, and 22.9° in the latter.

I. INTRODUCTION

One way to understand the micromechanics of shear band formation in polycrystalline materials is to study their initiation and growth in a single crystal. Several investigators, e.g. SAWKILL and HONEYCOMBE [1954], PRICE and KELLY [1964], SAIMOTO *et al.* [1965], and CHANG and ASARO [1981], have observed regions of localized shearing in fcc single crystals deformed quasistatically. ZIKRY and NEMAT-NASSER [1990] have recently studied numerically the phenomenon of shear banding in an fcc single crystal undergoing plane-strain tensile deformations at high strain rates. We refer the reader to their article for a list of references and a brief outline of the historical development of the subject. They used the double cross-slip model proposed by KOEHLER [1952] and later by OROWAN [1954] during the entire loading history. Here we study a similar problem with the crystal deformed in compression rather then tension, assume that all 12 slip systems are potentially active at any instant of loading, use constitutive relation for the critical shear stress that is different from the one employed by ZIKRY and NEMAT-NASSER [1990], employ a different technique to integrate the system of equations, and consider two loadings. With the axis of compression aligned along the crystallographic direction [010], the plane of deformation is taken to be either parallel to the plane (001) or $(10\bar{1})$ of the single crystal.

When the plane of deformation is parallel to the plane (001) of the single crystal, a single shear band making an angle of 45° with the horizontal line ensues from the centroid of the cross-section and is reflected back from the top loading surface, the angle of reflection being essentially equal to the angle of incidence. The slip strains on the slip systems $(111)[1\bar{1}0]$, $(11\bar{1})[1\bar{1}0]$, $(1\bar{1}\bar{1})[110]$, and $(1\bar{1}1)[110]$ are high, and these constitute

the primary slip systems. At a nominal strain of 0.108, the maximum angle of rotation of the crystal lattice in the central and reflected bands equal 18.54° counterclockwise and 20.29° clockwise, respectively. When the plane of deformation is parallel to the plane $(10\bar{1})$ of the single crystal, the shear band originating from the center of the cross-section makes an angle of 39.5° with the horizontal, and eventually splits into two bands. Slip systems $(111)[1\bar{1}0]$ and $(111)[0\bar{1}1]$ in both the central and the reflected bands, and slip systems $(1\bar{1}1)[110]$ and $(1\bar{1}1)[011]$ in the reflected band are found to be more active than other slip systems.

II. FORMULATION OF THE PROBLEM

We use a set of fixed rectangular Cartesian coordinates to describe the thermomechanical deformations of an fcc single crystal of square cross-section and compressed along the crystallographic direction [010] which is taken to coincide with the x_3-axis. We assume that the x_1–x_2 plane of deformation is either parallel to the plane (001) or $(10\bar{1})$ of the single crystal. In each case, the 12 slip systems are aligned symmetrically about the two centroidal axes. We presume that both elastic and plastic deformations of the single crystal are symmetric about the two centroidal axes, even after the band has formed, and accordingly study deformations of the material in the first quadrant only. In Eulerian description, equations governing the deformations of the single crystal are:

The balance of mass:

$$\dot{\rho} + \rho v_{i,i} = 0, \tag{1}$$

The balance of linear momentum:

$$\rho \dot{v}_i = \sigma_{ij,j}, \tag{2}$$

The balance of internal energy:

$$\rho c \dot{\theta} = -q_{i,i} + \sigma_{ij} D^p_{ij}, \tag{3}$$

where ρ is the present mass density, v_i the velocity of a material particle, a comma followed by i indicates partial differentiation with respect to the present position x_i of a material particle, σ_{ij} is the Cauchy stress tensor, a superimposed dot indicates the material time derivative, a repeated index implies summation over the range of the index, c is the constant specific heat, θ the temperature rise, q_i the heat flux per unit deformed area, and D^p_{ij} is the plastic part of the strain-rate tensor D_{ij}, defined as

$$D_{ij} = \tfrac{1}{2}(v_{i,j} + v_{j,i}). \tag{4}$$

D^p_{ij} is determined by the local plastic slip rate of all active slip systems at a material particle, and will be defined later. For plane strain deformations in the x_1–x_2 plane, various quantities are functions of x_1, x_2 and time t, and subscripts i, j range over 1 and 2. However, in the second term on the right-hand side of eqn (3), indices i and j extend to 3, since in plane strain deformations $\sigma_{33} \neq 0$ in general, and D^p_{33} need not equal zero during the plastic deformation. In eqn (3) we have assumed that all of the plastic working is converted into heating.

We now describe the constitutive relations for high strain-rate finite deformations of rate-dependent single crystals. We postulate Fourier's law of heat conduction, *viz.*

$$q_i = -k\theta_{,i}, \tag{5}$$

where k is the thermal conductivity, and is assumed to be independent of the deformation and temperature of the single crystal. We assume that the strain-rate tensor D_{ij} and the spin tensor W_{ij} defined as

$$W_{ij} = \tfrac{1}{2}(v_{i,j} - v_{j,i}) \tag{6}$$

have additive decompositions into elastic and plastic parts, *viz.*

$$D_{ij} = D^e_{ij} + D^p_{ij}, \qquad W_{ij} = W^e_{ij} + W^p_{ij}. \tag{7}$$

The Cauchy stress rate corotational with the elastic distortion of the single crystal is assumed to be related to the elastic distortion rate by Hooke's law. That is,

$$\mathring{\sigma}^e_{ij} = L_{ijkl} D^e_{kl}, \tag{8}$$

where

$$\mathring{\sigma}^e_{ij} = \dot{\sigma}_{ij} + \sigma_{ik} W^e_{kj} - W^e_{ik}\sigma_{kj}, \tag{9}$$

and L_{ijkl} is the fourth order tensor of the elasticities of the single crystal. Here we take the crystal lattice to be elastically isotropic. Thus,

$$L_{ijkl} = \lambda\delta_{ij}\delta_{kl} + \mu(\delta_{ik}\delta_{jl} + \delta_{il}\delta_{jk}),$$

where λ and μ are Lamé's constants for the crystal material. Recall that the Jaumann stress rate $\mathring{\sigma}_{ij}$ given by

$$\mathring{\sigma}_{ij} = \dot{\sigma}_{ij} + \sigma_{ik} W_{kj} - W_{ik}\sigma_{kj}, \tag{10}$$

is corotational with the material element. Equations (7), (8), (9), and (10) result in

$$\mathring{\sigma}_{ij} = L_{ijkl}(D_{kl} - D^p_{kl}) + \sigma_{ik} W^p_{kj} - W^p_{ik}\sigma_{kj}. \tag{11}$$

The Schmid stress or the resolved shear stress $\overset{(\alpha)}{\tau}$ of the αth slip system is assumed to be related to the local Cauchy stress σ_{ij} through

$$\overset{(\alpha)}{\tau} = \overset{(\alpha)}{\nu}_{ij}\sigma_{ij}, \tag{12}$$

where the Schmid factor $\overset{(\alpha)}{\nu}_{ij}$ is defined as

$$\overset{(\alpha)}{\nu}_{ij} = \tfrac{1}{2}\left(\overset{(\alpha)}{b}_i \overset{(\alpha)}{n}_j + \overset{(\alpha)}{b}_j \overset{(\alpha)}{n}_i\right), \tag{13}$$

$\overset{(\alpha)}{\mathbf{b}}$ and $\overset{(\alpha)}{\mathbf{n}}$ being the unit slip direction and the unit normal to the slip-plane of the αth slip system.

For a strain rate-dependent material of the single crystal, the slip rate of the αth slip system is assumed to be related to the resolved shear stress by the power law.

$$\overset{(\alpha)}{\dot{\gamma}}{}^{p} = \begin{cases} \overset{(\alpha)}{\dot{\gamma}_0}\left[\dfrac{\overset{(\alpha)}{\tau}}{\overset{(\alpha)}{\tau_c}}\right]\left[\dfrac{|\overset{(\alpha)}{\tau}|}{\overset{(\alpha)}{\tau_c}}\right]^{1/m-1}, & \overset{(\alpha)}{\tau} \geq \overset{(\alpha)}{\tau_c}, \quad (14a) \\ 0, & \overset{(\alpha)}{\tau} < \overset{(\alpha)}{\tau_c}, \quad (14b) \end{cases}$$

where m is the rate sensitivity parameter, and $\overset{(\alpha)}{\dot{\gamma}_0}$ is a reference shear strain rate such that if the crystal is to be deformed with each $\overset{(\alpha)}{\dot{\gamma}}{}^{p}$ set equal to $\overset{(\alpha)}{\dot{\gamma}_0}$, then $\overset{(\alpha)}{\tau} = \overset{(\alpha)}{\tau_c}$ (PAN & RICE [1983]). When the resolved shear stress of the αth slip system is below the critical resolved shear stress $\overset{(\alpha)}{\tau_c}$ required to cause plastic deformation on that slip system, the αth slip system is taken to be inactive. The critical resolved shear stress is assumed to be a function of the initial flow stress τ_0, work hardening, and the temperature θ. A simple combined isotropic–kinematic hardening expression for τ_c, proposed by WENG [1980], is modified as follows

$$\overset{(\alpha)}{\tau_c} = \left\{\tau_0 + \sum_{\beta}\left[g + (1-g)\cos\overset{(\alpha\beta)}{\psi}\cos\overset{(\alpha\beta)}{\phi}\right]h\left(\overset{(\beta)}{\gamma}{}^{p}\right)^{n}\right\}(1-\nu\theta) \quad (15)$$

to include thermal softening. In eqn (15), $\overset{(\alpha\beta)}{\psi}$ is the angle between the slip directions of the αth and βth slip systems, $\overset{(\alpha\beta)}{\phi}$ the angle between their slip normals, $\overset{(\beta)}{\gamma}{}^{p}$ the plastic strain of the βth slip system, h the strength coefficient, n the work hardening exponent, g the degree of isotropy in work hardening, and ν the thermal softening coefficient. The quantity in the square bracket represents the latent hardening coefficient, and the summation index β ranges over all slip systems. TAYLOR's [1938] isotropic hardening law follows from (15) by setting $g = 1$, and $g = 0$ corresponds to kinematic hardening.

We assume that the plastic slip rates $\overset{(\alpha)}{\dot{\gamma}}{}^{p}$ of all active slip systems at a material point contribute linearly to the plastic parts of the strain rate and spin tensors there through the Schmid factor $\overset{(\alpha)}{\nu_{ij}}$ and the antisymmetric part $\overset{(\alpha)}{\omega_{ij}}$ of the dyad **bn**. Thus,

$$D^{p}_{ij} = \sum_{\alpha}\overset{(\alpha)}{\nu_{ij}}\overset{(\alpha)}{\dot{\gamma}}{}^{p}, \qquad W^{p}_{ij} = \sum_{\alpha}\overset{(\alpha)}{\omega_{ij}}\overset{(\alpha)}{\dot{\gamma}}{}^{p}, \quad (16)$$

where

$$\overset{(\alpha)}{\omega_{ij}} = \tfrac{1}{2}\left(\overset{(\alpha)}{b_i}\overset{(\alpha)}{n_j} - \overset{(\alpha)}{b_j}\overset{(\alpha)}{n_i}\right). \quad (17)$$

The slip direction **b** and the unit normal **n** to the slip plane are orthogonal unit vectors, and are assumed to rotate with the elastic spin of the lattice. Thus, their rates of change are given by

$$\dot{b}_i = W^{e}_{ij}b_j, \qquad \dot{n}_i = W^{e}_{ij}n_j. \quad (18)$$

In plane strain deformations of the crystal, the rotation of a slip system can be characterized by the angle change ϕ of the projective direction of the slip vector in the x_1-x_2 plane. Using eqns $(7)_2$ and $(16)_2$ we obtain

$$\dot{\phi} = W_{21}^e = W_{21} - \sum_{\alpha} \overset{(\alpha)}{\omega}_{21} \overset{(\alpha)}{\dot{\gamma}}^p, \tag{19}$$

and rewrite eqns (18) in the form

$$b_1 = \sqrt{1 - b_3^2} \cos \phi_b, \qquad b_2 = \sqrt{1 - b_3^2} \sin \phi_b, \tag{20}$$

$$n_1 = \sqrt{1 - n_3^2} \cos \phi_n, \qquad n_2 = \sqrt{1 - n_3^2} \sin \phi_n, \tag{21}$$

where ϕ_b and ϕ_n are, respectively, the current angles between the x_1-axis and the projective directions of the slip vector and the slip plane normal to the x_1-x_2 plane. They equal the sum of their initial values and their changes with respect to the rotated lattice.

Scaling stress-like quantities by τ_0, mass density by ρ_0, length by H, time by H/v_0, and the temperature by θ_r, we rewrite the above equations in terms of nondimensional variables, and obtain the following.

$$\dot{\rho} + \rho v_{i,i} = 0, \tag{22}$$

$$\delta \rho \dot{v}_i = \sigma_{ij,j}, \tag{23}$$

$$\rho \dot{\theta} = \beta \theta_{,ii} + \sigma_{ij} \sum_{\alpha} \overset{(\alpha)}{\nu}_{ij} \overset{(\alpha)}{\dot{\gamma}}^p + \sigma_{33} \sum_{\alpha} \overset{(\alpha)}{\nu}_{33} \overset{(\alpha)}{\dot{\gamma}}^p, \tag{24}$$

$$\dot{\sigma}_{ij} = (K - \tfrac{2}{3}G) D_{kk} \delta_{ij} + 2G D_{ij} - \sum_{\alpha} (2G \overset{(\alpha)}{\nu}_{ij} + \overset{(\alpha)}{\omega}_{ik} \sigma_{kj} - \sigma_{ik} \overset{(\alpha)}{\omega}_{kj}) \overset{(\alpha)}{\dot{\gamma}}^p - \sigma_{ik} W_{kj} + W_{ik} \sigma_{kj}, \tag{25}$$

$$\sigma_{33} = -(\sigma_{11} + \sigma_{22}) - 3K \ln \rho, \tag{26}$$

$$\dot{\phi} = W_{21} - \sum_{\alpha} \overset{(\alpha)}{\omega}_{21} \overset{(\alpha)}{\dot{\gamma}}^p, \tag{27}$$

$$\overset{(\alpha)}{\dot{\gamma}}^p = \begin{cases} \overset{(\alpha)}{\dot{\gamma}}_0 \left[\dfrac{\overset{(\alpha)}{\tau}}{\overset{(\alpha)}{\tau_c}} \right] \left[\left[\dfrac{|\overset{(\alpha)}{\tau}|}{\overset{(\alpha)}{\tau_c}} \right]^{1/m-1}, & \overset{(\alpha)}{\tau} \geq \overset{(\alpha)}{\tau_c}, \\ 0, & \overset{(\alpha)}{\tau} < \overset{(\alpha)}{\tau_c}, \end{cases} \tag{28}$$

$$\overset{(\alpha)}{\tau_c} = \left\{ 1 + \sum_{\beta} [g + (1-g) \cos \overset{(\alpha\beta)}{\psi} \cos \overset{(\alpha\beta)}{\phi}] h(\overset{(\beta)}{\gamma}^p)^n \right\} (1 - \nu\theta) \tag{29}$$

where the nondimensional variables have been denoted by the same symbols as before. Henceforth we will use nondimensional variables only. We note that $2H$ equals the

height of the block, v_0 the steady value of the vertical component of velocity imposed on the top and bottom surfaces, ρ_0 is the mass density in the undeformed and unstressed configuration of the single crystal, and

$$\theta_r = \frac{\tau_0}{\rho_0 c}, \qquad \delta = \frac{\rho_0 v_0^2}{\tau_0}. \tag{30}$$

Furthermore, K and G equal, respectively, the bulk and shear moduli of the single crystal.

As pointed out earlier, because of the presumed symmetry of deformations about the horizontal and vertical centroidal axes, we study deformations of the material in the first quadrant. Hence, boundary conditions that follow from the symmetry of deformations are applied on the left and bottom surfaces. Both the top and the right surfaces are taken to be thermally insulated, the right surface is taken to be traction free, and on the top surface zero tangential tractions and a vertical component v_2 of velocity given by

$$-v_2(t) = \begin{cases} t/0.005, & 0 \le t \le 0.005, \\ 1, & t \ge 0.005, \end{cases} \tag{31}$$

are prescribed. For the initial conditions, we take

$$\rho(\mathbf{x},0) = 1.0, \qquad \mathbf{v}(\mathbf{x},0) = \mathbf{0}, \qquad \boldsymbol{\sigma}(\mathbf{x},0) = \mathbf{0},$$

$$\phi(\mathbf{x},0) = 0, \qquad \theta(\mathbf{x},0) = \begin{cases} \epsilon(1 - r^2)^9 \exp(-5r^2), & r \le 1, \\ 0, & r > 1, \end{cases} \tag{32}$$

where $r^2 = x_1^2 + x_2^2$. The initially nonuniform temperature field represents a possible imperfection in the single crystal and serves as a triggering mechanism for the localization of the deformation.

III. NUMERICAL SOLUTION AND RESULTS

The problem as formulated above is highly nonlinear and almost impossible to solve analytically. We seek its approximate solution by the finite element method. Equations (22) through (25) and (27) are reduced to a set of coupled nonlinear ordinary differential equations by using the Galerkin approximation (e.g., see HUGHES [1987]) and the lumped mass matrix obtained by assigning one-fourth of the mass of each element to each one of its four nodes. At each node, the mass density, two components of the velocity, temperature, three components σ_{11}, σ_{22}, and σ_{12} of the Cauchy stress, and the angle ϕ characterizing the rotation of the slip system are taken as unknowns. Thus, the number of nonlinear ordinary differential equations equals eight times the number of nodes. The coordinates of nodes are updated after each time increment. Therefore, the spatial domain occupied by the body and the shapes of these elements varies with time. The coupled nonlinear ordinary differential equations are integrated by using the backward-difference Adams method included in the subroutine LSODE taken from the package ODEPACK developed by HINDMARSH [1983], and set ATOL = 10^{-3}, RTOL = 10^{-3}. The subroutine adjusts the time step adaptively until a solution of the coupled nonlinear ordinary differential equations has been computed to the specified accuracy.

From the computed solution we evaluated $\overset{(\alpha)}{\tau}$, $\overset{(\alpha)}{\dot{\gamma}^p}$, $D_{ij}^{(p)}$, and $W_{ij}^{(p)}$ at each quadrature point, and found the plastic slip strain of the active slip system by using

$$\overset{(\alpha)}{\gamma^p}(t + \Delta t) = \overset{(\alpha)}{\gamma^p}(t) + \Delta t\left[\overset{(\alpha)}{\dot{\gamma}^p}(t) + \overset{(\alpha)}{\dot{\gamma}^p}(t + \Delta t)\right]/2.$$

The finite element code developed earlier by BATRA and LIU [1989] to analyze the initiation and growth of shear bands in plane strain compression of the viscoplastic material was modified to study the present problem.

We assigned the following values to various material and geometric parameters in order to compute numerical results.

$$\begin{aligned} &k = 237\ \mathrm{W\,m^{-1}\,^{\circ}C^{-1}}, \quad c = 960\ \mathrm{J\,kg^{-1}\,^{\circ}C^{-1}}, \quad \rho_0 = 2700\ \mathrm{kg\,m^{-3}}, \\ &G = 27.6\ \mathrm{GPa}, \quad K = 81.48\ \mathrm{GPa}, \quad \tau_0 = 55\ \mathrm{MPa}, \quad n = 0.52, \\ &h = 11.02\ \mathrm{MPa}, \quad m = 0.02, \quad \nu = 0.0222^{\circ}\mathrm{C}^{-1}, \quad H = 5\ \mathrm{mm}, \\ &g = 0.28, \quad v_0 = 5\ \mathrm{m\,s^{-1}}, \quad \epsilon = 1.0. \end{aligned} \tag{33}$$

Thus, the average applied strain rate equals $1000\ \mathrm{s^{-1}}$, and $\theta_0 = 21.2^{\circ}\mathrm{C}$. The aforestated values are for a typical single crystal of aluminum, except that a rather large value of the thermal softening coefficient ν is used to reduce the CPU time required to initiate a shear band.

An aluminum single crystal has a face-centered-cubic lattice structure, which is characterized by four octahedral slip planes {111} and three slip directions ⟨110⟩ on each plane to give 12 slip systems. Herein all slip systems are assumed to be equally active, and the crystal is compressed along the [010] direction. We study two different cases, namely, when the plane of deformation is parallel to the plane (001) or the plane $(10\bar{1})$ of the single crystal.

We use the maximum principal logarithmic strain ϵ_p, defined as

$$\epsilon_p = \ln \lambda_1 \cong -\ln \lambda_2 \tag{34}$$

to find the deformation at a point. Here λ_1^2, λ_2^2, and 1 are eigenvalues of the right Cauchy–Green tensor $C_{\alpha\beta} = x_{i,\alpha}x_{i,\beta}$, or the left Cauchy–Green tensor $B_{ij} = x_{i,\alpha}x_{j,\alpha}$, where $x_{i,\alpha} \equiv \partial x_i/\partial X_\alpha$, X_α being the coordinates of a material point in the stress-free undeformed configuration. The second equality in eqn (34) holds because plastic deformations of the crystal are isochoric, and within the band elastic deformations are minuscule.

We employed a finite element mesh consisting of 32×32 uniform elements in the undeformed configuration, and used 2×2 Gaussian quadrature rule to evaluate various integrals numerically.

III.1. *Results when the plane of deformation is parallel to the plane (001) of the single crystal*

Figure 1 depicts contours of the maximum principal logarithmic strain ϵ_p for four different values of the average strain, i.e., $\gamma_{avg} = 0.00355$, 0.02755, 0.07755, and 0.10755. These suggest that a shear band, indicated by higher values of the contours of the maximum principal logarithmic strain near the center, originates at the center and propagates along $\pm 45^{\circ}$ directions and is reflected back from the top surface, with the

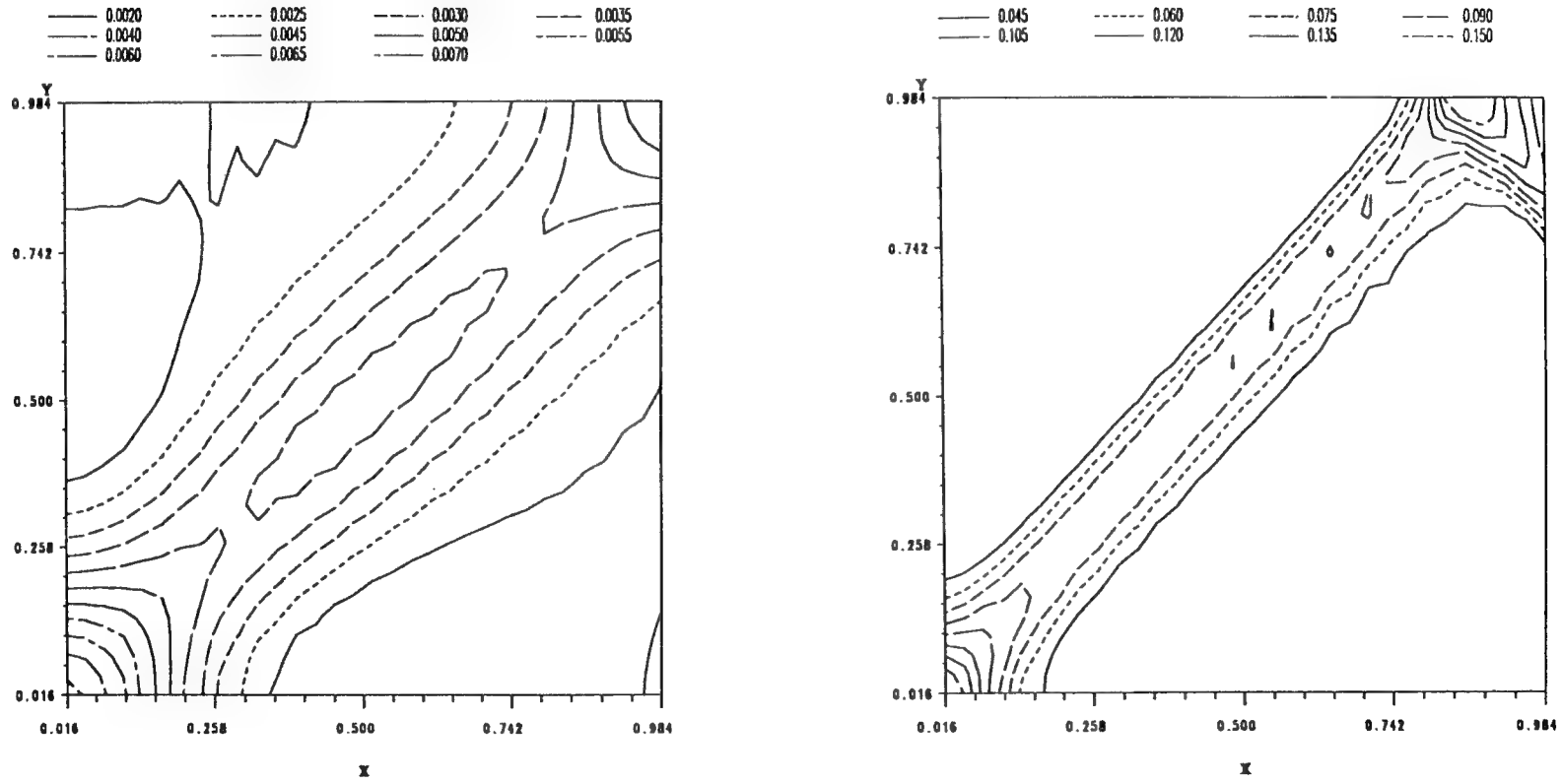

Fig. 1. Contours of the maximum principal logarithmic strain at four different values of the average strain. (a) $\gamma_{avg} = 0.00355$, (b) $\gamma_{avg} = 0.02755$. (Figure continues)

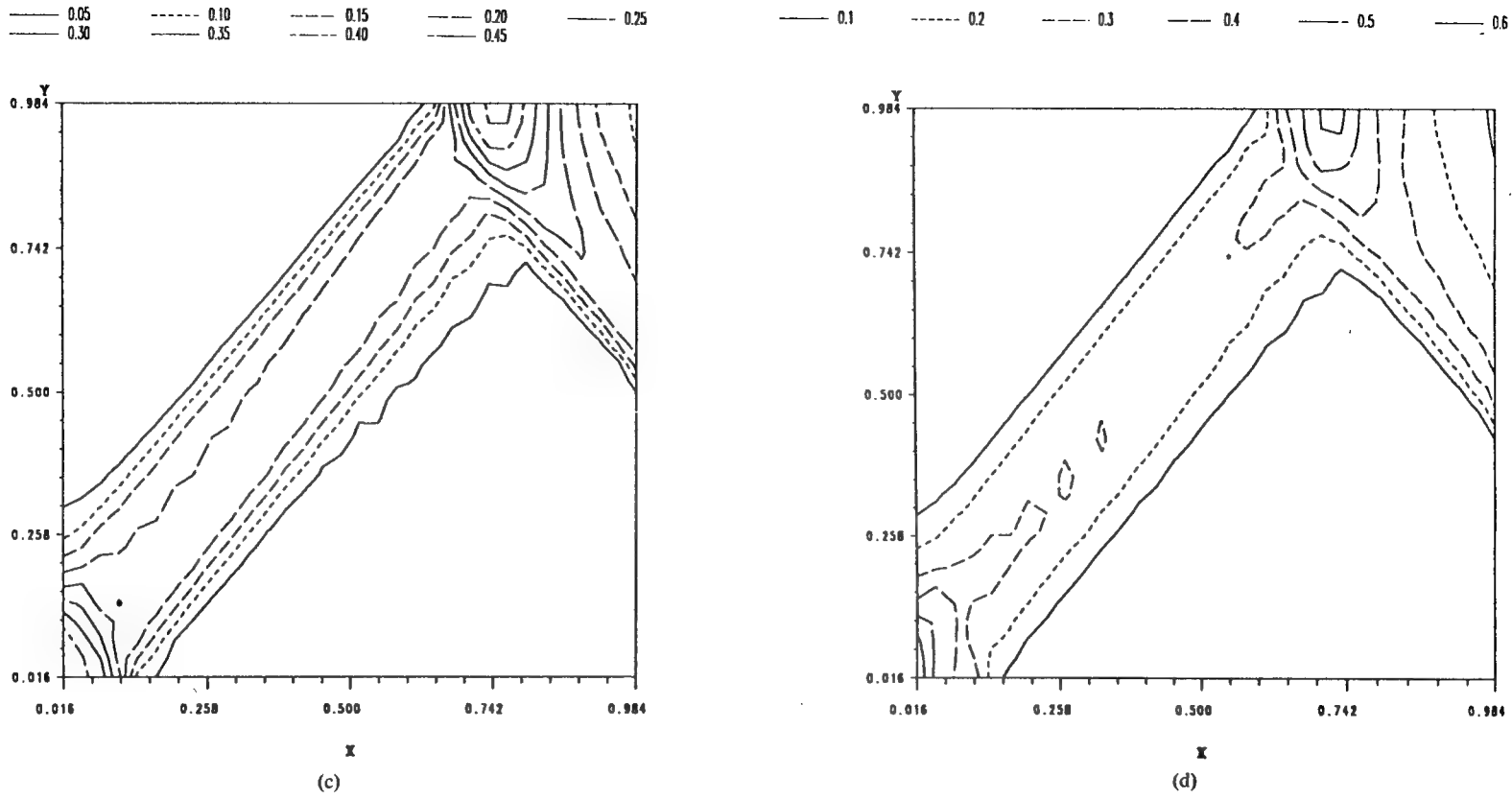

Fig. 1. (c) γ_{avg} 0.07755, (d) γ_{avg} 0.10755.

angle of reflection being nearly equal to the angle of incidence. The severely deforming region narrows down initially, but then widens, probably because of a change in the locations of the active slip systems. A closer look at the computed results suggests the following. In the beginning, the block is uniformly deformed elastically and all slip systems are inactive in the entire body. As the block continues to be deformed at the high strain rate, the top part of the square cross-section yields first, and the plastic deformation spreads into the body to make four slip systems, namely, $(111)[1\bar{1}0]$, $(11\bar{1})[1\bar{1}0]$, $(1\bar{1}\bar{1})[110]$, and $(1\bar{1}1)[110]$ active. It will be evidenced by results given below. The material surrounding the origin where the temperature perturbation is applied also yields early due to the lower value of the critical shear stress of slip systems at relatively higher temperature. The material adjoining the centroid of the cross-section undergoes more severe plastic deformations than the rest of the material. With further straining of the block, the plastic deformation spreads throughout the body.

The accumulated plastic strain of each active slip system is plotted in Fig. 2 at an average strain of 0.10755. It is clear that four primary slip systems $(111)[1\bar{1}0]$, $(11\bar{1})[1\bar{1}0]$, $(1\bar{1}\bar{1})[110]$, and $(1\bar{1}1)[110]$ contribute significantly to plastic deformations, that the maximum slip strain equals 0.4262, and the average slip strain within the band is approximately 0.175. These slip systems are more favorable to plastic deformation than the slip systems $(111)[0\bar{1}1]$, $(11\bar{1})[0\bar{1}\bar{1}]$, $(1\bar{1}\bar{1})[101]$, and $(1\bar{1}1)[10\bar{1}]$ in the central band, and $(\bar{1}11)[0\bar{1}1]$, $(1\bar{1}1)[011]$, $(111)[10\bar{1}]$, and $(11\bar{1})[101]$ in the reflected band. Note that the average slip strain of the four secondary slip systems in the central band equals 0.025, and that of the slip systems in the reflected band equals 0.01. During the early stages of the shear band formation, only the primary slip systems are active and contribute to the intense plastic deformation within the band. For simple compression in the crystallographic direction [010] and plane of deformation parallel to the crystallographic plane (001), the four primary slip systems are equally favorable to slip throughout the loading history. However, in a double-slip model for a single crystal employed by ZIKRY and NEMAT-NASSER [1990], the slip system $(111)[\bar{1}01]$, corresponding to $(111)[1\bar{1}0]$ in our coordinate system, is chosen as the primary slip system, and $(\bar{1}\bar{1}1)[011]$ ($(1\bar{1}\bar{1})[101]$ in our model) as the conjugate one. These two slip systems are not equally active, with the result that the primary slip system dominates the slip deformation. In our model, all potentially active slip systems are employed, and the slip system becomes active if its resolved shear stress reaches the critical value. The computed results show that all four primary slip systems, namely, $(111)[1\bar{1}0]$, $(11\bar{1})[1\bar{1}0]$, $(1\bar{1}\bar{1})[110]$, and $(1\bar{1}1)[110]$ are equally active. As the single crystal is deformed and the crystal lattice is reoriented by the deformation, other slip systems become active as conjugate slip systems resulting in multiple gliding. The slip systems $(111)[0\bar{1}1]$, $(11\bar{1})[0\bar{1}\bar{1}]$, $(1\bar{1}\bar{1})[101]$, and $(1\bar{1}1)[10\bar{1}]$ in the central band, and $(111)[10\bar{1}]$, $(11\bar{1})[101]$, $(\bar{1}11)[0\bar{1}1]$, and $(1\bar{1}1)[011]$ in the reflected band are the conjugate slip systems.

Figure 3 shows the contours of the slip-rate of the slip system $(111)[1\bar{1}0]$ at four different values of the average strain; similar results hold for the other three primary slip systems. At an average strain of 0.00355, the slip rate is nearly uniform throughout most of the single crystal, the only exception being near the block center where temperature perturbation is applied, and near the top right corner where the deformation is singular. With the continuous compression of the block, the region with an intensive slip rate of this system narrows down sharply and the band width equals nearly the smallest distance between two adjacent Gauss points. When compared with the contours of the second invariant of the strain rate and the plastic strain rate tensors given in Fig. 5 below, the slip-rate band of the primary slip systems is aligned in the same direction as the

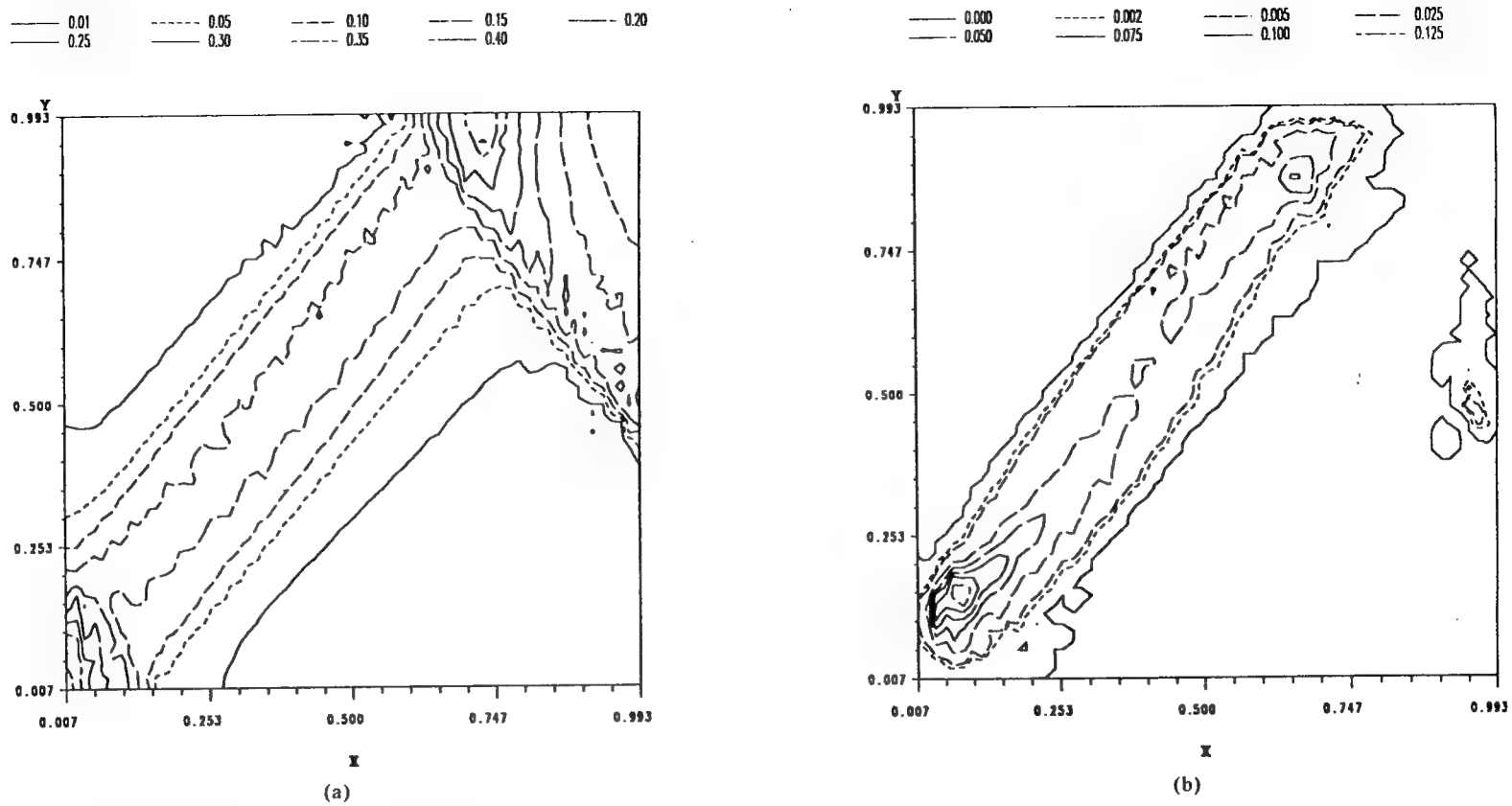

Fig. 2. Contours of the accumulated plastic slip strains of different slip systems at an average strain of 0.10755. (a) Slip systems: $(111)[1\bar{1}0]$, $(11\bar{1})[1\bar{1}0]$, $(1\bar{1}\bar{1})[110]$, and $(1\bar{1}1)[110]$, (b) Slip systems: $(111)[0\bar{1}1]$ and $(11\bar{1})[0\bar{1}\bar{1}]$. (Figure continues)

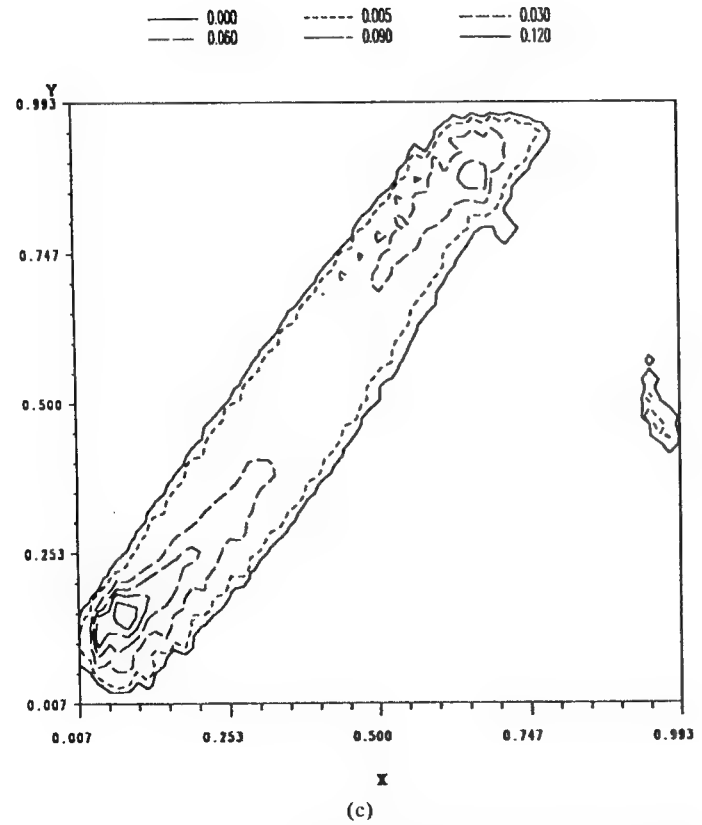

(c)

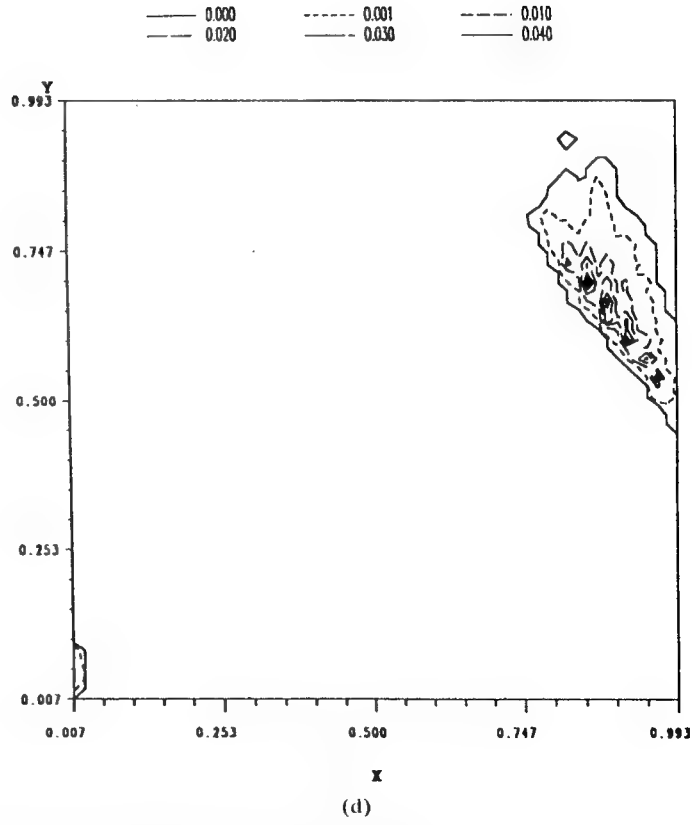

(d)

Fig. 2. (c) Slip systems: $(1\bar{1}\bar{1})[101]$ and $(1\bar{1}1)[10\bar{1}]$, (d) Slip systems: $(111)[10\bar{1}]$ and $(11\bar{1})[101]$. (Figure continues)

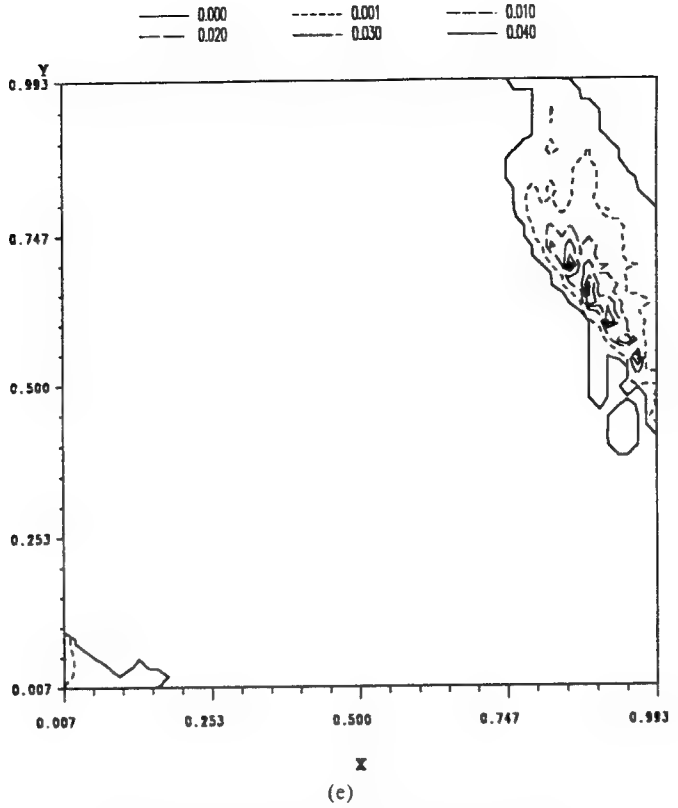

(e)

Fig. 2. (e) Slip systems: $(\bar{1}11)[0\bar{1}1]$ and $(1\bar{1}1)[011]$.

global strain-rate band. Note that the double slip model gives a misorientation between the bands of the primary slip system and the global one due to the heterogeneous slip deformations of the primary and the secondary slip systems. An examination of the slip-rate band of the primary slip system at four different values of the average strain suggests that the slip-rate bands broaden as the crystal is deformed. One reason for this widening of the slip-rate band is that once plastic deformation occurs within the slip bands, the work hardening raises the critical shear stress, and further slip deformation in the center of the band may become more difficult than that in the adjacent regions. This facilitates plastic deformation of the material adjacent to the centerline of the slip-rate band. Another reason is that the lattice of the single crystal is reoriented by the deformation, and the widening of the slip-rate band ensures that the centerline of the global band makes an angle of $\pm 45°$ with the direction of the compression loading.

In Fig. 4 we have plotted contours of the slip-rate of slip systems $(111)[0\bar{1}1]$ and $(11\bar{1})[0\bar{1}\bar{1}]$ at average strains of 0.02755, 0.05755, and 0.07755, and that of $(\bar{1}11)[0\bar{1}1]$ and $(1\bar{1}1)[011]$ at average strains of 0.05755 and 0.07755. The slip deformations of slip systems $(1\bar{1}\bar{1})[101]$ and $(1\bar{1}1)[10\bar{1}]$ are similar to that of $(111)[0\bar{1}1]$. At early stages of deformation, these conjugate slip systems are inactive. Even when the primary slip systems give a severe slip deformation at an average strain of 0.02755, slip systems $(\bar{1}11)[0\bar{1}1]$ and $(1\bar{1}1)[011]$ remain inactive. When the shear bands are fully formed, the

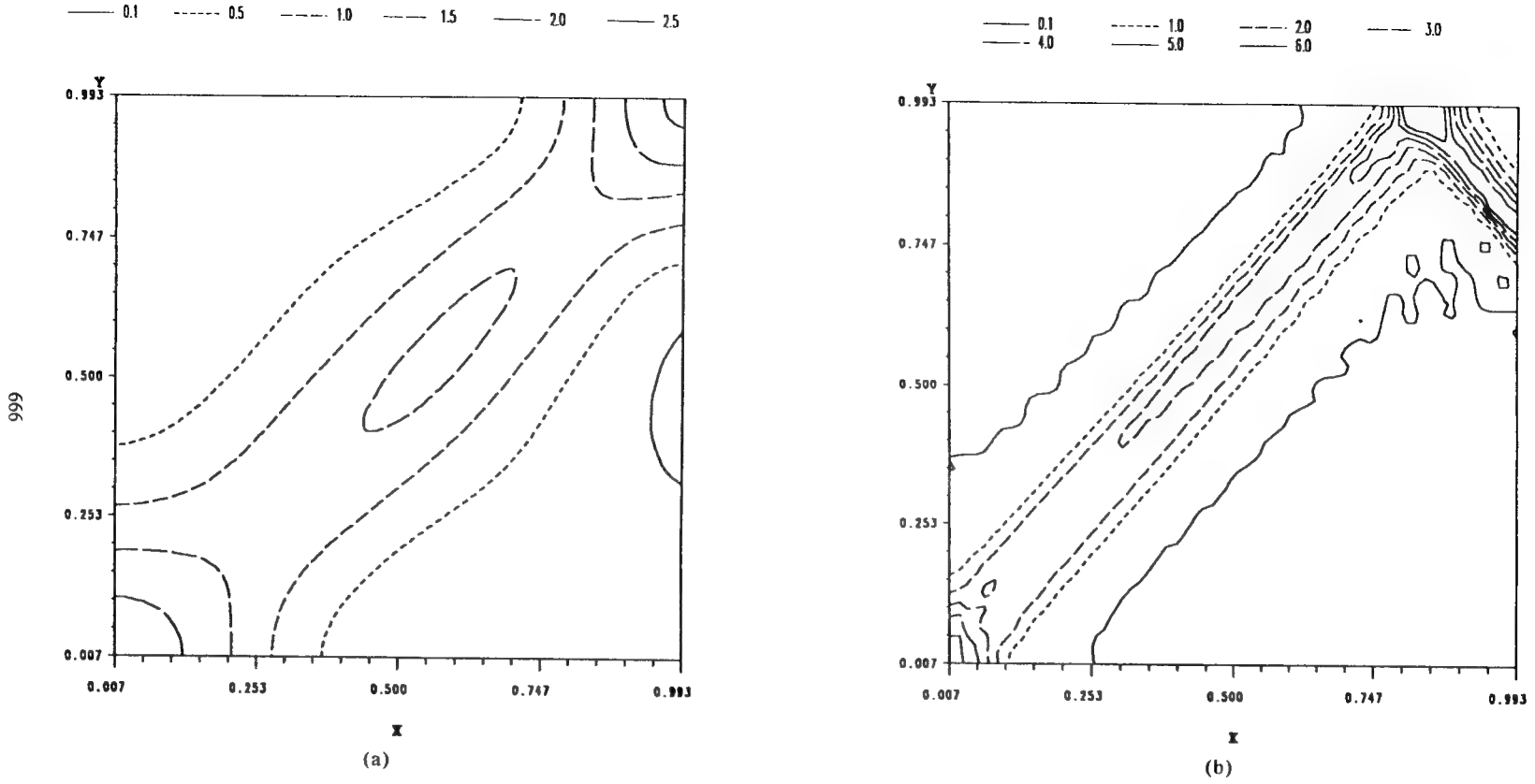

Fig. 3. Contours of the slip-strain-rate of the slip system $(111)[1\bar{1}0]$ at four different values of the average strain. (a) $\gamma_{avg} = 0.00355$, (b) $\gamma_{avg} = 0.02755$. (Figure continues)

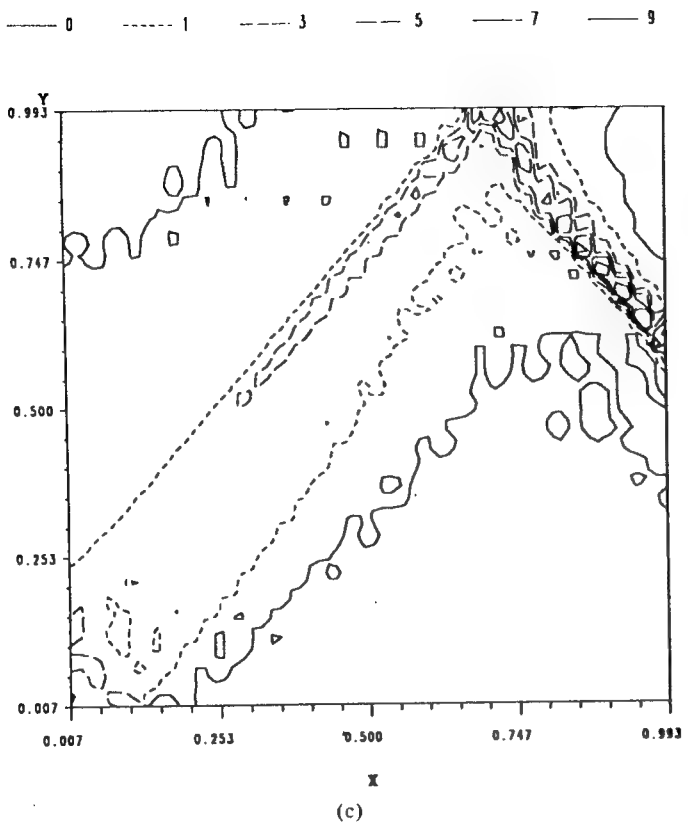

(c)

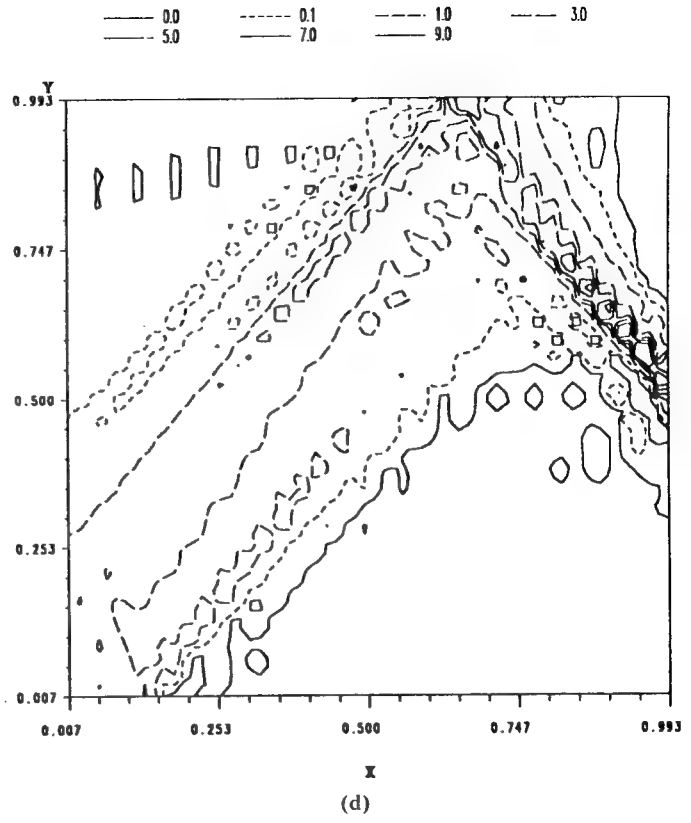

(d)

Fig. 3. (c) $\gamma_{avg} = 0.05755$, (d) $\gamma_{avg} = 0.07755$.

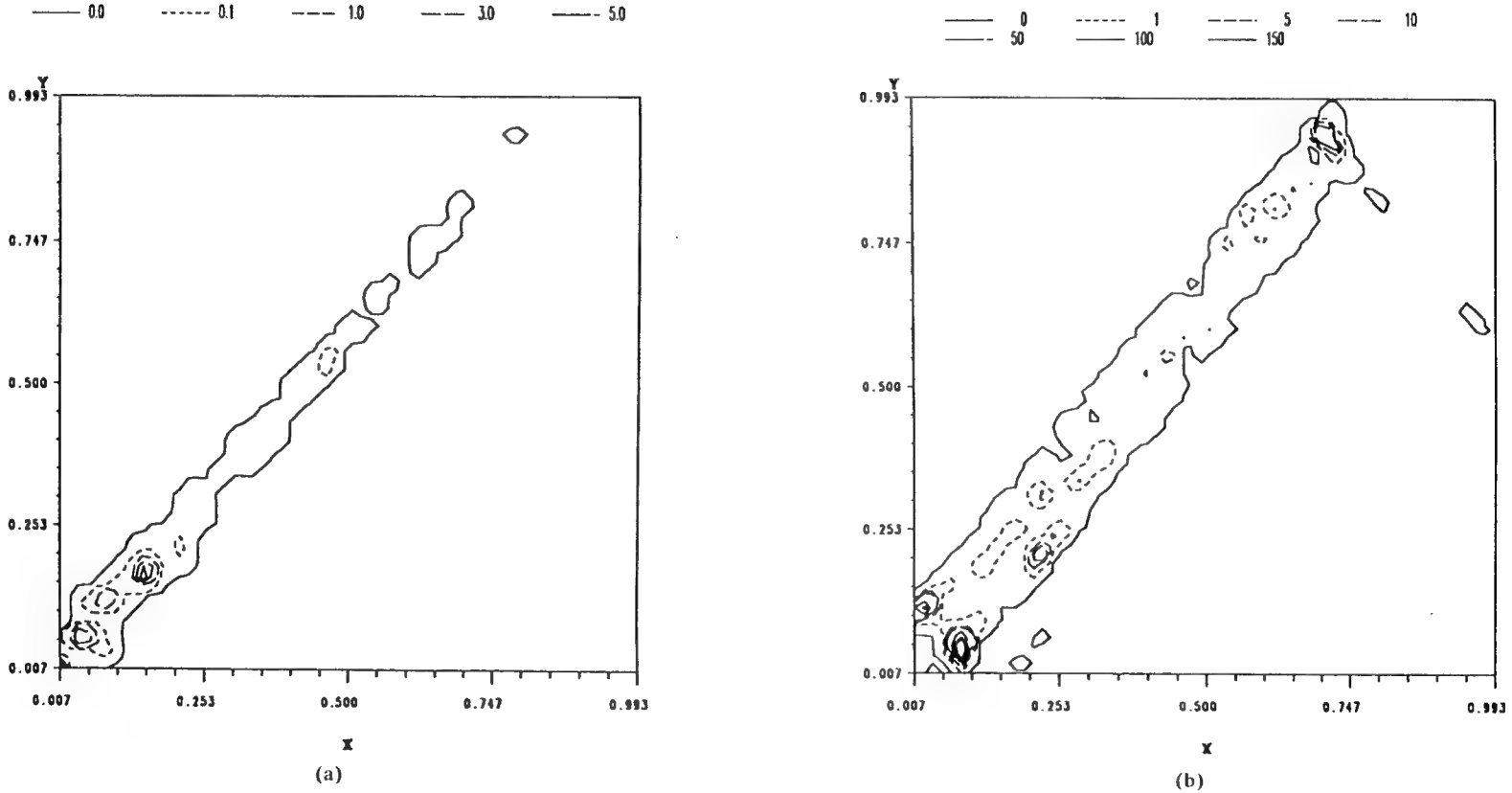

Fig. 4. Contours of the slip-strain-rate of slip systems (111)[0$\bar{1}$1] at (a) $\gamma_{avg} = 0.02755$, (b) $\gamma_{avg} = 0.05755$. (Figure continues)

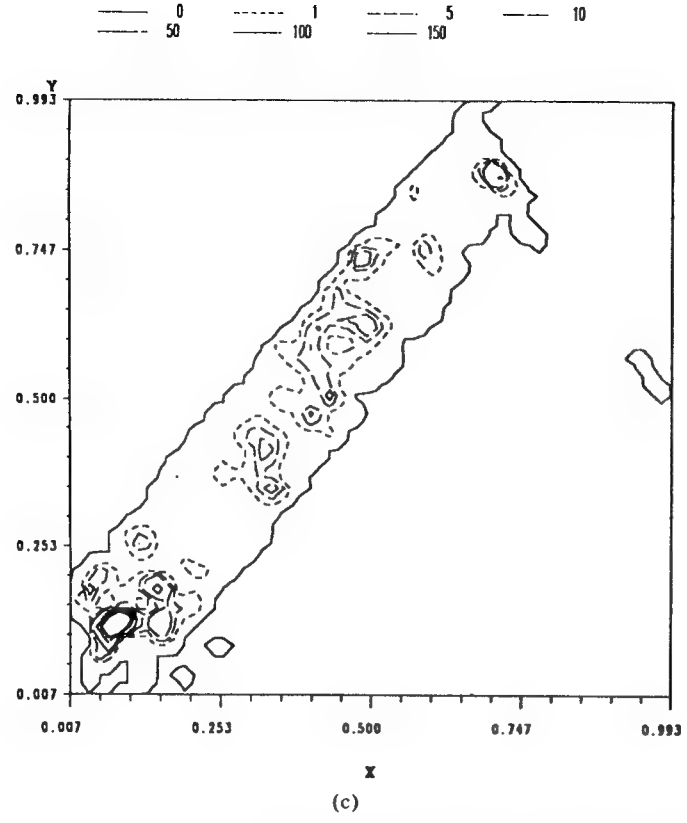

(c)

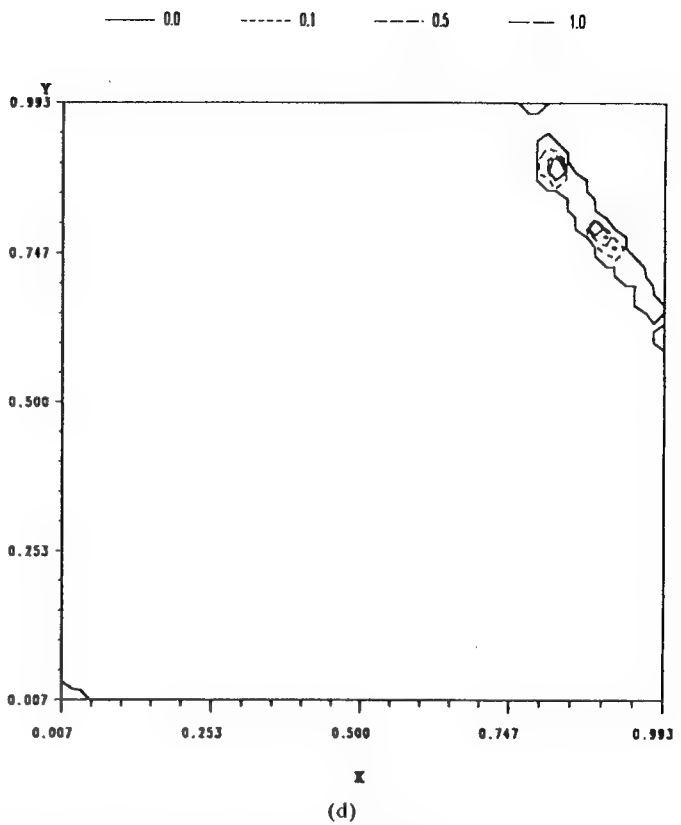

(d)

Fig. 4. (c) $\gamma_{avg} = 0.07755$, and that of slip systems $(\bar{1}11)[0\bar{1}1]$ and $(1\bar{1}1)[011]$ and (d) $\gamma_{avg} = 0.00755$. (Figure continues)

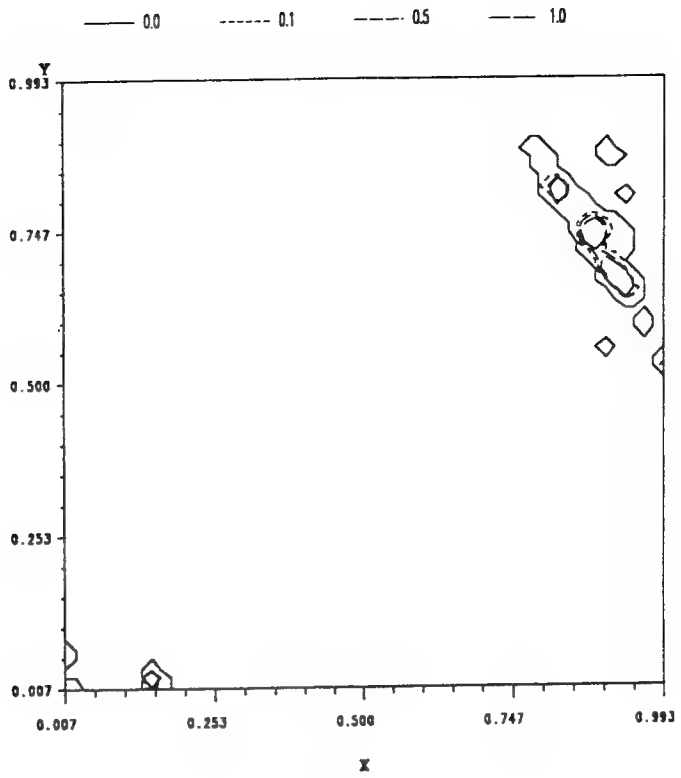

(e)

Fig. 4. (e) $\gamma_{avg} = 0.07755$.

rotation of the crystal lattice relative to the axis of compression results in the movement of the orientation of the stress axis out of its original stereographic triangle into the one adjoining it on the stereographic projection, and the conjugate slip systems become the preferred slip systems.

The contours of the angle of rotation ϕ of the crystal lattice are given in Fig. 5. Within the shear band passing through the block center, the average angle of rotation of slip systems at a nominal strain of 0.00755 is 0.6° counterclockwise, the maximum angle of rotation is 0.726° counterclockwise, and the angle of rotation in the reflected shear band near the top right corner of the block is 0.034° clockwise. However, at a nominal strain of 0.10755, the values of the average and maximum angle of rotation within the central shear band equal, respectively, 14.5° and 18.54° counterclockwise, and those within the reflected band equal 14.3° and 20.3° clockwise.

The contours of the second invariant I of the deviatoric strain-rate tensor $\tilde{D}_{ij}$, and of the second invariant I_p of the plastic strain-rate tensor D^p_{ij} are exhibited in Fig. 6. The invariants I and I_p are defined as

$$2I^2 = \tilde{D}_{ij}\tilde{D}_{ij}, \qquad 2I_p^2 = D^p_{ij}D^p_{ij}, \qquad \tilde{D}_{ij} = D_{ij} - \tfrac{1}{3}D_{kk}\delta_{ij}.$$

Recall that $D^p_{kk} = 0$, therefore $\tilde{D}^p_{ij} = D^p_{ij}$. Whereas contours of I or I_p illustrate how rapidly material particles are deforming at present, those of the principal logarithmic strain

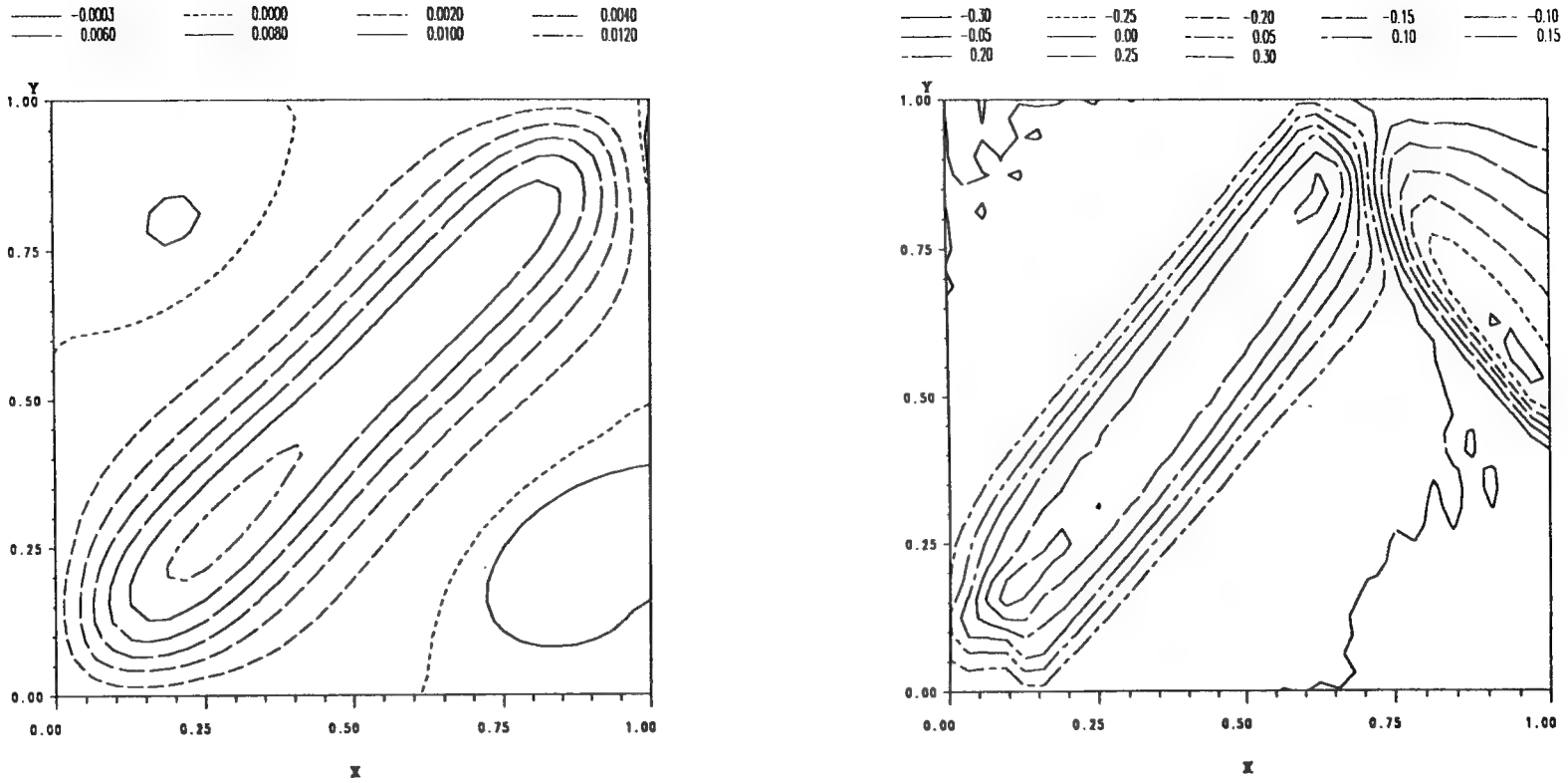

Fig. 5. Contours of the angle of rotation of the crystal lattice at (a) $\gamma_{avg} = 0.00755$, (b) $\gamma_{avg} = 0.10755$.

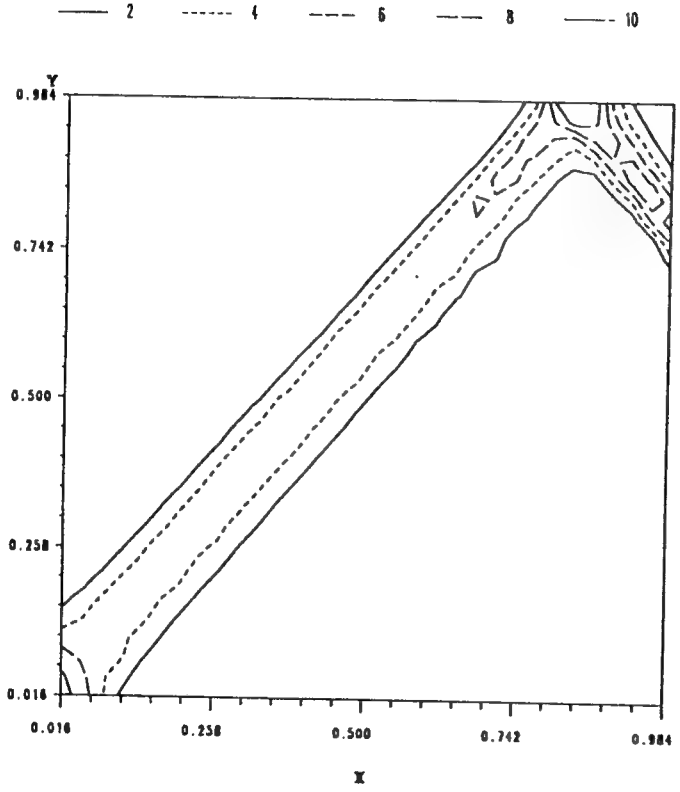

(a)

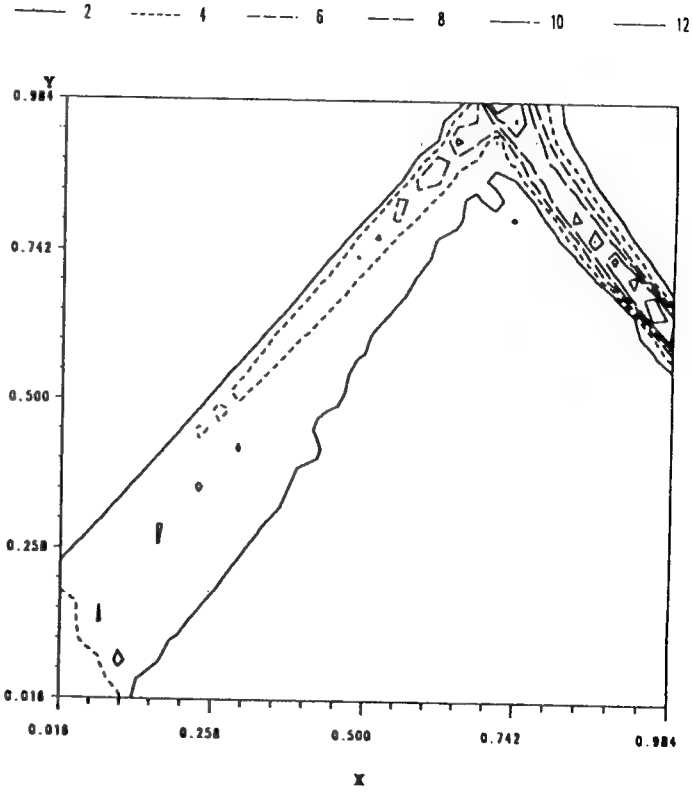

(b)

Fig. 6. Contours of the second invariant I of the deviatoric strain-rate tensor at (a) $\gamma_{avg} = 0.02755$, (b) $\gamma_{avg} = 0.05755$. (Figure continues)

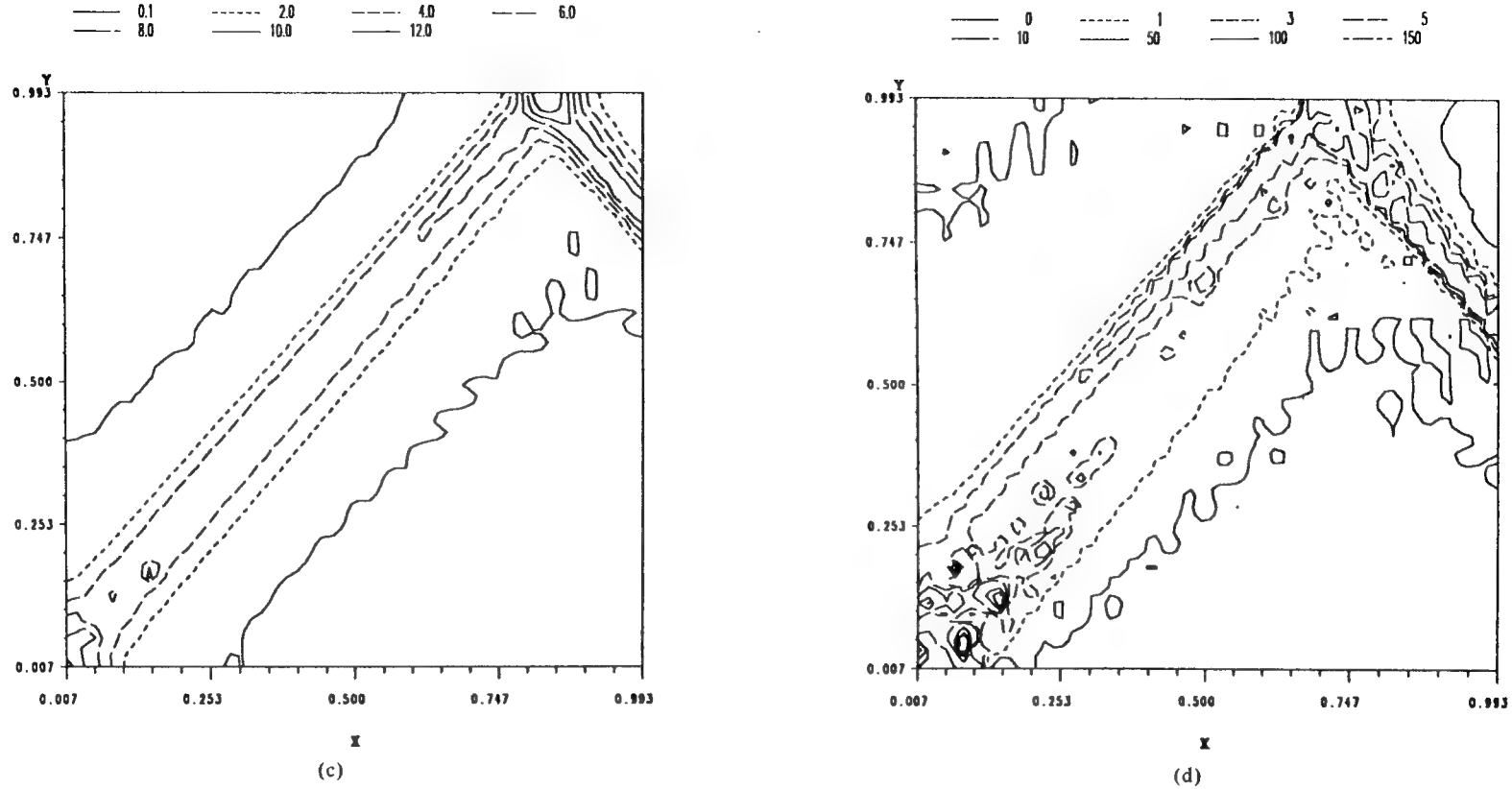

Fig. 6. Contours of the second invariant I_p of the plastic strain-rate tensor at (c) $\gamma_{avg} = 0.02755$, (d) $\gamma_{avg} = 0.05755$.

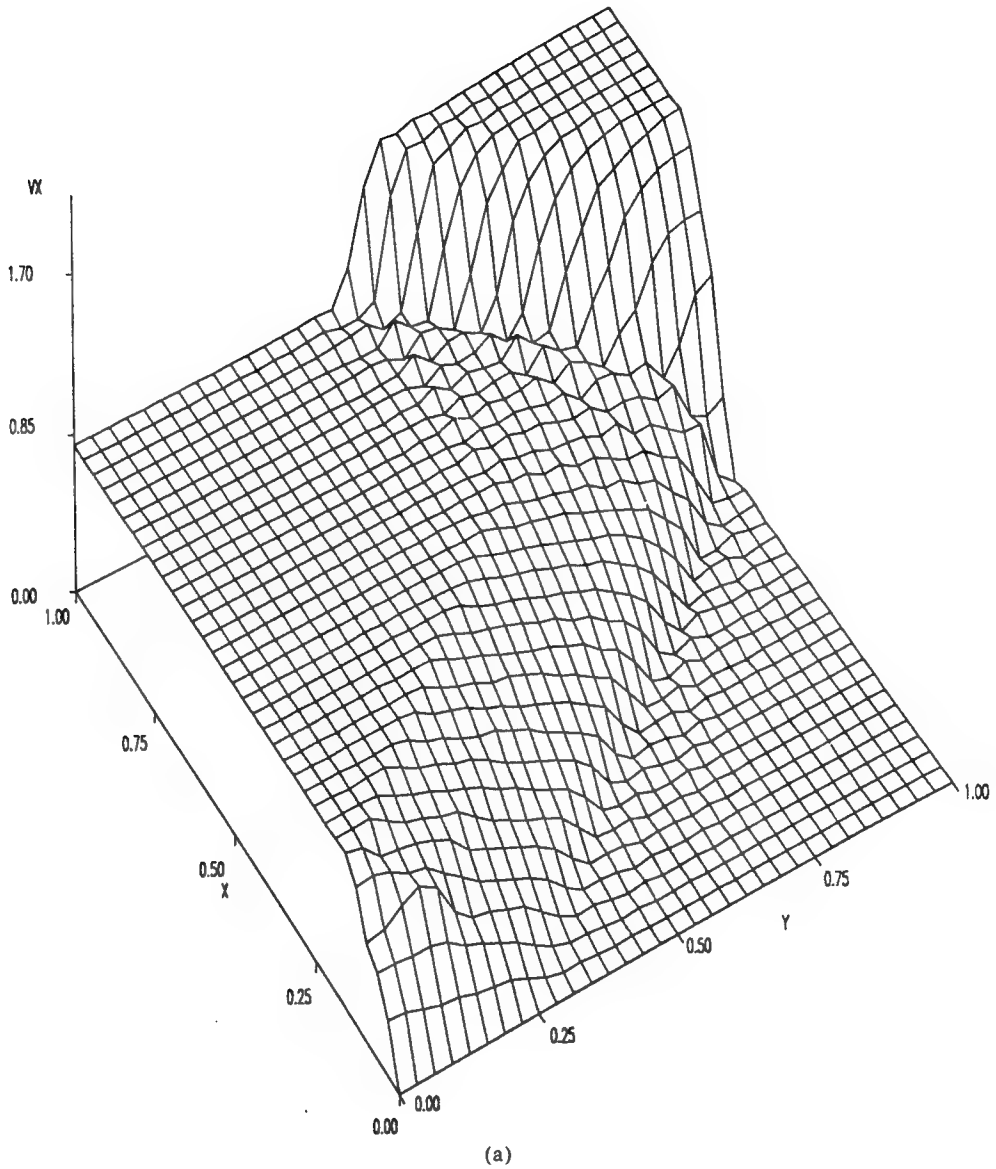

(a)

Fig. 7. (a) Distribution of v_x in the cross-section at an average strain of 0.07755. (Figure continues)

given in Fig. 2 correspond to the accumulated deformation of a material element. The values of D_{ij}^p are derived from the plastic straining of the slip systems. At an average strain of 0.02755, the maximum values of I and I_p equal 14.23 and 14.14, respectively, suggesting that the mesh used to calculate nodal values of various variables can delineate the micromechanisms of the slip deformation of active slip systems everywhere. The minimum value 0.00425 of I_p indicates that all of the material particles throughout the cross-section are deforming plastically at $\gamma_{avg} = 0.02755$. However, at an average strain of 0.05755, the maximum values of I_p and I equal 281.84 and 15.43, respectively, and the minimum value of I_p is zero. The contours of I_p in Fig. 6d reveal that the material

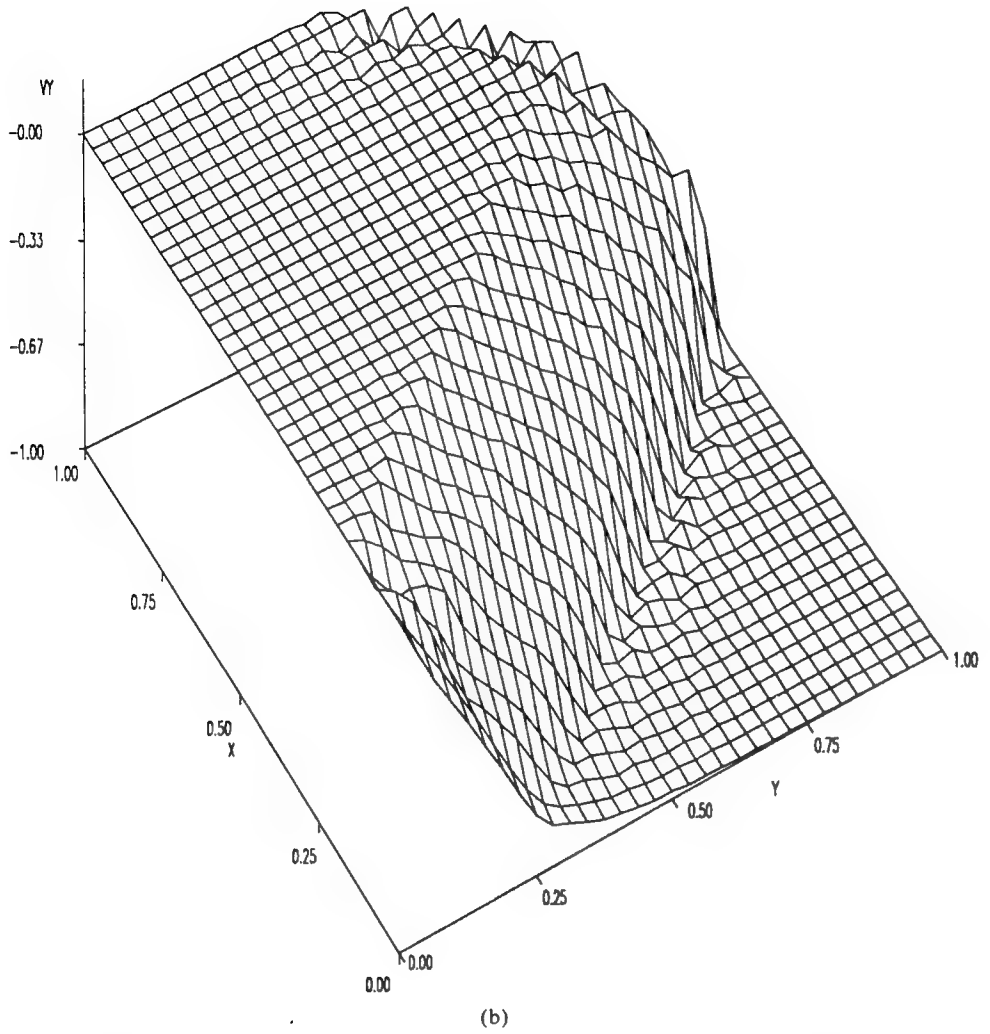

(b)

Fig. 7. (b) Distribution of v_y in the cross-section at an average strain of 0.07755.

near the top left and right corners and that near the bottom right corner of the block is deforming elastically, and all slip systems there are inactive. This unloading of the material and possibly the rather coarse mesh used, could cause the significant difference between the maximum values of I and I_p.

Figure 7 depicts the distribution, within the deforming region, of the x- and y-components of the velocity field at an average strain of 0.07755. It is clear that the velocity field increases sharply across the shear band. Note that in our formulation the velocity field is forced to stay continuous throughout the deforming region. Thus, this sharp change in the values of v_x and v_y may be construed as supporting assertions made by TRESCA [1878] and MASSEY [1921] that the tangential component of the velocity field is discontinuous across a shear band.

The deformed mesh at an average strain of 0.11555 is shown in Fig. 8 and confirms the aforestated observations that a shear band forms along a line passing through the

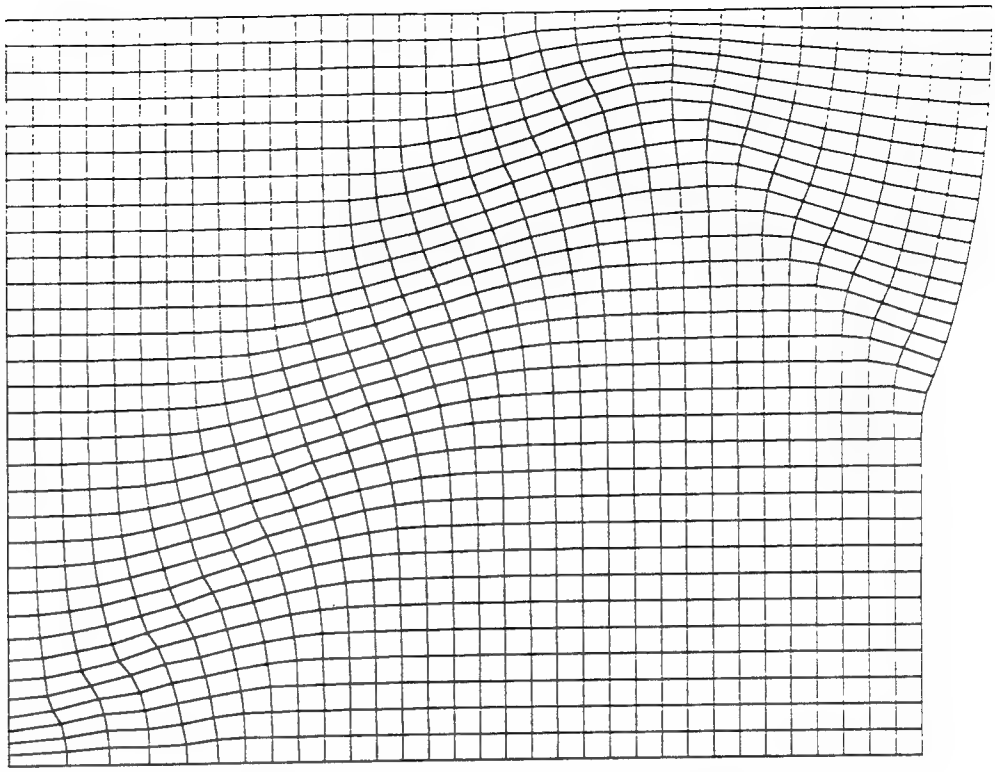

Fig. 8. The deformed mesh at an average strain of 0.11555.

center of the cross-section and making an angle of 45° with the horizontal. The band is reflected from the top surface, and the angle of reflection essentially equals the angle of incidence. The severely deformed region is wider than that obtained in previous computations involving plane strain compression of a homogeneous and isotropic polycrystalline body.

III.2. *The plane of deformation is parallel to the plane (10$\bar{1}$) of the single crystal*

Like the previous case when the plane of deformation is parallel to the plane (001), the initial plastic deformations of the block are essentially uniformly distributed throughout the cross-section, except near the center where a temperature perturbation is applied. With continuous compression of the block, a shear band initiates from the center and propagates into the body. This is evidenced by the plots, given in Fig. 9, of the contours of the maximum principal logarithmic strain at several values of the average strain. Results plotted in Fig. 9a show that the block is nearly uniformly deformed at an average strain of 0.00255. However, at an average strain of 0.02755, a shear band passing through the center and inclined at an angle of approximately 39.5° with the horizontal has developed. A comparison of this with the results plotted in Fig. 1 suggests that the direction of the shear band in a single crystal depends upon the orientation of the crystal relative to the axis of loading. The contours of the maximum principal logarithmic strain plotted in Figs. 9c and 9d at average strains of 0.07755 and 0.10755 suggest that

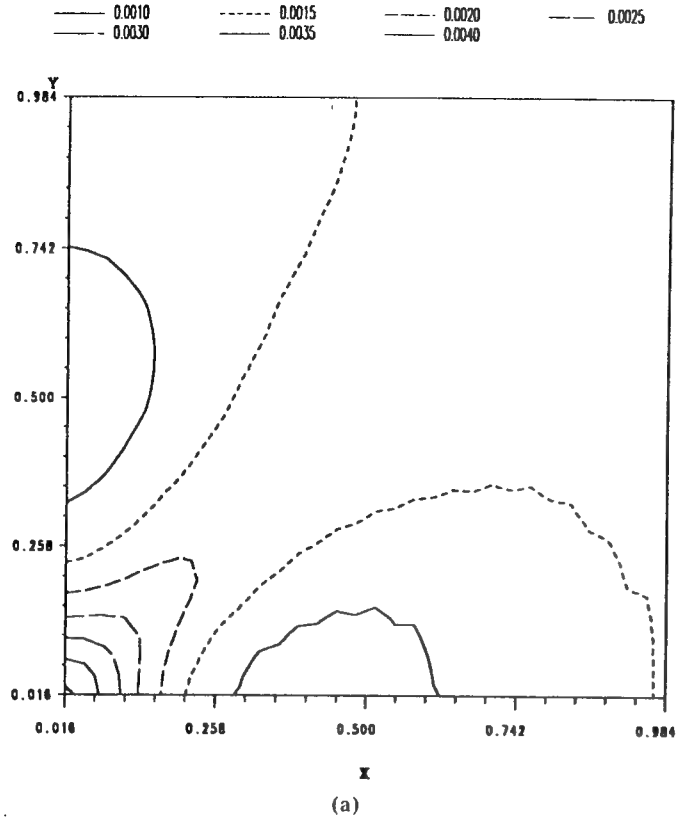

(a)

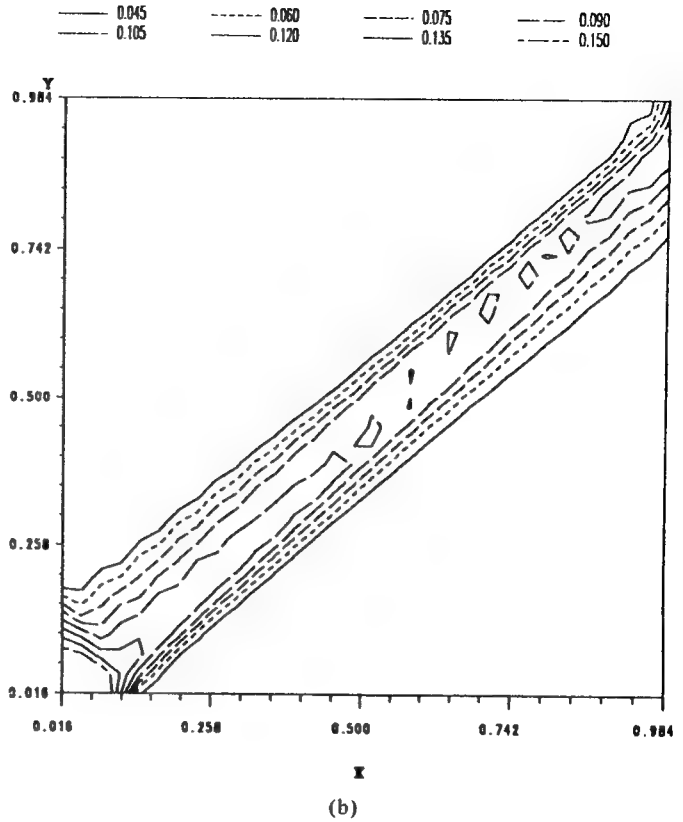

(b)

Fig. 9. Contours of the maximum principal logarithmic strain at four different values of the average strain. (a) $\gamma_{avg} = 0.00255$, (b) $\gamma_{avg} = 0.02755$. (Figure continues)

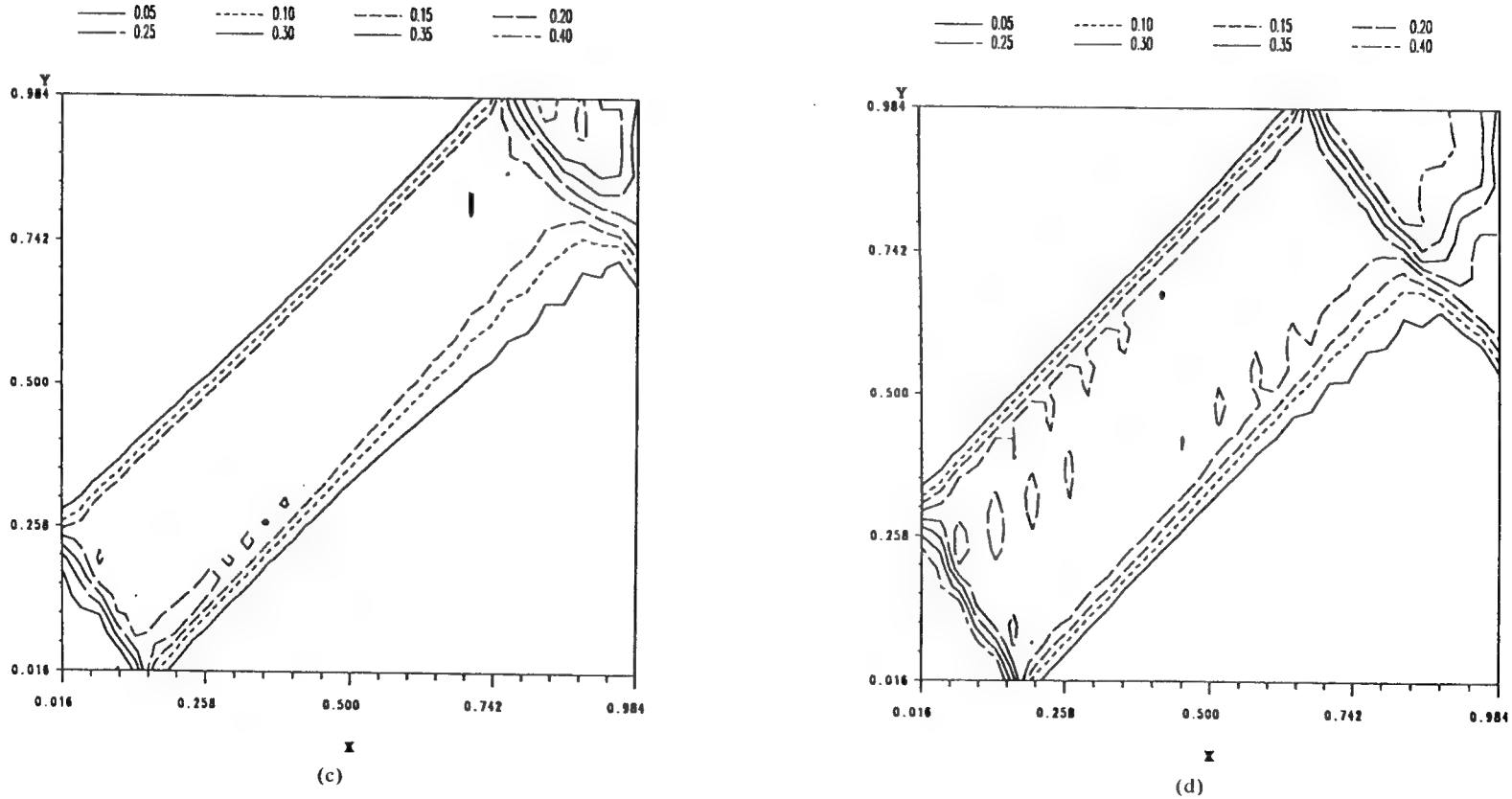

Fig. 9. (c) $\gamma_{avg} = 0.07755$, (d) $\gamma_{avg} = 0.10755$.

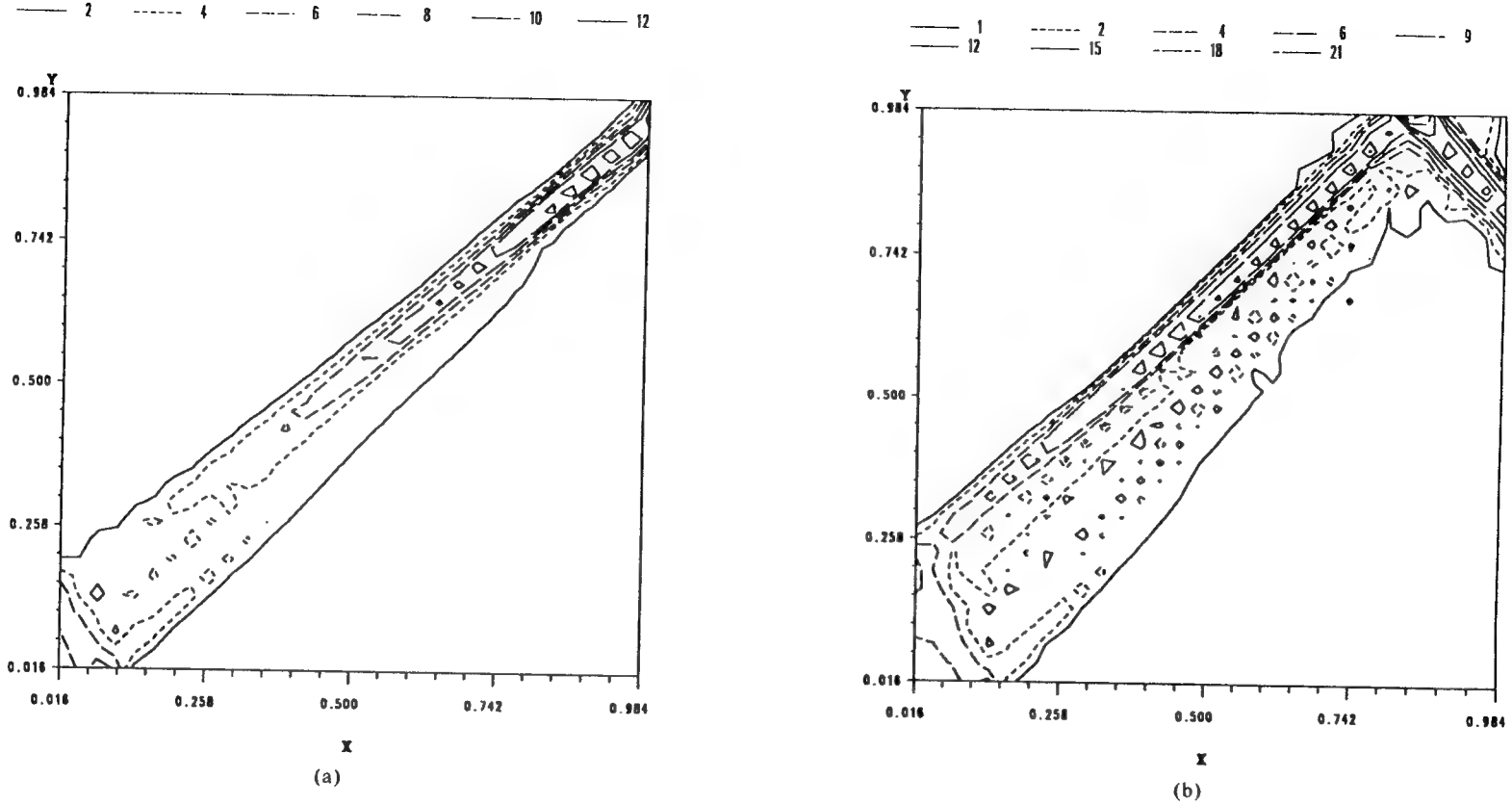

Fig. 10. Contours of the second invariant I of the deviatoric strain-rate tensor at three different values of the average strain. (a) $\gamma_{avg} = 0.02755$, (b) $\gamma_{avg} = 0.05755$. (Figure continues)

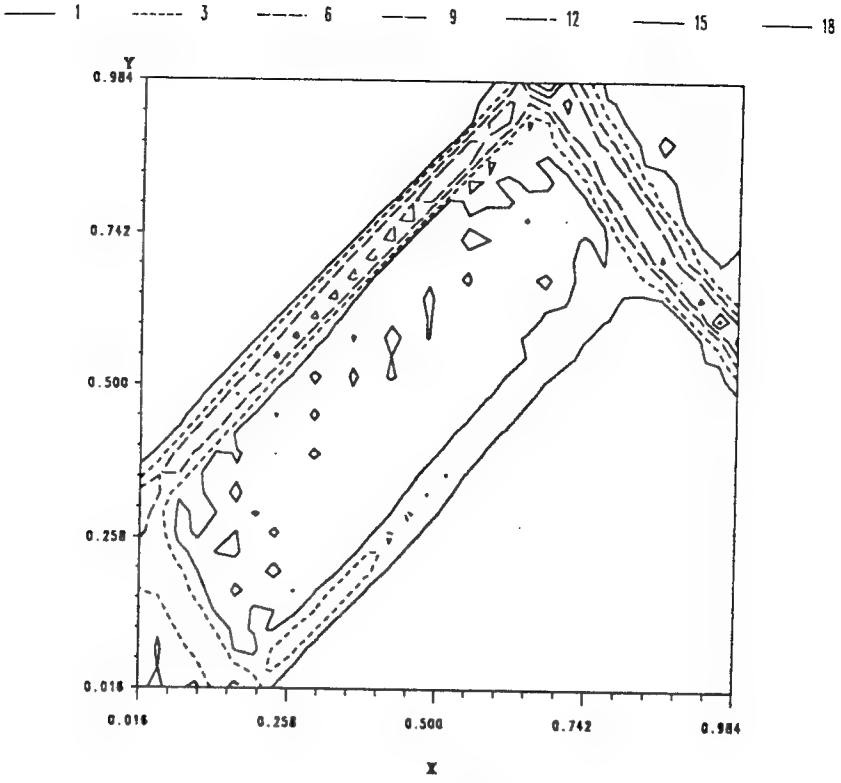

Fig. 10. (c) $\gamma_{avg} = 0.10755$.

the band widens as the body continues to be compressed, and the width of the severely deformed region is more than that in the previous case discussed in section III.1.

The contours of the second invariant I of the deviatoric strain-rate tensor and of the second invariant I_p of the plastic strain-rate tensor are given in Figs. 10 and 11, respectively. The results plotted in Fig. 10 suggest that initially the band initiating from the centroid of the cross-section meets the right traction free surface. As the band widens, another band reflected from the top surface also forms. With further loading of the body, the band through the center of the cross-section splits into two parallel bands of unequal intensity as measured by the maximum values of I in them; the upper stain-rate band has higher intensity of deformation than the lower one, and is reflected back into the body from the top loading surface. The lower band meets the reflected band and does not go through it, possibly because of the higher values of I in the reflected band. The contours of I_p in Fig. 11d reveal that a large region near the upper left and lower right corners of the cross-section is deforming elastically at an average strain of 0.10755. Since the body continues to be compressed at the prescribed rate, the unloading in regions near the upper left and lower right corners should intensify the rate of plastic deformation elsewhere.

We have plotted in Fig. 12 the angle of rotation of the crystal lattice at several different values of the average strain. At a nominal strain of 0.00755, the maximum and minimum values of the angle of rotation equal 1.47° counterclockwise and 0.08° clockwise. However, at a nominal strain of 0.10755, the average angle of rotation within the

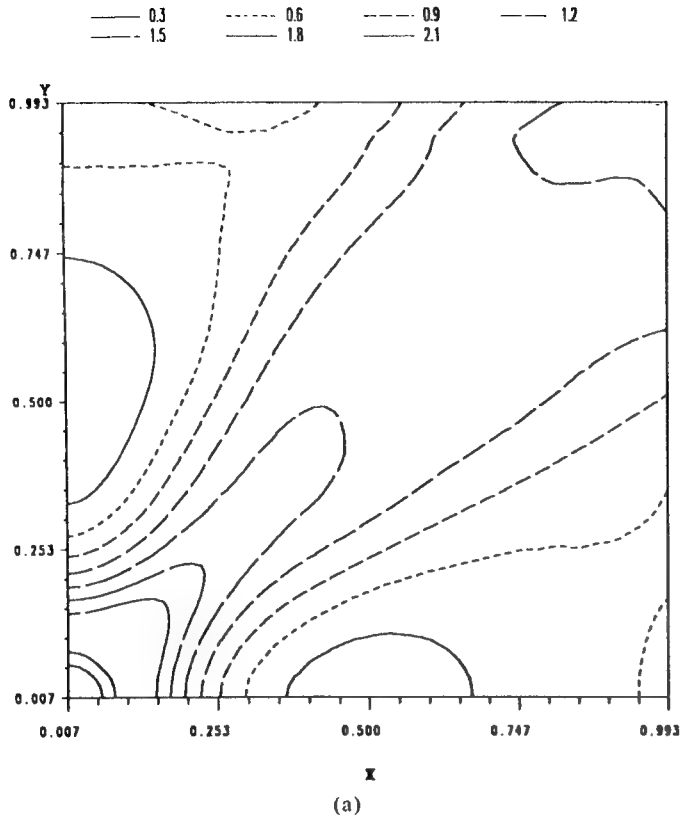

(a)

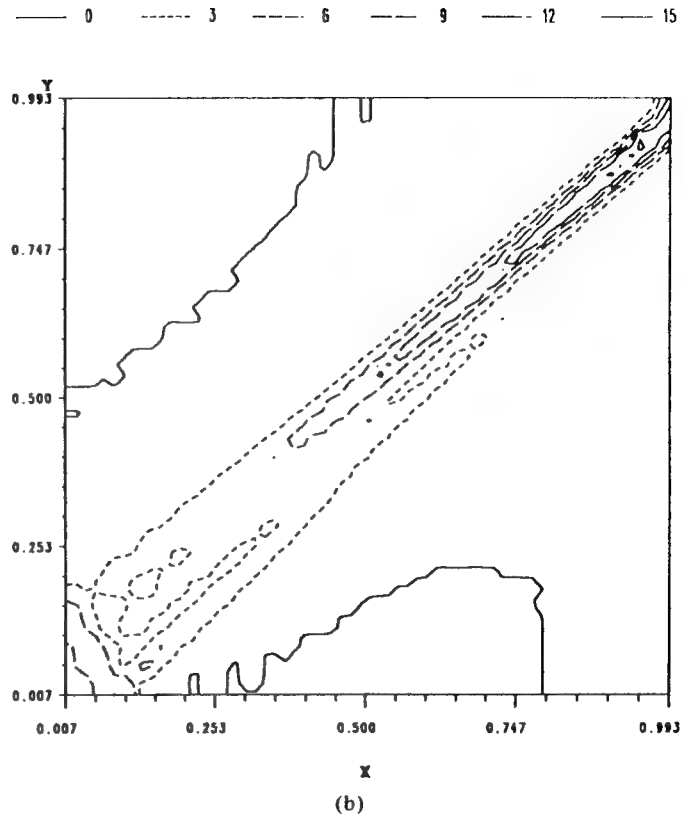

(b)

Fig. 11. Contours of the second invariant I_p of the plastic strain-rate tensor at four different values of the average strain. (a) $\gamma_{avg} = 0.00255$, (b) $\gamma_{avg} = 0.02755$. (Figure continues)

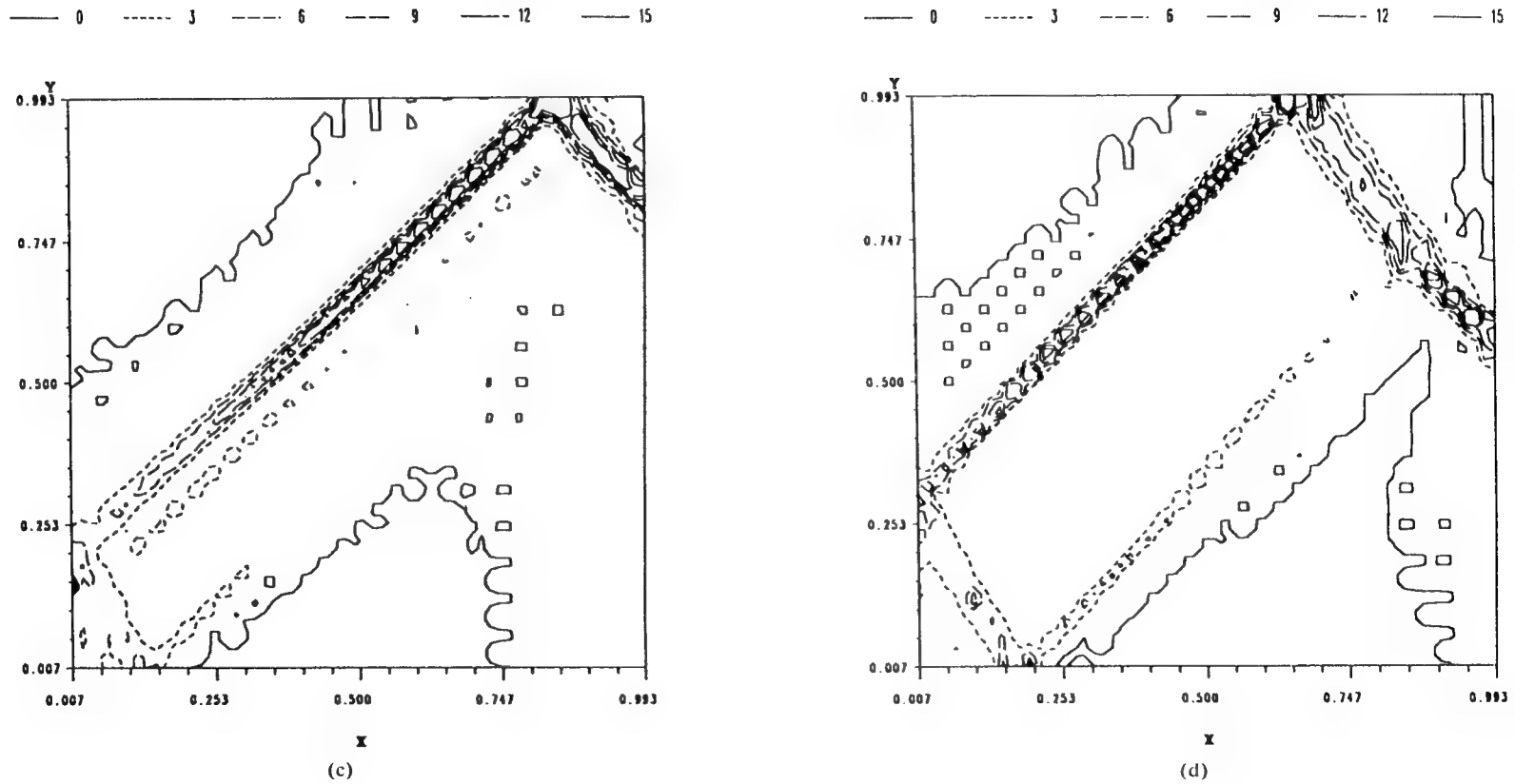

Fig. 11. (c) $\gamma_{avg} = 0.05755$, (d) $\gamma_{avg} = 0.10755$.

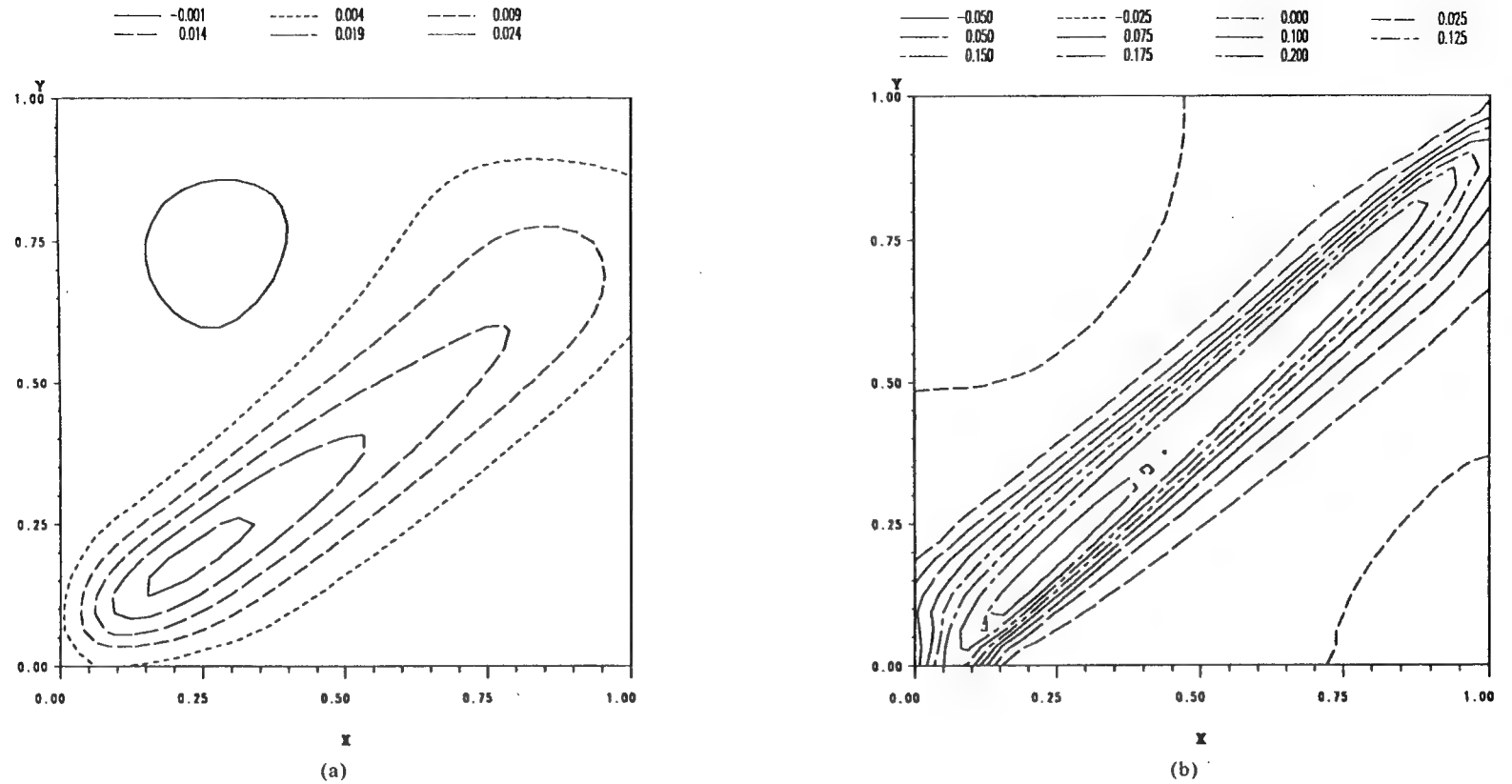

Fig. 12. Contours of the angle of rotation of the crystal lattice at three different values of the average strain. (a) $\gamma_{avg} = 0.00755$, (b) $\gamma_{avg} = 0.02755$. (Figure continues)

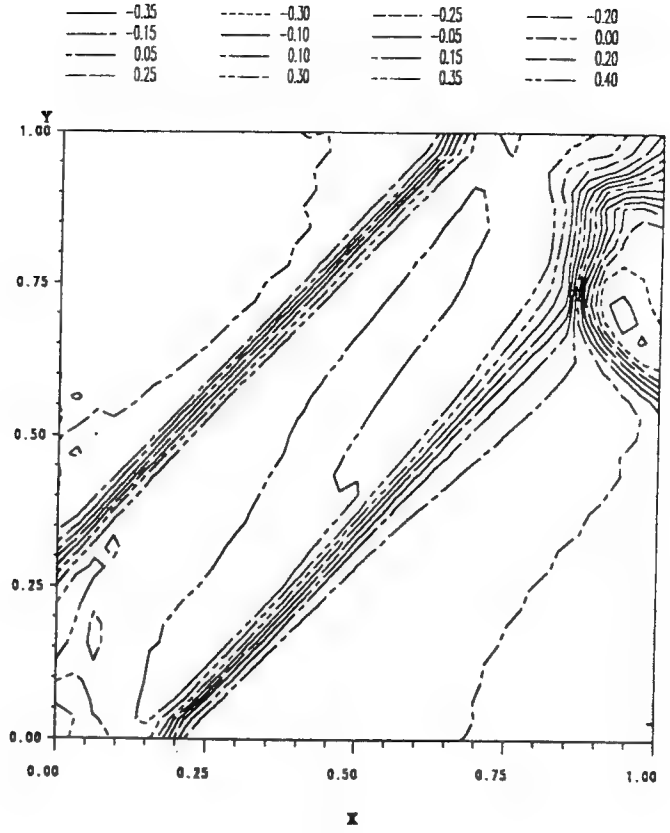

(c)

Fig. 12. (c) $\gamma_{avg} = 0.10755$.

central shear band is 22.9° counterclockwise, and in the reflected band is 17.2° clockwise. These values indicate that the crystal lattice undergoes significant rotations within the shear band.

The distribution of the x- and y-components of the velocity field within the cross-section, at an average strain of 0.0755, is plotted in Figs. 13a and 13b, respectively. It is clear that the deforming region is subdivided into several subregions and the velocity field changes sharply across boundaries between these regions; the changes in v_x and v_y across the upper central band are more than those across the lower central band.

The accumulated slip strains in different slip systems revealed that the slip systems $(111)[10\bar{1}]$ and $(1\bar{1}1)[10\bar{1}]$ remained inactive throughout the entire loading history. Slip systems $(111)[1\bar{1}0]$ and $(111)[0\bar{1}1]$ in both the central and the reflected band, and slip systems $(1\bar{1}1)[110]$ and $(1\bar{1}1)[011]$ in the reflected band were found to be more active than other slip systems. Figures 14 and 15 depict, respectively, the contours of slip strains and slip strain-rates at an average strain of 0.10755. At this value of the nominal strain, the average slip strain of slip systems $(111)[1\bar{1}0]$ and $(111)[0\bar{1}1]$ in the central band equals 0.2 and that in the reflected band is 0.5, and slip systems $(1\bar{1}1)[110]$ and $(1\bar{1}1)[011]$ have an average slip strain of 0.17 in the reflected band. Other active slip systems give very small values of the slip strains within the bands. From contours of slip strain rates in

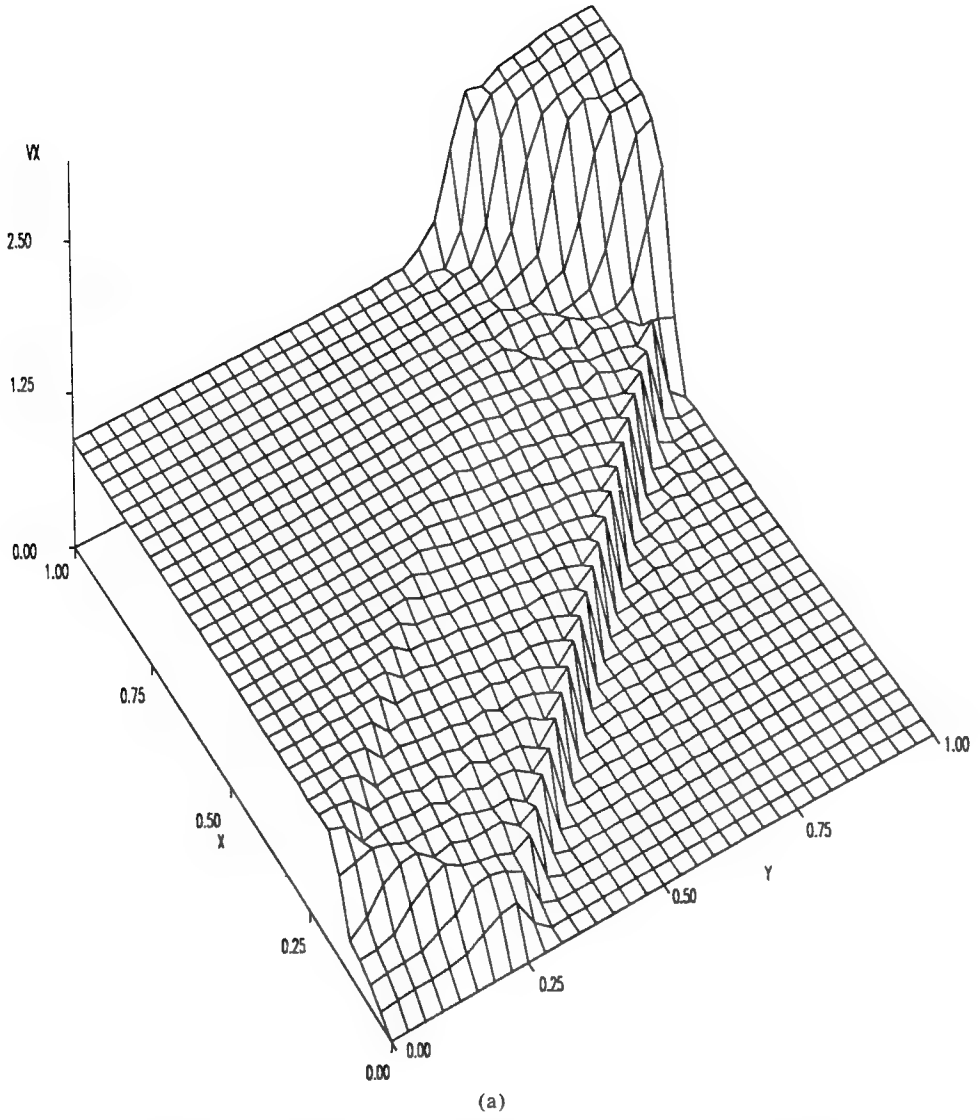

(a)

Fig. 13. (a) Distribution of v_x in the cross-section at an average strain of 0.07755.

Fig. 16, we see that at an average strain of 0.00255, only four slip systems, viz., $(111)[1\bar{1}0]$, $(111)[0\bar{1}1]$, $(1\bar{1}1)[110]$, and $(1\bar{1}1)[011]$ are active everywhere in the block. The narrow region with intensive slip-rate deformation for slip systems $(111)[1\bar{1}0]$ and $(111)[0\bar{1}1]$ differs from that for slip systems $(1\bar{1}1)[110]$ and $(1\bar{1}1)[011]$, in contrast with the case discussed in section III.1 wherein all four primary slip systems are equally active in the same narrow region. However, the intensity of slip-rates in the two narrow regions seems to be nearly the same. Since, in simple compression, the slip systems $(111)[1\bar{1}0]$ and $(111)[0\bar{1}1]$ are more favorable to slip than the other two primary slip systems, these two slip systems eventually dominate the slip deformation of the single crystal and the slip systems $(1\bar{1}1)[110]$ and $(1\bar{1}1)[011]$ become inactive in the central bands.

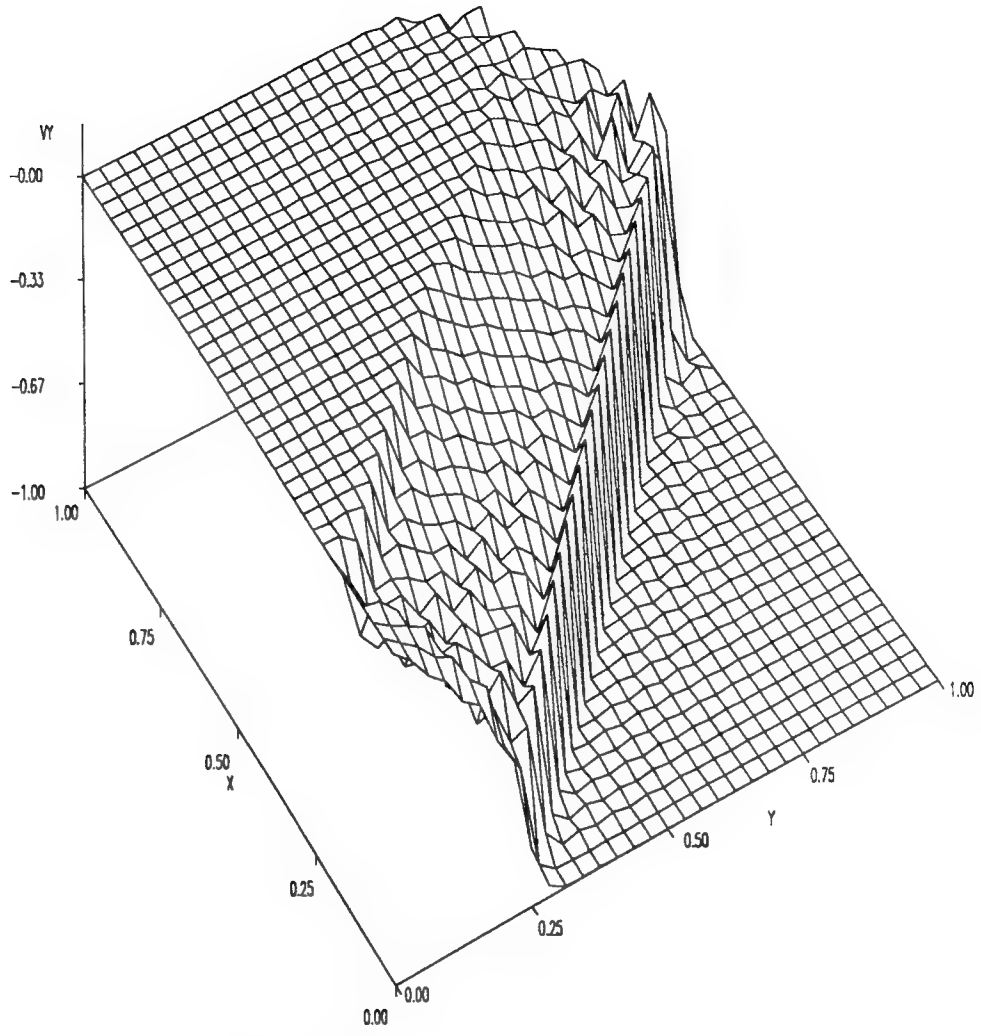

(b)

Fig. 13. (b) Distribution of v_y in the cross-section at an average strain of 0.07755.

Figure 17 exhibits the average axial stress versus the average axial strain for the two loading cases studied herein. The average axial stress is obtained by evaluating σ_{22} at quadrature points closest to the top surface of the block and taking their average. The average axial strain equals the vertical displacement of the top surface divided by the initial height of the specimen. In the figure compressive axial stress and compressive axial strain are plotted as positive. For the second loading case, the curve corresponding to the initial loading of the block is missing because of the loss of a part of the output from the computer code. For each loading case, the transient effects die out quickly, and the average axial stress decreases monotonically with an increase in the average strain because the softening of the material caused by its being heated up exceeds the combined hardening due to strain and strain-rate effects. It is due to the rather large value of the thermal softening coefficient assumed in our work.

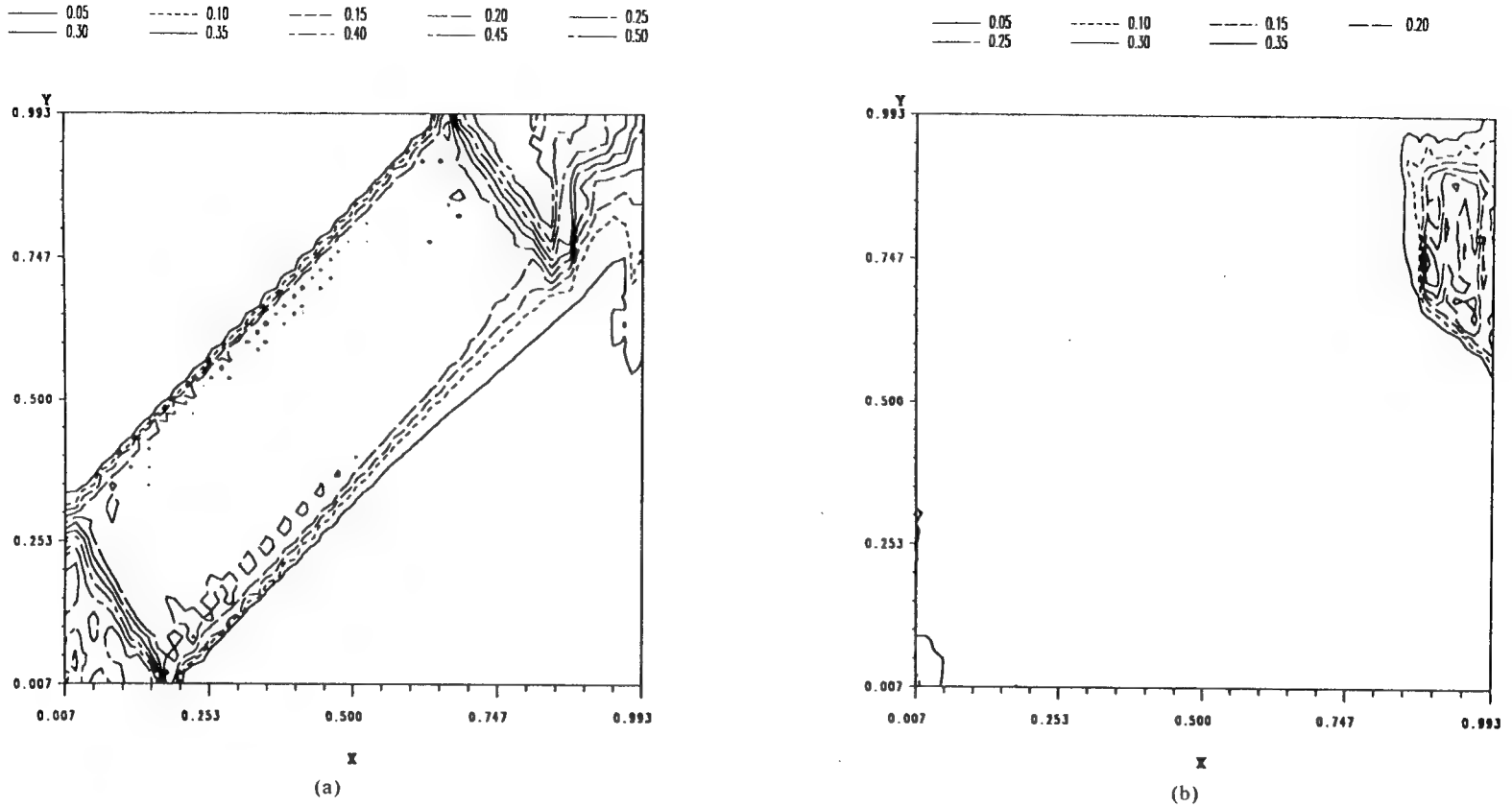

Fig. 14. Contours of the accumulated plastic slip strain in different slip systems at an average strain of 0.10755. (a) Slip systems (111)[1$\bar{1}$0] and (111)[0$\bar{1}$1], (b) Slip systems ($1\bar{1}1$)[110] and ($1\bar{1}1$)[011]. (Figure continues)

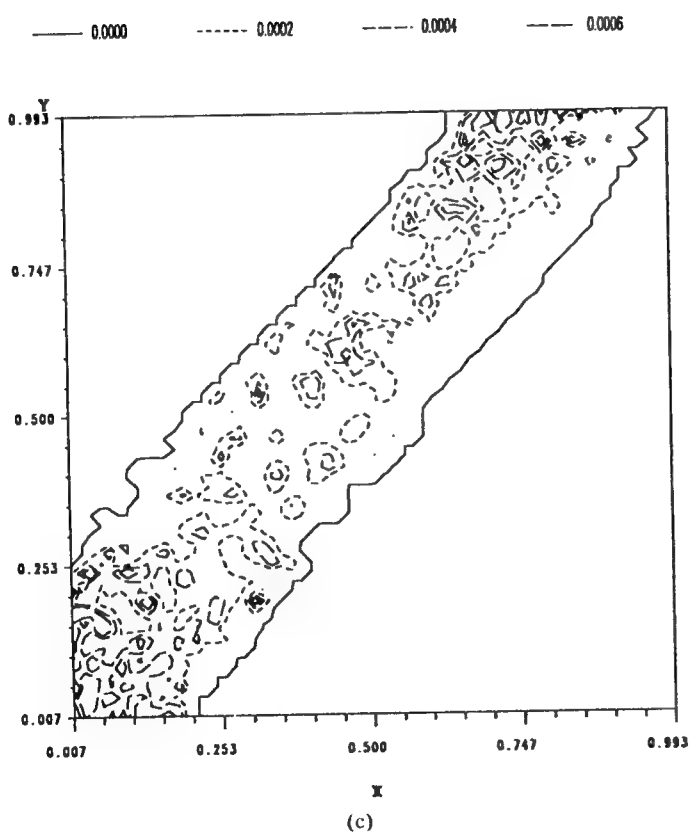

(c)

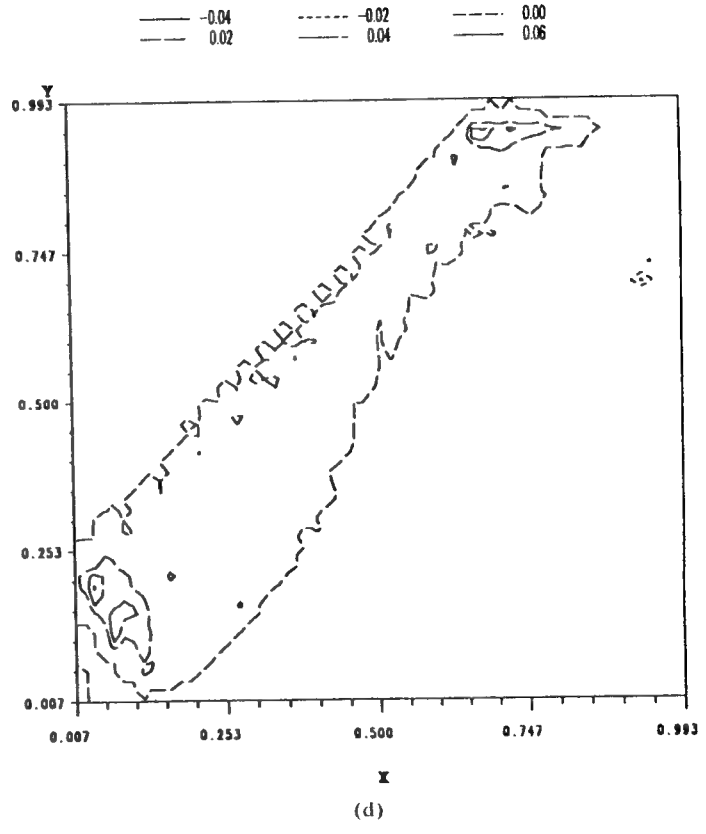

(d)

Fig. 14. (c) Slip systems $(11\bar{1})[0\bar{1}\bar{1}]$ and $(\bar{1}11)[\bar{1}\bar{1}0]$, (d) Slip systems $(11\bar{1})[10\bar{1}]$ and $(\bar{1}11)[\bar{1}0\bar{1}]$. (Figure continues)

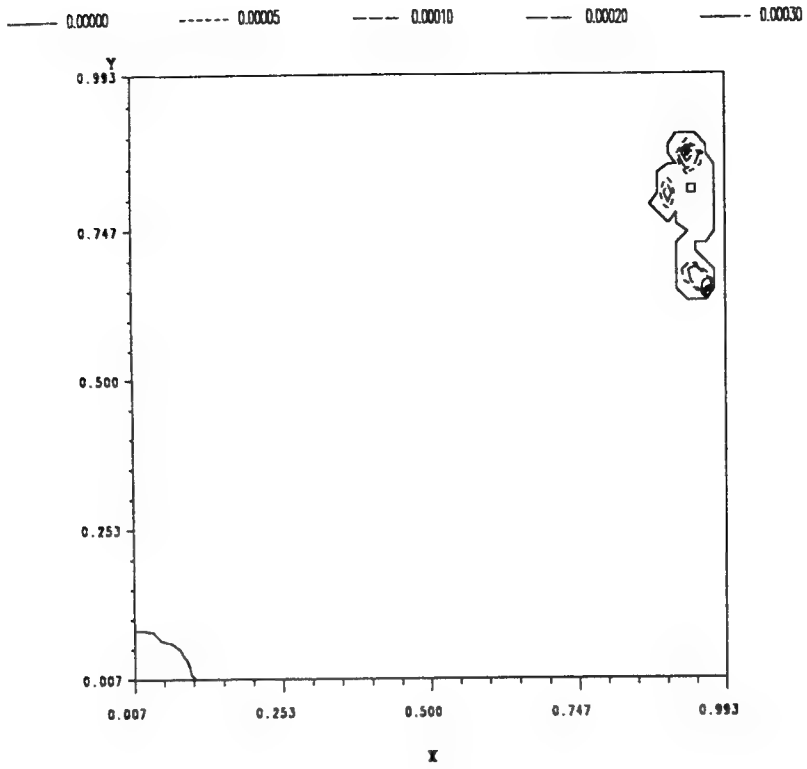

(e)

Fig. 14. (e) Slip systems $(11\bar{1})[1\bar{1}0]$ and $(\bar{1}11)[0\bar{1}1]$.

IV. CONCLUSIONS

We have studied the problem of the initiation and growth of dynamic shear bands in an fcc single crystal deformed in simple compression along the direction [010] of the crystal at a nominal strain-rate of 1000 sec^{-1}. The coupled nonlinear partial differential equations governing the dynamic thermomechanical plane–strain deformations of the single crystal are solved numerically. Two different cases, namely, when the plane of deformation is parallel to the plane (001) or $(10\bar{1})$ of the single crystal, are analyzed. In each case, the deformations are assumed to be symmetric about the horizontal and vertical centroidal axes, and all 12 slip systems are taken to be active. However, only those slip systems for which the resolved shear stress equals or exceeds the critical shear stress contribute to the plastic deformation. The effects of isotropic hardening, kinematic hardening, and thermal softening are incorporated in the expression for the critical shear stress. The deformations of the material in the first quadrant are examined closely.

It is found that when the plane of deformation is parallel to the plane (001) of the single crystal, a single shear band originates from the center of the cross-section and propagates along a line making an angle of 45° with the horizontal. The band is reflected back from the top loading surface, the angle of reflection being nearly equal to the angle

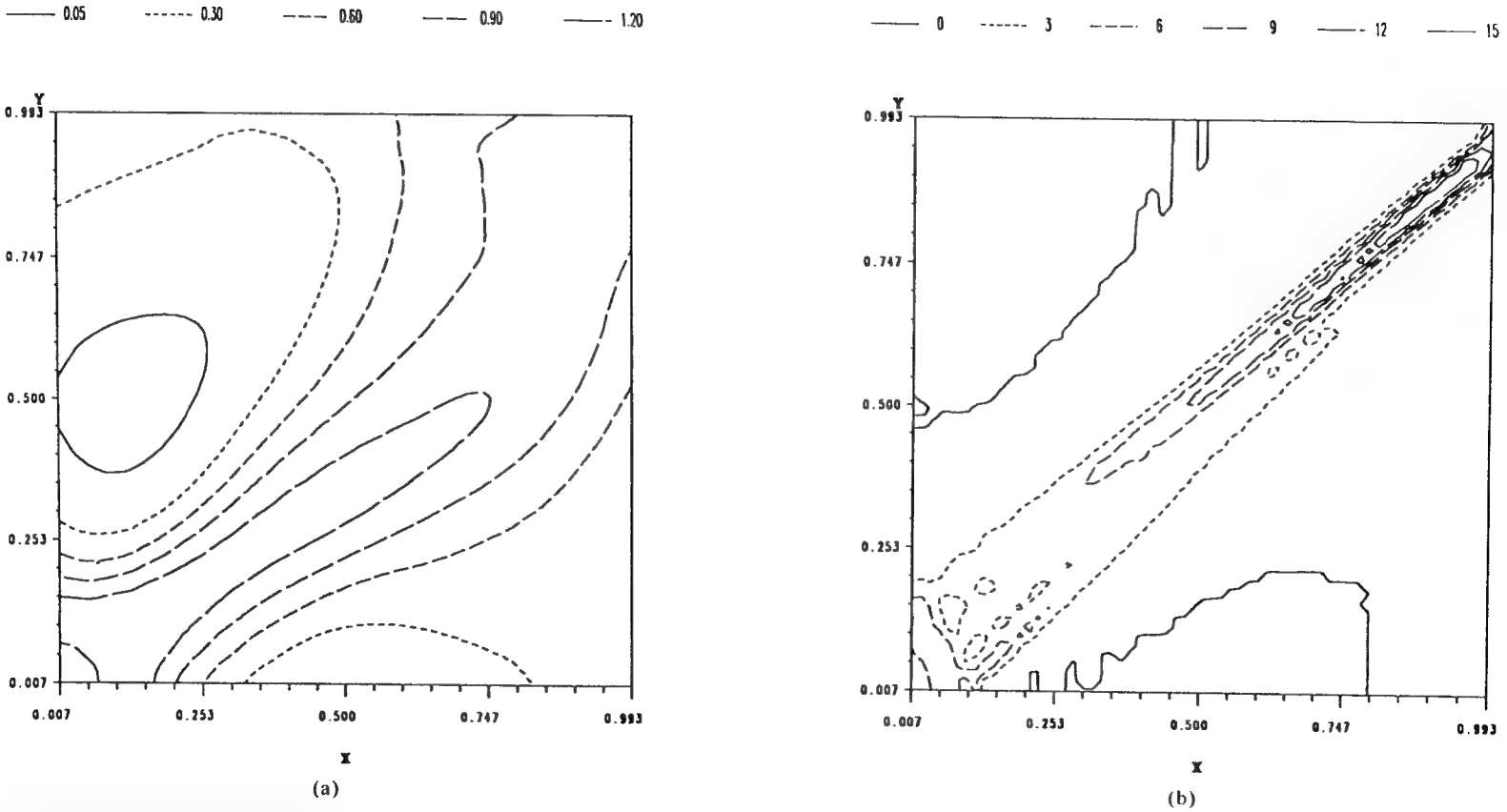

Fig. 15. Contours of the slip strain-rate of slip systems (111)[1$\bar{1}$0] and (111)[0$\bar{1}$1] (a, b, c) and that of slip systems (1$\bar{1}$1)[110] and (1$\bar{1}$1)[011] (d, e, f) at three different values, 0.00255, 0.02755, and 0.10755, of the nominal strain. (Figure continues)

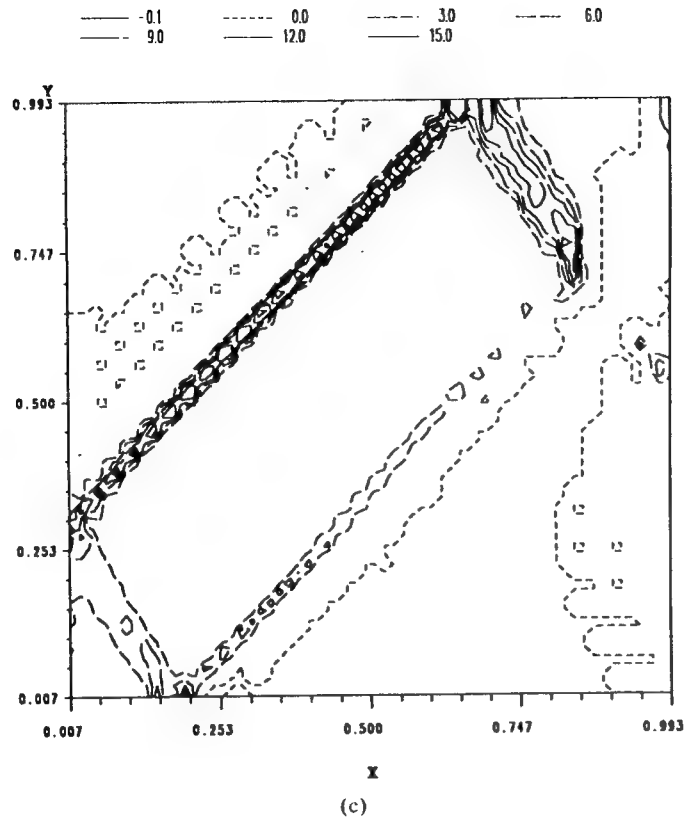

(c)

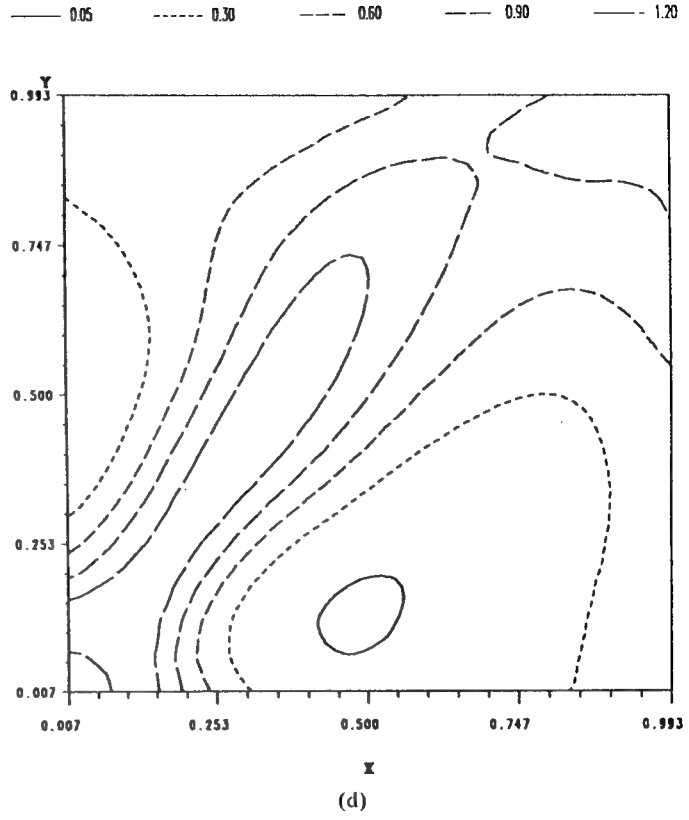

(d)

Fig. 15. (c, d). (Figure continues)

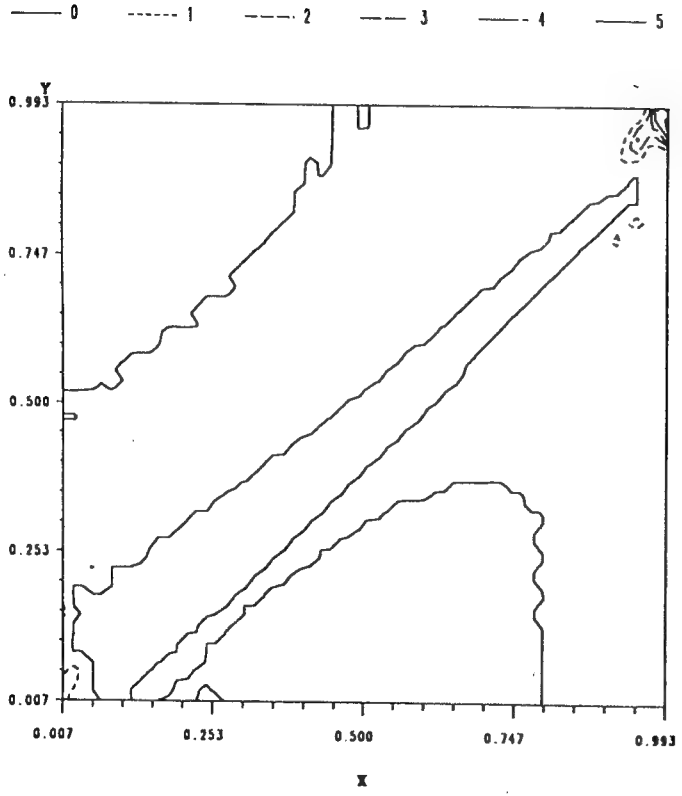
0
1
2
3
4
5
Y
0.993
0.747
0.500
0.253
0.007
0.007
0.253
0.500
0.747
0.993
X

(e)

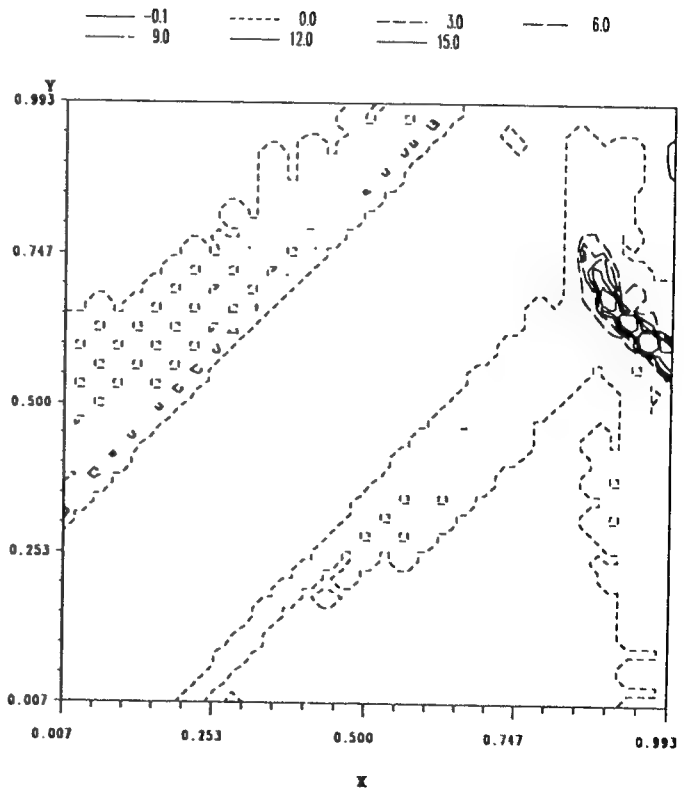
-0.1
0.0
3.0
6.0
9.0
12.0
15.0
Y
0.993
0.747
0.500
0.253
0.007
0.007
0.253
0.500
0.747
0.993
X

(f)

Fig. 15. (e, f)

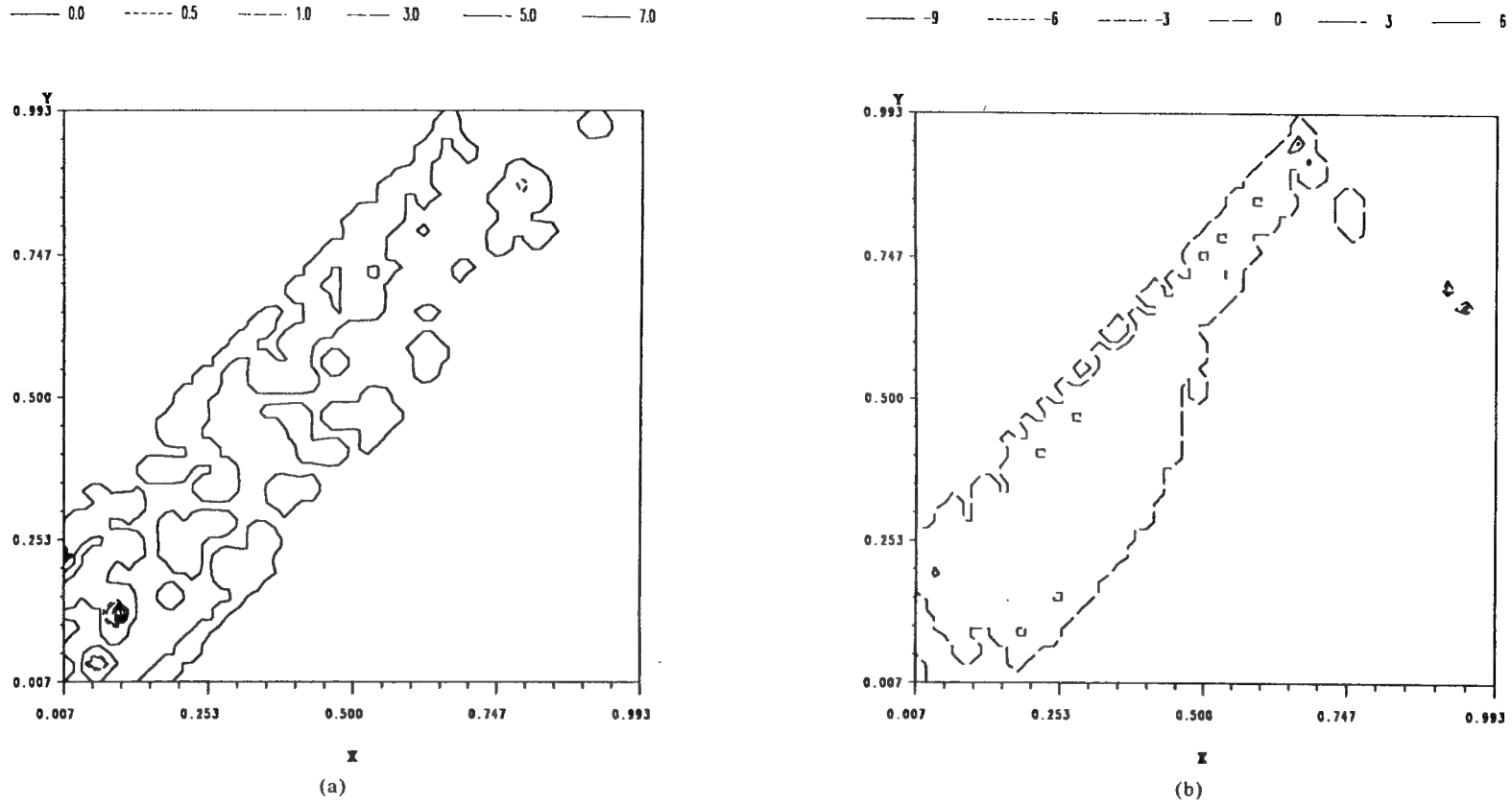

Fig. 16. Contours of the slip strain-rates of different slip systems at an average strain of 0.10755. (a) Slip systems $(11\bar{1})[0\bar{1}\bar{1}]$ and $(\bar{1}11)[\bar{1}\bar{1}0]$, (b) Slip systems $(11\bar{1})[\bar{1}0\bar{1}]$ and $(\bar{1}11)[\bar{1}0\bar{1}]$. (Figure continues)

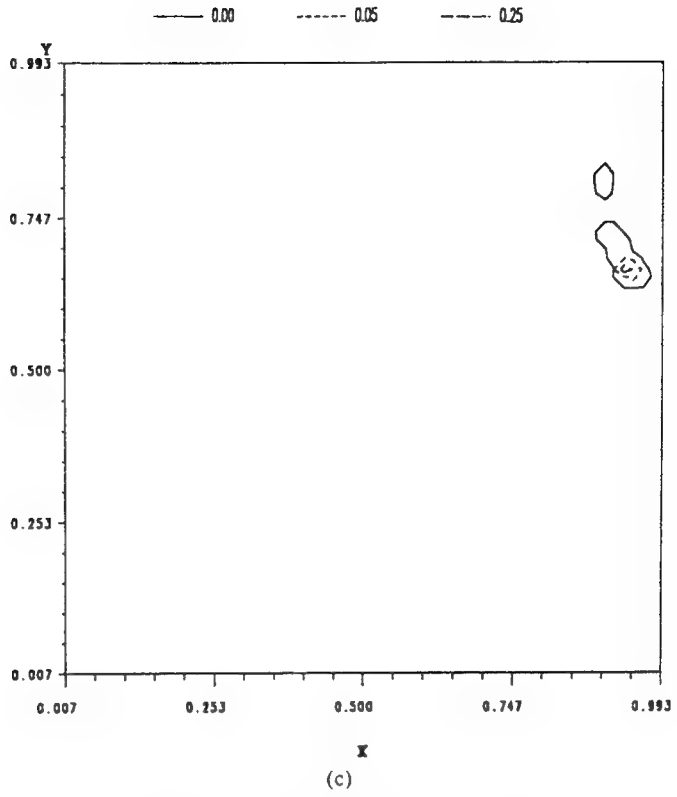

(c)

Fig. 16. (c) Slip systems $(11\bar{1})[1\bar{1}0]$ and $(\bar{1}11)[0\bar{1}1]$.

of incidence. The slip strains on the slip systems $(111)[1\bar{1}0]$, $(11\bar{1})[1\bar{1}0]$, $(1\bar{1}\bar{1})[110]$, and $(1\bar{1}1)[110]$ are very high, and these four slip systems are the primary slip systems. The slip systems $(111)[0\bar{1}1]$, $(11\bar{1})[0\bar{1}\bar{1}]$, $(1\bar{1}\bar{1})[101]$, and $(1\bar{1}1)[10\bar{1}]$ in the central band, and slip systems $(111)[10\bar{1}]$, $(11\bar{1})[101]$, $(\bar{1}11)[0\bar{1}1]$, and $(1\bar{1}1)[011]$ in the reflected band are the conjugate slip systems. At a nominal strain of 0.10755, the average angle of rotation of the crystal lattice within the central band is 14.5° counterclockwise, its maximum value is 18.54° counterclockwise, the average angle of rotation in the reflected band is 14.3° clockwise, and its maximum value is 20.29° clockwise.

When the plane of deformation is parallel to the plane $(10\bar{1})$ of the single crystal, the shear band originating from the center of the cross-section propagates along the line making an angle of 39.5° with the horizontal, and eventually splits into two bands. The intensity of slip-rate in the upper band is higher than that in the lower band. The upper band is reflected from the top surface, and this reflected band stops the lower band from reaching the top surface of the cross-section. Two slip systems, $(111)[10\bar{1}]$ and $(1\bar{1}1)[10\bar{1}]$, remain inactive throughout the entire loading history. Slip systems $(111)[1\bar{1}0]$ and $(111)[0\bar{1}1]$ in both the central and the reflected band, and slip systems $(1\bar{1}1)[110]$ and $(1\bar{1}1)[011]$ in the reflected band were found to be more active than other slip systems. The average value of the angle of rotation of the crystal lattice, at a nominal strain of 0.10755, equalled 22.9° counterclockwise in the central band, and 17.2° clockwise in the reflected band.

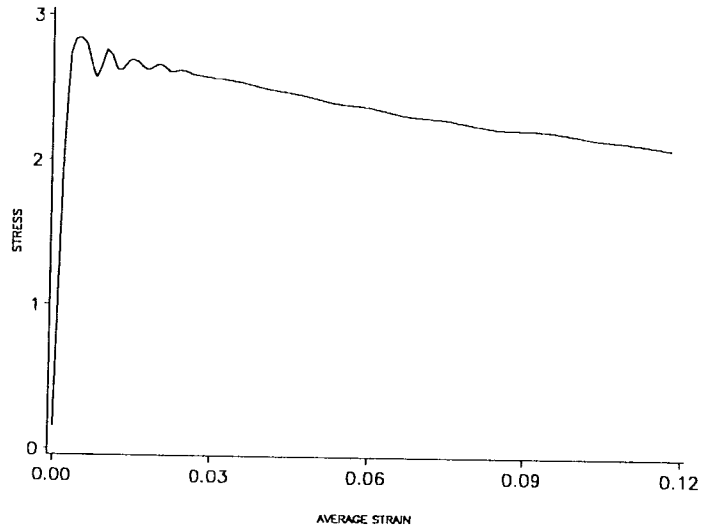

(a)

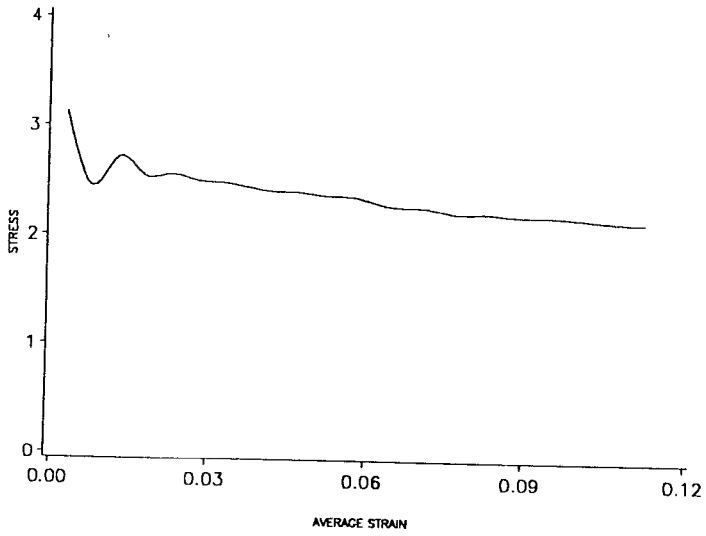

(b)

Fig. 17. Average axial stress vs. the average axial strain for the two cases studied. (a) Plane of deformation is parallel to the plane (001) of the single crystal, (b) Plane of deformation is parallel to the plane (101) of the single crystal.

Acknowledgements—This work was supported by the US Army Research Office grant DAAL03-91-G-0084 and the US NSF grant MSS9121279 to the University of Missouri-Rolla. Some of the computations were performed on the NSF sponsored supercomputer center in Ithaca, NY.

REFERENCES

1878 TRESCA, H., "On Further Application of the Flow of Solids," Proc. Inst. Mech. Engr. **30**, 301.
1921 MASSEY, H.F., "The Flow of Metal During Forging," Proc. Manchester Assoc. Engineers, 21.
1938 TAYLOR, G.I., "Plastic Strain in Metals," J. Inst. Metals, **62-1**, 307.
1952 KOEHLER, J.S., "The Nature of Work-Hardening," Phys. Review, **86**, 52.
1954 OROWAN, E., Dislocation in Metals, American Institute of Mining, Metallurgical and Petroleum Engineers, New York, p. 103.
1954 SAWKILL, J., and HONEYCOMBE, R.W.K., "Strain-Hardening in Face Centered Cubic Metal Crystals," Acta Metall., **2**, 854.
1964 PRICE, R.J., and KELLY, A., "Deformation of Age-Hardened Aluminum Alloy Crystals—II. Fracture," Acta Metall. **12**, 979.
1965 SAIMOTO, S., HOSFORD, W.F., and BACKOFEN, W.A., "Ductile Fracture in Copper Single Crystals," Phil. Mag., **12**, 319.
1980 WENG, G.J., "Dislocation Theories of Work Hardening and Yield Surfaces of Single Crystal," Acta Mechanica, **37**, 217.
1981 CHANG, Y.W., and ASARO, R.J., "An Experimental Study of Shear-Localization in Aluminum-Copper Single Crystals," Acta Metall., **29**, 241.
1983 HINDMARSH, A.C., "ODEPACK: A Systematized Collection of ODE Solvers," in STEPLEMAN, R.S. *et al.*, (eds.), Scientific Computing, Amsterdam, North Holland, pp. 55–64.
1983 PAN, J., and RICE, J.R., "Rate Sensitivity of Plastic Flow and Implication for Yield Surface Vertices," Inst. J. Solids and Structures, **19**, 973.
1987 HUGHES, T.J.R., The Finite Element Method. Linear Static and Dynamic Finite Element Analysis, Prentice-Hall, Englewood Cliffs, NJ.
1989 BATRA, R.C., and LIU, D.S., "Adiabatic Shear Banding in Plane Strain Problems," J. Appl. Mech., **56**, 527.
1990 ZIKRY, M.A., and NEMAT-NASSER, S., "High Strain-Rate Localization and Failure of Crystalline Materials," Mechs. Materials, **10**, 215.

Department of Mechanical and Aerospace Engineering and Engineering Mechanics
University of Missouri-Rolla
Rolla, MO 65401-0249, USA

(*Received* 4 *June* 1992; *in final revised form* 5 *November* 1992)

Computational Mechanics (1993) 12, 255-268

Computational Mechanics

An adaptive mesh refinement technique for two-dimensional shear band problems

R. C. Batra and **J. Hwang**

Department of Mechanical and Aerospace Engineering and Engineering Mechanics, University of Missouri-Rolla, Rolla, MO 65401-0249, USA

Abstract. We have developed an adaptive mesh refinement technique that rezones the given domain for a fixed number of quadrilateral elements such that fine elements are generated within the severely deformed region and coarse elements elsewhere. Loosely speaking, the area of an element is inversely proportional to the value of the deformation measure at its centroid. Here we use the temperature rise at a material point to gauge its deformations which is reasonable for the shear band problem since the material within the shear band is deformed intensely and is heated up significantly. It is shown that the proposed mesh refinement technique is independent of the initial starting mesh, and that the use of an adaptively refined mesh gives thinner shear bands, and sharper temperature rise and the growth of the second invariant of the plastic strain-rate within the band as compared to that for a fixed mesh having the same number of nodes. The method works well even when the deformation localizes into more than one narrow region.

1 Introduction

Most of the previous two-dimensional numerical studies of shear bands have used a fixed finite element mesh (e.g., see Batra and Liu 1989; Needleman 1989; Batra and Zhu 1991), an exception seems to be the recent work of Batra and Ko (1992) who developed a mesh refinement technique that generates fine triangular elements in the severely deforming region and coarse elements elsewhere. They added more elements to the region as the localization of the deformation into a narrow band progressed. Assuming that enough core storage is available in the computer being used, this technique enables one to resolve sharp gradients of the deformation within the severely deforming region in as great a detail as desired. Of course, adding new elements increases the computational cost, necessitates the generation of a new element topology, and may eventually make the system of algebraic equations to be solved ill-conditioned and/or extremely stiff. One could circumvent this by limiting the ratio of the largest to the smallest element in the mesh. Another way to refine a mesh is to use a fixed number of elements and nodes, and adjust the locations of nodes so as to concentrate fine elements in the severely deforming regions and coarse elements elsewhere. It keeps the element topology fixed and thus requires less bookkeeping and can be easily implemented in an existing code. It is shown that the mesh so generated is independent of the starting mesh and can adequately delineate the localization of the deformation into narrow bands.

For one-dimensional problems, Drew and Flaherty (1984) have used the moving grid method to develop an adaptive finite element code that locates regions with large gradients and concentrates fine elements there in order to minimize approximately the discretization error per time step. Pervaiz and Baron (1988) have discussed an adaptive technique which refines the spatial and or temporal grid whenever preselected gradients exceed the threshold levels and have applied it to study quasi-one-dimensional unsteady flow problems involving finite rate chemistry. Batra and Kim (1990) developed an adaptive mesh refinement technique that distributes uniformly the scaled residuals of equations expressing the balance of linear momentum and the balance of internal energy. They subdivided elements having large scaled residuals and noted that large values of the scaled residuals occurred, in general, in non-overlapping regions. Their technique did not combine elements with large scaled residuals, and thus did not result in an optimum mesh.

We refer the reader to Safjan et al. (1991) and Zienkiewicz and Zhu (1991) for an extensive list of references on adaptive mesh refinement, to Batra and Zhu (1991) for several references on adiabatic shear banding, and to the recent book by Bai and Dodd (1992) for a summary of the work completed on adiabatic shear banding till 1989.

2 Formulation of the shear band problem

We study plane strain thermomechanical deformations of a thermally softening viscoplastic prismatic body of square cross-section, and use a fixed set of rectangular Cartesian coordinates with origin at its centroid (see Fig. 1). In terms of the referential description, governing equations are:

$$(J)^{\cdot} = 0, \quad \rho \dot{v}_i = T_{i\alpha,\alpha}, \quad \rho \dot{e} = -Q_{\alpha,\alpha} + T_{i\alpha} v_{i,\alpha}, \tag{1-3}$$

where

$$J = \det F_{i\alpha}, \quad F_{i\alpha} = x_{i,\alpha} \equiv \partial x_i / \partial X_\alpha, \tag{4}$$

x_i is the present position of a material particle that occupied place X_α in the reference configuration, ρ its mass density, v_i its present velocity, a superimposed dot signifies the material time derivative, a comma followed by an index $\alpha(i)$ stands for partial derivative with respect to X_α (x_i), a repeated index implies summation over the range of the index, $\mathbf{T}$ is the first Piola–Kirchhoff stress tensor, e is the specific internal energy, and $\mathbf{Q}$ is the heat flux per unit undeformed area. Equation (1) implies that the deformations are isochoric. The balance laws (1)–(3) are supplemented by the following constitutive relations

$$\sigma_{ij} = -p\delta_{ij} + 2\mu D_{ij}, \quad T_{i\alpha} = X_{\alpha,j}\sigma_{ij}, \quad 2\mu = \frac{\sigma_o}{\sqrt{3}I}(1+bI)^m\left(1+\frac{\psi}{\psi_o}\right)^n(1-v\theta), \quad \dot{e} = c\dot{\theta}, \tag{5,6}$$

$$Q_\alpha = X_{\alpha,j}q_j, \quad q_i = -k\theta_{,i}, \quad \dot{\psi} = \sigma_{ij}D_{ij}\Big/\left(1+\frac{\psi}{\psi_o}\right)^n, \quad 2D_{ij} = v_{i,j} + v_{j,i}, \quad 2I^2 = D_{ij}D_{ij}. \tag{7,8}$$

Here $\boldsymbol{\sigma}$ is the Cauchy stress tensor, p the hydrostatic pressure not determined by the deformation history of the material point, $\mathbf{D}$ the strain-rate tensor, σ_o the yield stress of the material in a quasistatic simple tension or compression test conducted at the room temperature, parameters b and m characterize the strain-rate sensitivity of the material, ψ_o and n its strain-hardening, v is the thermal softening coefficient, c the specific heat, k the thermal conductivity, and θ equals the temperature rise of a material particle. All of the material parameters are assumed to be independent of the temperature. Here we have neglected elastic deformations of the body since our

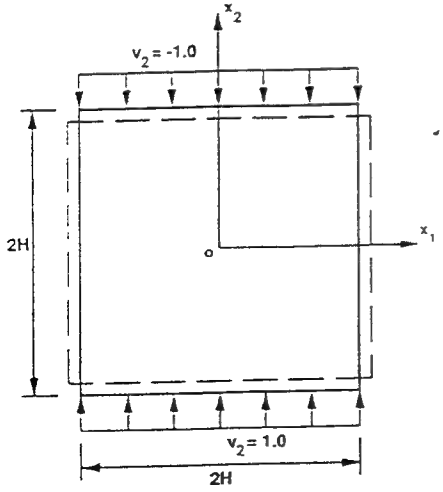

Fig. 1. A schematic sketch of the problem studied

interest is to study intense plastic deformations within the shear band. Also, all of the plastic working has been assumed to be converted into heating of the body.

We nondimensionalize variables by scaling stress like quantities by σ_o, time by H/v_o, length by H, and temperature by the reference temperature θ_r defined as

$$\theta_r = \sigma_o/(\rho c). \tag{9}$$

Here 2H is the height of the square block and v_0 the steady value of the velocity applied to the top and bottom surfaces in the x_2-direction. Henceforth we use nondimensional variables only and indicate them by the same symbols as those used for dimensional variables.

We assume that the initial and boundary conditions are such that the deformations of the block are symmetrical about the horizontal and vertical centroidal axes, and study deformations of the material in the first quadrant. We take all four surfaces of the region studied to be thermally insulated and free of tangential tractions. Because of the assumed symmetry of deformations, the normal velocity is zero on the left and bottom surfaces. The right vertical surface is taken to be free of normal tractions also, and a uniform vertically downward velocity of unit magnitude is applied on the top surface. For the initial conditions, we take

$$v_1(\mathbf{x}, 0) = x_1, \quad v_2(\mathbf{x}, 0) = -x_2, \tag{10.1}$$

$$\theta(\mathbf{x}, 0) = \theta_o + \varepsilon(1 - r^2)^9 e^{-5r^2}, \quad r^2 \equiv X_1^2 + X_2^2 \leqq 1,$$
$$= \theta_o, \quad r > 1. \tag{10.2}$$

That is, the transients have died out. It is highly unlikely that the transients will die out simultaneously throughout the body. However, the assumption is justified on the grounds that it does not affect the qualitative nature of results and reduces significantly the CPU effort necessary to solve the problem. The initial temperature distribution (10.2) models a material inhomogeneity; the height ε of the temperature bump can be thought of as representing the strength of the singularity.

The problem formulated above is highly nonlinear. We assume that it has a solution and find its approximation by the finite element method. We use four-noded quadrilateral elements, take the hydrostatic pressure to be constant within each element, and use 2×2 Gauss quadrature rule to evaluate various integrals over an element, and the lumped mass matrix obtained by employing the special lumping technique (e.g. see Hughes (1987)). The Galerkin approximation of the governing equations gives a set of coupled highly nonlinear ordinary differential equations (ODEs) for nodal values of two components of the velocity, temperature, internal variable ψ, and the values of the hydrostatic pressure p within each element. The ODEs are integrated by using the trapezoidal rule, hydrostatic pressure p is eliminated at the element level, and the nonlinear algebraic equations are solved iteratively by using one of the following two convergence criteria at each node point:

$$\frac{|\Delta v_1|}{|v_1|} + \frac{|\Delta v_2|}{|v_2|} + \frac{|\Delta\theta|}{\theta} + \frac{|\Delta\psi|}{\psi} \leqq \varepsilon_1, \quad |\Delta v_1| + |\Delta v_2| + |\Delta\theta| + |\Delta\psi| \leqq \varepsilon_2. \tag{11.1, 11.2}$$

Here ε_1 and ε_2 are preassigned small numbers, and $\Delta\theta$ equals the difference in the nodal values of θ during two successive iterations within the same time increment. At boundary points where v_1 or v_2 is prescribed to be zero, Eq. (11.1) is not valid.

3 Adaptive mesh refinement technique

Here we discuss a mesh refinement technique in which the total number of elements, nodes and the element connectivity are kept fixed. The nodes are repositioned so that

$$a_e = \int_{\Omega_e} \eta \, d\Omega, \quad e = 1, 2, \ldots, n_{el}, \tag{12}$$

is nearly the same for each element Ω_e. In (12), η is a measure of the deformation such as the second invariant of the strain-rate tensor, temperature rise θ, the equivalent plastic strain, or the internal

variable ψ, n_{el} equals the number of elements desired in the mesh and Ω_e is one of the elements. Our reason for making a_e the same over each element Ω_e is that within the region of localization of the deformation values of η are expected to be very high as compared to those in the remaining region. The refined mesh will depend upon what deformation measure is associated with η; here we take η to be the temperature rise θ.

Having solved the problem on an initial mesh we refine it as follows. We begin with either the horizontal boundary or the vertical one and relocate nodes on it according to the criterion described below. To be definite, let us begin with the left vertical edge. After having repositioned nodes on it we do the same on the almost vertical curve that passes through nodes next to the left vertical side, and continue the process till we reach the right vertical edge. The procedure is then repeated beginning with the top or bottom horizontal edge and going to the other end.

Referring to Fig. 2, let AB be the curve on which nodes are to be relocated. We plot the temperature distribution on AB with abscissa as the distance of a point from A measured along AB and ordinate as the temperature at that point. Values of temperature at numerous points on AB are obtained by linear interpolation from the values at node points. If S equals the total area under the curve, the approximate location s_n^a of the nth node on AB is given by

$$\int_{s_{n-1}}^{s_n^a} \theta \, ds = \frac{S}{N_{es}}, \tag{13}$$

where N_{es} equals the number of elements on AB. We reposition the node to the interpolation point immediately to the left of its approximate location determined from Eq. (13). In Fig. 2c, the position of a node as found from Eq. (13) is shown by a superimposed prime, and its relocation in Fig. 2d by superimposed two primes. Since the end points on AB are kept fixed, the aforestated procedure can be employed by starting from either A or B. Note that when nodes on an approximate horizontal curve are relocated, positions of nodes A and B will change.

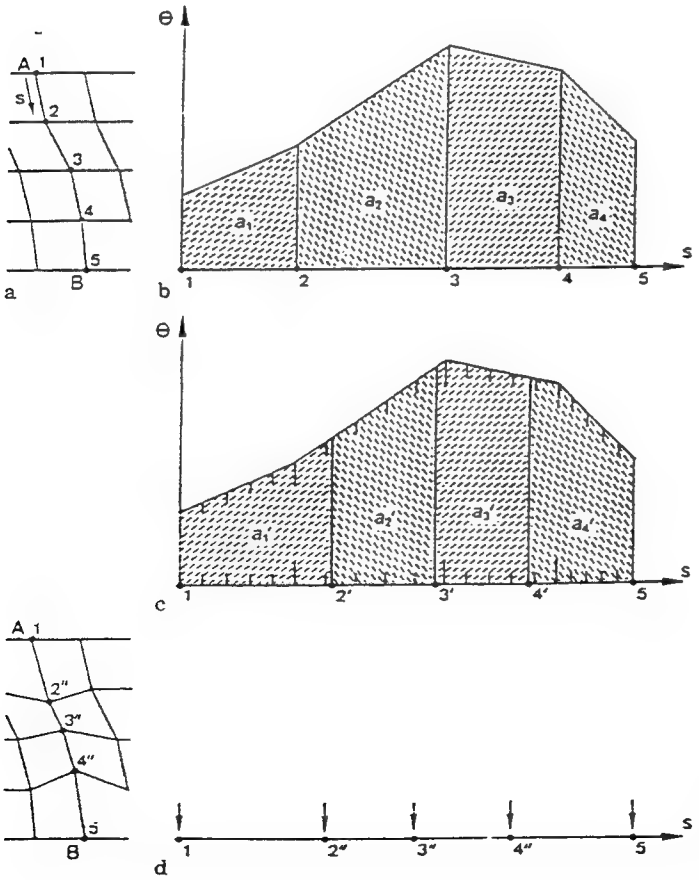

Fig. 2. a Curve AB on which nodes are to be relocated. b Temperature distribution on curve AB on which nodes are to be repositioned. c Temporary position on curve AB of relocated nodes. d Repositioned nodes on curve AB

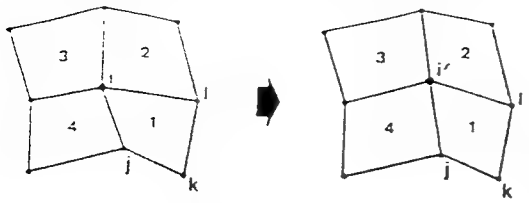

Fig. 3. Relocation of an interior node to smoothen out the generated mesh

The quadrilateral elements produced by the aforestated simple technique are not always well shaped in the sense that one of the interior angles may be either too small or too large. It usually happens in regions where the element size varies noticeably. We use the mesh smoothing method of Zhu et al. (1991) to improve upon the shapes of quadrilateral elements. Each internal node is repositioned to the centroid of the polygon formed by all of the elements meeting at the node. As illustrated in Fig. 3, the internal node i is moved to i' with coordinates given by

$$x_i' = \frac{1}{4M}\sum_{a=1}^{M}(x_j + 2x_k + x_l)_a, \quad y_i' = \frac{1}{4M}\sum_{a=1}^{M}(y_j + 2y_k + y_l)_a. \tag{14}$$

where M is the number of elements sharing node i. After having relocated all of the internal nodes, the element shapes are checked to see if all interior angles of every element are between 20° and 160°. If not, the nodes are repositioned according to Eq. (14) till such is the case. For the problems studied herein, the mesh smoothing procedure had to be applied atmost three times to generate a satisfactory mesh. Because of the smoothening of the mesh, the value of a_e defined by Eq. (12) is only approximately the same for all elements in the mesh.

4 Results and discussion

In order to illustrate the aforestated mesh refinement technique we compute results for the shear band problem with various variables assigned the following values.

$$b = 10000\,\text{sec}, \quad \nu = 0.0222\,^{\circ}\text{C}^{-1}, \quad \sigma_0 = 333\,\text{MPa}, \quad k = 49.22\,\text{Wm}^{-1}\,^{\circ}\text{C}^{-1},$$
$$c = 473\,\text{Jkg}^{-1}\,^{\circ}\text{C}^{-1}, \quad \rho = 7860\,\text{kg m}^{-3}, \quad m = 0.025, \quad n = 0.09,$$
$$\psi_0 = 0.017, \quad H = 5\,\text{mm}, \quad v_0 = 25\,m/s, \quad \varepsilon = 0.2, \quad \varepsilon_1 = 10^{-3}, \quad \varepsilon_2 = 10^{-3}, \quad \theta_0 = 0. \tag{15}$$

These values except that for ν are for a typical steel and were also used by Batra and Ko (1992). Note that here we also account for the work hardening of the material through the internal variable ψ. Values of parameters given in (15) imply that the average strain-rate equals $5000\,\text{sec}^{-1}$, $\theta_r = 89.6\,^{\circ}\text{C}$, and the nondimensional melting temperature equals 0.503. The higher values of ν and ε speed up the initiation of a shear band and cut down significantly the CPU time required to study the problem without affecting the qualitative nature of results. The test data to find values of material parameters at strain-rates, strains and temperatures likely to occur in a shear band is not currently available, and a quantitative comparison of computed results with test findings is still not feasible.

Figure 4a shows the initial mesh consisting of 400 uniform elements, the generated refined meshes when the temperature θ at the centroid equalled 0.25, 0.35, and 0.45 are plotted in Figs. 4b, 4c, and 4d, respectively; the mesh was also refined when θ at the centroid reached 0.30 and 0.40, but these are not depicted in the figure for the sake of brevity. We choose to refine the mesh for equal increments of the temperature rise. However, other criteria such as the second invariant I of the strain-rate tensor attaining certain values, or equal increments in the value of ψ would be equally good. The meshes shown in Fig. 4 vividly reveal that the aforestated refinement technique generated a nonuniform mesh with finer elements in the severely deformed region and coarse elements elsewhere. The mesh smoothing criterion (14) had to be applied atmost three times to satisfy the requirement that the interior angles of every quadrilateral element be between 20° and 160°. We note that the mesh generation scheme does not impose any restriction on the ratio of

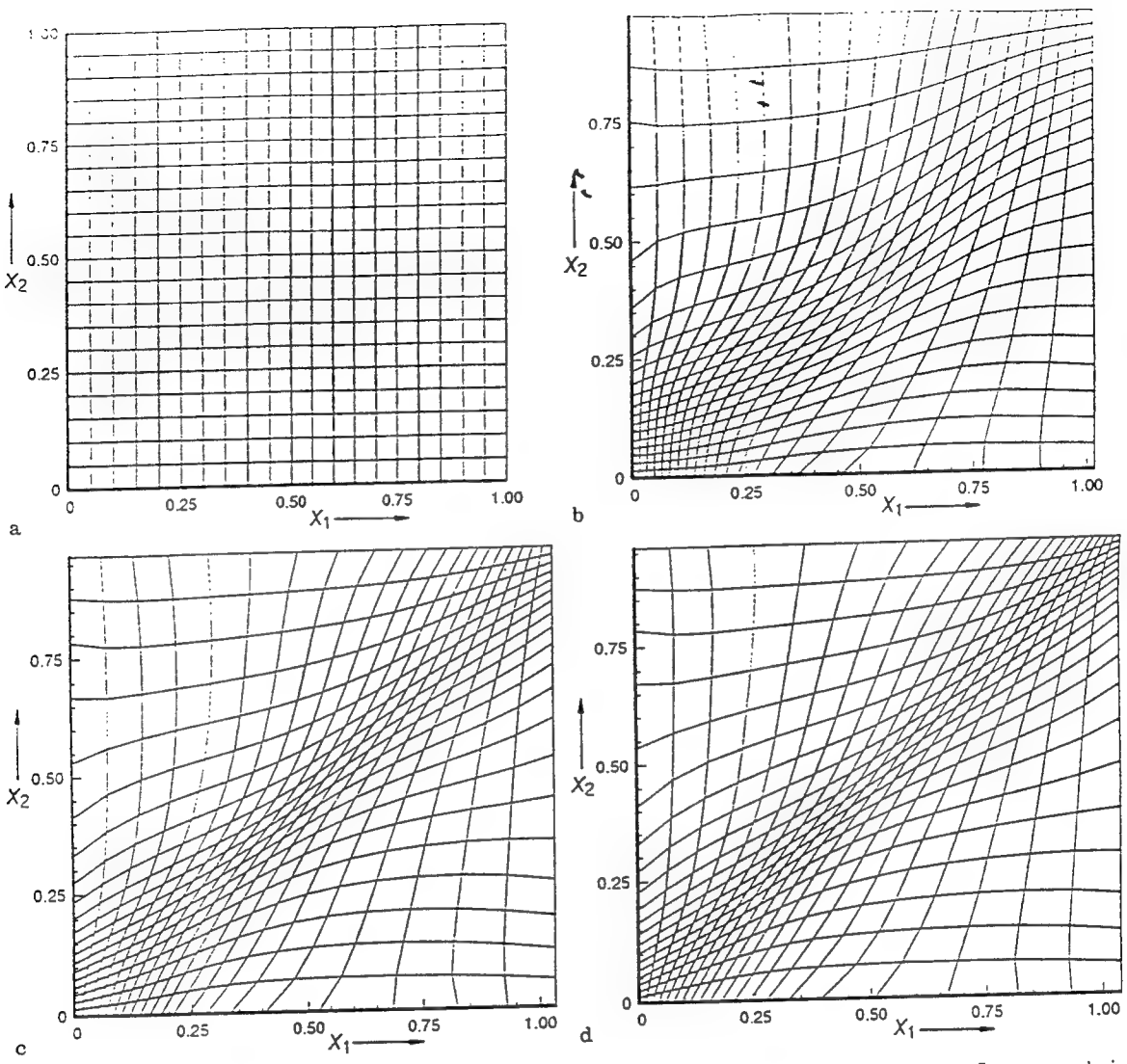

Fig. 4. a Initial uniform mesh of 400 elements. b–d Finite element meshes generated by using the mesh refinement technique when the temperature at the center of the specimen reached 0.25, 0.35, and 0.45

the area of the largest to that of the smallest element in the mesh. Even though this did not cause an unduly skewed mesh to be generated for the present problem, in other situations such a restriction may be necessary. One could avoid this either by having more elements in the initial mesh or by adding more elements at a few intermediate stages. The latter would necessitate the creation of a new element topology.

Figure 5 exhibits, in the deformed configuration, contours of the second invariant I of the deviatoric strain-rate tensor when the average strain $\bar{\gamma}_{avg} = 0.0166$, 0.0352, and 0.044. These evidence that as the block continues to be deformed, the deformation localizes into an increasingly narrower band. The contours of I in the deformed configuration at $\bar{\gamma}_{avg} = 0.044$ obtained by using a fixed mesh of initially 400 uniform elements plotted in Fig. 5d affirm the advantage of using an adaptively refined mesh. Not only the computed peak values of I within the band are higher for the refined mesh, the width of the region of localization is much narrower as compared to that obtained with a fixed mesh. From these contours one can estimate the band centerline to be the curve CED shown in Fig. 6a. In Figs. 6b and 6c, we have exhibited the variation, at different times, of the temperature rise θ and the second invariant I of the deviatoric strain-rate tensor on line AB that is perpendicular to the estimated band centerline and is shown in Fig. 6a. These plots confirm

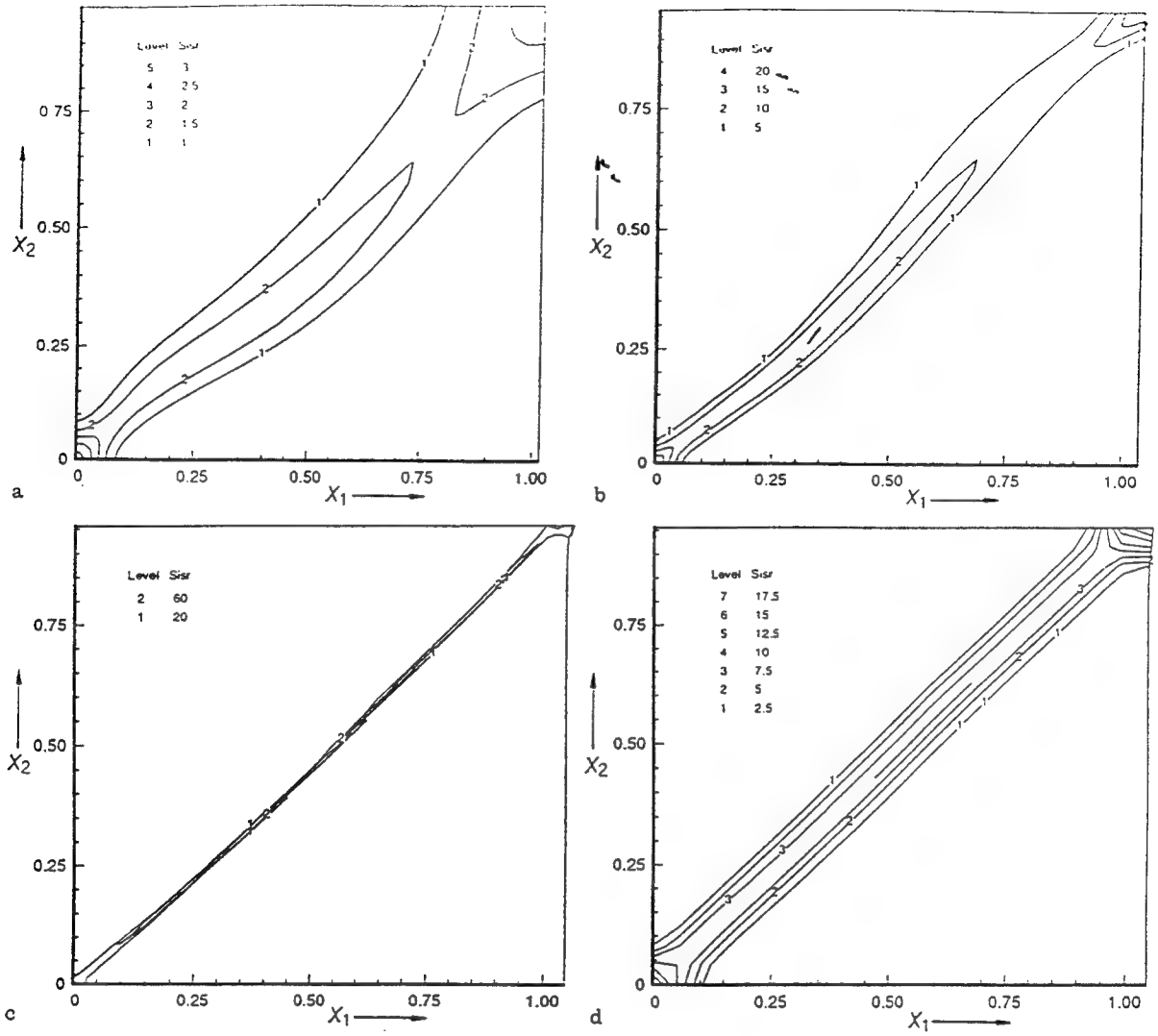

Fig. 5. a–c Contours of the second invariant I of the deviatoric strain-rate tensor at $\gamma_{avg} = 0.0166, 0.0352$, and 0.044 d Contours of the second invariant I of the deviatoric strain-rate tensor at $\gamma_{avg} = 0.044$ for a fixed mesh of 400 elements

the localization of the deformation into a narrow band as the block continues to be compressed. We note that the temperature rise θ is a measure of the total plastic work done at a point since the final nondimensional time of 0.044 equals 8.8 μs and the heat conducted away from a point during that interval is indeed minuscule. Thus, not only the accumulated deformation within the band is large, the material there is deforming severely at $t = 0.044$ as indicated by the high values of I there.

In Fig. 7 we have plotted for the fixed uniform mesh and for the adaptively refined mesh the evolution at the origin of the temperature rise, the second invariant I of the deviatoric strain-rate tensor and the effective stress s_e defined as

$$s_e = \sqrt{\frac{2}{3}}(1 - v\theta)(1 + bI)^m(1 + \psi/\psi_0)^n. \tag{16}$$

It is clear that the rates of growth of θ and I and the rate of drop of s_e at the origin are sharper for the refined mesh as compared to that for the fixed mesh with the same number of nodes. Computations were stopped when the temperature at the origin reached the presumed melting temperature of the material. There is no assurance that the computed results are optimum for the

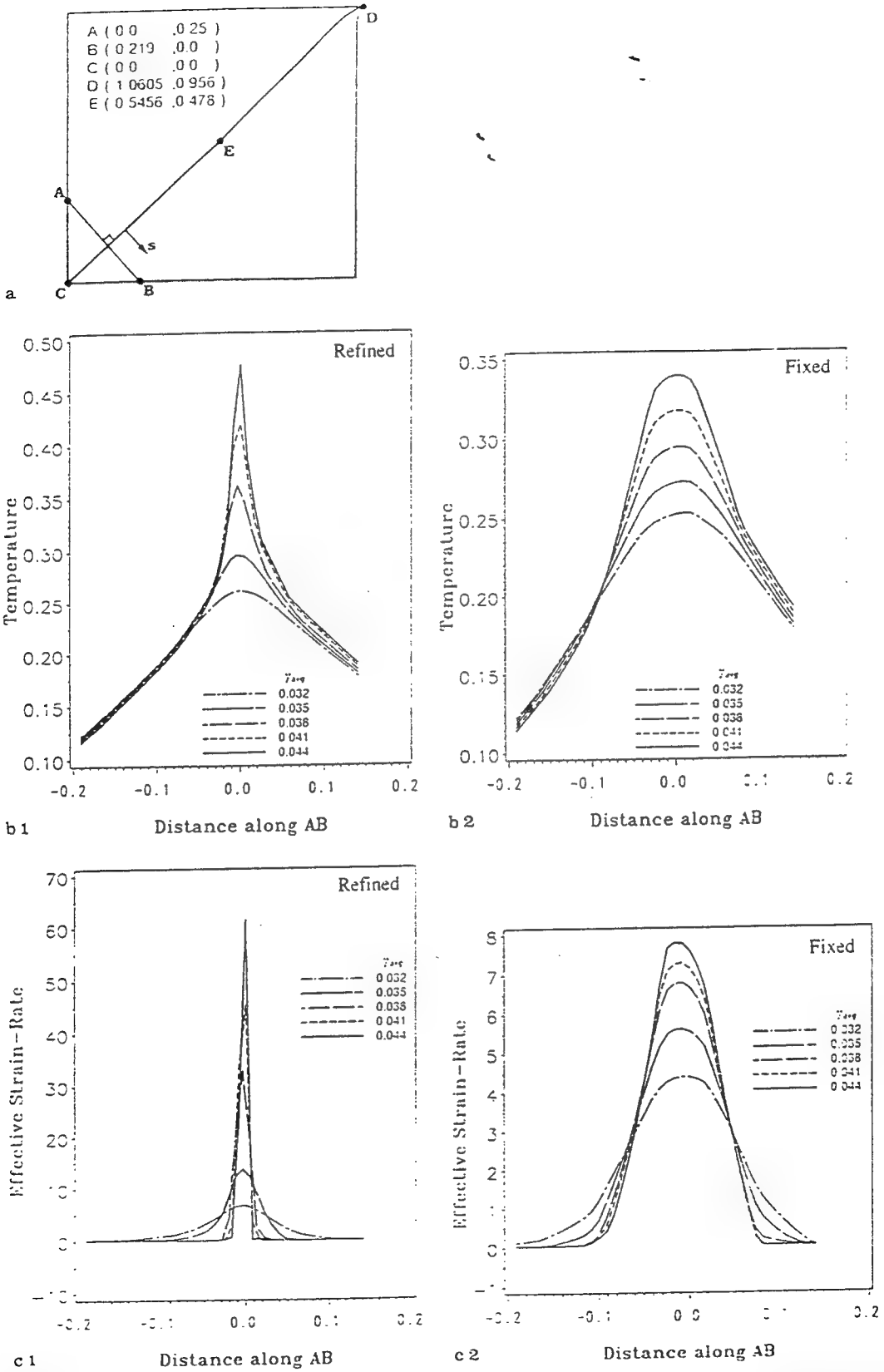

Fig. 6. a Estimated centerline of the shear band, and location of the transverse line AB. b–c variation at $\gamma_{avg} = 0.032$, 0.035, 0.038, 0.041, and 0.044 of the temperature rise θ and the second invariant I of the deviatoric strain-rate tensor on line AB

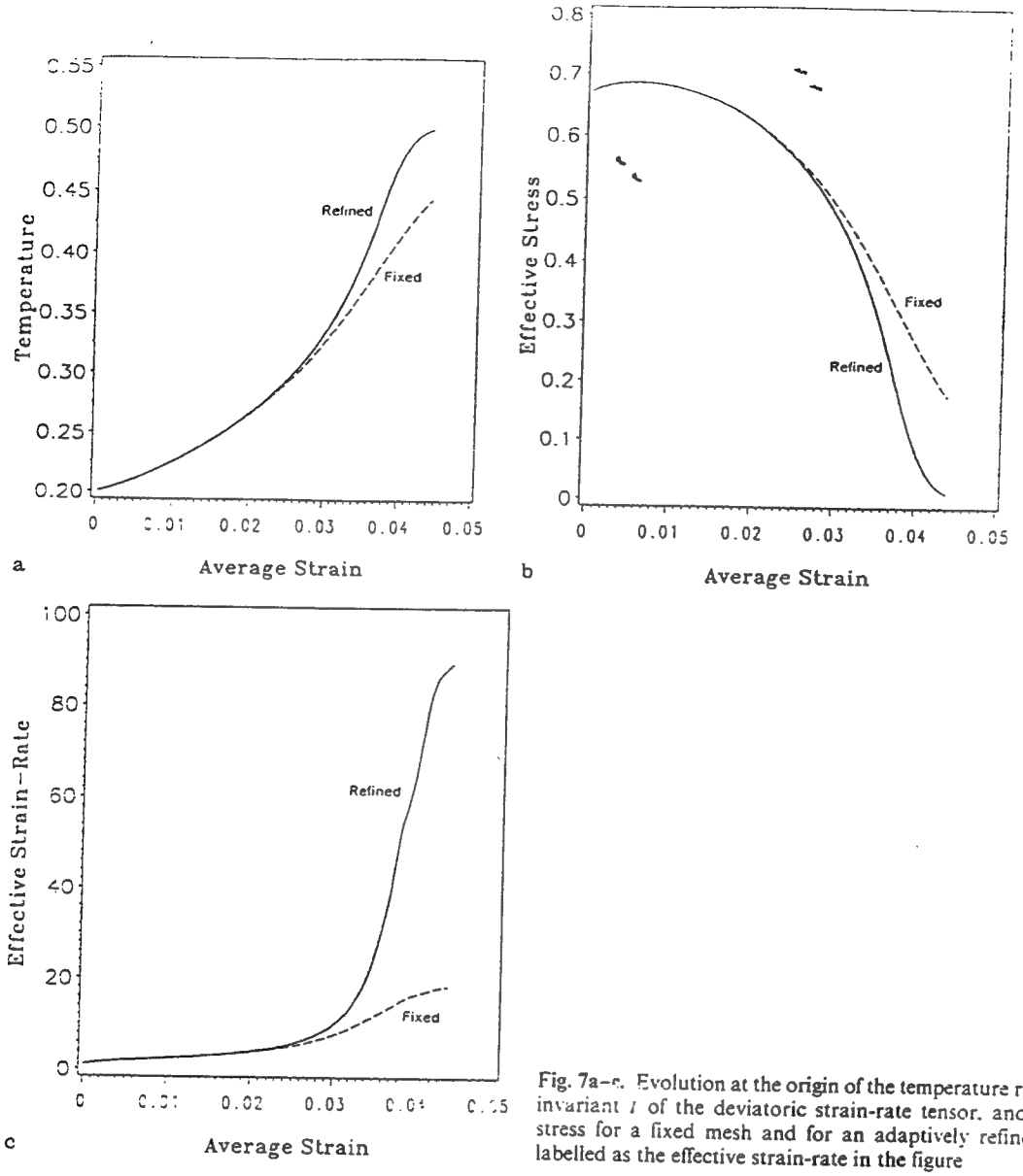

Fig. 7a–c. Evolution at the origin of the temperature rise, the second invariant I of the deviatoric strain-rate tensor, and the effective stress for a fixed mesh and for an adaptively refined mesh. I is labelled as the effective strain-rate in the figure

given number of nodes since they may also depend upon the finite element basis functions used to approximate the solution of the problem. For the refined mesh the second invariant of the deviatoric strain-rate tensor at the origin seems to reach a plateau due to the temperature there approaching the melting point of the material. Once that happens, the effective stress there vanishes. However, the surrounding material still contributes to the strength of the body.

We now investigate the improvement, if any, in the quality of the approximate solution obtained by refining the mesh adaptively. Since the analytical solution of the problem is unknown and there is no hope of finding one in the near future, we compare the approximate solution with a higher-order approximate solution (Hinton and Campbell 1974) obtained by smoothening out the computed solution. Let g be one of the variables to be smoothened. For the four-noded quadrilateral element, we write

$$g(\xi,\eta) = a + b\xi + c\eta + d\xi\eta \tag{17}$$

where (ξ,η) are the coordinates of a point with respect to a set of local coordinate axes, and constants a, b, c, and d are determined from the values of g at the four quadrature points within

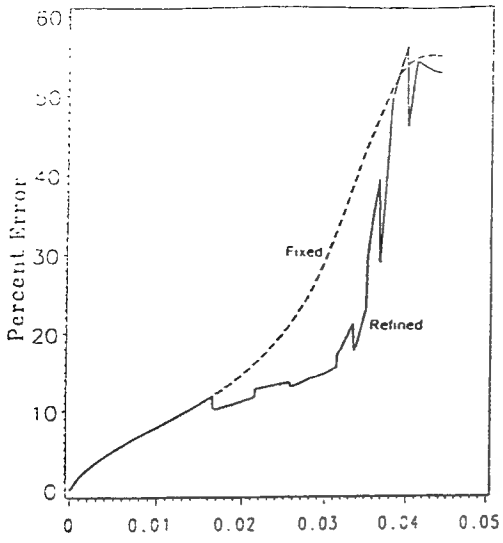

8

Figs. 8 and 9. **8** Comparison of the error in the approximate solution computed with a fixed mesh and an adaptively refined mesh. In each case, the error is determined by comparing the computed solution with a higher-order approximate solution. **9a–d** a Initial nonuniform mesh of 400 elements. **b** Comparison of the evolution at the origin of the temperature rise, second invariant of the deviatoric strain-rate tensor and the effective stress obtained by using meshes refined from two different initial meshes

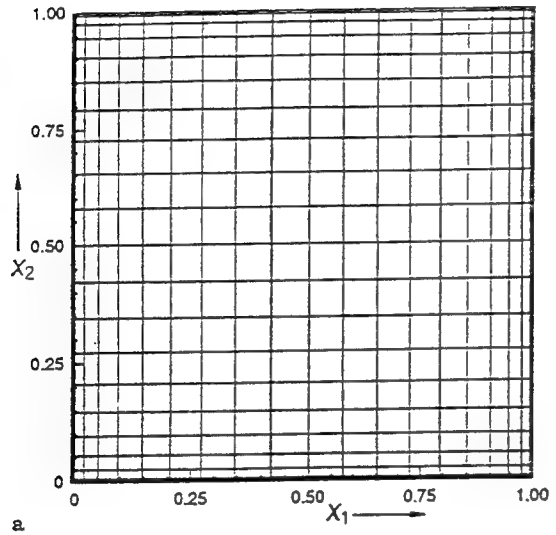

a

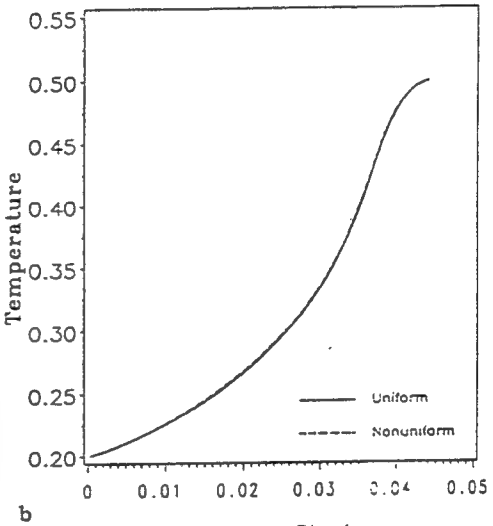

b

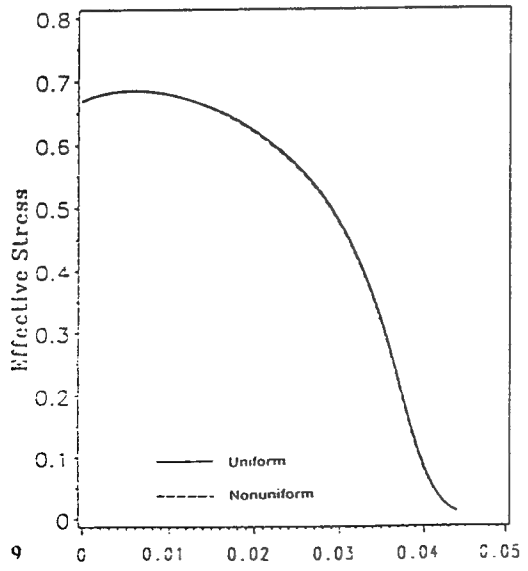

c

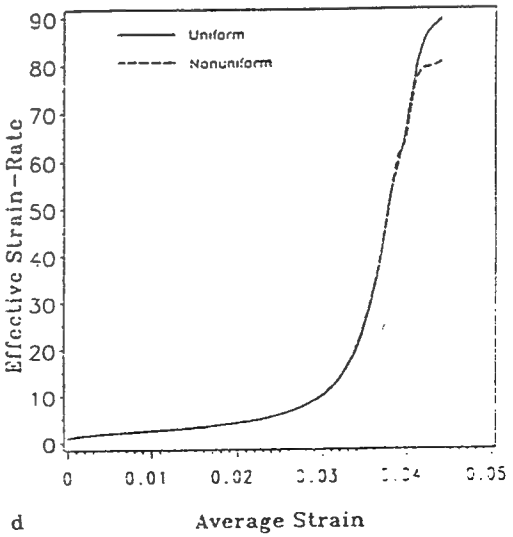

d

the element. We use Eq. (17) to evaluate g at the vertices of the quadrilateral element. The value g_n^* of the smoothened solution at the nth node is given by

$$g_n^* = \frac{1}{N_e} \sum_{m=1}^{N_e} g_{nm}, \tag{18}$$

where N_e equals the number of elements meeting at the node n, and g_{nm} equals the value of g at the nth node belonging to element m. Knowing g^* at each node, we can interpolate its value at any other point by using the finite element basis functions. The percentage error E in the deviatoric strain-rate tensor $\mathbf{D}$ defined by

$$E = \left(\frac{\|\mathbf{e}\|_0^2}{\|\mathbf{e}\|_0^2 + \|\mathbf{D}\|_0^2} \right) \times 100, \tag{19}$$

$$\mathbf{e} = \mathbf{D} - \mathbf{D}^*, \quad \|\mathbf{e}\|_0^2 = \sum_{m=1}^{N_{el}} \int_{\Omega_m} \mathbf{e}^T \mathbf{e} d\Omega, \tag{20.1, 20.2}$$

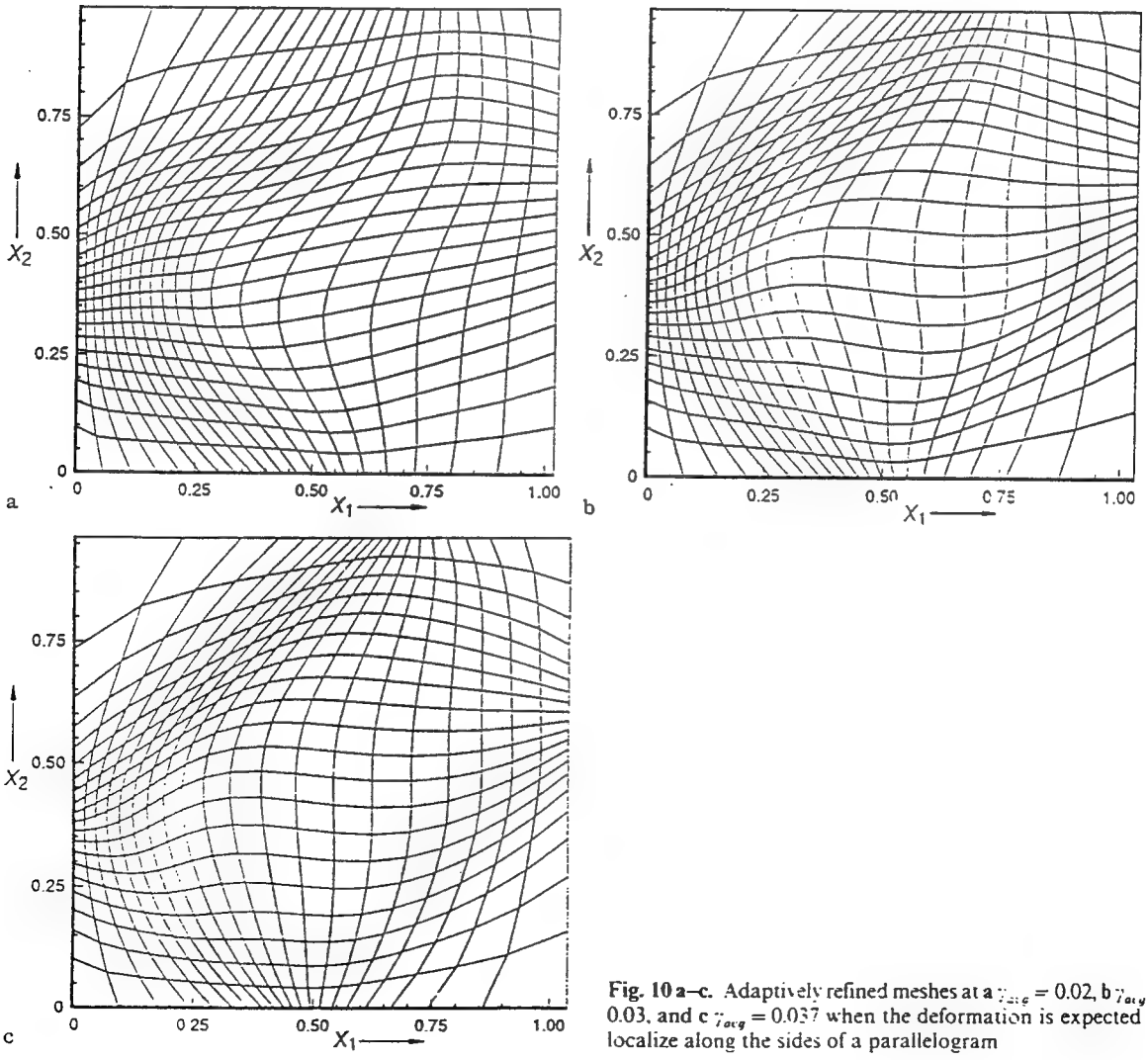

Fig. 10 a–c. Adaptively refined meshes at **a** $\gamma_{avg} = 0.02$, **b** $\gamma_{avg} = 0.03$, and **c** $\gamma_{avg} = 0.037$ when the deformation is expected to localize along the sides of a parallelogram

where N_{el} equals the number of elements in the mesh, is plotted in Fig. 8. The error for the solution obtained by using the adaptively refined mesh is lower for $\gamma_{avg} \leqq 0.037$ and it then suddenly increases to match with that obtained for the solution computed by using a fixed mesh. It probably is due to the large errors caused by smoothening out of the approximate solution in the late stages of the band development when the deformations within the band are very intense. Batra and Ko (1992) found that, contrary to the intuitive thinking, the error as given by Eq. (19) was higher for the approximate solution computed by using a fixed mesh of three-noded triangular elements with 841 nodes as compared to that for a similar mesh with 441 nodes. They remarked that the error measure (19) is rather crude.

Since the adaptively refined meshes are obtained by repositioning the nodes, one might suspect that the solution so obtained will depend upon the initial mesh at time $t = 0$. That such is not case is confirmed by results depicted in Fig. 9 and obtained by using two different initial meshes, namely, a uniform mesh of 400 elements and a nonuniform mesh of 400 elements shown in Fig. 9a. The curves delineating the evolution at the origin of the temperature rise, effective strain-rate and the effective stress, and of the error measure (19) for the two solutions essentially coincide with each other. We note that the error measure is not plotted in Fig. 9.

In an attempt to study the interaction between bands originating from two different locations, Batra and Liu (1990) introduced two identical temperature perturbations with their centers

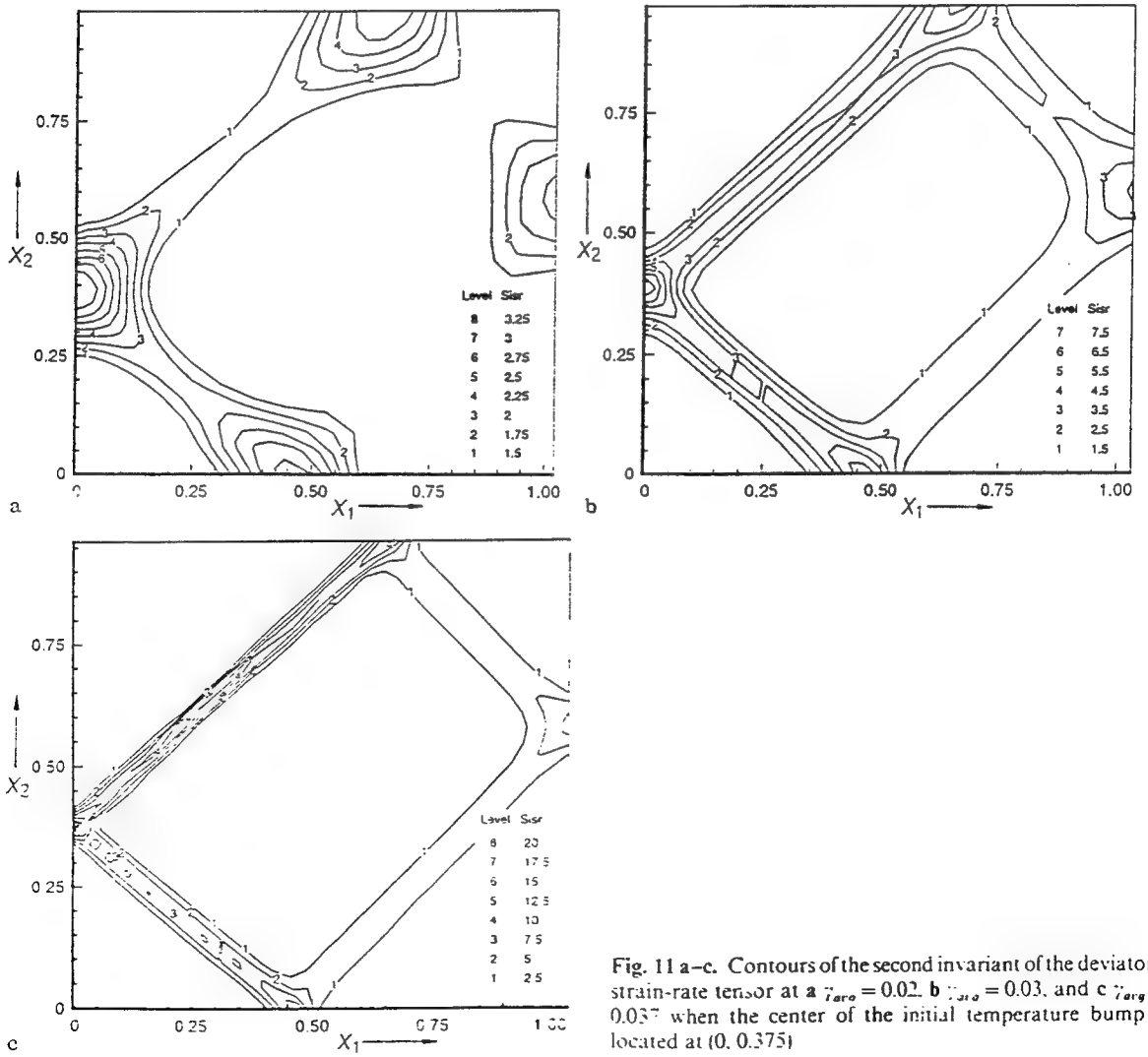

Fig. 11 a–c. Contours of the second invariant of the deviatoric strain-rate tensor at **a** $\gamma_{avg} = 0.02$, **b** $\gamma_{avg} = 0.03$, and **c** $\gamma_{avg} = 0.037$ when the center of the initial temperature bump is located at (0, 0.375)

situated on the vertical centroidal axis and equidistant on either side of the horizontal centroidal axis. Assuming that the deformation of the block was symmetrical about the two centroidal axes, they studied deformations of the region in the first quadrant only and found that deformation localized into regions with their centerlines forming a parallelogram. We analyzed the problem defined in Sect. 2 except that the center of the temperature bump (10.2) is now located at (0, 0.375) rather than at the origin. The initial mesh consisted of 400 uniform quadrilateral elements, the meshes generated at $\gamma_{avg} = 0.02$, 0.03, and 0.037 by using the mesh refinement technique of Sect. 3 and depicted in Fig. 10 show that fine elements are generated within severely deformed regions and coarse elements elsewhere. The contours of the effective strain-rate plotted in Fig. 11 at $\gamma_{avg} = 0.02$, 0.03, and 0.037 show that the material along the side passing through the center of the temperature bump and making an angle of nearly 45° clockwise with the vertical line is deforming more severely than that along the other three sides of the parallelogram. Similar results were obtained by Batra and Liu (1990) who used a fixed mesh of nine-noded quadrilateral elements.

5 Conclusions

We have developed an adaptive mesh refinement technique that generates quadrilateral elements such that the integral of a deformation measure over an element is nearly the same for all elements in the mesh and all interior angles of the elements generated have values between 20° and 160°. The technique is easy to implement in an existing code since it only repositions the nodes and does not change the element connectivity. Values of solution variables at the relocated nodes are obtained by first determining to which element in the previous mesh a particular node belonged, and then interpolating values by using the finite element basis functions. The technique can be easily modified to generate triangular elements obtained by subdividing a quadrilateral into four triangles. Adaptively refined meshes when used to study the localization of the deformation into narrow bands in a thermally softening viscoplastic material give considerably sharper results as compared to those obtained by using a fixed mesh. Computed results for the shear band problem obtained by using adaptively refined meshes are found to be independent of the initial mesh used. The method was quite successful in analyzing the localization problem in which the deformation was expected to concentrate into narrow regions around the sides of a parallelogram.

Acknowledgements

This work was supported by the U.S. Army Research Office Grant DAAL03-91-G-0084 and the U.S. NSF Grant MSS9121279 to the University of Missouri-Rolla. Some of the computations were performed on the Ohio Supercomputer Center and the NSF Sponsored Supercomputer Center in Ithaca, NY.

References

Bai, Y.; Dodd, B. (1992): Adiabatic shear localization. Occurrence, theories and applications. New York: Pergamon Press

Batra, R. C.; Liu, D. S. (1989): Adiabatic shear banding in plane strain problems. J. Appl. Mech. 56, 527–534

Batra, R. C.; Kim, C. H. (1990): An adaptive mesh refinement technique for the analysis of adiabatic shear banding. Mech. Res. Commun. 17, 81–91

Batra, R. C.; Liu, D. S. (1990): Adiabatic shear banding in dynamic plane strain compression of a viscoplastic material. Int. J. Plasticity 6, 231–246

Batra, R. C.; Zhu, Z. G. (1991): Dynamic shear band development in a bimetallic body containing a void. Int. J. Solids Struct. 27, 1829–1854

Batra, R. C.; Ko, K. I. (1992): An adaptive mesh refinement technique for the analysis of shear bands in plane strain compression of a thermoviscoplastic solid. Computational Mech. 10, 369–379

Drew, D. A.; Flaherty, J. E. (1984): In: Gurtin, M. E. (ed): Phase transformations and material instabilities in solids, pp. 37–60. Academic Press

Hinton, E.; Campbell, J. S. (1974): Local and global smoothing of discontinuous finite element functions using a least squares method. Int. J. Num. Meth. Eng. 8, 461–480

Hughes, T. J. R. (1987): The finite element method. Linear static and dynamic finite element analysis. New York: Pergamon Press
Needleman, A. (1989): Dynamic shear band development in plane strain. J. Appl. Mech. 56, 1–9
Pervaiz, M. M.; Baron, J. R. (1988): Commun. Appl. Num. Meth. 4, 97–111
Safjan, A.; Demkowicz, L.; Oden, J. T. (1991): Adaptive finite element methods for hyperbolic systems with application to transient acoustics. Int. J. Num. Meth. Eng. 32, 677–707
Zhu, J. Z.; Zienkiewicz, O. C.; Hinton, O.; Wu, J. (1991): A new approach to the development of automatic quadrilateral mesh generation. Int. J. Num. Meth. Eng. 32, 849–886
Zienkiewicz, O. C.; Zhu, J. Z. (1991): Adaptivity and mesh generation. Int. J. Num. Meth. Eng. 32, 783–810

Communicated by S. N. Atluri, January 22, 1993

On the Propagation of a Shear Band in a Steel Tube

R. C. Batra

Xiangtong Zhang

Department of Mechanical and Aerospace Engineering and Engineering Mechanics, University of Missouri-Rolla, Rolla, MO 65401-0249

Marchand and Duffy tested thin-walled steel tubes in a split Hopkinson torsion bar at a nominal strain-rate of approximately 1600/s and could not determine conclusively whether a shear band initiating at a point in the tube propagated around the circumference in one direction or in both directions. They estimated the speed of propagation to be 520 m/s in the former case and 260 m/s in the latter. Here we simulate their test numerically, and find that the shear band propagates in both directions around the circumference of the tube. When the tube is twisted at a nominal strain-rate of 5000/s, the band speed varies from 180 m/s at the site of the initiation to approximately 1000 m/s at the nearly diametrically opposite point. The band speed increases with an increase in the nominal strain-rate. The material defect is modeled by assuming that a small region near the center of the tubular surface is made of a material weaker than that of the rest of the tube.

1 Introduction

Duffy and his co-workers (Marchand and Duffy, 1988; Hartley et al., 1987) have twisted thin-walled tubular steel specimens in a split Hopkinson bar at a nominal strain-rate of approximately 1600/s to study the initiation, development, and propagation of shear bands. Several investigators, e.g., Molinari and Clifton (1987), Wright and Walter (1987), Batra (1992), Wu and Freund (1984), have analyzed one-dimensional simple shearing problems to delineate factors that influence the initiation and growth of shear bands. Two-dimensional plane strain and axisymmetric problems have been studied numerically by Batra and Zhu (1991), Batra and Zhang (1990), Anand et al. (1988), and Batra and Ko (1992, 1993). Zbib and Jubran (1992) have recently studied numerically a three-dimensional problem involving the development of shear bands in a steel bar pulled in tension. Among the studies enumerated above, Batra and Zhu (1991) estimated the speed of propagation of the contours of maximum principal logarithmic strain in a steel block deformed in plane strain compression. They found that the speed depended upon the magnitude of the strain and the state of deformation of the material into which the contours propagated. Batra and Ko (1992) have developed an adaptive mesh refinement technique that generates small elements in the severely deforming region and coarse elements elsewhere.

Here we study numerically the three-dimensional dynamic thermomechanical deformations of 4340 steel thin tube twisted in a split Hopkinson bar at nominal strain-rates of 1000/s, 5000/s, and 25000/s. It is found that the increase in the nominal strain-rate delays the initiation of the shear band originating from the site of the weaker material, and the speed of propagation of the band, taken here to be the same as the speed of propagation of the contour of the effective plastic strain of two, increases with an increase in the nominal strain-rate. At a nominal strain-rate of 1000/s, the band propagates in both directions around the circumference, and its speed increases from 40 m/s at the site of initiation of the band to 260 m/s by the time it has traversed an angular distance of 150 deg.

2 Formulation of the Problem

We study dynamic, adiabatic thermomechanical deformations of a thin-walled tube governed by the following balance laws of mass, linear momentum and internal energy written in the spatial description.

$$\dot{\rho} + \rho \operatorname{div} \mathbf{v} = 0, \tag{1}$$

$$\rho \dot{\mathbf{v}} = \operatorname{div} \sigma, \tag{2}$$

$$\rho \dot{e} = tr(\sigma \mathbf{D}), \tag{3}$$

where

$$\mathbf{D} = \frac{1}{2}(\operatorname{grad} \mathbf{v} + (\operatorname{grad} \mathbf{v})^T), \tag{4}$$

is the strain-rate tensor, ρ the mass density, $\mathbf{v}$ the present velocity of a material particle, σ the Cauchy stress tensor, e the specific internal energy, and a superimposed dot indicates the material time derivative. In Eq. (3) we have neglected the effect of heat conduction thus presuming that the deformations are locally adiabatic. In view of the rather short time, of the order of a millisecond, needed for the band to form, this assumption is reasonable except possibly for copper whose thermal conductivity is greater than ten times that of steel. Also during the late stages of the shear band development when severe temperature gradients have developed, heat conduction probably plays a crucial role in determining the band width. For the simple shearing problem, Batra and Kim (1991) have shown that the band-width decreases with a decrease in the value of the thermal conductivity; however, no simple relation exists between the band-width and the thermal con-

Contributed by the Materials Division for publication in the JOURNAL OF ENGINEERING MATERIALS AND TECHNOLOGY. Manuscript received by the Materials Division May 4, 1993. Associate Technical Editor: D. Hui.

ductivity. In Eq. (3) we have also assumed that all of the plastic working, rather than 90 to 95 percent, as asserted by Taylor and Quinney (1925), and Sulijoadikusumo and Dillon (1979) is converted into heating.

We assume that the material of the tube is isotropic and for its constitutive relations, we take

$$\sigma = -p\mathbf{1} + \mathbf{s}, \quad p = K\left(\frac{\rho}{\rho_0} - 1\right), \tag{5}$$

$$\dot{\sigma} = \overset{\nabla}{\sigma} + \sigma\,\mathbf{W}^T - \mathbf{W}\,\sigma, \quad \mathbf{W} = \frac{1}{2}(\text{grad}\,\mathbf{v} - (\text{grad}\,\mathbf{v})^T), \tag{6}$$

$$\overset{\nabla}{\mathbf{s}} = 2\mu(\overline{\mathbf{D}} - \overline{\mathbf{D}}^p), \quad tr\,\mathbf{D}^p = 0, \quad \overline{\mathbf{D}} = \mathbf{D} - \left(\frac{1}{3}tr\,\mathbf{D}\right)\mathbf{1}, \tag{7}$$

$$\dot{e} = c\dot{\theta} - p\left(\frac{\dot{\rho}}{\rho^2}\right). \tag{8}$$

Here K is the bulk modulus of the material of the tube, ρ_0 its mass density in the stress-free reference configuration, μ the shear modulus, and c the specific heat. Furthermore, $\overset{\nabla}{\sigma}$ denotes the Jaumann derivative of σ, $\mathbf{W}$ the spin tensor, $\mathbf{s}$ the deviatoric Cauchy stress tensor, and $\overline{\mathbf{D}}$ the deviatoric strain-rate tensor. The deviatoric part $\overline{\mathbf{D}}^p$ of the plastic strain-rate tensor is assumed to be given by

$$\overline{\mathbf{D}}^p = \frac{\dot{\gamma}_p}{\tau}\mathbf{s}, \quad \dot{\gamma}_p = \left(\frac{2}{3}tr(\overline{\mathbf{D}}^p\overline{\mathbf{D}}^p)\right)^{1/2}, \tag{9}$$

$$\tau = (A + B\gamma_p^n)(1 + D\ln\dot{\gamma}_p)(1 - T^m), \quad \gamma_p = \int\dot{\gamma}_p dt, \tag{10}$$

$$T = \frac{\theta - \theta_0}{\theta_m - \theta_0}. \tag{11}$$

Here $\dot{\gamma}_p$ equals the effective plastic strain rate, γ_p the effective plastic strain, τ the equivalent stress, θ_0 the room temperature, θ_m the melting temperature of the material, and A, B, n, D, and m are material parameters. Equation (9) was proposed by Johnson and Cook (1983) based upon the torsion tests of thin tubular specimens conducted at different strain-rates and temperatures. However, the range of temperatures and strain-rates studied is not close to that likely to occur in a shear band problem. For the initial conditions we take

$$\sigma(\mathbf{x}, 0) = \mathbf{0}, \quad \rho(\mathbf{x}, 0) = \rho_0, \quad \mathbf{v}(\mathbf{x}, 0) = \mathbf{0}, \quad \theta(\mathbf{x}, 0) = \theta_0. \tag{12}$$

That is, the body is initially at rest, is stress free at a uniform temperature θ_0, and the initial mass density of every material point is ρ_0. For the boundary conditions, we take

$$\sigma\,\mathbf{n} = \mathbf{0} \quad \text{on the inner and outer surfaces of the tube,} \tag{13}$$

$$\mathbf{v}(x_1, x_2, 0, t) = \mathbf{0}, \tag{14}$$

$$\mathbf{v}(x_1, x_2, L, t) = \omega(t)(x_1^2 + x_2^2)^{1/2}\mathbf{e}, \tag{15}$$

$$\text{grad}\,\theta\cdot\mathbf{n} = 0 \text{ on all bounding surfaces,} \tag{16}$$

where $\mathbf{n}$ is a unit outward normal to the surface, ω is the angular speed of the end surface $x_3 = L$ of the tube, and $\mathbf{e}$ is a unit vector in the surface $x_3 = L$ and is perpendicular to a radial line. The boundary condition (16) is consistent with the assumption that the deformations of the tube are locally adiabatic. The end $x_3 = 0$ of the tube is kept fixed while the other end is twisted at an angular speed $\omega(t)$. We assume that

$$\omega(t) = \begin{cases} \omega_0\, t/20, & 0 \le t \le 20\ \mu s, \\ \omega_0, & t > 20\ \mu s, \end{cases} \tag{17}$$

where ω_0 is the steady value of the angular speed on the end surface $x_3 = L$. The rise time of 20 μs is typical for torsional tests done in a split Hopkinson bar.

3 Computation and Discussion of Results

In order to compute numerical results we assigned following values to various material and geometric parameters.

$$\rho = 7860\ \text{kg/m}^3,\ \mu = 76\ \text{GPa},\ \theta_m = 1520^\circ\text{C},\ c = 473\ \text{J/kg}^\circ\text{C},$$
$$\theta_0 = 25^\circ\text{C},\ A = 792.19\ \text{MPa},\ B = 509.51\ \text{MPa},\ D = 0.014,$$
$$n = 0.26,\ m = 1.03,\ \text{Tube thickness} = 0.38\ \text{mm},$$
$$\text{Inner radius of the tube} = 4.75\ \text{mm},$$
$$\text{axial length of the tube} = 2.5\ \text{mm}. \tag{18}$$

The values of material parameters for the 4340 steel in the Johnson-Cook model are taken from Rajendran (1992). The thickness of the tube, its inner radius and its gage length correspond to that used by Marchand and Duffy (1988) in their tests. The value of the angular speed ω_0 was varied so as to produce the desired nominal strain-rate.

The aforestated problem was solved by using the explicit large scale finite element code DYNA3D (Whirley and Hallquist, 1991). The code computes the size of the time step based on the Courant condition thereby ensuring the stability of the computed solution. For the parameters listed above, the computed shear stress versus nominal shear strain curves for the 4340 steel tube twisted at nominal strain-rates of 1000/s, 5000/s, and 25000/s are depicted in Fig. 1. It is clear that softening of the material because of its being heated up overcomes its hardening due to strain and strain-rate effects at nominal strains of 0.64, 0.67, and 0.78, respectively.

The finite element mesh consisted of 8-noded brick elements with 30 elements along the gage length of the tube, 4 elements across the thickness, and 80 elements along the circumference. A material defect was modeled by presuming that the yield stress in a quasistatic simple compression test for the material in the region consisting of two rows of four elements through the thickness and located near the center of the gage length

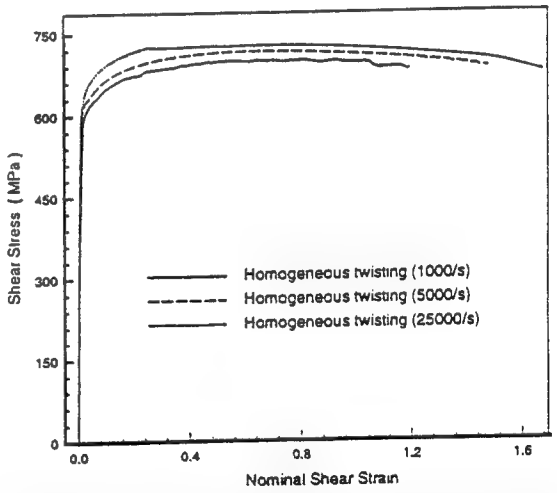

Fig. 1 Shear stress-shear strain curves for homogeneous deformations of the tube at nominal strain-rates of 1000/s, 5000/s, and 25000/s

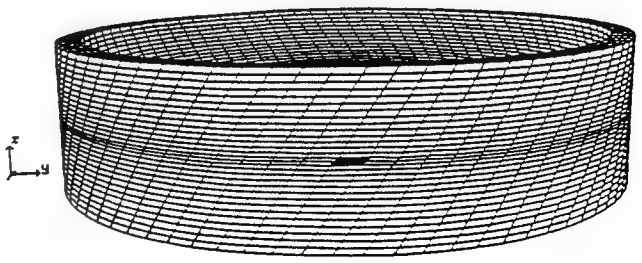

Fig. 2(a)

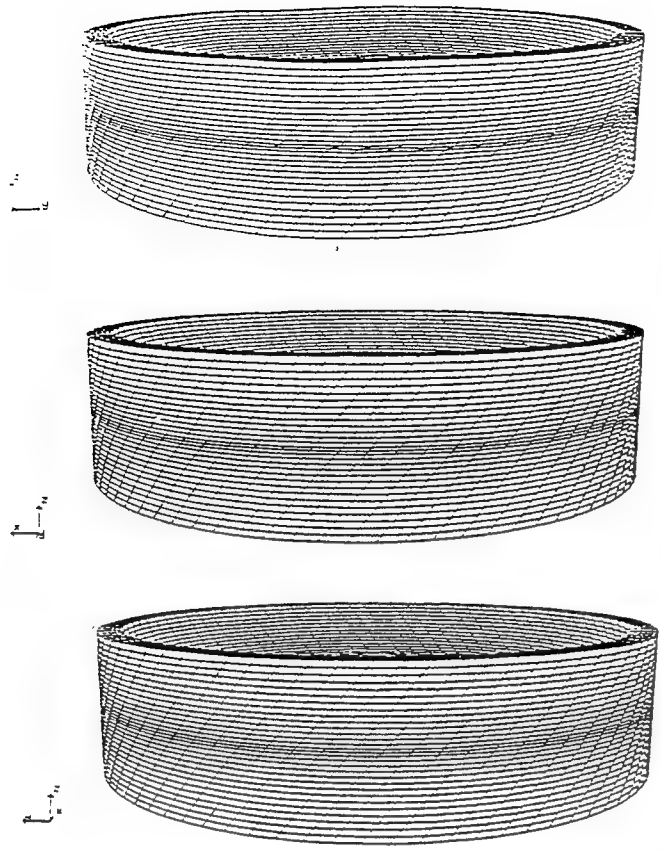

Fig. 2(b)

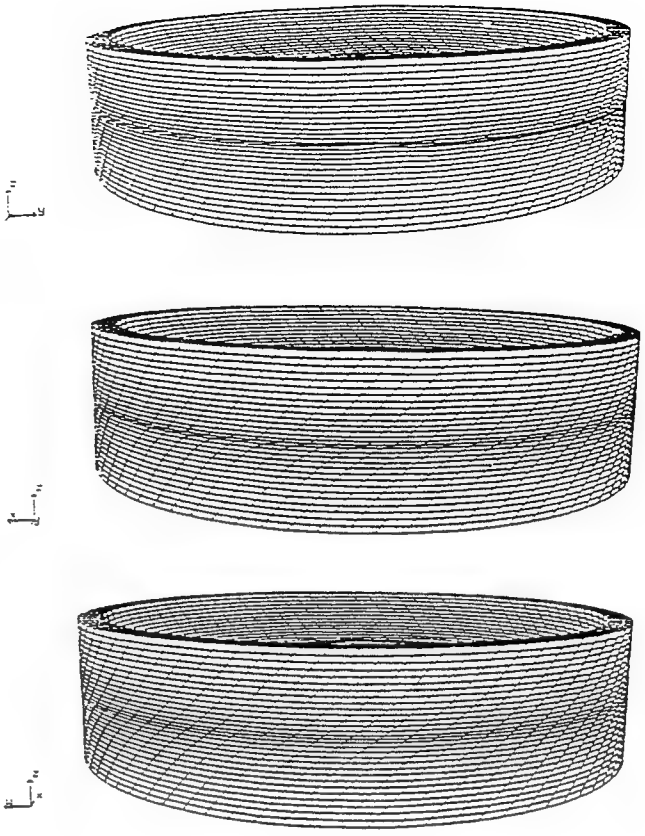

Fig. 2(d)

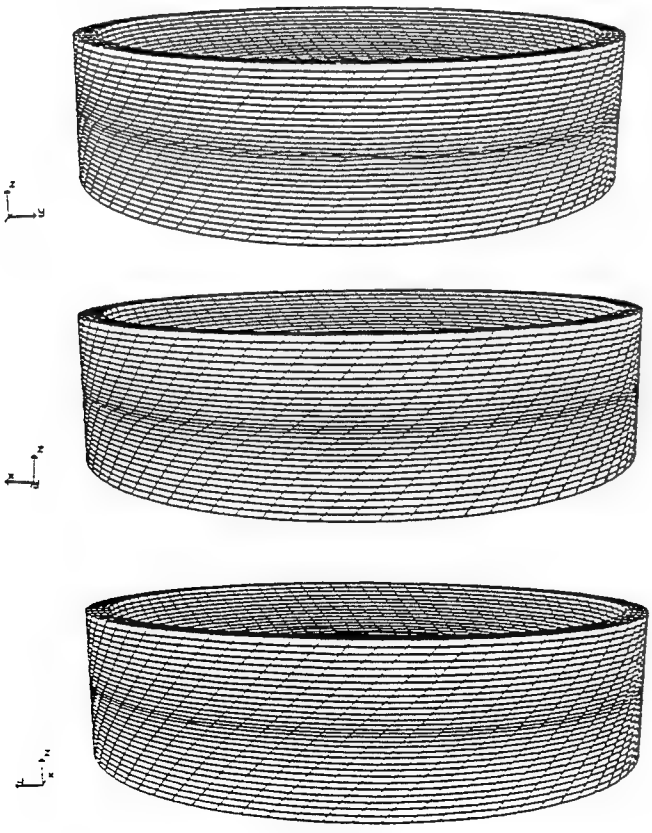

Fig. 2(c)

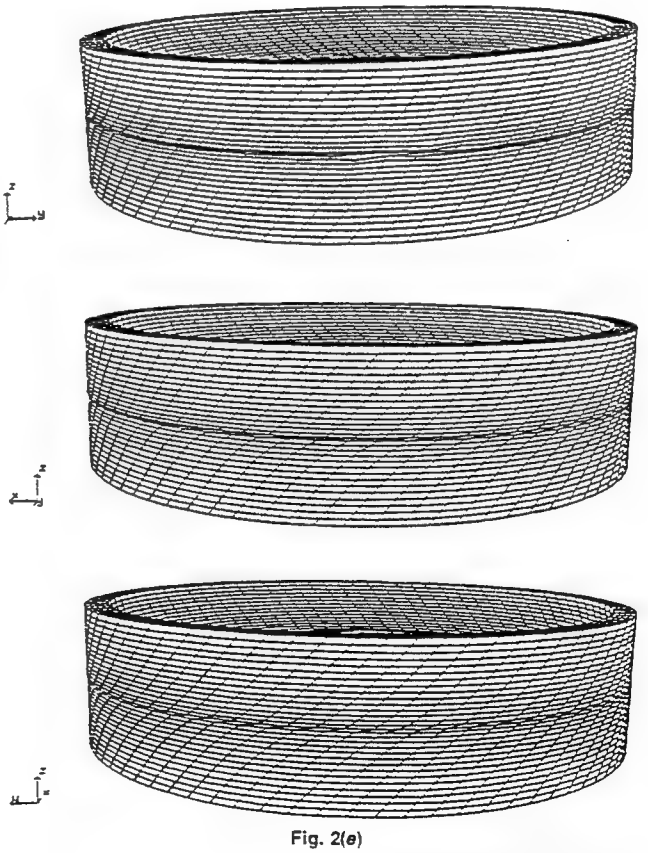

Fig. 2(e)

Fig. 2 Deformed meshes at (a) $t = 140$ μs, (b) 180 μs, (c) 200 μs, (d) 220 μs, and (e) 240 μs for the tube twisted at an average strain-rate of 5000/s. For Figs. 2(b) through (e), the top, middle, and bottom pictures depict views of the deformed mesh from the front, right side, and the back, respectively.

was 10 percent lower than that of the rest of the material. It was accomplished by reducing the aforelisted values of A and B by 10 percent. The two weak elements as seen from the front are shown as shaded in Fig. 2(*a*).

Figure 2 depicts the deformed meshes at time $t = 140$ μs, 180 μs, 200 μs, 220 μs, and 240 μs for the tube twisted at an average strain-rate of 5000/s. The initially vertical lines on the outer surface of the untwisted tube correspond to the lines scribed on the outer surface of the tube and parallel to its axis in Marchand and Duffy's (1988) experiments. The tangent of the angle through which one of these lines rotates clockwise at a point is a measure of the shear strain induced there. At $t = 140$ μs, from the front view of the deformed mesh shown in Fig. 2(*a*), one can conclude that the weaker region has been deformed more than the rest of the body and deformations everywhere except in the small weaker region are essentially homogeneous. In each of Figs. 2(*b*) through Fig. 2(*e*), the top, middle, and bottom pictures depict the deformed meshes as seen from the front, right side, and the back. At $t = 180$ μs (cf. Fig. 2(*b*)) the severe deformations initiating from the weaker region have propagated along the circumference of the tube. However, views from the side and the back reveal that these intense deformations are confined to a small arc length around the weak region. At $t = 200$ μs (Fig. 2(*c*)) and 220 μs (Fig. 2(*d*)), the severe deformations have propagated further along the circumference, but the views from the back indicate that they have not progressed all around the circumference. At $t = 240$ μs (Fig. 2(*e*)), a thin narrow region near the middle of the tube and all around its circumference has undergone significant deformations. The deformed shapes of initial vertical lines match closely with those reported by Marchand and Duffy (1988). Notice that only one element near the center of the tube has been distorted severely. The deformed shapes of initially vertical lines outside of this element are virtually straight and parallel to each other implying thereby that the material there is deforming homogeneously. Once a shear band has formed across the circumference of the tube, the material for subsequent deformations is divided into three regions; the lower one adjoining the fixed end remains essentially stationary, the middle one consisting of one element which undergoes nearly all of the deformations, and the upper one adjoining the moving end which rotates as a rigid body. These results are similar to those obtained by Batra and Kim (1992) who analyzed simple shearing deformations of a viscoplastic block and studied the problem for twelve different materials. In the present work, the deformations were found to be uniform through the thickness of the tube.

In order to delineate further whether a shear band propagates in one direction or in both directions along the circumference of the tube and to determine its speed of propagation, we have plotted in Figs. 3(*a*), 3(*b*), and 3(*c*) the evolution of the effective plastic strain at several points along the circumference of the tube being twisted at nominal strain-rates of 1000 s^{-1}, 5000 s^{-1}, and 25000 s^{-1}, respectively. The angular location of these points is also shown in the figures. These points are on the circumference passing through point A which is at the center of the band in the weak region. We note that the curves corresponding to points B and H, C and G, and D and F coincide with each other implying thereby that the material instability initiating from point A propagates in both directions along the circumference at the same speed. Since the lengths of circular segments AB, BC, CD, and DE are equal to each other, unequal horizontal distance between the curves for points B and C, C and D, and D and E suggests that the speed of propagation is a function of the angular position θ and hence of the state of deformation at a material point. At a nominal strain-rate of 1000/s, the curve for point E is parallel to that for points B, C, and D but such is not the case at nominal strain-rates of 5000/s and 25000/s. An explanation for this could be that there is a strong interaction between the circumferentially propagating disturbances meeting at point E at the higher strain-rates. We note that Batra (1988) pointed out that inertia forces begin playing a noticeable role in the simple shearing problem at a nominal strain-rate of 5000/s.

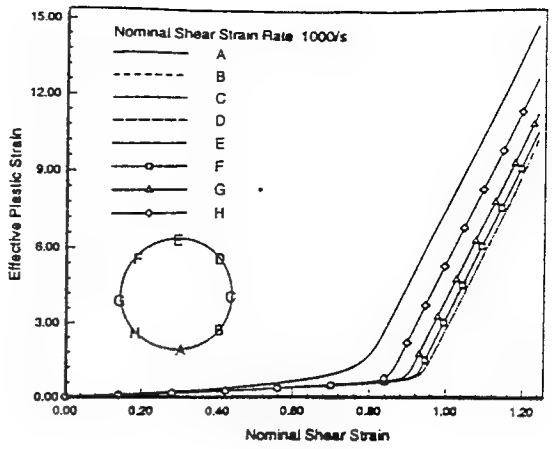

Fig. 3(*a*)

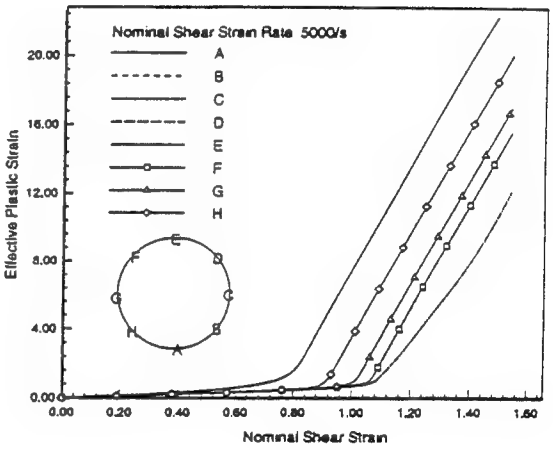

Fig. 3(*b*)

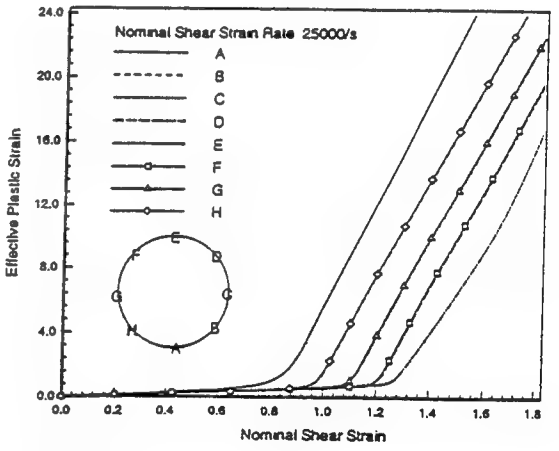

Fig. 3(*c*)

Fig. 3 Evolution of the effective plastic strain at several points along the circumference of the tube. (*a*) $\dot{\gamma}_0 = 1000$/s, (*b*) $\dot{\gamma}_0 = 5000$/s, (*c*) $\dot{\gamma}_0 = 25000$/s.

In Fig. 3 the curves depicting the evolution of the effective plastic strain at points A, B, C, and D after the shear band has initiated stay essentially parallel to each other suggesting that the speed of propagation of different strain levels is nearly the same. In order to illustrate the spatial variation of the speed of propagation of the shear band, we concentrate on how the strain level $\gamma_p = 2$ propagates along the circumference.

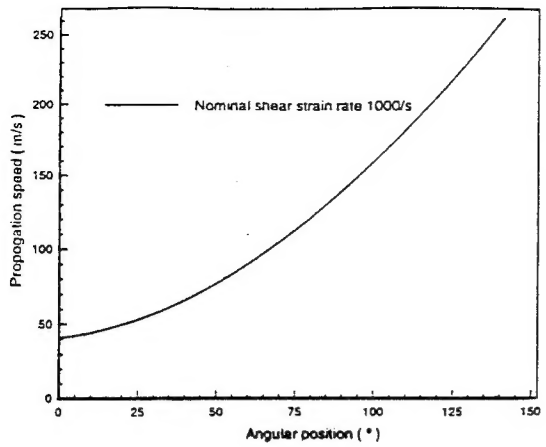

Fig. 4(*a*)

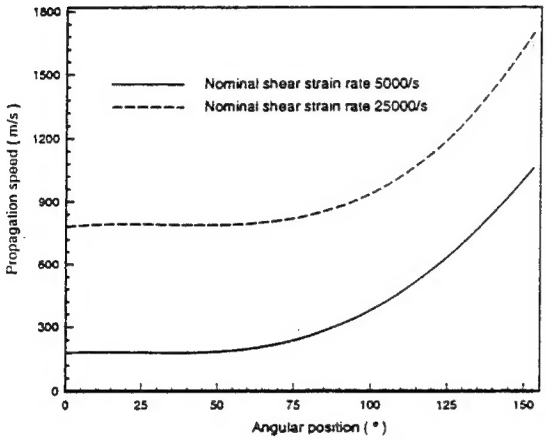

Fig. 4(*b*)

Fig. 4 Variation of the band speed with the angular position. (*a*) $\dot{\gamma}_0 =$ 1000/s, (*b*) $\dot{\gamma}_0 =$ 5000/s, and 25000/s.

The speed of propagation of $\gamma_p = 2$ was determined by dividing the arc length joining the centroids of two adjoining elements by the time taken for γ_p to equal 2 at these points. The value of band speed so computed was assigned to the midpoint of the arc length joining the centroids of the abutting elements. As evidenced in Figs. 4(*a*) and 4(*b*), the band speed varies significantly along the circumference of the tube and at a point increases with the nominal strain-rate. At a nominal strain-rate of 25000/s, the band speed increases from 750 m/s at point A to 1700 m/s at a point 150 deg along the circumference through A. However, at a nominal strain-rate of 1000/s, the band speed varies from 40 m/s to 260 m/s between the same two points. Thus, the band speed is a function of the angular position, and hence of the state of deformation at a point.

The evolution of the homologous temperature at points A through H at the three nominal strain-rates studied is depicted in Fig. 5. The homologous temperature of a material point is defined as its absolute temperature divided by the melting temperature of the material. Since deformations have been assumed to be locally adiabatic, the temperature rise at a point is proportional to the energy dissipated there. As for the evolution of the effective plastic strain-rate, the curves for the evolution of the temperature at points B, C, and D coincide with those for points H, G, and F, respectively. At the nominal strain-rate of 1000/s the curves for points B, C, D, and E are parallel to each other, but at the higher strain-rates of 5000/s and 25000/s curves for points B, C, and D only are parallel to each other.

The torque required to twist the tube as a function of the nominal strain is plotted in Fig. 6. The value of the torque was

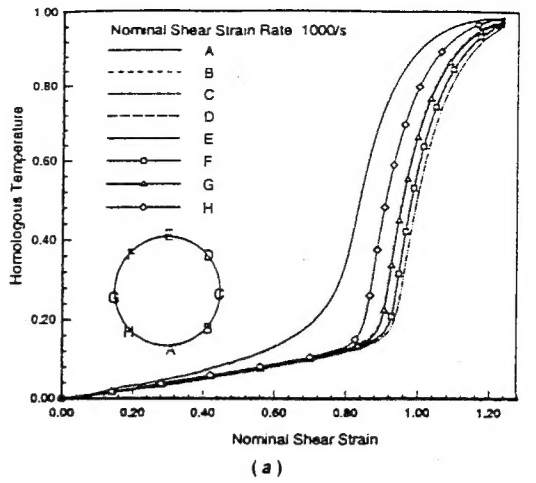

(*a*)

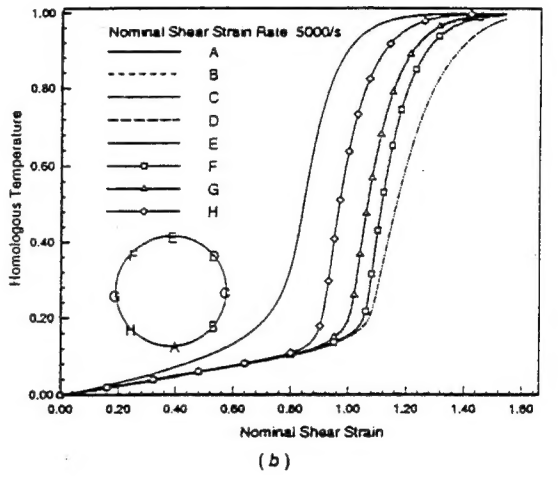

(*b*)

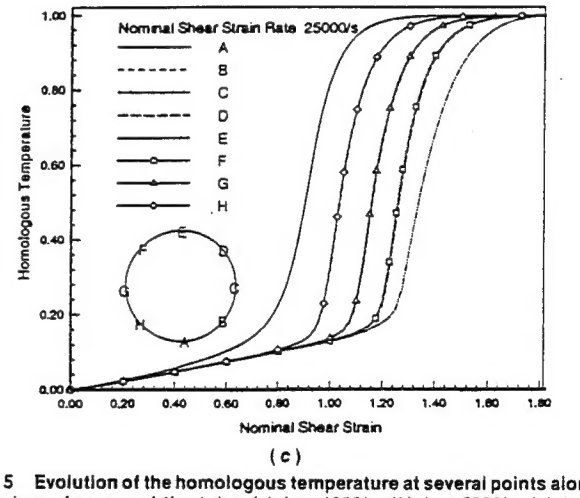

(*c*)

Fig. 5 Evolution of the homologous temperature at several points along the circumference of the tube. (*a*) $\dot{\gamma}_0 =$ 1000/s, (*b*) $\dot{\gamma}_0 =$ 5000/s, (*c*) $\dot{\gamma}_0 =$ 25000/s.

determined from the shear stresses computed at numerous points on the end face of the tube. Since the radius of a material point and hence the tube thickness remains essentially unchanged during the deformations of the tube, the ordinate can also be interpreted as the nominal shear stress. The torque first increases linearly because of the elastic deformations of the tube, and subsequently increases slowly when plastic deformations of the tube are predominant. The peak value of the torque increases with the increase in the nominal strain-rate, however the increase in the peak value of the torque is less when the nominal strain-rate is increased from 5000/s to 25000/s than when it is increased from 1000/s to 5000/s. For each one of

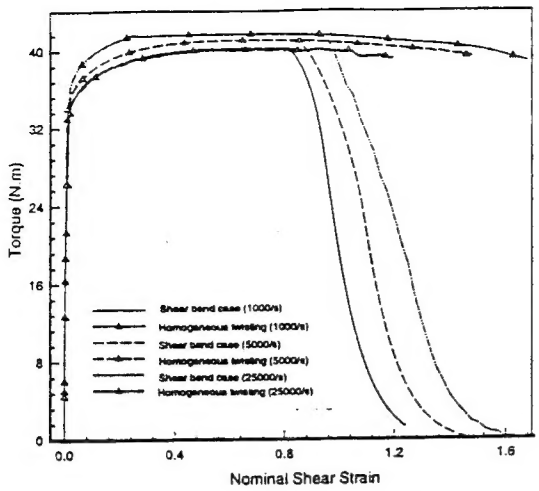

Fig. 6 Torque required to twist the tube versus the nominal strain

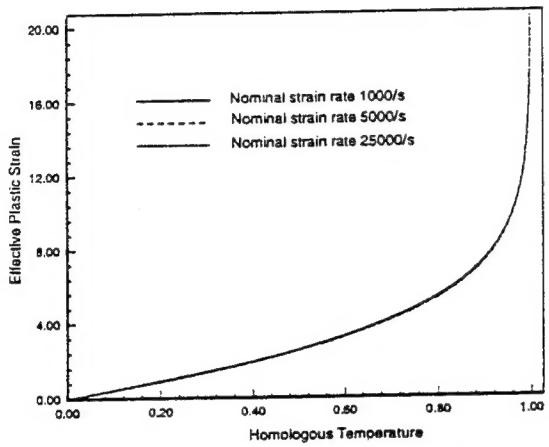

Fig. 7 Effective plastic strain versus the homologous temperature at the band center for the three values of the nominal strain-rate studied

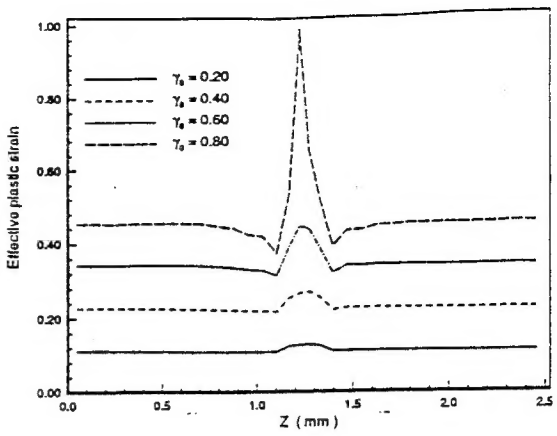

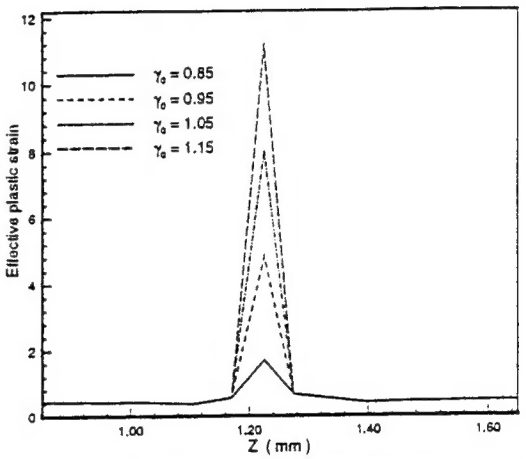

Fig. 8 Distribution, at different times, of the effective plastic strain along an axial line

these three values of the nominal strain-rates, the torque versus nominal shear strain curve follows that for the homogeneous tube well beyond the peak value of the torque. Similar observation was first made by Wright and Batra (1985) who studied a simple shearing problem. The precipitous drop in the torque signifies the initiation of a shear band, and suggests that a shear band initiates at nominal strains of 0.80,0.84, and 0.94 for $\dot{\gamma}_0 = 1000/s$, 5000/s, and 25000/s, respectively. These values of the nominal strains equal essentially those in Fig. 3 at which the effective plastic strain at point A begins to increase sharply. This sudden drop in the torque, and thus the load carrying capacity of the tube, was also observed by Marchand and Duffy (1988) in their tests. Thus, the nominal strain at which a shear band initiates increases with an increase in the value of the nominal strain-rate. The incremental increase in the value of the nominal strain at the initiation of the shear band is more when the nominal strain-rate is increased from 5000/s to 25000/s than that when it is increased from 1000/s to 5000/s. However, in every case the rate of drop of the torque appears to be nearly the same. From Fig. 5 we see that the homologous temperature at point A at the instant of the precipitous drop in the torque equals 0.35, 0.48, and 0.65 for $\dot{\gamma}_0 = 1000/s$, 5000/s, and 25000/s, respectively. For each one of the three values of $\dot{\gamma}_0$, the homologous temperature at point A begins to rise sharply prior to the initiation of the shear band.

Batra and Ko (1993) studied the development of a shear band in a cylindrical block undergoing either axisymmetric or plane strain deformations. They found that the nominal axial strain at the initiation of the shear band was significantly more for axisymmetric deformations as compared to that for plane strain deformations. However, in both cases, the temperature at the band center was nearly the same when the band initiated. They thus stated that the temperature at the band center rather than the nominal strain was a better indicator of when a shear band initiates. The observation made above that the homologous temperature at the band center equalled 0.35, 0.48, and 0.65 for $\dot{\gamma}_0 = 1000/s$, 5000/s, and 25000/s respectively implies that the homologous temperature is not necessarily a good indicator of when a shear band initiates. Nevertheless, we have plotted in Fig. 7 the effective plastic strain versus the homologous temperature at the band center at point A for the three nominal strain-rates studied. It is clear that the three curves essentially coincide with each other. However, it is hard to decipher from them the value of the homologous temperature at the instant of the initiation of the shear band. Why the three curves overlap should be apparent from the following equation (Cao, 1993)

$$\rho c\dot{\theta} = (A + B\gamma_p^n)(1 + D\ln\dot{\gamma}_p)(1 - T^m)\dot{\gamma}_p \qquad (19)$$

obtained from Eqs. (3), (9), and (10). Since $D \ll 1$, Eq. (19) is a functional relationship between the temperature and the effective plastic strain which is virtually independent of the nominal strain-rate, and the three curves in Fig. 7 depict this functional relationship. If the effect of heat conduction were included in Eq. (3), then Eq. (19) will still hold to a good approximation since the thermal conductivity of steel is very small. It should explain the observations of Batra and Ko (1993) who incorporated the effect of heat conduction in the balance of internal energy.

In Figs. 8(a) and 8(b) we have plotted, at different times,

the variation of the effective plastic strain along an axial line for the case when the tube is twisted at a nominal strain-rate of 5000/s. The time is measured in terms of the nominal strain. Note that the horizontal scale in Fig. 8(b) is enlarged to demonstrate vividly the strain distribution. These plots show that once the deformation has localized into a shear band at a nominal strain of 0.85, the material outside of it undergoes essentially no deformations during the subsequent twisting of the tube and all of the deformations are concentrated within the band. When the nominal strain increases from 0.85 to 1.15, the peak value of the effective plastic strain within the band increases from 1.6 to 11.5. Because of the rather coarse mesh used, it is not feasible to ascertain the band-width. A finer mesh could not be used because of the limited computational resources available.

Conclusions

We have studied the initiation, growth, and the propagation of a shear band in a thin steel tube twisted at nominal strain-rates of 1000/s, 5000/s, and 25000/s. One end of the tube is kept fixed while the other end is twisted at a prescribed rate. The inner surface and the mantle of the tube are taken to be traction free, and its deformations are presumed to be locally adiabatic. A material defect has been modeled by presuming that a small region consisting of two elements along the axis of the tube situated midway between the tube ends is made of a material weaker than that of the rest of the tube. This weak region extends through the thickness of the tube and 6 deg across its circumference. It is found that a shear band initiates from the site of the weak region and propagates in both directions along the circumference. Its speed of propagation varies with the nominal strain-rate and also depends upon the state of deformation at a point. At a nominal strain-rate of 1000/s, the band speed varies from 40 m/s to 260 m/s. The nominal strain at which a shear band initiates increases with the nominal strain-rate.

Acknowledgments

This work was supported by the U.S. Army Research Office grant DAAL03-91-G-0084 and the NSF grant MSS9121279 to the University of Missouri-Rolla. We are grateful to Dr. Robert G. Whirley of the Lawrence Livermore Laboratory, California, for his help with the DYNA3D code. Some of the computations were performed on the NSF Supercomputer Center at the Cornell University in Ithaca, NY.

References

Anand, L., Lush, M., and Kim, K. H., 1988, *Thermal Aspects of Shear Localization in Viscoplastic Solids, in Thermal Stresses in Manufacturing*, M. H. Attia and L. Kops, eds., ASME-PED-Vol. 30, New York, pp. 89–103.

Batra, R. C., 1993, *Analysis of Shear Bands in Simple Shearing Deformations of Nonpolar and Dipolar Viscoplastic Materials, in Material Instabilities*, H. M. Zbib, T. G. Shawki, and R. C. Batra, eds., *Applied Mechanics Reviews*, Vol. 45, pp. S123–S131.

Batra, R. C., and Kim, C. H., 1991, "Effect of Thermal Conductivity on the Initiation, Growth, and Bandwidth of Adiabatic Shear Bands," *Int. J. Engr. Sci.*, Vol. 29, pp. 949–960.

Batra, R. C., and Ko, K. I., 1992, "An Adaptive Mesh Refinement Technique for the Analysis of Shear Bands in Plane Strain Compression of a Thermoviscoplastic Solid," *Computational Mechs.*, Vol. 10, pp. 369–379.

Batra, R. C., and Ko, K. I., 1993, "Analysis of Shear Bands in Dynamic Axisymmetric Compression of a Thermoviscoplastic Cylinder," *Int. J. Engr. Sci.*, Vol. 31, pp. 529–547.

Batra, R. C., and Zhang, X. T., 1990, "Shear Band Development in Dynamic Loading of a Viscoplastic Cylinder Containing Two Voids," *Acta Mechanica*, Vol. 85, pp. 221–234.

Batra, R. C., and Zhu, Z. G., 1991, "Shear Band Development in a Thermally Softening Viscoplastic Body," *Computers and Structures*, Vol. 39, pp. 459–472.

Cao, Y., 1993, Private Communications.

Farren, W. S., and Taylor, G. I., 1925, "The Heat Developed During Plastic Extrusion of Metals," *Proc. Roy. Soc. London*, Series A107, pp. 422–451.

Hartley, K. A., Duffy, J., and Hawley, R. H., 1987, "Measurement of the Temperature Profile During Shear Band Formation in Steels Deforming at High Strain Rates," *J. Mech. Phys. Solids*, Vol. 35, pp. 283–301.

Johnson, G. R., and Cook, W. H., 1983, "A Constitutive Model and Data for Metals Subjected to Large Strains, High Strain Rates, and High Temperatures," *Proc. 7th Int. Symp. on Ballistics*, The Hague, The Netherlands, pp. 541–548.

Marchand, A., and Duffy, J., 1988, "An Experimental Study of the Formation Process of Adiabatic Shear Bands in a Structural Steel," *J. Mech. Phys. Solids*, Vol. 36, pp. 251–283.

Molinari, A., and Clifton, R. J., 1987, "Analytical Characterization of Shear Localization in Thermoviscoplstic Materials," ASME *Journal of Applied Mechanics*, Vol. 54, pp. 806–812.

Rajendran, A. M., 1992, "High Strain Rate Behavior of Metals, Ceramics and Concrete," Report #WL-TR-92-4006, Wright-Patterson Air Force Base.

Sulijoadikusumo, A. U., and Dillon, O. W., 1979, "Temperature Distribution for Steady Axisymmetric Extrusion, with an Application of Ti-6Al-4V. I and II," *J. Thermal Stresses*, Vol. 2, pp. 97–112 and 113–126.

Whirley, R. G., and Hallquist, J. O., 1991, "DYNA3D User's Manual (A Nonlinear, 'Explicit,' Three-Dimensional Finite Element Code for Solid and Structural Mechanics)," UCRL-MA-107254, University of California, Lawrence Livermore National Laboratory.

Wright, T. W., and Batra, R. C., 1985, "The Initiation and Growth of Adiabatic Shear Bands," *Int. J. Plasticity*, Vol. 1, pp. 205–212.

Wright, T. W., and Walter, J. W., 1987, "On Stress Collapse in Adiabatic Shear Bands," *J. Mech. Phys. Solids*, Vol. 35, pp. 701–720.

Wu, F. H., and Freund, L. B., 1984, "Deformation Trapping due to Thermoplastic Instability in One-Dimension Wave Propagation," *J. Mech. Phys. Solids*, Vol. 32, pp. 119–132.

Zbib, H. M., and Jubran, J. S., 1992, "Dynamic Shear Banding: A Three-Dimensional Analysis," *Int. J. Plasticity*, Vol. 8, pp. 619–641.